8-2016

Experimental and Numerical Modeling of Wildfire Spread via Fire Spotting

Ali Tohidi
Clemson University

Experimental and Numerical Modeling of Wildfire Spread via Fire Spotting

---

A Dissertation
Presented to
the Graduate School of
Clemson University

In Partial Fulfillment
of the Requirements for the Degree
Doctor of Philosophy
Civil Engineering

---

by
Ali Tohidi
August 2016

Accepted by:
Dr. Nigel Berkeley Kaye, Committee Chair
Dr. Abdul A. Khan
Dr. William C. Bridges Jr.
Dr. Weichiang Pang

Abstract

Wildfire spread via fire spotting phenomenon has three major stages, namely formation and break-off of firebrands from vegetative structures, lofting and transport of them through the ambient velocity field, and finally deposition of firebrands upon landing and ignition of spot fires. This dissertation develops novel models in different areas related to fire spotting phenomenon and integrates them to improve understanding of the firebrand flight through a multiphysics model. In this regard, a mechanical break-off model for the formation of cylindrical firebrands from coniferous trees is proposed; And by geometric scaling analysis, it is shown that the firebrand surface area scales on the mass raised to the $2/3^{rds}$ power. By applying a non-linear regression model to the available experimental data on firebrands, a predictive statistical model for estimating mass and shape distribution of firebrands is proposed, that can be used as realistic input into the current fire spotting models. Further, the aerodynamic behavior of the cylindrical firebrands is characterized by conducting free-fall experiments where it is shown that the governing equations of the transport are highly sensitive to the initial conditions of the release. On this matter, near field dynamics of highly buoyant bent-over plumes are thoroughly characterized and, it is shown, analytically, that the steep trajectories of wildfire plumes necessitate for the inclusion of the boundary layer shearing effects in the mathematical models of the velocity field. Moreover, for the first time, the most extensive large scale wind tunnel experiments of the lofting and downwind transport of non-combusting model firebrands is conducted. It is found that the normalized landing location of firebrands with their maximum rise height have similar probability density functions (PDF) regardless of the aspect ratio. This implies that unlike previous studies the lofting and transport cannot be decoupled. Given the wind tunnel experiment results, a highly scalable coupled stochastic parametric model for firebrand flight is developed by synthesizing `OpenFOAM` and `MATLAB` solutions. This model couples the fine resolution time-varying Large Eddy Simulation (LES) resolved velocity field of the jets/plumes in

non-uniform cross-flow boundary layers with the fully deterministic 3D 6-D.O.F. firebrand transport model. Comparisons between the experiments and corresponding numerical simulations with this model show very good agreement in estimating the average statistics of the flight. Also, it is shown that the transport equations are highly sensitive to the spatial and temporal variations in the ambient velocity field.

Dedication

To my parents,

Narjes & Ebrahim,

who gave me their unconditional *Love*.

Acknowledgments

I wish to thank committee members for their constructive comments, encouragement, and consistent support. Especially, I would like to extend a wholehearted thank you to Dr. Nigel Berkeley Kaye for his brilliant ideas, motivation, guidance, and exclusively, his patience during my Ph.D. program here at Clemson University. I, also, would like to thank Prof. William C. Bridges Jr. for his invaluable guidance in data analysis.

I would like to thank Dr. Samuel Manzello, his research team, and collaborators for providing the firebrand mass and size data for use in this study. Also, I would like to thank Dr. James Michael Grayson for releasing the debris transport model that is adopted in this work. I must thank our lab technologists Mr. Danny Metz, Mr. Scott Black, and Sam Biemann for their crucial assistance in construction and preparation of the experimental setups. I, also, would like to thank Dr. Galen Collier, Dr. Marcin Ziolkowski, and Mr. Ashwin Trikuta Srinath for their help in using Clemson University's Palmetto Cluster.

Also, I would like to thank our undergraduate research assistants Leigh Allison, Francis Filosa, Alexandra Maass, and Meredith Frye and my friends Mehrdad Yousefzadeh, and Parishad Rahbari for their assistance in conducting experiments.

This material is based upon work supported by the *National Science Foundation* (NSF) under Grant *No.*1200560. Any opinions, findings, and conclusions or recommendations expressed in the material are those of the author and do not necessarily reflect the views of the NSF.

Table of Contents

Page

Title Page . . . . . **i**

Abstract . . . . . **ii**

Dedication . . . . . **iv**

Acknowledgments . . . . . **v**

List of Tables . . . . . **viii**

List of Figures . . . . . **x**

1 Introduction **1**
Bibliography 4

2 Statistical description of firebrand size and shape distribution from coniferous trees for use in Metropolis Monte Carlo simulations of firebrand flight distance **9**
2.1 Introduction 10
2.2 Firebrand geometry 14
2.3 Firebrand formation model 17
2.4 Firebrand characterization 25
2.5 Statistical description of firebrands 28
2.6 Summary and conclusions 36
Bibliography 36

3 Free-fall experiments **43**
3.1 Introduction 43
3.2 Firebrand flight numerical model 46
3.3 Free fall experiments 53
3.4 Results 59
3.5 Sensitivity analysis 74
3.6 Concluding remarks 84
Bibliography 86

4 Highly buoyant bent-over plumes in a boundary layer **90**
4.1 Introduction 91
4.2 Evolution equations 94
4.3 Comparison with previous experiments 99
4.4 Influence of source conditions 103

4.5 Model selection criteria case studies . . . 110
4.6 Discussion and conclusions . . . 112
Bibliography . . . 114

5 Wind tunnel experiments . . . 120
5.1 Introduction . . . 120
5.2 Experimental setup . . . 121
5.3 Data acquisition method . . . 128
5.4 Results . . . 133
5.5 Conclusions . . . 142
Bibliography . . . 145

6 Model development . . . 149
6.1 Introduction . . . 149
6.2 Model development . . . 151
6.3 Results . . . 170
6.4 Coupling LES with the transport model . . . 182
Bibliography . . . 185

7 Results . . . 192
7.1 Introduction . . . 192
7.2 Comparison with experimental data . . . 194
7.3 Sensitivity analysis . . . 201
7.4 Conclusions . . . 205
Bibliography . . . 206

8 Concluding remarks . . . 207
Bibliography . . . 210

Appendices . . . 211

A Plume Fluxes Equations . . . 212
Bibliography . . . 218

B High performance scientific computing . . . 219

List of Tables

Page

Table 2.1 Characteristics of the isolated burnt trees in the absence of wind. In the table, abbreviations M.C. and N.A. stand for Moisture Content and Not Available, respectively. 16

Table 2.2 Results of various statistical tests on the firebrand mass (m) from each individual tree in logarithmic domain. Status of the decision on null hypothesis is denoted by h_0 where the value of one rejects the corresponding null hypothesis of the test. DOF stands for the degree of freedom of the test and p-value shows the probability of the test result. The significance level is set to 0.05 for all tests. 33

Table 3.1 Physical properties of the model firebrands used in free experiments. Here, ρ is the mass density, D is the diameter, L is the length, and $\eta = L/D$ is the aspect ratio of the model firebrands. 54

Table 3.2 Specifics of the free fall experiments. D.O.F. stands for degrees of freedom in each set that is number of free falls conducted. 54

Table 3.3 Results of various statistical tests on the measured radial distances in free fall experiments against their corresponding numerical simulations. Null hypothesis status is denoted by h_0 for each test where the value of one rejects the corresponding null hypothesis of the test. DOF stands for the degrees of freedom of the test, and $p - value$ shows the probability of observing a test statistic as extreme as, or more extreme than, the observed value under the null hypothesis. For this parameter small values raises concerns about the credibility of the test. Also, significance level for all tests is set to $\alpha = 0.05$. 77

Table 3.4 Results of the statistical tests, i.e. Kolmogorov-Simirnov, T-, and F-test, on the mean (μ) and standard deviation (σ) of the radial distances obtained from experiments (denoted by subscript $_{Exp}$) and their corresponding numerical simulations (shown by subscript $_{Num}$). The significance level α is 0.05. 79

Table 4.1 Summery of input parameters for various bent-over plume rise models. . . . 93

Table 4.2 Commonly used values of longitudinal (α) and transverse (β) entrainment coefficients for top-hat formulations of the bent-over plume equations. 98

Table 4.3 Velocity ratio, source Froude number, velocity profile power-law exponent, and momentum length scale normalized on the release height for the experimental test cases. The test cases are taken from Contini et al. [2011] (cases 1-4), Contini and Robins [2001] (5-8), Contini et al. [2009] (9-12), and Marro et al. [2014] (13-16). 100
Table 4.4 Ranges of stack and atmospheric boundary layer parameters for the plume cases (1-6) are excerpted from Carson and Moses [1969]. Parameter values in case (7) are adopted based on Bhutia et al. [2010] for small-scale wildfires. 113

Table 5.1 Specifics of the lofting and transport experiments. Where wind setup is the wind tunnel dial that delivers U_0 at the reference height of $z_0 = 0.04\,m$, jet setup denotes dials on blowers that were connected to different regions (I, O) inside the jet nozzle and deliver the jet centerline velocity $U_{j|r=0}$, $\eta = L_z/Lx, y$ is the planks (model firebrands) aspect ratio, and D.O.F. stands for the degrees of freedom (nominal number of releases). 124
Table 5.2 Calculated source parameters of the jet under different settings. 128

Table 6.1 Utilized physical properties in precursor LES of the channel flows. 160
Table 6.2 Initial conditions of the channel flow precursor simulations. 160
Table 6.3 Details of the computational mesh used in precursor LES of the channel flow. 161
Table 6.4 Summary of the utilized boundary conditions in precursor LES of the channel flow. Here, n denotes the normal vector to the patch surface. 163
Table 6.5 Physical properties of the precursor LES of the pipe flows. 164
Table 6.6 Input parameters of the pipe flow precursor simulations. 164
Table 6.7 Summary of the boundary conditions in precursor LES of the pipe flow where, n denotes the normal vector to the patch surface. 166
Table 6.8 Specifics of the JINCF computational domain. 167
Table 6.9 Input (initial) parameters in the LES of the main domain. 167
Table 6.10 Non-dimensional parameters embedded in the physics of JINCF. 168
Table 6.11 Summary of the implemented boundary conditions in LES of the wind tunnel test section. 170

Table 7.1 Parameters of the simulated wind tunnel experiments where p is exponent of the power-law fit to the boundary layer velocity profile, DOF stands for the number of model firebrands released through the generated velocity fields, and R denotes the radius of the initial distribution of model firebrands within the jet nozzle area. 192

List of Figures

Page

Figure 2.1 Schematic diagram of the spotting process from firebrand formation and break-off through lofting, wind driven transport, and spot fire ignition. 12

Figure 2.2 Schematic of a cylindrical firebrand showing the length, diameter, volume, and approximate surface area. 15

Figure 2.3 log-log scale plot of measured firebrand surface area versus mass for different tree sizes. Also shown is a line (not fitted) of slope $\alpha = 2/3$ to illustrate the power law scaling relationship given in (2.8). Data is excerpted from Manzello et al. [2007b, 2008a, 2009] studies. 17

Figure 2.4 Plots of, from top left to right and bottom, the mean firebrand (a) mass (μ_m), (b) surface area (μ_s), (c) aspect ratio (μ_η), (d) length (μ_L), and (e) diameter (μ_D) versus tree height. 18

Figure 2.5 Plots of, from top left to right and bottom, the standard deviation of firebrand (a) mass (σ_m), (b) surface area (σ_s), (c) aspect ratio (σ_η), (d) length (σ_L), and (e) diameter (σ_D) versus tree height. 19

Figure 2.6 Schematic diagram of a cylindrical firebrand supported on the left with (a) bending moment due to the distributed load w=weight per unit length (b) bending moment due to the distributed aerodynamic drag per unit length f_D. 20

Figure 2.7 Plots of firebrand aspect ratio versus length for each of the four tree heights tested by [Manzello et al., 2007b, 2008a, 2009]. 22

Figure 2.8 (Left) log-log plots of calculated firebrand aspect ratio versus corresponding measured surface area for each tree in experimental data. (Right) log-log plots of calculated firebrand aspect ratio versus corresponding measured mass for each tree in experimental data. Pearson and Spearman correlation coefficients along with their significance level are shown above of each pair. P-values less than 0.05 show statistically significant correlations. 27

Figure 2.9 (Left) log-log plots of calculated firebrand aspect ratio versus corresponding measured surface area for each tree in experimental data. (Right) log-log plots of calculated firebrand aspect ratio versus corresponding measured mass for each tree in experimental data. Pearson and Spearman correlation coefficients along with their significance level are shown above of each pair. P-values less than 0.05 show statistically significant correlations. 28

Figure 2.10 (Left) log-log plot of calculated firebrand aspect ratio versus corresponding measured surface area in experimental data. (Right) log-log plots of calculated firebrand aspect ratio versus corresponding measured mass in experimental data. Pearson and Spearman correlation coefficients along with their significance level are shown above of each pair. P-values less than 0.05 show statistically significant correlations. 29
Figure 2.11 Long-normal quantile-quantile plots of the calculated aspect ratio, measured surface area and mass for all trees. Plots are ordered with respect to tree height, $2.4(m), 3.6(m), 4.0(m), 4.5(m)$, from left to right. Also shown is the red dashed line with the slope of one. 30
Figure 2.12 Comparison of the generated describing pairs with corresponding experimental data for each individual tree. 31
Figure 2.13 Comparison of the simulated mass versus surface area with corresponding experimental data for each individual tree. 32
Figure 2.14 Log-log scale plots of firebrand surface area versus mass for 1337 synthetic firebrands and the 1337 firebrands from laboratory measurements of Manzello et al. [2007b, 2008a, 2009] 33
Figure 2.15 (Left) Empirical cumulative density function of mass from all experiments against the Metropolis Monte-Carlo simulations. Statistics of the Kolmogorov-Smirnov test is 0.0688 with p-value of 0.0034 under the null hypothesis which is rejected. (Right) Empirical cumulative density function of surface area from all experiments against the predicted values by regression analysis. Statistics of the Kolmogorov-Smirnov test is 0.0419 with p-value of 0.1872 under the null hypothesis that is accepted. 34
Figure 2.16 Plots of (Left) the average length scales of each firebrand data set and (Right) the coefficient of variation for the length scale versus height. Where, σ is the standard deviation and μ is the mean value. 35

Figure 3.1 Definition of firebrand coordinates and flow angles (γ, ϵ) with respect to global translating non-rotating coordinate system (X_e, Y_e, Z_e), and principal coordinate system of the firebrands (X_p, Y_p, Z_p), respectively. $\bar{V}$ is the firebrand velocity vector, $\bar{W}$ is the ambient velocity vector, and $\bar{U}_p$ is the relative velocity vector of the firebrand in its principal coordinate system. 48
Figure 3.2 From top to bottom, analysis of sensitivity to the initial angles of pitch, roll, and yaw. (Left) Radial distances of the contact point from the projection of the release point to the ground elevation. (Right) Coordinate of the contact point to the ground. $\Delta\theta = 0.01^\circ$ and release height $5\,(m)$. 50
Figure 3.3 From top to bottom, analysis of sensitivity to the initial angles of pitch, roll, and yaw. (Left) Radial distances of the contact point from the projection of the release point to the ground elevation. (Right) Coordinate of the contact point to the ground. $\Delta\theta = 0.01^\circ$ and release height $10\,(m)$. 51

Figure 3.4 From top to bottom, analysis of sensitivity to the initial angles of pitch, roll, and yaw. (Left) Radial distances of the contact point from the projection of the release point to the ground elevation. (Right) Coordinate of the contact point to the ground. $\Delta\theta = 0.01^\circ$ and release height 20 (m). 52
Figure 3.5 Experimental setup of non-combusting firebrand free fall experiments. (Top-left) A custom made frame with designated release location on its beam, and a place for high speed camera to be mounted on the exact location of the release. (Bottom-left) projected release point to the ground on a plane with white background. (Top-right) A sample release procedure from height $H = 9.2\,m$. (Bottom-right) Various aspect ratios of model firebrands. 55
Figure 3.6 Time history of the normalized amplitude of sound waves, i.e. A/A_{max}, with maximum observed amplitude in free fall experiments of a firebrand model with aspect ratio $\eta = 3$ that is released from (Top) $H = 5.6\,m$, and (Bottom) $H = 9.2\,m$. 56
Figure 3.7 (Top-left) Background image with projected release point to the plane of contact by plumb bob; (Top-right) an image from the exact moment when firebrand model contacts to the ground, also referred to as target image. (Bottom-left) Converted traget image from RGB to double; (Bottom-right) identified firebrand model in the image from which the background image is subtracted. 58
Figure 3.8 (Top-left) Shows results of convolving the explained Gaussian filter over the background subtracted image; (Top-right) demonstrates color coded image after stretching the intensities to the range of $0 - 1$. (Bottom-left) shows the original frame of contact in relation to the morphed image by a structuring element (bottom-right) through which centroid coordinates of the firebrand model is calculated. 59
Figure 3.9 (Above) Shows before (left) and after (right) images of an independent ember model drop. (Below-left) shows the composite image of the two instances which illustrates the difference between them. The pale red and green area illustrates the difference, i.e. contact point. (Below-right) shows the coordinates of the contact point which is identified with overlay adjustment on the background subtracted image. Also, shown is a blue line between the projection of the release point to the ground and the contact point of ember to the ground which is marked with a red star. 60
Figure 3.10 (Left) Qualitative comparison between coordinates of contact point to the ground in experiments with corresponding numerical simulations conducted for the release of firebrand models with $\eta = 3$, and D.O.F. of the orders of magnitude of 100. Also, shown are empirical PDFs (middle) and CDFs (right) of the normalized radial distances with the release height. From top to bottom the release height increases from $H = 1.64\,m$ to $5.6\,m$ and $9.23\,m$. 62

Figure 3.11 (Left) Qualitative comparison between coordinates of contact point to the ground in experiments with corresponding numerical simulations conducted for firebrand models with $\eta = 4$, and D.O.F. of the orders of magnitude of 100. Also, shown are empirical PDFs (middle) and CDFs (right) of the normalized radial distances with the release height. From top to bottom the release height increases from $H = 1.64\,m$ to $5.6\,m$ and $9.23\,m$. 63
Figure 3.12 (Left) Qualitative comparison between coordinates of contact point to the ground in experiments with corresponding numerical simulations conducted for firebrand models with $\eta = 6$, and D.O.F. of the orders of magnitude of 100. Also, shown are empirical PDFs (middle) and CDFs (right) of the normalized radial distances with the release height. From top to bottom the release height increases from $H = 1.64\,m$ to $5.6\,m$ and $9.23\,m$. 64
Figure 3.13 (Left) Qualitative comparison between coordinates of contact point to the ground in experiments with corresponding numerical simulations conducted for firebrand models with $\eta = 7.6$, and D.O.F. of the orders of magnitude of 100. Also, shown are empirical PDFs (middle) and CDFs (right) of the normalized radial distances with the release height. From top to bottom the release height increases from $H = 1.64\,m$ to $5.6\,m$ and $9.23\,m$. 65
Figure 3.14 (Left) Qualitative comparison between coordinates of contact point to the ground in experiments with corresponding numerical simulations conducted for firebrand models with $\eta = 9$, and D.O.F. of the orders of magnitude of 100. Also, shown are empirical PDFs (middle) and CDFs (right) of the normalized radial distances with the release height. From top to bottom the release height increases from $H = 1.64\,m$ to $5.6\,m$ and $9.23\,m$. 66
Figure 3.15 (Left) Qualitative comparison between coordinates of contact point to the ground in experiments with corresponding numerical simulations conducted for firebrand models with $\eta = 12$, and D.O.F. of the orders of magnitude of 100. Also, shown are empirical PDFs (middle) and CDFs (right) of the normalized radial distances with the release height. From top to bottom the release height increases from $H = 1.64\,m$ to $5.6\,m$ and $9.23\,m$. 67
Figure 3.16 (Left) Qualitative comparison between coordinates of contact point to the ground in experiments with corresponding numerical simulations conducted for firebrand models with $\eta = 18$, and D.O.F. of the orders of magnitude of 100. Also, shown are empirical PDFs (middle) and CDFs (right) of the normalized radial distances with the release height. From top to bottom the release height increases from $H = 1.64\,m$ to $5.6\,m$ and $9.23\,m$. 68
Figure 3.17 (Left) Qualitative comparison between coordinates of contact point to the ground in experiments with corresponding numerical simulations conducted for firebrand models with $\eta = 25$, and D.O.F. of the orders of magnitude of 100. Also, shown are empirical PDFs (middle) and CDFs (right) of the normalized radial distances with the release height. From top to bottom the release height increases from $H = 1.64\,m$ to $5.6\,m$ and $9.23\,m$. 69

Figure 3.18 (Left) Qualitative comparison between coordinates of contact point to the ground in experiments with corresponding numerical simulations conducted for firebrand models with $\eta = 36$, and D.O.F. of the orders of magnitude of 100. Also, shown are empirical PDFs (middle) and CDFs (right) of the normalized radial distances with the release height. From top to bottom the release height increases from $H = 1.64\,m$ to $5.6\,m$ and $9.23\,m$. 70
Figure 3.19 (Left) Scatter plot of simulated landing locations of firebrand models with $\eta = 18$ that are released from $H = 9.2\,(m)$. (Middle) Plot of radial distance for each independent simulated drop where n denotes the number of independent drops. (Right) Semilogarithmic plot of cumulative mean and standard deviation of the obtained radial distances, as the number of independent drops (simulations) increases up to 10000. 71
Figure 3.20 (Left) Qualitative comparison between coordinates of contact point to the ground in experiments with corresponding numerical simulations conducted for firebrand models with $\eta = 3$, and D.O.F. of the orders of magnitude of 1000. Also, shown are empirical PDFs (middle) and CDFs (right) of the normalized radial distances with the release height. From top to bottom the release height increases from $H = 1.64\,m$ to $5.6\,m$ and $9.23\,m$. 72
Figure 3.21 (Left) Qualitative comparison between coordinates of contact point to the ground in experiments with corresponding numerical simulations conducted for firebrand models with $\eta = 9$, and D.O.F. of the orders of magnitude of 1000. Also, shown are empirical PDFs (middle) and CDFs (right) of the normalized radial distances with the release height. From top to bottom the release height increases from $H = 1.64\,m$ to $5.6\,m$. 73
Figure 3.22 (Left) Qualitative comparison between coordinates of contact point to the ground in experiments with corresponding numerical simulations conducted for firebrand models with $\eta = 12$, and D.O.F. of the orders of magnitude of 1000. Also, shown are empirical PDFs (middle) and CDFs (right) of the normalized radial distances with the release height. The release height is $9.23\,m$. 73
Figure 3.23 (Left) Qualitative comparison between coordinates of contact point to the ground in experiments with corresponding numerical simulations conducted for firebrand models with $\eta = 25$, and D.O.F. of the orders of magnitude of 1000. Also, shown are empirical PDFs (middle) and CDFs (right) of the normalized radial distances with the release height. The release height is $9.23\,m$. 74
Figure 3.24 (Left) Qualitative comparison between coordinates of contact point to the ground in experiments with corresponding numerical simulations conducted for firebrand models with $\eta = 36$, and D.O.F. of the orders of magnitude of 1000. Also, shown are empirical PDFs (middle) and CDFs (right) of the normalized radial distances with the release height. The release height is $9.23\,m$. 74
Figure 3.25 Comparison between cumulative rolling average of the mean and standard deviation of radial distances for $\eta = 3$ released from $H = 1.64\,m$ (left), and $H = 5.6\,m$ (right). 75

Figure 3.26 Comparison between cumulative rolling average of the mean and standard deviation of radial distances for $\eta = 3$ released from $H = 9.2\,m$ (left), and $\eta = 9$ released from $H = 1.64\,m$ (right). 75
Figure 3.27 Comparison between cumulative rolling average of the mean and standard deviation of radial distances for $\eta = 9$ released from $H = 5.6\,m$ (left), and $\eta = 12$ released from $H = 9.2\,m$ (right). 76
Figure 3.28 Comparison between cumulative rolling average of the mean and standard deviation of radial distances for $\eta = 25$ released from $H = 9.2\,m$ (left), and $\eta = 36$ released from $H = 9.2\,m$ (right). 76
Figure 3.29 On the top, horizontal axis shows the mean normalized radial distances measured experimentally, μ_e, versus the mean corresponding numerical results; denoted by μ_n on the vertical axis. On the bottom, horizontal axis shows the standard deviation of the normalized radial distances measured experimentally, σ_e, versus the standard deviation of the corresponding numerical results; denoted by σ_n on the vertical axis. (Color version) Blue, yellow, and green markers show release of firebrand models from $H = 1.64\,m$, $5.6\,m$, and $9.2\,m$ respectively. Also, markers with bold edge line (red edge line in color paper) signify the cases where degrees of freedom is of the order of 1000. 78
Figure 3.30 On the left, logarithmic contour plots of the average normalized radial distances with release height, over one thousand drops, due to variations in embedded length scales in firebrand free fall; On the right logarithmic contour plots of the standard deviation of the normalized radial distances with the released height, over one thousand drops. In addition, parameter space of the second round of free fall experiments is collapsed on the plots where: $\times \longrightarrow (\eta = 3,\ H = 9.2\,m)$, $\square \longrightarrow (\eta = 3,\ H = 5.6\,m)$, $\circ \longrightarrow (\eta = 3,\ H = 1.64\,m)$, $\diamond \longrightarrow (\eta = 9,\ H = 5.6\,m)$, $\triangledown \longrightarrow (\eta = 3,\ H = 1.64\,m)$, $\bigstar \longrightarrow (\eta = 12,\ H = 9.2\,m)$, $+ \longrightarrow (\eta = 25,\ H = 9.2\,m)$, $\triangle \longrightarrow (\eta = 3,\ H = 9.2\,m)$. 79
Figure 3.31 On the left, vertical axis shows the mean radial distances for the numerical simulations where the $\pm 20\%$ change in force coefficients is implemented and results, i.e. $\pm\mu$, are drawn against the corresponding estimations of the original numerical model; denoted by μ_n on the horizontal axis. On the right, vertical axis shows the standard deviation of the radial distances for the numerical simulations where the $\pm 20\%$ change in force coefficients is implemented and results, i.e. $\pm\sigma$, are drawn against the corresponding estimations of the original numerical model; denoted by σ_n on the horizontal axis. (Color version) red and blue markers show 20% increase and decrease, respectively. In addition, the (pale brown) dashed and the (green) dotted lines show 20% and 10% change from the solid line with slope $1 : 1$, respectively. 80

Figure 3.32 On the left, vertical axis shows the mean radial distances for the numerical simulations where the ±20% change in moment coefficients is implemented and results, i.e. $\pm\mu$, are drawn against the corresponding estimations of the original numerical model; denoted by μ_n on the horizontal axis. On the right, vertical axis shows the standard deviation of the radial distances for the numerical simulations where the ±20% change in moment coefficients is implemented and results, i.e. $\pm\sigma$, are drawn against the corresponding estimations of the original numerical model; denoted by σ_n on the horizontal axis. (Color version) red and blue markers show 20% increase and decrease, respectively. In addition, the (pale brown) dashed and the (green) dotted lines show 20% and 10% change from the solid line with slope 1 : 1, respectively. 81

Figure 3.33 On the left, vertical axis shows the mean radial distances for the numerical simulations where the +20% change in density is implemented and results, i.e. $+\mu$, are drawn against the corresponding estimations of the original numerical model; denoted by μ_n on the horizontal axis. On the right, vertical axis shows the standard deviation of the radial distances for the numerical simulations where the +20% change in density is implemented and results, i.e. $+\sigma$, are drawn against the corresponding estimations of the original numerical model; denoted by σ_n on the horizontal axis. (Colored version) the (pale brown) dashed and the (green) dotted lines show 20% and 10% change from the solid line with slope 1 : 1, respectively. 82

Figure 3.34 On the left, vertical axis shows the mean radial distances for the numerical simulations where the +20% change in mass moment of inertia components (I_x, I_y, I_z) is implemented and results, i.e. $+\mu$, are drawn against the corresponding estimations of the original numerical model; denoted by μ_n on the horizontal axis. On the right, vertical axis shows the standard deviation of the radial distances for the numerical simulations where the +20% change in mass moment of inertia components (I_x, I_y, I_z) is implemented and results, i.e. $+\sigma$, are drawn against the corresponding estimations of the original numerical model; denoted by σ_n on the horizontal axis. (Color version), the (pale brown) dashed and the (green) dotted lines show 20% and 10% change from the solid line with slope 1 : 1, respectively. 83

Figure 4.1 Image of the smoke plume rising from the 2005 Buncefield oil depot fire (copyright Thames Valley Police). 92

Figure 4.2 Plots of experimental trajectory (squares) for cases 1-4 (left to right and down) listed in Table 4.3 along with model results for Hoult and Weil [1972] - solid & thick dashed lines, Abraham [1963]/Ooms and Mahieu [1981] - dot-dashed & dotted lines, and the Briggs [1984] generalized algebraic equation (4.14) - thin dashed line. 102

Figure 4.3 Plots of experimental trajectory (squares) for cases 5-8 (left to right and down) listed in Table 4.3 along with model results for Hoult and Weil [1972] - solid & thick dashed lines, Abraham [1963]/Ooms and Mahieu [1981] - dot-dashed & dotted lines, and the Briggs [1984] generalized algebraic equation (4.14) - thin dashed line. 103
Figure 4.4 Plots of experimental trajectory (squares) for cases 9-12 (left to right and down) listed in Table 4.3 along with the model results. Lines are the same as for Figure 4.2. 104
Figure 4.5 Plots of experimental trajectory (squares) for cases 13-16 (left to right and down) listed in Table 4.3 along with the model results. Lines are the same as for Figure 4.2. 105
Figure 4.6 Log-log scale contour plots of z_{45} as a function of Fr and μ with z_{45} scaled on (left) z_m and (right) z_f. 106
Figure 4.7 Contour plots of $\chi = z_{45.p}/z_{45.u}$ as a function of Fr and μ for $p = 0.1$ and (a) $z_m/h_s = 0.1$; (b) $z_m/h_s = 1$; (c) $z_m/h_s = 10$; (d) $z_m/h_s = 100$. 109
Figure 4.8 Contour plots of $\chi = z_{45.p}/z_{45.u}$ as a function of Fr and μ for $p = 0.2$ and (a) $z_m/h_s = 0.1$; (b) $z_m/h_s = 1$; (c) $z_m/h_s = 10$; (d) $z_m/h_s = 100$. 110
Figure 4.9 Contour plots of $\chi = z_{45.p}/z_{45.u}$ as a function of Fr and μ for $p = 0.3$ and (a) $z_m/h_s = 0.1$; (b) $z_m/h_s = 1$; (c) $z_m/h_s = 10$; (d) $z_m/h_s = 100$. 111
Figure 4.10 Contour plots of $\chi = z_{45.p}/z_{45.u}$ as a function of Fr and μ for $p = 0.4$ and (a) $z_m/h_s = 0.1$; (b) $z_m/h_s = 1$; (c) $z_m/h_s = 10$; (d) $z_m/h_s = 100$. 112
Figure 4.11 Contour plot of $\chi = z_{45.p}/z_{45.u}$ as a function of U_0/u_0 and z_m/h_s for $Fr = 1.2$. Symbols are given in Table 4.4. 113
Figure 4.12 Contour plot of $\chi = z_{45.p}/z_{45.u}$ as a function of U_0/u_0 and z_m/h_s for $Fr = 4.0$. Symbols are given in Table 4.4. 114
Figure 4.13 Contour plot of $\chi = z_{45.p}/z_{45.u}$ as a function of U_0/u_0 and z_m/h_s for $Fr = 6.0$. Symbols are given in Table 4.4. 115

Figure 5.1 Polyurethane firebrand models; Scale shown is 1 cm in the image. 123
Figure 5.2 (Left) Inside the wind tunnel chamber where the surface roughness elements and spire elements are installed. Also, on the right, the camera position at the side view of the release point (jet location) is shown. 124
Figure 5.3 Details of the mounted air jet underneath of the wind tunnel. Also, shown are blowers, and the flow straightener. 125
Figure 5.4 Shown are vertical profiles of the boundary layer horizontal (stream-wise) velocity component measured in the wind tunnel. Also, U_0 is the horizontal velocity of the corresponding power-law fits at reference height $z_0 = 0.04\,m$. 126
Figure 5.5 On the left are the time averaged vertical velocities of the jet at the centerline $r = 0$ where r is the radial distance from the jet center; And shown on the right are cross section vertical velocities which are measured at $z = 0.138\,m$ from the nozzle exit. 127
Figure 5.6 On the left are the time averaged vertical velocities of the jet at the centerline $r = 0$ where r is the radial distance from the jet center; And shown on the right are cross section vertical velocities which are measured at $z = 0.138\,m$ from the nozzle exit. 127
Figure 5.7 An extracted calibration image that shows the utilized scale. There are four points on the scale that build a square with sides of $100\,mm$, and the other two are used to check the calculated picture ratio. 129

Figure 5.8 (Left) Color coded background image, with light intensities, constructed by averaging over at least 100 empty frames. (Right) an original (unprocessed) empty frame from the test section while the velocity field is running. 130
Figure 5.9 The utilized rotationally symmetric low-pass *Gaussian* filter that is used for noise reduction. The given height is color coded with the intensity range before noise reduction. 131
Figure 5.10 (Top-left) Untouched image from a model firebrand model during its flight through the velocity field. (Top-right) Shown is the result of background subtraction and the *Guassian* filter convolution on the original image. The image with mapped intensity along with the morphologically opened image are shown at the bottom-left and bottom right, respectively. The dot in the middle is a model firebrand with $\eta = 1$ that is identified in frame 1035 of the video, that is 17 s after the release operation has started. 132
Figure 5.11 Calculated trajectories of the model firebrands with aspect ratio $\eta = 1$ in an experimental case where the boundary layer reference velocity was $U_0 = 2.23\, m/s$, and the jet centerline velocity at the exit was $8.05\, m/s$. 132
Figure 5.12 The identified pattern in complete trajectories by calculating adjacent differencing of the rise height (left). On the right shown are samples of the incomplete or partially complete trajectories that do not follow the same pattern as the completed ones. 134
Figure 5.13 Obtained trajectories from the image processing analysis. Presented data are trajectories of the cubic firebrand models with longitudinal and side aspect ratio of one, i.e. $\eta = \eta_s = 1$. From left to right, the reference velocities of the wind tunnel boundary layer are 1.79, 2.23, and $2.85\,(m/s)$, and from top to bottom, the jet centerline velocities are 8.05, 9.0, and $12\,(m/s)$. 135
Figure 5.14 Obtained trajectories from the image processing analysis. Presented data are trajectories of the cylindrical firebrand models with longitudinal aspect ratio $\eta = 4$. From left to right, the reference velocities of the wind tunnel boundary layer are 1.79, 2.23, and $2.85\,(m/s)$, and from top to bottom, the jet centerline velocities are 8.05, 9.0, and $12\,(m/s)$. 136
Figure 5.15 Obtained trajectories from the image processing analysis. Presented data are trajectories of the cylindrical firebrand models with longitudinal aspect ratio $\eta = 6$. From left to right, the reference velocities of the wind tunnel boundary layer are 1.79, 2.23, and $2.85\,(m/s)$, and from top to bottom, the jet centerline velocities are 8.05, 9.0, and $12\,(m/s)$. 137
Figure 5.16 Shown are the empirical (kernel) probability density functions (PDF) of z_{max}/z_m for different aspect ratios, under various initial conditions of the wind tunnel experiments. From left to right, U_0 is constant while $U_{j|r=0}$ is increasing. From top to bottom, U_0 is increasing and $U_{j|r=0}$ is constant. 138

Figure 5.17 Shown are the empirical (kernel) probability density functions (PDF) of x_l/z_m for different aspect ratios, under various initial conditions of the wind tunnel experiments. From left to right, U_0 is constant while $U_{j|r=0}$ is increasing. From top to bottom, U_0 is increasing and $U_{j|r=0}$ is constant. 139
Figure 5.18 Shown are the empirical (kernel) probability density functions (PDF) of x_l/z_{max} for different aspect ratios, under various initial conditions of the wind tunnel experiments. From left to right, U_0 is constant while $U_{j|r=0}$ is increasing. From top to bottom, U_0 is increasing and $U_{j|r=0}$ is constant. 140
Figure 5.19 Illustrated are variations of the mean (top) and standard deviation (bottom) of the normalized landing location (left), and the normalized rise height (right) of model firebrands with respect to Ω. 141
Figure 5.20 Contour plots of the mean x_l/z_m (left) and the mean z_{max}/z_m (right) for model firebrands with aspect ratio $\eta = 1$ within the parameter space of Ω-$U_0/U_{j|r=0}$ 142
Figure 5.21 Contour plots of the mean x_l/z_m (left) and the mean z_{max}/z_m (right) for model firebrands with aspect ratio $\eta = 4$ within the parameter space of Ω-$U_0/U_{j|r=0}$ 143
Figure 5.22 Contour plots of the mean x_l/z_m (left) and the mean z_{max}/z_m (right) for model firebrands with aspect ratio $\eta = 6$ within the parameter space of Ω-$U_0/U_{j|r=0}$ 143

Figure 6.1 Illustrated is the computational domain of the Large Eddy Simulations. Also, shown are the dimensions of the domain. (Color version) The pink rectangular prism is the wind tunnel's test section where the model firebrands are released, the yellow (smaller) rectangular prism is the precursor channel flow domain, and the blue cylinder is the precursor pipe flow domain. 152
Figure 6.2 Graphical representation of the CM3 mesh from different view angles. From top left to bottom right, side view angle in $x-z$, top view angle in $x-y$ plane, side view angle in $y-z$ plane, and finally an azimuth view. 161
Figure 6.3 Shown are the pairs of periodic (cyclic) boundary conditions used in the precursor simulations. In OpenFOAM terminology, patch stands for boundary surface. 162
Figure 6.4 Perspective view from the pipe flow domain. 165
Figure 6.5 Cross-section view of the O-grid mesh used in pipe flow precursor simulations. The maximum and minimum mesh size are $0.00268\,m$ and $0.000438\,m$, respectively. 165
Figure 6.6 Perspective view of the computational domain discretized with hexahedral cells. Throughout the wind tunnel test section, the mesh size is kept uniform ($\Delta x = \Delta y = \Delta z = 0.01m$) except the jet bounding strips where the minimum and maximum mesh size are $0.00268\,m$ and $0.000438\,m$, respectively. The total number of cells is $11,696,860$ with $34,944,452$ internal faces. 169
Figure 6.7 Shown are results of mesh convergence study for precursor LES of channel flow with W2 setting and three different computational mesh (CM1-CM3). See table 6.3 for details of the simulations' setup. 171

Figure 6.8 Distribution of relative error through height for mesh types CM1-CM3. See table 6.3 for details of the simulations' setup. On the vertical axes $U_{p.f.}$ stands for the power-law fit velocity profile values, and the horizontal line shows 5% error margin. 172
Figure 6.9 Comparison of boundary layer velocity profile throughout the height of the wind tunnel section with results from precursor LES of the channel flow for boundary layer setup W1 (left) and W2 (right). The computational mesh is CM3. 174
Figure 6.10 Development of the boundary layer velocity field (in $x-z$ centerline plane) where the reference velocity is $2.85\,(m/s)$ at $0.04\,m$ reference height. From top to bottom, shown are the contour plots of velocity at 20.06, 20.12, 20.18, and $20.24h/U_{j|r=0}$ time unit after the start of simulations. The equivalent time interval is $0.01\,s$. 175
Figure 6.11 Sample vorticity structures over the floor (left) and ceiling (right) walls of the channel flow domain. 175
Figure 6.12 Comparison of the time-averaged and instantaneous pipe flow cross section velocity profiles with experimental measurements in the cases with centerline velocity $U_{j|r=0} = 9.0\,(m/s)$ (left) and $U_{j|r=0} = 12.0\,(m/s)$ (right). 176
Figure 6.13 Development of the boundary layer velocity field (in $z-y$ centerline plane) for the pipe flow $U_{j|r=0} = 9\,(m/s)$. From top to bottom, shown are the contour plots of velocity at 10.06, 10.12, 10.18, and $10.24(h/U_{j|r=0})$ time unit after the start of simulations. The equivalent time interval is $0.01\,s$. 177
Figure 6.14 Developed vorticity structures on the pipe wall in the precursor LES of the pipe with setting I5-O3; see table 6.6 for more details. 177
Figure 6.15 From top to bottom, shown are the contour plots of SGS turbulent kinetic velocity (k_{sgs}), and turbulent viscosity (ν_{sgs}) along with vorticity contours (ω). Results are excerpted from the symmetry plane of the computational domain, i.e. $y = 0$, at $3\,s$ after the flushing time. 178
Figure 6.16 From top to bottom, shown are the contour plots of resolved instantaneous turbulent velocity field ($\bar{U}$), and time-averaged velocity field ($\langle \bar{U} \rangle$) along with the corresponding resolved instantaneous kinematic pressure ($\bar{p} = P/rho$). Results are excerpted from the symmetry plane of the computational domain, i.e. $y = 0$, at $3\,s$ after the flushing time. 179
Figure 6.17 Obtained coherent structures of the JINCF in case W1-I5-O3 with iso-surfaces of the Q-criterion, where $Q = 100$ and iso-surfaces are color coded with instantaneous velocity contours. 180
Figure 6.18 (Left) Obtained coherent structures of the JINCF in case W2-I10-O5 with iso-surfaces of the Q-criterion, where $Q = 175$ and iso-surfaces are color coded with instantaneous velocity contours. (Right) Close-up view of the iso-surfaces at near-field. 181
Figure 6.19 Coupling algorithm of LES data with the firebrand/debris transport model. 183
Figure 6.20 Spatial interpolation of the ambient velocity components based on the model firebrand position in the computational mesh. 184

Figure 7.1 Black dotted lines are simulated trajectories which are superimposed over the Q-criterion contours of the velocity filed at $3\,s$. The $Q = 100$ contours are color coded with the velocity magnitude. 194
Figure 7.2 Obtained trajectory of model firebrands with aspect ratio $\eta = 4$ from wind tunnel experiments (top) in relation to trajectories from corresponding simulations (bottom) using the developed model where $U_0 = 2.23\,(m/s)$, and $U_{j|r=0} = 9.0\,(m/s)$. 195
Figure 7.3 Obtained trajectory of model firebrands with aspect ratio $\eta = 1$ from wind tunnel experiments (top) in relation to trajectories from corresponding simulations (bottom) using the developed model where $U_0 = 2.85\,(m/s)$, and $U_{j|r=0} = 12.0\,(m/s)$. 196
Figure 7.4 Shown are PDF (left) and CDF (right) plots of the normalized downwind distance x_l/z_m (top), normalized rise height z_{max}/z_m (middle), and normalized downwind distance with the rise height x_l/z_{max} (bottom) that are drawn for the release of $\eta = 6$ model firebrands through the JINCF velocity field generated by the W1-I5-O3 setting. The dashed lines are experimental data and the solid lines present corresponding numerical results. 197
Figure 7.5 Shown are the mean μ (left) and the standard deviation σ (right) of the normalized downwind distance (top), and normalized rise height (bottom). Estimations based on the experimental data are drawn along horizontal axis and denoted with the subscript $(_e)$, whereas calculated results from the numerical simulations are presented in vertical axis with subscript $(_n)$. Also, the red solid line has $1:1$ slope. 198
Figure 7.6 Probability density function (PDF) of the normalized downwind distance (on the left), and the normalized rise height (on the right) obtained from the simulation of model firebrands' transport through the velocity field of W1-I5-O3 (top) and W2-I10-O5 (bottom). The solid, dashed, and dotted-dashed lines show the results pertinent to the model firebrands with $\eta = 1$, 4 & 6, respectively 200
Figure 7.7 Probability density function (PDF) of the normalized downwind distance (left) and the normalized maximum rise height (right) for different release radius of the model firebrands with aspect ratio $\eta = 6$ through the velocity field of W2-I10-O5 case. 202
Figure 7.8 Shown are variations of the mean of the normalized landing location and rise height versus R value (left) and their corresponding standard deviation against R (right). 202
Figure 7.9 Shown are spatially-averaged trajectories of the model firebrands with aspect ratio $\eta = 6$ that are released within the circular area of the jet nozzle with different radii R. Each trajectory line is averaged over 600 sample of model firebrands' path. Also, the (green) symbolic line presents the spatially-averaged trajectory of the corresponding experimental case. 203

Figure 7.10 Illustrated is the side view comparison of the spatially-averaged trajectories obtained from transport simulations through the time-varying turbulent velocity field of W1-I5-O3 against simulations in the time-averaged velocity field of the same turbulent flow. 204

Figure A.1 (Right) Coordinate system for a bent-over buoyant plume through a cross flow; (Left) Normal cross section area of the plume perpendicular to the centerline s. 212

Figure A.2 Schematic of an infinitesimal bent-over plume element. Net buoyancy force, that is $(\varrho_a - \varrho)g\pi\lambda b^2 ds$, is denoted by F. Through above diagrams, sharp head arrows denote velocity vectors, bold head arrows denote flux vectors, and hollow arrows denote force vectors. 214

Figure B.1 Shown are the allocated zones of the computational domain to the available processors. Each zone is color coded with the processor identification number in the list of processors. 220

Chapter 1

Introduction

Detrimental consequences of Climate Change such as temperature rise, severe and frequent droughts, and changes in precipitation patterns along with the increased development in rural areas especially at wild-land urban interface (WUI), and change in fuel management policies have caused a drastic increase in the risk of wildfires over the past few decades [Caton et al., 2016]. Each year on average, wildfires burn almost 865 million acres of land throughout the globe in which the United States' share is approximately 7 to 9 million acres [Howard, 2014]. The situation is not different in other parts of the world; For instance, every year, forest fires are destroying more than 6% of the forests in Iran [Allard, 1990]. Wildfires expose people, property, infrastructure, and ecosystems to a pervasive threat that is projected to increase even more in the future [Foster, 2014]. As a result, wildfires are becoming costlier than current estimates, which is between $\$20 - \$125$ billion annually in the U.S. [Howard, 2014].

Apart from the economic burden on the federal government, and social and ecological hardship on the local communities and the ecosystem, the main responsibility once a wildfire happens is to contain and protect people and their properties. To this end, understanding wildfire spread mechanisms is of paramount importance. Despite wildfires can propagate by convective heat transfer and radiation, there is a growing body of evidence to suggest that firebrand showers are the source of heat transfer [Coleman et al., 2013] that leads to fire spotting and further ignitions which are called spot fires. Although flame impingement on the fuel beds (convective heat transfer), and radiation can cause fire spread in forests, firebrand spotting is a major cause of fire spread at WUIs

and subsequently, property and infrastructure destruction as well as potential loss of lives [Manzello et al., 2007; Wei et al., 2009].

Fire spotting phenomenon is a complex multi-physics phenomenon that involves firebrand lofting through the envelope of buoyant plumes and thermals formed above the flame zone, various lofting to downwind transport transition scenarios [Tohidi and Kaye, 2013], flight through the atmospheric boundary layer [Albini, 1983a], and fire ignition upon landing. Multitude factors such as size, shape, number, and mass of firebrands, moisture content of the fuel bed, dynamics of the fire plume, terrain, meteorology and the time of exposure to radiant and convective heat fluxes [Boonmee and Quintiere, 2002] are involved in estimating the susceptibility of a region to spot fires. Amongst these, firebrand flight is one of the most complex, stochastic, and highly nonlinear processes that strongly affects the downwind travel distance of the firebrands and eventually fire spread. Hence, the goal of this study is to improve understanding of the firebrand flight.

Since the transport process depends on the size and shape of the individual particles, the first step is to understand the formation of firebrands. So far, several studies have been conducted to examine the generation of firebrands [Huang et al., 2007; Manzello and Maranghides, 2007; Manzello et al., 2008, 2009; Suzuki et al., 2012a,b, 2013]. Nonetheless, almost all of them are conducted in the absence of wind field and do not provide a predictive model for the distribution of mass and shape upon landing. Also, very little studies [Barr and Ezekoye, 2013] have focused on investigating the break-off process from vegetative/woody structures. To date, there are many works done on the transport of wind-borne debris and firebrands [Tarifa et al., 1965, 1967; Lee and Hellman, 1969, 1970; Albini, 1979, 1981; Fernandez-Pello, 1982; Albini, 1983a,b; Tachikawa, 1983, 1988; Woycheese et al., 1997; Woycheese and Pagni, 1999; Woycheese et al., 1998; Holmes, 2004; Anthenien et al., 2006; Sardoy et al., 2006; Baker, 2007; Sardoy et al., 2007; Visscher and Kopp, 2007; Sardoy et al., 2008; Richards et al., 2008; Bhutia et al., 2010; Richards, 2010; Karimpour and Kaye, 2012; Koo et al., 2012; Richards, 2012]. However, in the majority of these studies, there are simplifying assumptions in the aerodynamic model that either decouples lofting from transport or converts the 3D trajectories of firebrands to a 2D phenomenon. Also, despite the flight is highly affected by the turbulence characteristics of the velocity field and buoyancy of the fire plume, dynamics of the generated velocity field by the interaction of the fire plume and the boundary layer is not

effectively considered. In fact, the velocity field of the wildfires which can be approximated as the flow of a buoyant plume in a non-uniform cross-flow boundary layer, is considered as a steady or a quasi-steady flow field in most of the studies [Sardoy et al., 2007, 2008; Koo et al., 2012]. Besides, the near field dynamics of the buoyant plumes through non-uniform boundary layer cross-flows are overlooked by considering a uniform cross-flow [Hoult et al., 1969; Briggs, 1975a,b, 1984; Davidson, 1986; Contini and Robins, 2001; Contini et al., 2009, 2011]. Hence, there is no data on the near-field effects of the highly buoyant bent-over plumes on the modeling of firebrand transport. Further, there has been little work done on the flight of thin disk and cylindrical shape firebrands, although there is a strong evidence to suggest that they are very well representative of the generated firebrands during wildfires at WUIs [Manzello et al., 2008; Koo et al., 2012]. More importantly, almost all of the existing models and studies suffer from the lack of thorough experimental validation.

Given the synopsis of studies related to firebrand transport, the first objective of the present work is to understand the firebrand formation and the role of shape on the flight. The second objective is to investigate the influence of near-field dynamics of the highly buoyant bent-over plumes as well as temporal and spatial variations in their velocity field on the lofting and downwind travel distance of firebrands. Lastly, this study aims to provide a comprehensive model validation data set for the flight of rod-like firebrands, and develop a coupled stochastic parametric numerical flight model which is experimentally validated.

On this matter, the dissertation is composed of seven themed chapters in addition to this introduction. Chapter two discusses the break-off process, and the firebrands' mass and shape distributions. Then, the aerodynamics of the flight of cylindrical shape firebrands are characterized in chapter three. Through chapter four, dynamics of the highly buoyant plumes bent-over in a non-uniform boundary layer cross-flow is discussed in detail. The fifth chapter presents the most comprehensive large-scale wind tunnel experiments of the lofting and downwind travel distance of rod-like firebrands that are ever conducted. Also, the sixth chapter presents the development procedure of the highly scalable coupled stochastic parametric model for firebrand transport. In this regard, chapter seven deals with detailed experimental validation of the developed model, and finally concluding remarks are given in chapter eight.

Bibliography

Albini, F. A. (1979). *Spot fire distance from burning trees : a predictive model*. United States.

Albini, F. A. (1981). *Spot fire distance from isolated sources : extensions of a predictive model*. United States.

Albini, F. A. (1983a). Transport of Firebrands by Line Thermals. *Combustion Science and Technology*, 32(5-6):277–288.

Albini, F. A. F. A. . (1983b). *Potential spotting distance from wind-driven surface fires / Frank A. Albini*.

Allard, G. (1990). The fire situation in islamic republic of iran. *FRA global forest fire assessment*, 2000.

Anthenien, R. A., Tse, S. D., and Fernandez-Pello, A. C. (2006). On the trajectories of embers initially elevated or lofted by small scale ground fire plumes in high winds. *Fire Safety Journal*, 41(5):349–363.

Baker, C. J. (2007). The debris flight equations. *Journal of Wind Engineering and Industrial Aerodynamics*, 95(5):329–353.

Barr, B. W. and Ezekoye, O. (2013). Thermo-mechanical modeling of firebrand breakage on a fractal tree. *Proceedings of the Combustion Institute*, 34(2):2649–2656.

Bhutia, S., M.Jenkins, and Sun, R. (2010). Comparison of Firebrand Propagation Prediction by a Plume Model and a Coupled Fire/Atmosphere Large Eddy Simulator. *J. Adv. Model. Earth Syst.*, 2:1–15.

Boonmee, N. and Quintiere, J. G. (2002). Glowing and Flaming Autoignition of Wood. *Proceedings of the Combustion Institute*, 29:289–296.

Briggs, G. A. (1975a). A comparison of the trajectories of rising buoyant plumes with theoretical empirical models. *Atmospheric Environment (1967)*, 9(4):455–457.

Briggs, G. A. (1975b). Plume rise predictions, Lectures on Air Pollution and Environment Impact Analysis. *Am. Meteorol. Soc., Boston, USA*, 10.

Briggs, G. A. (1984). Plume rise and buoyancy effects. *Atmospheric Science and Power Production*, pages 327–366.

Caton, S., Hakes, R., Gorham, D., and Gollner, M. (2016). A review of pathways for building fire spread in the wildland urban interface part ii: Response of components and systems and mitigation strategies in the united states. *Fire Technology*, pages 1–41.

Coleman, R. J., Pimlott, K., Richwine, M., and Hoover, T. (2013). *WUI Command Operations for the Company Officer*. California Department of Forestry and Fire Protection, Office of the State Fire Marshal, State Fire Training, P.O.Box. 944246, Sacramento, CA, 94244-2460.

Contini, D., Cesari, D., Donateo, a., a.G. Robins, and a.G. Robins (2009). Effects of Reynolds number on stack plume trajectories simulated with small scale models in a wind tunnel. *Journal of Wind Engineering and Industrial Aerodynamics*, 97(9-10):468–474.

Contini, D., Donateo, A., Cesari, D., and Robins, A. G. (2011). Comparison of plume rise models against water tank experimental data for neutral and stable crossflows. *Journal of Wind Engineering and Industrial Aerodynamics*, 99(5):539–553.

Contini, D. and Robins, A. (2001). Water tank measurements of buoyant plume rise and structure in neutral crossflows. *Atmospheric Environment*, 35(35):6105–6115.

Davidson, G. A. (1986). Gaussian versus top-hat profile assumptions in integral plume models. *Atmospheric Environment (1967)*, 20(3):471–478.

Fernandez-Pello, A. C. (1982). An analysis of the forced convective burning of a combustible particle. *Combustion Science and Technology*, 28(5-6):305–313.

Foster, J. M. (2014). Federal Government Loss to Fund Wildfire Fighting Without Having to Raid Wildfire Prevention.

Holmes, J. D. (2004). Trajectories of spheres in strong winds with application to wind-borne debris. *Journal of Wind Engineering and Industrial Aerodynamics*, 92(1):9–22.

Hoult, D. P., Fay, J. A., and Forney, L. J. (1969). A theory of plume rise compared with field observations. *Journal of the Air Pollution Control Association*, 19(8):585–590.

Howard, P. (2014). Flammable Planet: Wildfires and the Social Cost of Carbon. Technical Report September, The Cost of Carbon Projec.

Huang, R. F., Wu, Y. D., Chen, H. D., Chen, C. C., Chen, C. W., Chang, C. P., and Shih, T. S. (2007). Development and Evaluation of an Air-Curtain Fume Cabinet with Considerations of its Aerodynamics. *Ann. Occup. Hyg., Vol. 51, No. 2, pp. 189206, 2007*, 51(2):189–206.

Karimpour, A. and Kaye, N. B. (2012). On the stochastic nature of compact debris flight. *J. Wind Eng. & Ind. Aero.*, 100(1):77–90.

Koo, E., Linn, R. R., Pagni, P. J., and Edminster, C. B. (2012). Modelling firebrand transport in wildfires using HIGRAD/FIRETEC. *International Journal of Wildland Fire*, 21(4):396–417.

Lee, S. L. and Hellman, J. M. (1969). Study of Firebrand Trajectories in a Turbulent Swirling Natural Convection Plume. *Combustion and Flame*, 13(6):645–&.

Lee, S.-L. and Hellman, J. M. (1970). Firebrand trajectory study using an empirical velocity-dependent burning law. *Combustion and Flame*, 15(3):265–274.

Manzello, S. L. and Maranghides, A. (2007). Measurement of firebrand production and heat release rate (HRR) from burning Korean pine trees. *Proc. 7th Asia- ....*

Manzello, S. L., Maranghides, A., Shields, J. R., Mell, W. E., Hayashi, Y., and Nii, D. (2009). Mass and size distribution of firebrands generated from burning Korean pine (Pinus koraiensis) trees. *Fire and Materials*, 33(1).

Manzello, S. L., Shields, J. R., Hayashi, Y., and Nii, D. (2008). Investigating the vulnerabilities of structures to ignition from a firebrand attack. *Fire Safety Science*, pages 143–154.

Manzello, S. L., Shields, J. R., Yang, J. C., Hayashi, Y., and Nii, D. (2007). On the use of a firebrand generator to investigate the ignition of structures in wildland–urban interface (WUI) fires. In *Eleventh International Fire Science and Engineering Conference (INTERFLAM)*, pages 3–5.

Richards, P. J. (2010). Steady Aerodynamics of Rod and Plate Type Debris.pdf. In *17th Australian Fluid Mechanics Conference*.

Richards, P. J. (2012). Dispersion of windborne debris. *J. Wind Eng. & Ind. Aero.*, 104-106:594–602.

Richards, P. J., Williams, N., Laing, B., McCarty, M., and Pond, M. (2008). Numerical calculation of the three-dimensional motion of wind-borne debris. *Journal of Wind Engineering and Industrial Aerodynamics*, 96(10):2188–2202.

Sardoy, N., Consalvi, J. L., Kaiss, a., Fernandez-Pello, a. C., Porterie, B., and a.C. Fernandez-Pello (2008). Numerical study of ground-level distribution of firebrands generated by line fires. *Combustion and Flame*, 154(3):478–488.

Sardoy, N., Consalvi, J.-L., Porterie, B., and Fernandez-Pello, A. (2007). Modeling transport and combustion of firebrands from burning trees. *Combustion and Flame*, 150(3):151–169.

Sardoy, N., Consalvi, J.-L., Porterie, B., and Kaiss, A. (2006). Transport and combustion of Ponderosa Pine firebrands from isolated burning trees. In *2006 1st International Symposium on Environment Identities and Mediterranean Area, ISEIM, July 9, 2006 - July 12*, pages 6–11, Corte-Ajaccio, France. Polytech'Marseille, Dept. of Mechanical Engineering, CNRS UMR 6595, Technopole Chateau-Gombert, 5 rue Enrico Fermi, 13453 Marseille, France, Inst. of Elec. and Elec. Eng. Computer Society.

Suzuki, S., Manzello, S. L., and Hayashi, Y. (2012a). The size and mass distribution of firebrands collected from ignited building components exposed to wind. *Proceedings of the Combustion Institute*.

Suzuki, S., Manzello, S. L., and Hayashi, Y. (2013). The size and mass distribution of firebrands collected from ignited building components exposed to wind. *Proceedings of the Combustion Institute*, 34(2):2479–2485.

Suzuki, S., Manzello, S. L., Lage, M., and Laing, G. (2012b). Firebrand generation data obtained from a full-scale structure burn. *International Journal of Wildland Fire*.

Tachikawa, M. (1983). Trajectories of Flat Plates in Uniform-Flow with Application to Wind-Generated Missiles. *Journal of Wind Engineering and Industrial Aerodynamics*, 14(1-3).

Tachikawa, M. (1988). A Method for Estimating the Distribution Range of Trajectories of Wind-Borne Missiles. *Journal of Wind Engineering and Industrial Aerodynamics*, 29(1-3).

Tarifa, C. S., Del Notario, P. P., Moreno, F. G., and Villa, A. R. (1967). Transport and combustion of firebrands, final report of grants FG-SP-11 and FG-SP-146. *US Department of Agriculture Forest Service*.

Tarifa, C. S., Notario, P., and Moreno, F. G. (1965). On the flight paths and lifetimes of burning particles of wood. In *Symposium (international) on combustion*, volume 10, pages 1021–1037. Elsevier.

Tohidi, A. and Kaye, N. B. (2013). The Sensitivity of Modeled Flight Distance to the Lofting to Transport Transition Criterion in Coupled Ember Flight Models. In *12th Americas Conference on Wind Engineering*, pages 433–448, Seattle, WA, USA.

Visscher, B. T. and Kopp, G. a. (2007). Trajectories of roof sheathing panels under high winds. *J. Wind Eng. & Ind. Aero.*, 95(8):697–713.

Wei, F., Ke, Z., Juan, S., and Meizhen, Y. (2009). Heat source temperature on the distribution of pollutant concentration in stack ventilation room. *Energy & Environment (Chinese)*, (3):15–19.

Woycheese, J. P. and Pagni, P. J. (1999). Combustion Models for Wooden Brands. In *Third International Conference on Fire Research and Engineering. Society of Fire Protection Engineers*, pages 53–71.

Woycheese, J. P., Pagni, P. J., and Liepmann, D. (1997). Brand Lofting Above Large-Scale Fires. In *Second International Conference on Fire Research and Engineering. Society of Fire Protection Engineers.*

Woycheese, J. P., Pagni, P. J., and Liepmann, D. (1998). Brand propagation from large-scale fires. *J. Fire Protection Eng.*, 10(2):32–44.

Chapter 2

Statistical description of firebrand size and shape distribution from coniferous trees for use in Metropolis Monte Carlo simulations of firebrand flight distance

The process of ember/firebrand formation, lofting, wind driven transport, and resulting spot fire ignition during a wildfire is still poorly understood. Lack of a tractable firebrand formation model along with a detailed statistical description of the size and shape distribution of typical firebrand that could be used in simulations of firebrand flight and combustion may result in unrealistic outcomes. In this regard, a simple, yet quite informative, mechanical failure model of the firebrand break-off process is proposed. This model suggests that the previous laboratory scale firebrand generation experiments would likely provide a reasonable analogue for the formation process in a full scale

wildfire. In addition, geometric scaling analysis is conducted and shows that the firebrand surface area scales with the firebrand mass raised to the $2/3^{rds}$ power. This is in close agreement with measurements of firebrand from previously published data in the literature that are obtained under controlled laboratory combustion of coniferous tress of different sizes. Also, a detailed statistical characterization of the size and shape of these firebrands are presented. A nonlinear regression model on the firebrands' data led to the generation of a set of virtual firebrands. The resulting data could be used as inputs to a Monte-Carlo simulation of firebrands' transport through the velocity field induced by the interaction of a fire plume and the atmospheric boundary layer. Moreover, it is shown that the size distribution of firebrands is more dependent on the mechanics of combustion and limb failure than on a simple geometric relationship with the tree height.

2.1 Introduction

Wildfires are a major threat to people and property. In 2010 there were over 70,000 wildfires recorded in the US by the National Interagency Fire Center NIFC [2011], which burned over 3.4 million acres. In an average year over 1,000 homes, 1,000 outbuildings and 40 businesses are destroyed by wildfires in the US. In 2014 only San Diego County wildfires burned over 29,300 acres of land which resulted in damage or destruction of more than 55 properties. So far, this has caused the total cost of $60 million (2014 USD) and damage estimate still continues [Repard, 2014]. Also on June 2012 Waldo Canyon fire, the most destructive fire in Colorado fire history in terms of consumed homes after Black Forest fire [Parker et al., 2013], burned a total of 18,247 acres in Colorado and Manitou Springs area that led to evacuation of more than 32,000 residents and ultimately insurance claims totaling more than $453.7 million [Murphy, 2013]. Wildfires are becoming even costlier as more people choose to live at the wildland urban interface (WUI).

Once a wildfire starts the main goal of responders is containment and protection of people and property. In order to do this one needs to understand how wildfires spread, and how they cause home ignitions. Wildfire spread is a complex multi-physics phenomenon that depends on the available fuel (vegetation and moisture content), topography, and meteorology. Wildfires can spread by ignition due to radiant heat transfer from burning vegetation to surrounding fuel sources [Sardoy et al., 2008], flame impingement on un-burned fuels [Tran et al., 1992], and fire spotting from firebrands blown ahead of the fire front [Fernandez-Pello, 2009]. Fire spread can also be strongly

influenced by the terrain and atmospheric conditions [Mermoz et al., 2005]. Various models have been developed to predict fire spread from radiation and convection [Tran et al., 1992], from firebrand spotting [Albini, 1979], and by using clustered network models [Porterie et al., 2007].

There is strong evidence to suggest that firebrand showers, when firebrands are cast downwind, is a source of heat transfer [Coleman et al., 2013] and, while radiant and convective fire propagation is responsible for the destruction of forests, firebrand spotting is a major cause of home destruction at the WUI [Manzello et al., 2007a; Weiser, 2009]. For instance, in large forest fires as the fire front reaches residential neighborhoods, the density of vegetation often decreases due to landscaping of the houses and communities, and wildfire management techniques such as creating designated defensible space around buildings and mechanical thinning close to WUIs [Nader, 2007; Syphard et al., 2014]. As a result the intensity of the fire decreases [Dupuy and Morvan, 2005]. Then propagation occurs mainly via either a ground fire or spotting. Spotting can also be a significant hazard to firefighters. While it is relatively easy to monitor the location of fire front in a fire, it is much harder to predict the location of spot fires created by firebrands transported by wind ahead of the fire front. Such spot fires can potentially trap firefighters, or residents who have yet to evacuate [Sullivan, 2009].

Firebrand transport is a complex process involving firebrand lofting into the atmosphere by buoyant plumes (continues release of buoyant fluid [Morton, 1965]) and thermals (finite release of buoyant fluid [Turner, 1969]) formed above the fire, downwind transport by atmospheric winds [Albini, 1983b], and ignition upon landing. During all these steps, lofted firebrands combust through pyrolysis and charring [Tse and Fernandez-Pello, 1998]. A schematic diagram is shown in figure 2.1. Spotting is, also, highly stochastic. The lofting height will depend on the size and shape of the individual firebrands and the buoyancy of the fire plume. Turbulence characteristics of the plume, also, affects the induced velocity field through which lofting occurs. Karimpour and Kaye [2012] show that ignoring turbulence fluctuations underestimates the aerodynamic forces that are being exerted on firebrands. The downwind transport distance will depend on the velocity and turbulence characteristics of the wind and the physical properties of the firebrands. The combustion rate will depend on the size, shape, density, and chemical properties of the firebrand. Finally, the potential for creating a spot fire upon landing will depend on the remaining fuel and heat content of the firebrand on impact, and the available fuel sources at the point of impact. On this note, the formation of firebrands from burning vegetation is a complex phenomenon that is influenced by the size of the

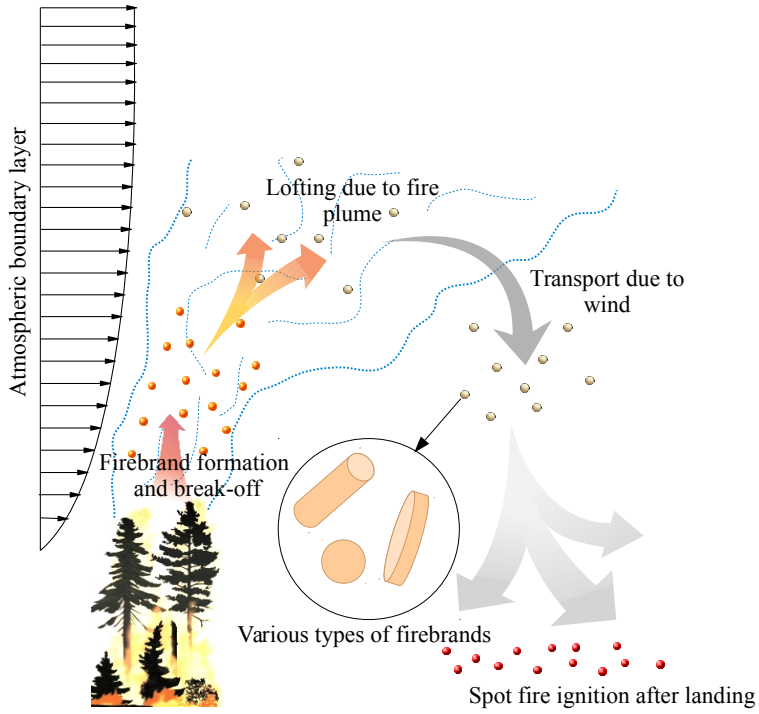

Figure 2.1: Schematic diagram of the spotting process from firebrand formation and break-off through lofting, wind driven transport, and spot fire ignition.

tree due to self-similarity characteristics of the vegetative structures [Mandelbrot, 1983; Barr and Ezekoye, 2013], the fire intensity, and the wind speed which varies with height. Even the interaction of the wind with a non-combusting tree is complex. As the wind speed increases, the frontal area of the tree reduces as the leaves and branches align with the wind direction. The drag coefficient of the tree decreases with increasing wind speed, and the total drag scales linearly with the wind speed [Guan et al., 2000; Kane and Smiley, 2006; Wilson et al., 2010].

To date, several studies have been conducted to examine the generation of firebrands from individual burning trees in the absence of a wind field [Manzello et al., 2007b,c, 2008a, 2009]. For the tested coniferous trees it is observed that the firebrands were predominantly cylindrical in shape, see details of experiments in Manzello et al. [2007b, 2009]. There appears to be no controlled laboratory data in the literature on firebrand generation rates from collections of trees, or from trees in a wind field. Parameterization of the shape of firebrands is often in terms of mass, surface area, and shape, though Huang et al. [2007] did a series of experiments to parametrize disk shaped firebrands in terms

of their mass and Stokes equivalent diameter. In addition, Barr and Ezekoye [2013] have developed a model for predicting the size distribution of brands being lofted from a fractal tree that is based on mechanical breakage models which are coupled to a thermal decomposition model.

Once the firebrands are formed they are lofted into the atmosphere and blown down wind by the ambient wind field. There are a number of models in the literature on lofting and wind driven transport which primarily build on the work of Albini [1979, 1981, 1983b,a] who presented a range of models for the lofting and transport of firebrands. These models have been extended to look at lofting in more detail [Woycheese et al., 1998a], bent line-fire plumes [Sardoy et al., 2008], and various criteria for transition from lofting to transport [Woycheese et al., 1998b]. More detailed reviews of these models are available in the literature; see, [Woycheese and Pagni, 1999; Koo et al., 2010]. These models are often coupled with combustion models to account for the change in firebrand mass and volume during flight. Combustion occurs on the firebrand surface and, therefore, the rate of combustion depends on the shape and surface area of the firebrand.

All firebrand transport models are based on the wind borne debris flight equations of Tachikawa [2012, 1988] who presented equations for the flight of solid objects in terms of their mass and shape. Different equations have been developed for compact debris (approximately spherical), rod-like debris, and plate-like debris [Richards et al., 2002]. On this note, a combustion model for different firebrand shapes is investigated by Baum and Atreya [2014].

Ignition of spot fires caused by landing firebrands depends on the state of the fuel bed the firebrands land on and the time of exposure to radiant and convective heat fluxes [Boonmee and Quintiere, 2002]. Spot fire ignition therefore depends on the size, number, temperature, and heat capacity of the landing firebrands, and the available fuel at ground level. This process has been investigated through a series of experiments by Manzello et al. [2008a].

In summary, the lofting height, flight distance, combustion rate, and spot fire ignition potential of an firebrand are strongly dependent on the firebrand shape and mass. One approach to fully understand the risk of spot fire formation during a wildfire is to run the models discussed above for a broad range of statistically appropriate firebrand sizes and shapes using Monte Carlo type simulations similar to those conducted to understand the risk of wind borne debris in severe storms by Karimpour and Kaye [2012]. However, a detailed characterization of the formation, size, and shape of firebrands is lacking within the literature. The main objective of this study is to begin to fill this gap by presenting simple physical models for firebrand formation and break-off

and characterizing firebrand geometric properties by detailed statistical analysis of available data on firebrand size and mass from coniferous trees of various heights.

The remainder of the paper is structured as follows. In Section (2.2) a simple model and scaling analysis of firebrand geometry is presented followed in Section (2.3) a mechanical model for firebrand break-off that can be applied to both laboratory test burns and to real wildfire events. In Section (2.4) preliminary statistical analysis of available firebrand geometric data is presented relating firebrand surface area, mass, and aspect ratio. These results are used in Section (2.5) to develop a statistical description of the firebrand size and shape and to present a method for developing statistically appropriate sets of virtual firebrands for use in Monte Carlo simulations. The results are discussed and conclusions are drawn in Section (5.5).

2.2 Firebrand geometry

There is currently a substantial amount of data published in the literature on the size and shape of firebrands from various pine trees (Douglas pine and Korean pine) [Manzello et al., 2007b, 2008b, 2009]. These papers present the results of a series of experiments in which individual trees were set alight and allowed to burn under controlled laboratory conditions. During the burning, the firebrands that fell from the trees were extinguished and then weighed and measured. Results were presented for the weight distribution, size distribution and surface area. A total of 1337 firebrands were collected and measured from five different tree burning tests. The results suggest that the mass distribution is significantly skewed toward low mass firebrands (80% of firebrands had a mass of 0.2 g or less). Through these studies, it is also shown that the firebrand surface area is scaled on the firebrand mass, although the exact nature of the scaling is not discussed.

Based on the observations of [Manzello et al., 2007b, 2008b, 2009] from burning coniferous trees in no wind condition, the generic shape of a firebrand can be characterized as a long thin cylinder of length L, diamater D and density ρ (assumed constant), see figure 2.2. The volume $\forall$ and surface area s are given by

$$\forall = \frac{\pi D^2 L}{4} \quad \text{and} \quad s = \pi D L + \frac{\pi D^2}{2} \tag{2.1}$$

respectively. The mass of the firebrand is $m = \rho\forall$ and the aspect ratio is denoted by

$$\eta = \frac{L}{D}. \tag{2.2}$$

If one assumes that in most of the firebrands $L \gg D$ or $\eta \gg 1$, then the effective surface area can be approximated by

$$s \approx \pi DL. \tag{2.3}$$

The mass and surface area of an firebrand can be written in terms of the firebrand length and the

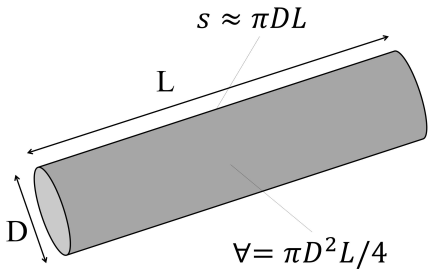

Figure 2.2: Schematic of a cylindrical firebrand showing the length, diameter, volume, and approximate surface area.

firebrand aspect ratio,

$$m = \rho\frac{\pi L^3}{4\eta^2} \quad \text{and} \quad s = \frac{\pi L^2}{\eta} + \frac{\pi L^2}{\eta^2}. \tag{2.4}$$

Provided the aspect ratio is relatively large ($\eta \gg 1$), then the equation for the firebrand surface area (2.4) is dominated by the first of the two terms. Ignoring the second term one can write

$$L = \sqrt{\frac{s\eta}{\pi}} = \left(\frac{4m\eta^2}{\rho\pi}\right)^{1/3} \tag{2.5}$$

which can be simplified to

$$\eta = \frac{L}{D} = \frac{s^3\rho^2}{16\pi m^2}. \tag{2.6}$$

Therefore, given mass and surface area information, it is possible to approximate the firebrand aspect ratio by expression (2.6).

Assuming for a moment that the aspect ratio of all the firebrands (generated from coniferous

trees in no wind condition) is the same, then both the mass and surface area will only be functions of the firebrand length. The mass will scale on the L^3 and the surface area on L^2. Therefore, the cube root of the mass and square root of the surface area will scale linearly on the firebrand length. That is,

$$m^{1/3} \sim L \sim s^{1/2}, \tag{2.7}$$

and therefore,

$$s \sim m^{2/3}. \tag{2.8}$$

The same approximate scaling result can be gained from dimensional analysis as the dimensions of volume and surface area are $[\forall] = L^3$ and $[S] = L^2$, respectively. For a given density, one non-dimensional group (Π) can be formed. Possible forms for the Π include

$$\Pi_1 = \frac{s}{m^{2/3}} \quad \text{or} \quad \Pi_2 = \frac{L}{D} = \eta. \tag{2.9}$$

In order to test this scaling relationship the mass and surface area data in the literature [Manzello et al., 2007b, 2008a, 2009] is re-plotted on a log-log scale in figure 2.3. Also, shown is a line with a slope of 2/3 indicating the power law relationship derived in (2.8) and (2.9). Specifics of the experimental data can be found on table 2.1. Figure 2.3, clearly illustrates two points. First, the

Table 2.1: Characteristics of the isolated burnt trees in the absence of wind. In the table, abbreviations M.C. and N.A. stand for Moisture Content and Not Available, respectively.

Vegetation Type	Source	Height (m)	Girth (m)	M.C. at Ignition
Douglas-fir	Manzello et al. [2007b]	2.6	1.5	(10-50)%±10%
Douglas-fir		5.2	3.0	(10-50)%±10%
Korean Pine	Manzello et al. [2009]	3.6	N.A.	(10-80)%±15%
Korean Pine	Manzello et al. [2008b]	4.0	N.A.	(10-80)%±15%

broad trend in the data strongly agrees with the scaling proposed in (2.8) and (2.9). Second, there is substantial variability around this underlying trend. This variability is because the assumption of a fixed aspect ratio which is clearly not correct. Variation in the aspect ratio of the firebrands will result in variation about the power law trend shown in figure 2.3.

The data plotted in figure 2.3 is derived from four separate experiments in which conifers of different heights were burnt. The dependence of firebrand size and shape on tree height is shown in figures 2.4 and 2.5. The mean and standard deviation of the firebrand mass, surface area, aspect

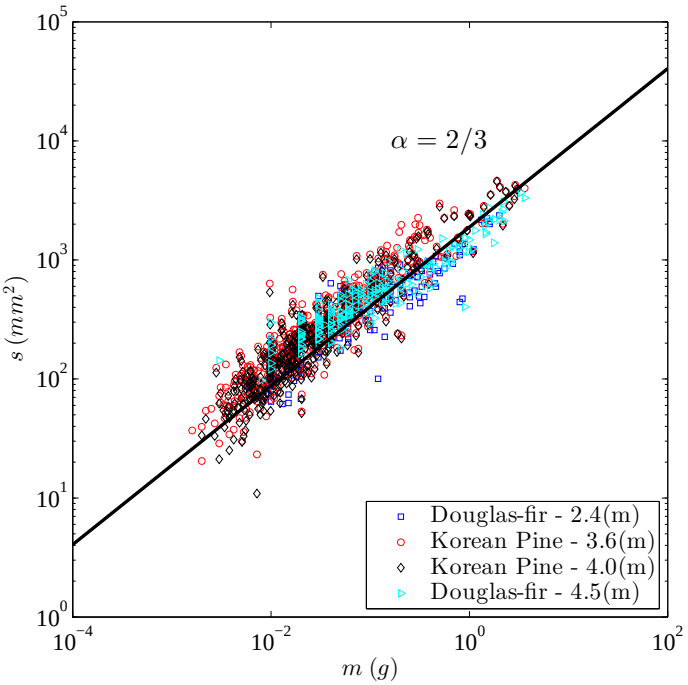

Figure 2.3: log-log scale plot of measured firebrand surface area versus mass for different tree sizes. Also shown is a line (not fitted) of slope $\alpha = 2/3$ to illustrate the power law scaling relationship given in (2.8). Data is excerpted from Manzello et al. [2007b, 2008a, 2009] studies.

ratio, length, and diameter are plotted versus the height of the tree from which they fell. While there is significant variation in these parameters from tree to tree there is no strong correlation between them and the height of the tree from which they fell.

2.3 Firebrand formation model

The failure of trees, when the energy of distortion, whether due to uprooting or bending moments on the branches, exceeds the yield energy of the tree material, is a very complex problem [Vogel, 1996]. Tree crowns have highly complex fractal geometries [Zeide and Pfeifer, 1991; Zhang et al., 2007] and a canopy frontal area that changes with the wind speed [Spatz and Bruechert, 2000]. There is also evidence that the drag coefficient of a tree crown varies with wind speed [Wilson et al., 2010; Kane and Smiley, 2006]. Trees also exhibit complex dynamic responses to wind loads that can lead to a broad range of failure mechanisms [James et al., 2006]. A full predictive model for firebrand formation through tree failure is beyond the scope of this paper. Instead, a simple mechanical model for firebrand formation is presented in order to investigate possible relationships

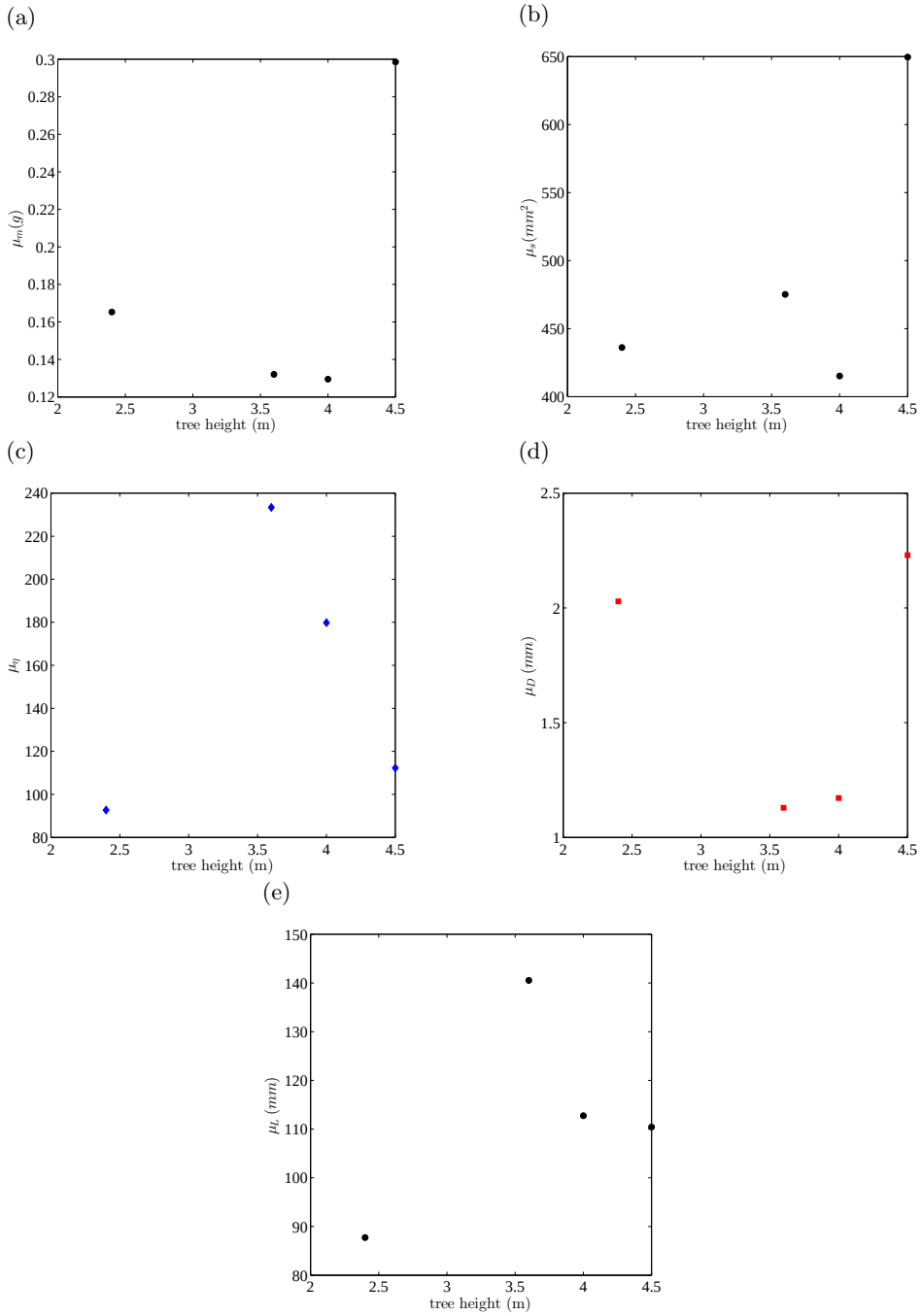

Figure 2.4: Plots of, from top left to right and bottom, the mean firebrand (a) mass (μ_m), (b) surface area (μ_s), (c) aspect ratio (μ_η), (d) length (μ_L), and (e) diameter (μ_D) versus tree height.

between the aspect ratio, mass, surface area, length and diameter of firebrands that form and the height of the tree from which they form.

The model assumes that firebrands form when a twig or branch snaps off due to the shear

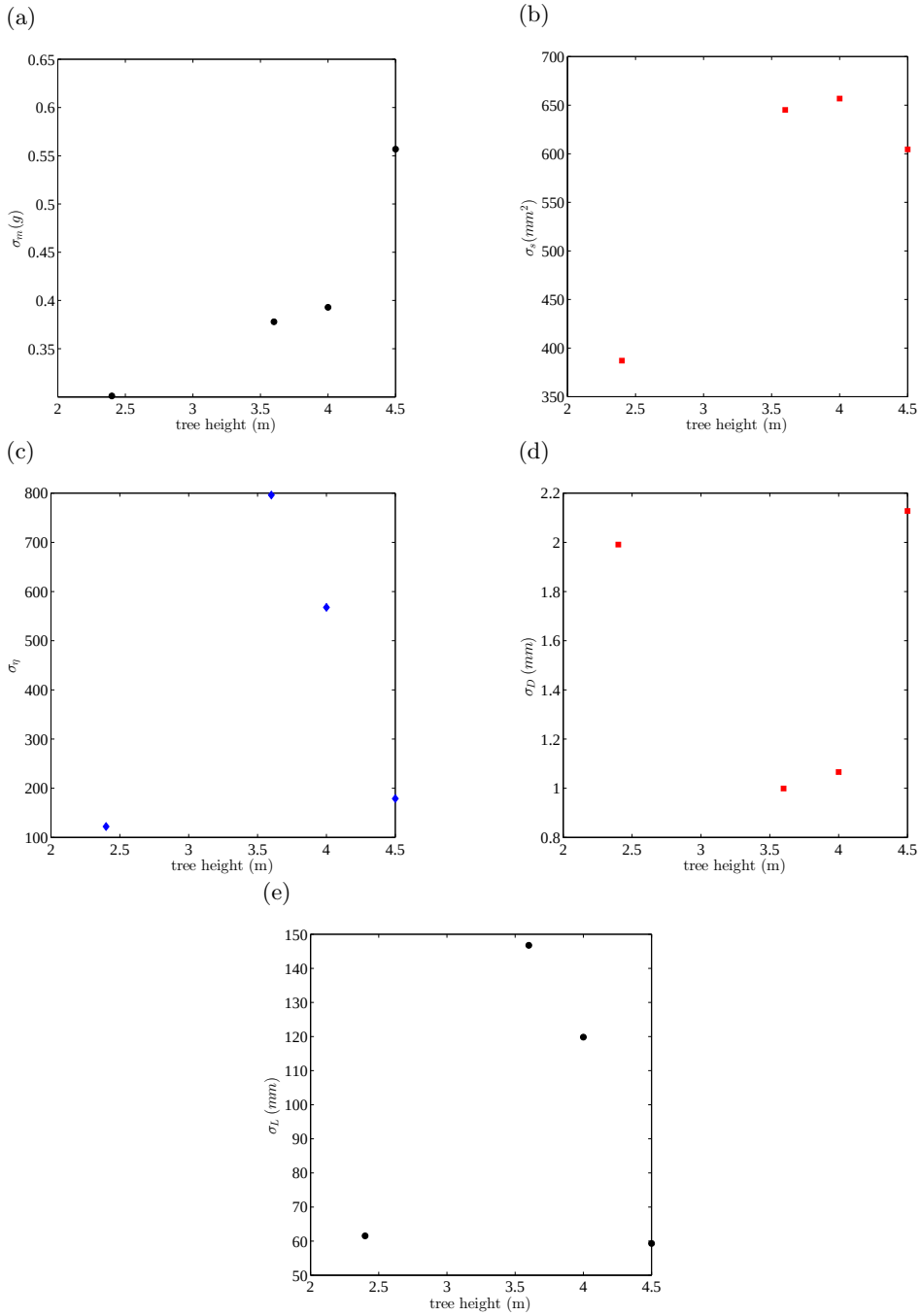

Figure 2.5: Plots of, from top left to right and bottom, the standard deviation of firebrand (a) mass (σ_m), (b) surface area (σ_s), (c) aspect ratio (σ_η), (d) length (σ_L), and (e) diameter (σ_D) versus tree height.

stress associated with internal bending moment exceeding the capacity of the material to resist it. The model for firebrand formation will, therefore, focus on firebrands formed from relatively long

thin cylinders such as those observed in the experiments of [Manzello et al., 2007b, 2008a, 2009]. This is also consistent with Koo et al. [2012] who mentions that a large fraction of firebrands generated from vegetation or burning structures can be represented as cylinders. The model does not examine the formation of disk like firebrands from bark being stripped from tree trunks or from components of burning man-made structures [Suzuki et al., 2013].

Consider a cylindrical twig or branch attached at one end to a larger branch such that the attachment can be regarded as built in connection. Any loading on the firebrand due to either firebrand weight or aerodynamic drag, will result in a bending moment at the support. For a given firebrand diameter and set of material properties, the maximum bending moment that the connection can resist before failing is controlled by the maximum shear stress the material can support

$$\sigma_{max} = \frac{M_0 D}{2I} \tag{2.10}$$

where M_0 is the bending moment at the connection, D is the firebrand diameter, and

$$I = \frac{\pi D^4}{64} \tag{2.11}$$

is the second moment of area of the cylinders circular cross section about its centerline.

There are two possible sources of bending moment that can result in break off; weight (see figure 2.6-left) and drag which can be due to either the vertical air flow induced by the heat release from the fire or from the horizontal airflow from ambient winds and induced by the thermal plume that forms above the fire (see figure 2.6-right).

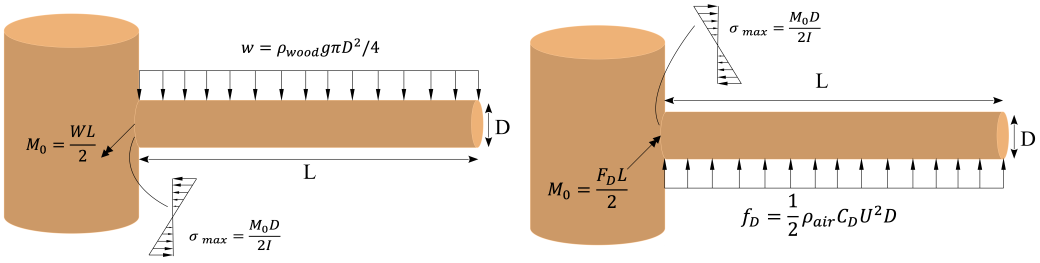

Figure 2.6: Schematic diagram of a cylindrical firebrand supported on the left with (a) bending moment due to the distributed load w=weight per unit length (b) bending moment due to the distributed aerodynamic drag per unit length f_D.

When the loading is due primarily to the weight ($W = wL$) of the firebrand, the bending

moment at the connection is

$$M_0 = \frac{wL^2}{2} = \frac{WL}{2} = \frac{\rho_{wood} g \pi D^2 L^2}{8}. \tag{2.12}$$

Therefore, the critical shear stress at which the firebrand will break off is given by

$$\sigma_{max} = \frac{4\rho_{wood} g L^2}{D} = 4\rho_{wood} g L \eta. \tag{2.13}$$

Assuming that the maximum allowable shear stress is somewhat constant then, when firebrand break off is due to firebrand self weight, then the firebrand aspect ratio is inversely proportional to the length of the firebrand. This relationship is clearly not seen in the experimental data of [Manzello et al., 2007b, 2008a, 2009] as shown in figure 2.7.

When the loading is due to aerodynamic drag the bending moment is given by

$$M_0 = \frac{1}{4}\rho_{air} C_D U^2 L^2 D \tag{2.14}$$

where C_D is the drag coefficient for a cylinder. The resulting critical shear stress condition is given by

$$\sigma_{max} = \frac{8\rho_{air} C_D U^2 \eta^2}{\pi}. \tag{2.15}$$

Assuming again that the material property σ_{max} is somewhat constant then, for a given wind speed U, the firebrand aspect ratio will be a constant. In reality vertical drag, horizontal drag, and weight will all act simultaneously and the resulting break off condition will be

$$\sigma_{max} = \sqrt{\left(\frac{8\rho_{air} C_D U_h^2 \eta^2}{\pi}\right)^2 + \left(\frac{8\rho_{air} C_D U_v^2 \eta^2}{\pi} - 4\rho_{wood} g L \eta\right)^2}. \tag{2.16}$$

where U_v and U_h are the vertical and horizontal components of the air velocity.

The geometric results for the three cases of weight, drag, and weight and drag controlled break off are clearly overly simplistic. In a real combustion event the material properties of the wood change and the material becomes heterogeneous due to charring of the surface. As such, the distribution of shear stress within the cylinder will not be linear and the maximum allowable shear stress will likely decrease over time. As such, the critical condition is also likely to be a function of

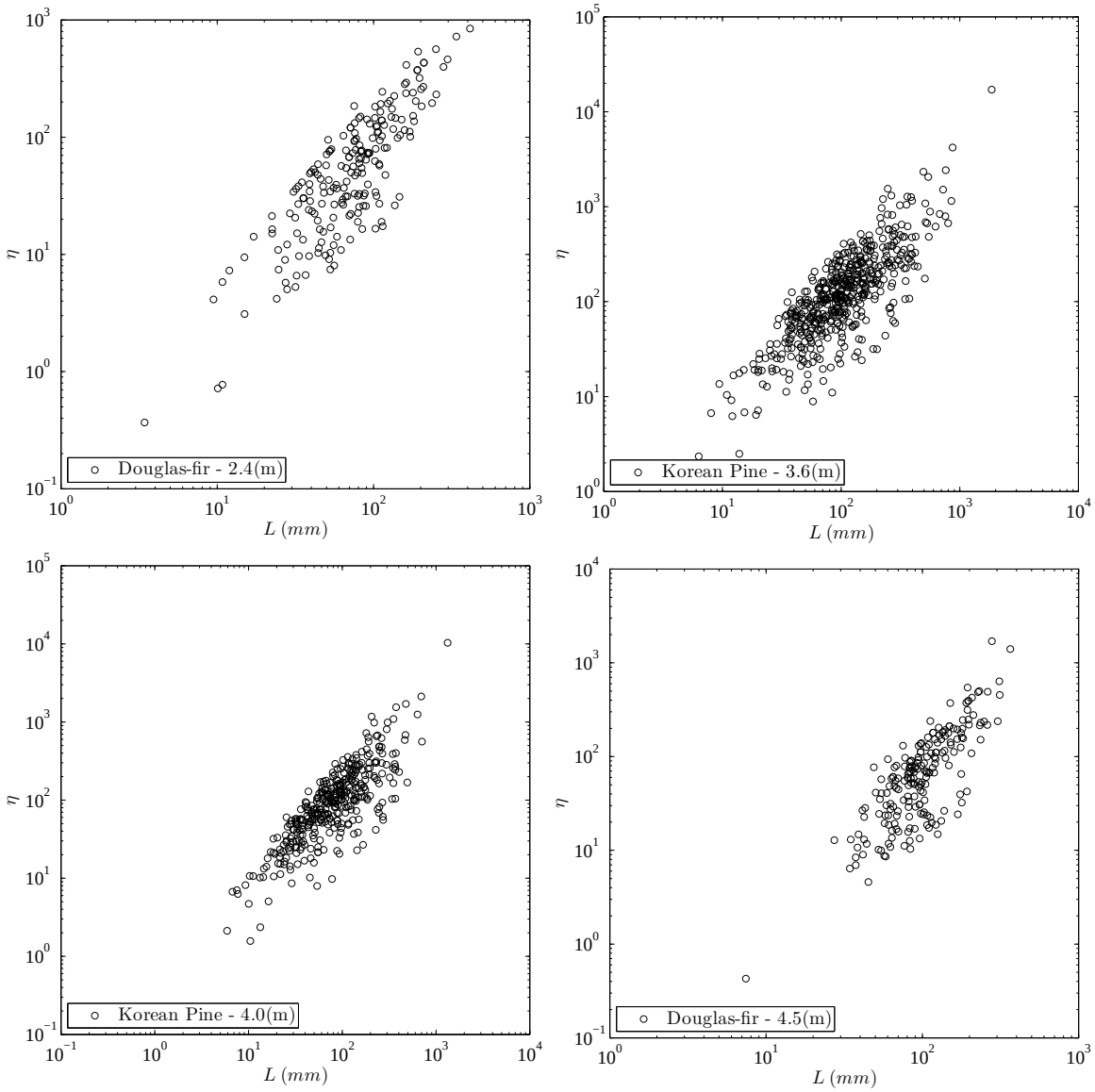

Figure 2.7: Plots of firebrand aspect ratio versus length for each of the four tree heights tested by [Manzello et al., 2007b, 2008a, 2009].

combustion time.

However, despite their simplicity, the models presented above do conform to a couple of intuitive results regarding firebrand formation. For example, for a given set of conditions, the models indicate that larger aspect ratio firebrands (longer and thinner) are more susceptible to break-off. Further, during the combustion of a twig or branch the length and diameter of the cylinder will decrease over time. Assuming that the wood burns at a constant rate over the entire

surface, the cylinder length and diameter will decrease at the same rate and the aspect ratio of the cylinder will increase over time. Therefore, the maximum shear stress at the connection will increase over time until the critical condition for break off is achieved. Again, this result is consistent with observations showing that firebrands break off continuously over the course of a combustion event as more branches burn down to reach break off criteria. It is, therefore, worth examining some of the implications of these simple models. We consider two cases. One is a single tree being burnt in a laboratory with no ambient wind. In this case $U_h = 0$ and the break off criteria is

$$\sigma_{max} = \left| \frac{8\rho_{air} C_D U_v^2 \eta^2}{\pi} - 4\rho_{wood} g L \eta \right|. \tag{2.17}$$

Dividing both sides by $8\rho_{air} C_D D U_v^2 \eta^2 / \pi$ allows (2.17) to be written as

$$\hat{\sigma}_{max} = \left| 1 - \frac{\Gamma}{\eta} \right|. \tag{2.18}$$

where

$$\hat{\sigma}_{max} = \frac{\pi \sigma_{max}}{8\rho_{air} C_D D U_v^2 \eta^2} \tag{2.19}$$

is a non-dimensional maximum shear stress and

$$\Gamma = \frac{\pi \rho_{wood} g L}{2\rho_{air} C_D U_v^2} \tag{2.20}$$

is a non-dimensional parameter that quantifies the relative importance of firebrand weight and vertical drag on the bending moment at the firebrand connection. If $\Gamma/\eta > 1$ then the firebrand weight is the main contributor to break off. Whereas, if $\Gamma/\eta < 1$ then the vertical drag controls break off. For a given value of Γ, this implies that firebrands with aspect ratio $\eta < \Gamma$ will tend to fall off due to their weight whereas longer thinner firebrands with $\eta > \Gamma$ will be broken off due to vertical drag. The updraft velocity will depend on the intensity of the fire, often parameterized in terms of the heat release rate (HRR) of the fire. Following the result for the near source fire plume velocity presented by Baum and McCaffrey [1989] the peak vertical velocity is given by

$$U_{max} = 2.45 \left(\frac{g^2 HRR}{\rho_{air} C_p T_0} \right)^{1/5}. \tag{2.21}$$

where C_p is the specific heat of air and T_0 is the absolute ambient air temperature (see Bhutia et al. [2010]). Numerical simulations of individual tree burning experiments indicated mass loss rates of up to 2 kg/s indicating a heat release rate of 34 MW (see Mell et al. [2010]). This gives a peak vertical velocity of approximately 4 m/s. Substituting this value into (2.20) along with $\rho_{wood} = 450\ kg/m^3$, $\rho_{air} = 1.23\ kg/m^3$, $C_D = 1$ [Munson et al., 2010], and using the average firebrand length measured of approximately 10 cm gives $\Gamma = 35$. This suggests that firebrands with aspect ratios larger than 35 will break off due to vertical air flow and be lofted. For smaller aspect ratios the firebrands would break off due to their own self weight. For the trees tested the majority of the firebrands measured had aspect ratios greater than 35 indicating that vertical drag is likely the dominant loading that leads to firebrand break off. This is consistent with the lofting of firebrands that was observed during the tree burning experiments. See for example figure 1 of Manzello et al. [2007b].

In the formulation presented the vertical air flow is a function of the HRR which in turn should be a function of the tree height as the HRR should depend on the amount of available fuel. Therefore, the HRR should scale with the surface area of the tree (SA_T). For regular shaped objects $SA_T \sim H^2$. However, trees have fractal geometries [Zeide and Pfeifer, 1991; Zhang et al., 2007] and as such the tree surface area scales on

$$SA_T \sim H^{\delta} \tag{2.22}$$

where $\delta > 2$ is the fractal dimension of the tree. Measurements of conifers suggest that δ is in the range $2.2 - 2.8$ depending on the exact tree species. Making a first order steady combustion assumption that the heat release rate is linearly proportional to the surface area available for combustion ($HRR \sim SA_T$) and substituting (2.22) and (2.21) into (2.20) indicates that

$$\Gamma \sim H^{-2\delta/5}. \tag{2.23}$$

That is, Γ is roughly inversely proportional to the tree height. This would imply that single tree burns of larger trees could produce smaller aspect ratio firebrands. This is not observed in the data shown in figure 2.4 though it should be noted that there is significant variability in the experimental data and this variability could hide any underlying relationship between tree height and firebrand aspect ratio. That said, for the three larger tree sizes the average firebrand aspect ratio does clearly decrease with increasing tree height.

The second case considered is of a larger scale forest fire with hundreds of trees burning. In

this case the fire HRR will be orders of magnitude larger. There will also be a substantial horizontal wind field due to ambient wind and entrainment of ambient air into the fire plume. Assuming that the HRR is 500 times that of a single tree then the peak vertical wind speed will be $14\,m/s$ (about $50\,km/h$). In the absence of substantial ambient wind, this would lead to a much smaller value of $\Gamma \approx 3$. As such, wind driven break off will dominate firebrand formation relative to single tree burns and the weight term in (2.16) can be ignored.

There are clearly many assumptions in the proposed model. Firstly, the model is entirely deterministic whereas there is clearly considerable variation in the size and shape of the firebrands formed during either a single tree burn or a forest fire. Variability could be introduced into the model as many of the input parameters will either vary over time (wind speed), vary within the tree (initial twig size), or vary during burning (wood density, maximum shear stress). Variability in firebrand size and shape will be due to all of these. One would, therefore, not expect the model to be quantitatively predictive. However, given appropriate average flow and material properties, the model can be qualitatively predictive.

The main qualitative result of the proposed model is that the majority of the firebrands formed during the single tree burn experiments had a large enough aspect ratio that they were most likely formed by vertical drag forces from the fire updraft. This is the same firebrand formation mechanism one would expect from larger scale wildfires. As such, the laboratory experiments of [Manzello et al., 2007b, 2008a, 2009] likely provide a reasonable analog for the formation of firebrands from branches and twigs in full scale wildfires.

2.4 Firebrand characterization

To adequately and accurately describe the size and shape of cylindrical firebrands two parameters, other than density that is assumed constant, are needed. For instance, length and mass, or surface area and length. The goal of the remainder of the paper is to develop a method for numerically generating statistically appropriate virtual firebrands for use in Monte Carlo type simulations of firebrand flight. As such, the describing pair of parameters would ideally satisfy two conditions. First, the two parameters should be unrelated, that is, the information in one variable is not simply explained by a linear regression on the other variable. Otherwise the independent sampling procedure in Monte-Carlo simulations would be altered. Second, they should be well

described by a standard statistical distribution function in order to generate proper random values from the sample space that the distribution provides.

Clearly firebrand mass and firebrand surface area are related and correlated (see figure 2.3) and so a third parameter needs to be considered. The most obvious and easily calculated parameter is the firebrand aspect ratio (η) given by (2.6). A useful measure of relation between aspect ratio, surface area and mass is the coefficient of determination, i.e. R-squared value. The pair of variables with the smallest R^2 value should be used as the describing pair. Values of R^2 for each experimentally available set of pairs of η, m and s are shown on log-log plots in figures 2.8-2.9. The lower the R^2 value the less the two variables are linearly related. That is, the variability of one variable cannot be captured using a linear regression model to the other one. According to the reported R^2-values, η and s are the least linearly related. Nonetheless, it is possible to observe a strong relationship with significantly low R^2, if the relationship is strongly non-linear. To determine the significance of the linear relation between the pairs, the Pearson and Spearman correlations of η with m and s are calculated and shown on figures 2.8-2.9. The data in figures 2.8-2.9 indicates that there is very little if any statistically significant correlation between η and s. Spearman values show evidence of weak nonlinear correlation. However, between m and η, stronger and more significant correlations can be observed. In order to confirm η and s as the describing pair, it would be useful to collapse all the data for the different trees together and observe the overall trend. On this matter, the calculated ηs of all firebrands, regardless of tree burn, are plotted against their corresponding values of m and s on figure 2.10. For the combined data set, the Spearman correlation between η and s is 0.076 with significance level of 0.006 and R^2-value of 0.0002. Whereas, for m and η, these values are -0.264, 0.000 and 0.004 respectively. This indicates that η and s are much less related and correlated than m and η.

The second criteria for determining the describing pair to be used a Monte Carlo simulation is that each of the describing pair parameters be well represented by a standard probability distribution function. The main requirement of the probability distribution function to be fitted is that it not allow negative values for either η or s. A set of quantile-quantile plots of η, s, and m are shown on figure 2.11, for a log-normal distribution. The plots indicate that the log-normal distribution provides the best description for η followed by s while m is the parameter least well represented by a log-normal distribution.

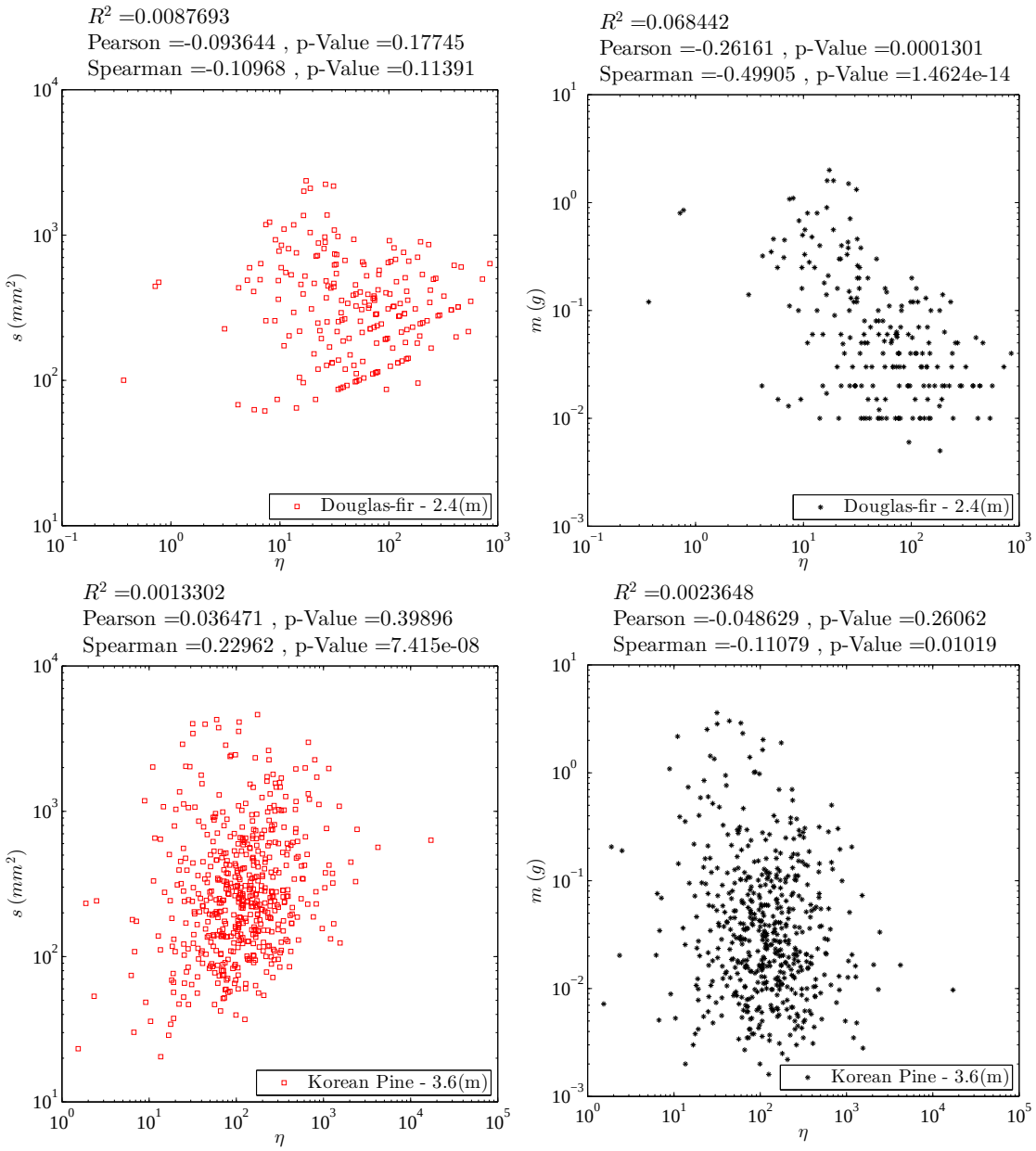

Figure 2.8: (Left) log-log plots of calculated firebrand aspect ratio versus corresponding measured surface area for each tree in experimental data. (Right) log-log plots of calculated firebrand aspect ratio versus corresponding measured mass for each tree in experimental data. Pearson and Spearman correlation coefficients along with their significance level are shown above of each pair. P-values less than 0.05 show statistically significant correlations.

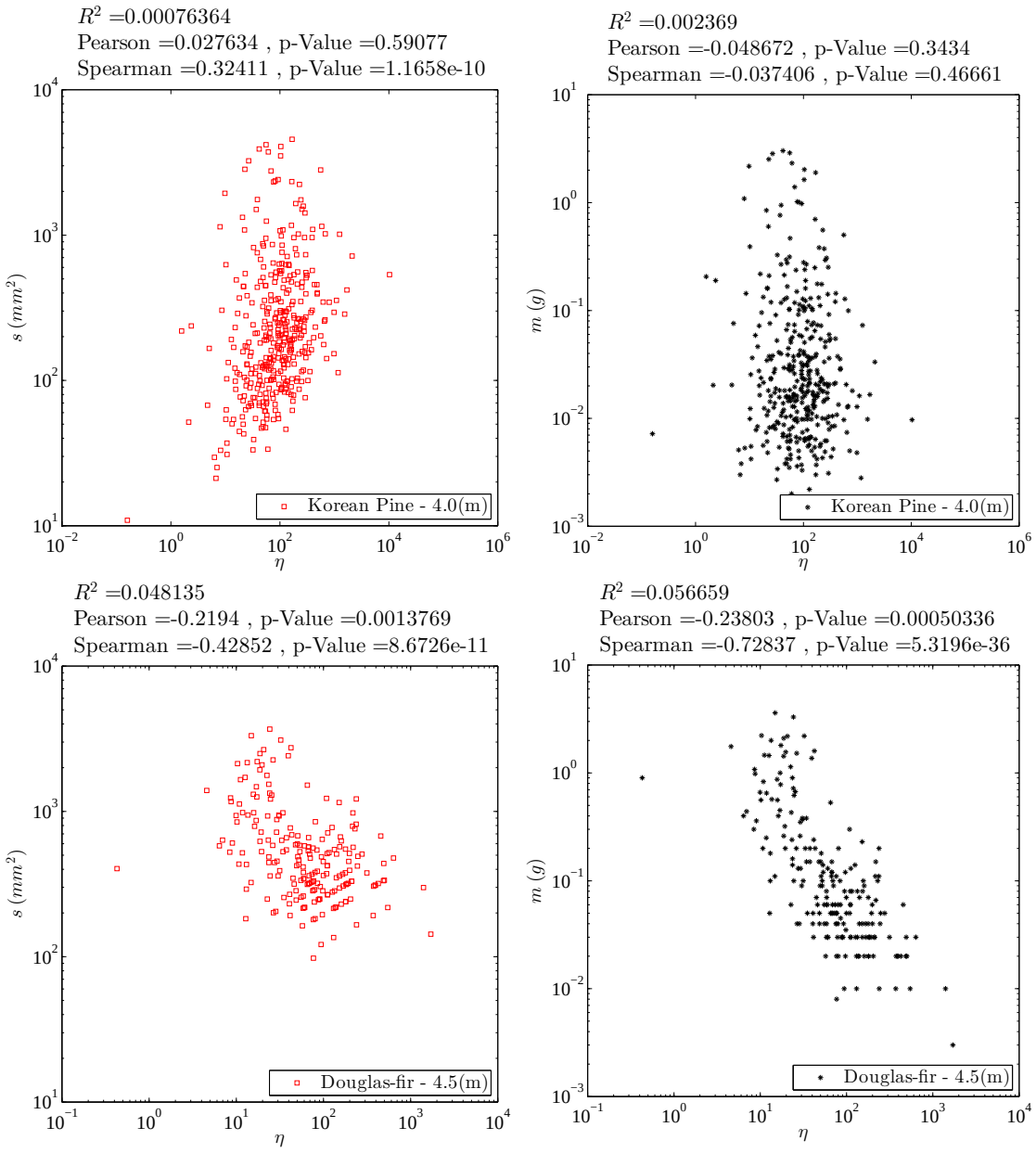

Figure 2.9: (Left) log-log plots of calculated firebrand aspect ratio versus corresponding measured surface area for each tree in experimental data. (Right) log-log plots of calculated firebrand aspect ratio versus corresponding measured mass for each tree in experimental data. Pearson and Spearman correlation coefficients along with their significance level are shown above of each pair. P-values less than 0.05 show statistically significant correlations.

2.5 Statistical description of firebrands

As η and s are, at best, only weakly related and are also the two parameters that are best described by the log-normal distribution function, they are adopted as the describing pairs for the

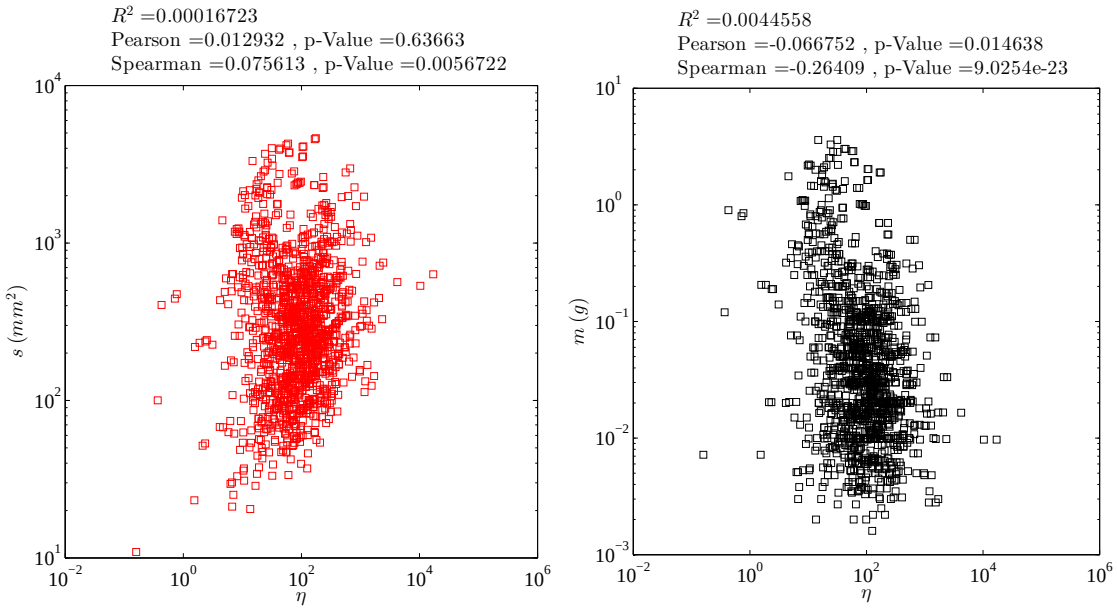

Figure 2.10: (Left) log-log plot of calculated firebrand aspect ratio versus corresponding measured surface area in experimental data. (Right) log-log plots of calculated firebrand aspect ratio versus corresponding measured mass in experimental data. Pearson and Spearman correlation coefficients along with their significance level are shown above of each pair. P-values less than 0.05 show statistically significant correlations.

Metropolis Monte-Carlo simulation analysis. Further, η is chosen as the independent (predictor) variable for a nonlinear regression model as it is the parameter best represented by the log-normal PDF. The regression model is used to estimate corresponding values of s.

The relationship between η and s is unknown. Therefore, the computational domain is mapped to a logarithmic domain such that the nonlinear regression problem is transformed to a linear regression problem and both variable's distribution's are approximately normal. The surface area simulation assumptions are as follows. There is a normally distributed subpopulation of s for each value of η and these subpopulations all have a common variance, i.e. $s \mid \eta \sim N(\mu_{s|\eta}, \sigma_e^2)$. The means of the subpopulations fall on a straight-line function $\mu_{s|\eta} = \Phi + \Psi\eta$ and that $\hat{s} = \hat{\Phi} + \hat{\Psi}\eta$ estimates the mean response for s. The selection of an observation from any of the subpopulations is independent of the selection of any other observation. The η values are adopted randomly from the best fitted normal distribution and are assumed to be fixed through the procedure.

The rest of the simulation procedure is as follows. Assuming a linear relation between $ln(\eta)$ and $ln(s)$, simple regression is applied, using the least squares method. Virtual aspect ratios, η_v, equal to the number of samples collected in the previously published tree burn experiments are

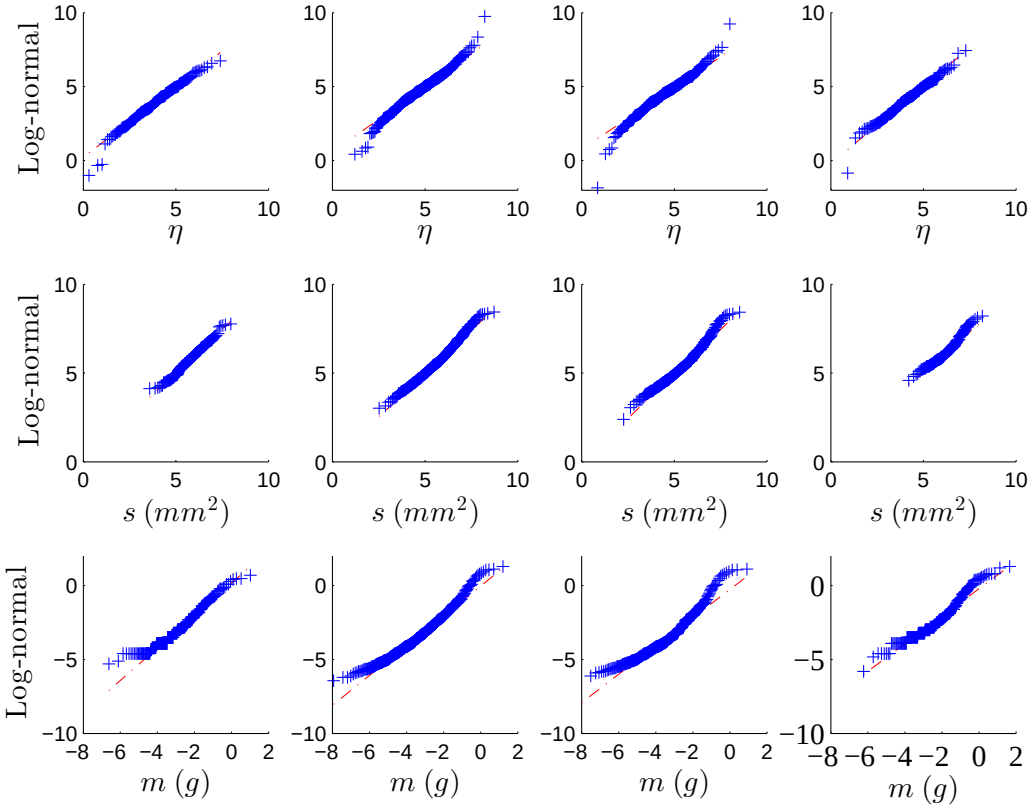

Figure 2.11: Long-normal quantile-quantile plots of the calculated aspect ratio, measured surface area and mass for all trees. Plots are ordered with respect to tree height, $2.4\ (m), 3.6\ (m), 4.0\ (m), 4.5\ (m)$, from left to right. Also shown is the red dashed line with the slope of one.

generated, randomly, from the fitted normal distribution. Corresponding predicted values of s are calculated utilizing linear regression with associated standard error to the mean predicted value ($\sigma_{\hat{s}}$), according to the following expression

$$\sigma_{\hat{s}} = \hat{\sigma_e}\left(1 + \frac{1}{n} + \frac{(\eta_v - \bar{\eta_v})^2}{\Sigma_{i=1}^{n}(\eta_i - \bar{\eta_v})^2}\right)^{1/2} \tag{2.24}$$

where $\hat{\sigma_e}$ is the common standard deviation of subpopulations, $\bar{\eta_v}$ is the average value of virtual aspect ratios, η_i is the value of experimental aspect ratio and n is the number of firebrand samples from each individual tree experiment.

Having calculated the corresponding surface area values of the virtual aspect ratios, the results are transformed back to the non-logarithmic domain. Figure 2.12, shows the simulated describing pairs along with the corresponding experimental data. The estimated describing pair was

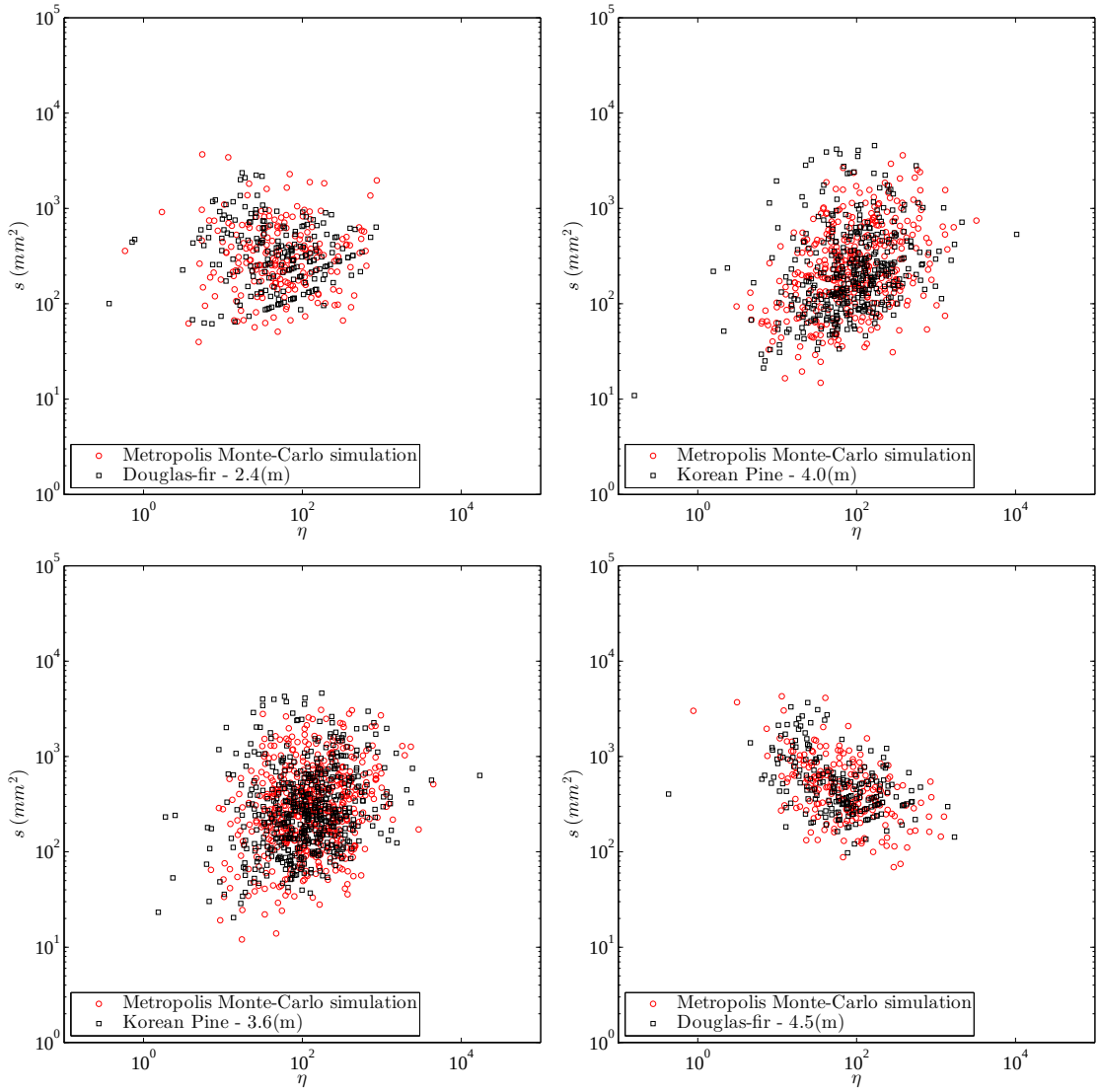

Figure 2.12: Comparison of the generated describing pairs with corresponding experimental data for each individual tree.

then used to calculate each firebrands' mass using (2.6). The resulting mass from Metropolis Monte-Carlo simulations is plotted against estimated surface area and compared with the corresponding experimental data on figure 2.13. There is very good agreement between the results of the simulations and experimental data. It should be noted that the noticeable vertical lines in the experimental data (black squares on the top-left and the bottom right of the figure 2.13) are due to measurement resolution in the mass. In this regard, the synthetic firebrand data from all trees is superimposed and plotted next to the experimental data and shown in figure 2.14. The similarity of the results

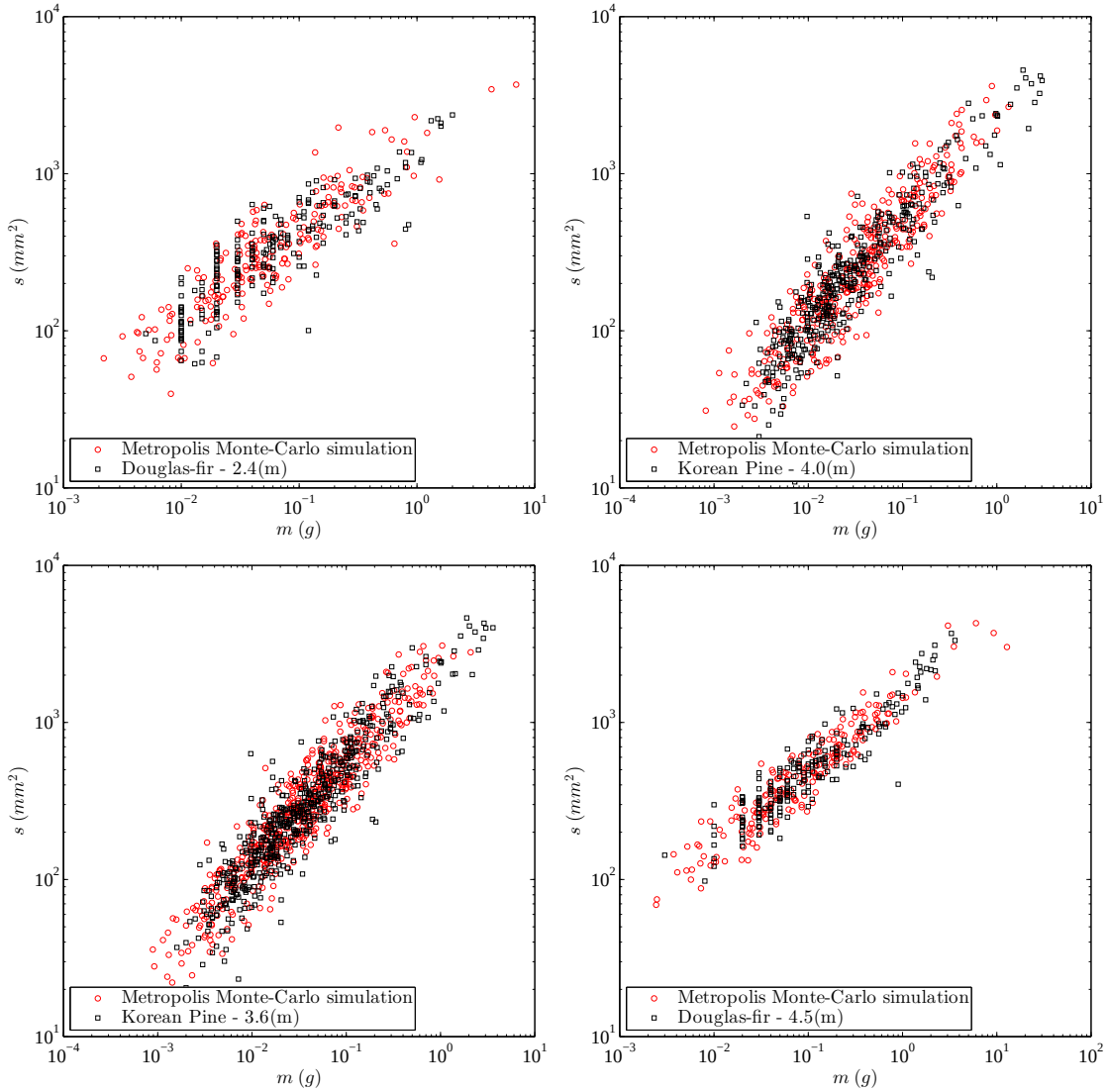

Figure 2.13: Comparison of the simulated mass versus surface area with corresponding experimental data for each individual tree.

corroborates the proposed modeling approach. In order to find out if the simulated mass and experimental mass of firebrands are identically distributed a series of graphical techniques and statistical test are conducted and the empirical cumulative density functions (CDF) of mass and surface area versus the corresponding CDFs of the simulated data are shown on figure 2.15. From figure 2.15, it appears that the simulated firebrand mass and experimental data are coming from the same continuous distribution. To confirm this, a series of tests are performed for each tree.

Through the logarithmic domain a null hypothesis is designated such that the experimental

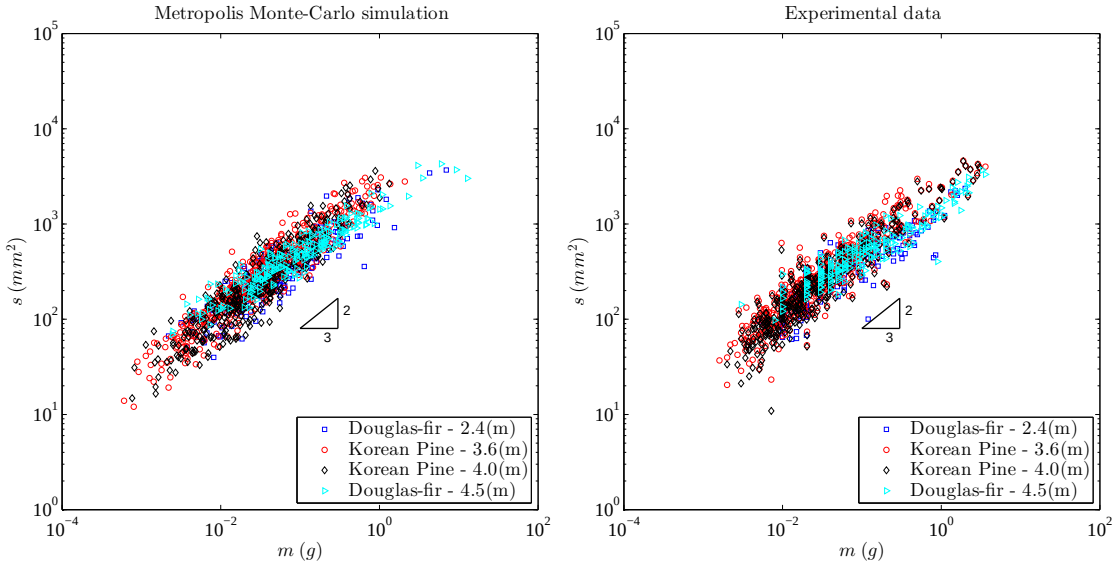

Figure 2.14: Log-log scale plots of firebrand surface area versus mass for 1337 synthetic firebrands and the 1337 firebrands from laboratory measurements of Manzello et al. [2007b, 2008a, 2009]

.

and estimated masses for each individual tree are from the same continuous distribution. The test of this hypothesis is known as the two-sample Kolmogorov-Smirnov (K-S) test. The results are presented in table 2.2 where a zero value of h_0 indicates that the null hypothesis is not rejected. As can be seen, only in the data set from four meter Korean Pine is the null hypothesis rejected. Hence, it can be inferred that the estimated mass values possess the same continuous distribution as the corresponding experimental ones for three out of four trees. One possible explanation for the test

Table 2.2: Results of various statistical tests on the firebrand mass (m) from each individual tree in logarithmic domain. Status of the decision on null hypothesis is denoted by h_0 where the value of one rejects the corresponding null hypothesis of the test. DOF stands for the degree of freedom of the test and p-value shows the probability of the test result. The significance level is set to 0.05 for all tests.

Tree type	K-S test			T-test			F-test		
	h_0	h-statistic	p-value	h_0	DOF	p-value	h_0	DOF	p-value
Douglas-fir, 2.4 (m)	0	0.1005	0.220	0	416	0.399	0	208	0.761
Korean pine, 3.6 (m)	0	0.0652	0.197	0	1072	0.843	0	536	0.804
Korean pine, 4.0 (m)	1	0.1234	0.005	0	760	0.530	0	380	0.474
Douglas-fir, 4.5 (m)	0	0.1095	0.151	0	418	0.293	0	209	0.277

result is that the surface area (s) is approximated in the calculations such that the contribution of the two ends of the firebrand is neglected. This may introduce errors in firebrands with low aspect

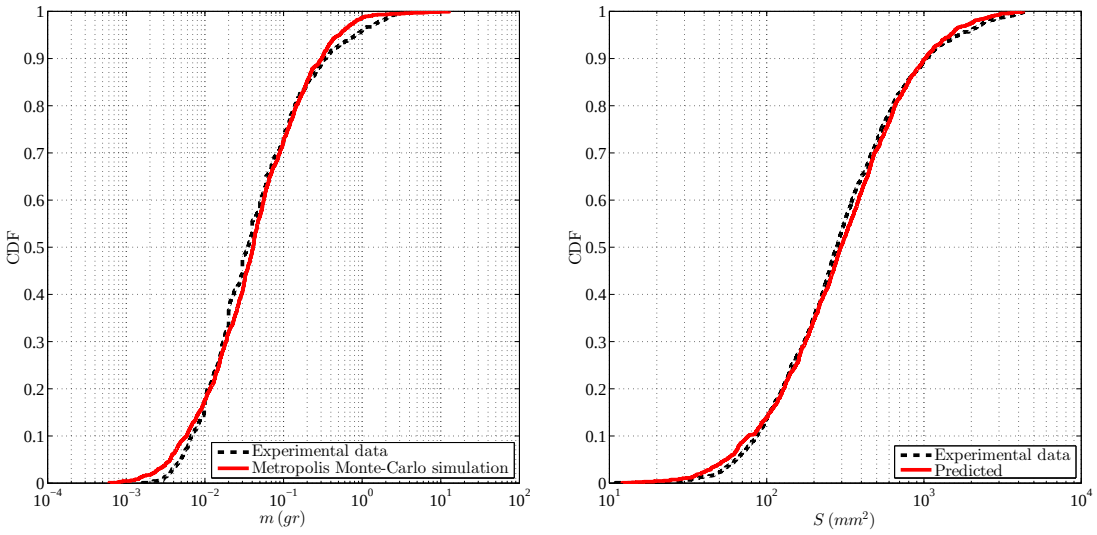

Figure 2.15: (Left) Empirical cumulative density function of mass from all experiments against the Metropolis Monte-Carlo simulations. Statistics of the Kolmogorov-Smirnov test is 0.0688 with p-value of 0.0034 under the null hypothesis which is rejected. (Right) Empirical cumulative density function of surface area from all experiments against the predicted values by regression analysis. Statistics of the Kolmogorov-Smirnov test is 0.0419 with p-value of 0.1872 under the null hypothesis that is accepted.

ratios and may affect the mass distribution obtained, in particular at tails of the distribution.

If the simulated and experimental data are from the same continuous distribution, then the mean of experimental mass should be equal to the mean of simulated mass. Therefore, a null hypothesis was created such that the two distribution means are equal. A test of this hypothesis is the well known two sample T-test. The results for each individual tree data set are shown on table 2.2 in which DOF represents the degree of freedom of the test. Results on table 2.2 indicate that the means of the estimated masses are not statistically significantly different from the means of experimental data. Lastly, if the distributions are equal, then their variances should be equal. Thus, a null hypothesis is created such that the distributions' variances are equal. The test of this hypothesis is the two-sample F-test of variance. According to the presented results on table 2.2, the variance of the simulated data is not statistically significantly different from the corresponding experimental data.

Moreover, experimental mass and surface area are subjected to Leave-One-Out Cross Validation (LOOCV) to further investigate the credibility of the power-law model against the linear model, although it is computationally expensive. It is worth mentioning that the training and

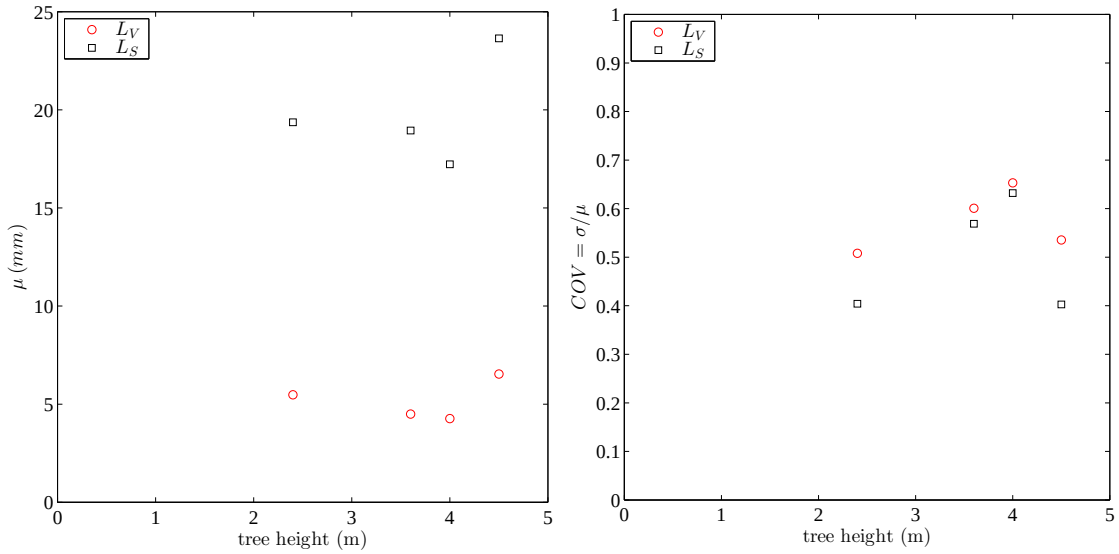

Figure 2.16: Plots of (Left) the average length scales of each firebrand data set and (Right) the coefficient of variation for the length scale versus height. Where, σ is the standard deviation and μ is the mean value.

test sets are drawn from the same population with fixed values. In this regard, 0.51% and 0.60% are the mean square root cross validation errors for the power-law and linear models, respectively. From the Cross-Validation results, it can be inferred that the power-law model better describes the relationship between mass and surface area than the linear model.

The synthetic data set presented in figure 2.14 was based on nonlinear regression analysis of firebrands from four trees [Manzello et al., 2007b, 2008a, 2009]. However, this approach assumes that the size distribution of the firebrands is independent of the size of the tree. To test this hypothesis volume and surface area characteristic length scales, $L_V = \forall^{1/3}$ and $L_S = s^{1/2}$, were calculated for each firebrand in each data set. For each data set, the mean and coefficient of variation of each of these two length scales were calculated and plotted against the tree height. The data, shown in figure 2.16, shows only a slight dependence of the firebrand size on the tree height. This is a somewhat surprising result given the fractal nature of many tree crowns [Zeide and Pfeifer, 1991]. One might expect the branch and twig dimensions of a given tree to scale on the tree height and there to be a linear relationship between the tree height and the characteristic length scale of the firebrands produced. This does not appear to be the case given the results in figure 2.16. Pearson correlation coefficients were calculated between the tree height and each of the length scales obtained from the experimental data and found to be 0.18 for L_V and 0.40 for L_S. the Spearman correlation

coefficient is 0.2 for both of the length scales. These are not particularly high. Therefore, more tree burns over a broader range of tree heights are needed to fully understand the relationship.

2.6 Summary and conclusions

A simple mechanical firebrand break off model is presented for the formation of cylindrical firebrands similar to those collected from full scale tree burn experiments Manzello et al. [2007b, 2008a, 2009]. The firebrand formation model suggests that the majority of firebrands that would form by a single tree burn experiment in isolation would have large enough aspect ratio such that they are most likely to be formed by a vertical drag force from the fire updraft. This implies that the size distribution of firebrands produced by a tree burning in a large wildfire might be the same as those produced under the controlled laboratory conditions. Further, geometric scaling analysis of firebrands indicated that the firebrand surface area scales on the firebrand mass raised to the $2/3^{rds}$ power. This was in very good agreement with firebrands from the previously published data cited above.

This model and analysis served as the motivation to statistically analyze the available firebrands' data. Results of the thorough analysis showed that, for the firebrands formed, the aspect ratio and surface area are only weakly correlated. The collection of firebrands can be well described by the log-normally distributed surface area and aspect ratio pair. Further, the results of statistical analysis led to generation of a set of virtual firebrands utilizing a nonlinear regression model on the experimental data. The synthesized firebrands compared well with the experimental data on a plot of firebrand mass versus surface area. The resulting statistical description of firebrand size and shape can be used as input in Monte-Carlo simulations of firebrand transport models to provide more realistic spot fire location predictions.

Moreover, the size of each firebrand was characterized in terms of two length scales, the cube root of volume and the square root of the surface area. Interestingly, the average of each of these length scales for the different tree burns did not correlate with the tree height. This implies that the size distribution of firebrands is more dependent on the mechanics of combustion and limb failure than on a straight geometric relationship with the tree height.

Bibliography

Albini, F. A. (1979). Spot fire distance from burning trees–a predictive model. General Technical Report INT-GTR-56, USDA Forest Service, Intermountain Forest and Range Experiment Station, Ogden UT, USA.

Albini, F. A. (1981). Spot fire distance from isolated sources-extensions of a predictive model. Research Note INT-RN-309, USDA Forest Service, Intermountain Forest and Range Experiment Station, Ogden UT, USA.

Albini, F. A. (1983a). Potential spotting distance from wind-driven surface fires. Research paper RP-INT-309, USDA Forest Service, Intermountain Forest and Range Experiment Station, Ogden UT, USA.

Albini, F. A. (1983b). Transport of Firebrands by Line Thermals. *Combustion Science and Technology*, 32(5-6):277–288.

Barr, B. and Ezekoye, O. (2013). Thermo-mechanical modeling of firebrand breakage on a fractal tree. *Proceedings of the Combustion Institute*, 34(2):2649–2656.

Baum, H. R. and Atreya, A. (2014). A model for combustion of firebrands of various shapes. *Fire Safety Science*, 11:147–147.

Baum, H. R. and McCaffrey, B. J. (1989). Fire induced flow fieldtheory and experiment. In *Fire Safety ScienceProceedings of the Second International Symposium*, pages 129–148. Hemisphere Publishing Newport,, Australia.

Bhutia, S., M.Jenkins, and Sun, R. (2010). Comparison of Firebrand Propagation Prediction by a Plume Model and a Coupled Fire/Atmosphere Large Eddy Simulator. *J. Adv. Model. Earth Syst.*, 2:1–15.

Boonmee, N. and Quintiere, J. G. (2002). Glowing and Flaming Autoignition of Wood. *Proceedings of the Combustion Institute*, 29:289–296.

Coleman, R. J., Pimlott, K., Richwine, M., and Hoover, T. (2013). *WUI Command Operations for the Company Officer*. California Department of Forestry and Fire Protection, Office of the State Fire Marshal, State Fire Training.

Dupuy, J.-L. and Morvan, D. (2005). Numerical study of a crown fire spreading toward a fuel break using a multiphase physical model. *International Journal of Wildland Fire*, 14(2):141–151.

Fernandez-Pello, C. (2009). Modeling Wildland Fire Propagation and Spotting. In *Fire Interdisciplinary Research on Ecosystem Services (FIRES), Seminar 2.*, Manchester, UK. University of Manchester.

Guan, D., Zhu, T., and Han, S. (2000). Wind tunnel experiment of drag of isolated tree models in surface boundary layer. *Journal of Forestry Research*, 11(3):156–160.

Huang, H., Ooka, R., Kato, S., and Hayashi, Y. (2007). A numerical study of firebrands scattering in urban fire based on CFD and firebrands aerodynamics measurements. *Journal of Fire Sciences*, 25(4):355–378.

James, K. R., Haritos, N., and Ades, P. K. (2006). Mechanical stability of trees under dynamic loads. *Am. J. Bot.*, 93(10):1522–1530.

Kane, B. and Smiley, E. T. (2006). Drag coefficients and crown area estimation of red maple. *Canadian Journal of Forestry Research*, 35:1951–1958.

Karimpour, A. and Kaye, N. B. (2012). On the stochastic nature of compact debris flight. *J. Wind Eng. & Ind. Aero.*, 100(1):77–90.

Koo, E., Linn, R. R., Pagni, P. J., and Edminster, C. B. (2012). Modelling firebrand transport in wildfires using HIGRAD/FIRETEC. *International Journal of Wildland Fire*, 21(4):396–417.

Koo, E., Pagni, P. J., Weise, D. R., and Woycheese, J. P. (2010). Firebrands and spotting ignition in large-scale fires. *International Journal of Wildland Fire*, 19(7):818–843.

Mandelbrot, B. B. (1983). *The fractal geometry of nature*. Macmillan, New York, U.S.A.

Manzello, S., Shields, J., Yang, J., Hayashi, Y., and Nii, D. (2007a). On the use of a firebrand generator to investigate the ignition of structures in wui fires. In *Proceedings of the 11th International Conference on Fire Science and Engineering (INTERLFAM), Interscience Communications, London*, pages 861–872.

Manzello, S. L., Cleary, T. G., Shields, J. R., Maranghides, A., Mell, W., and Yang, J. C. (2008a). Experimental investigation of firebrands: Generation and ignition of fuel beds. *Fire Safety Journal*, 43(3):226–233.

Manzello, S. L., Maranghides, A., and Mell, W. E. (2007b). Firebrand generation from burning vegetation. *International Journal of Wildland Fire*, 16(4).

Manzello, S. L., Maranghides, A., Shields, J. R., Mell, W. E., Hayashi, Y., and Nii, D. (2007c). Measurement of firebrand production and heat release rate (hrr) from burning korean pine trees. *Fire Safety Science*, 7:108–108.

Manzello, S. L., Maranghides, A., Shields, J. R., Mell, W. E., Hayashi, Y., and Nii, D. (2009). Mass and size distribution of firebrands generated from burning Korean pine (Pinus koraiensis) trees. *Fire and Materials*, 33(1).

Manzello, S. L., Shields, J. R., Cleary, T. G., Maranghides, A., Mell, W. E., Yang, J. C., Hayashi, Y., Nii, D., Kurita, T., Sheilds, J. R., and T., K. (2008b). On the development and characterization of a firebrand generator. *Fire Safety J.*, 43(4):258–268.

Mell, W. E., Manzello, S. L., Maranghides, A., Butry, D., and Rehm, R. G. (2010). The wildland–urban interface fire problem–current approaches and research needs. *International Journal of Wildland Fire*, 19(2):238–251.

Mermoz, M., Kitzberger, T., and Veblin, T. T. (2005). Landscape Influences on Occurrence and Spread of Wildfires in Patagonian Forests and Shrublands. *Ecology*, 86(10):2705–2715.

Morton, B. (1965). Modeling fire plumes. 10(1):973–982.

Munson, B. R., Young, D. F., and Okiishi, T. H. (2010). *Fundamentals of fluid mechanics*. Wiley, New York, USA.

Murphy, C. (2013). Insurance cost of waldo canyon fire: $453 million. `https://web.archive.org/web/20131202232359/http://www.koaa.com/news/insurance-cost-of-waldo-canyon-fire-453-million/`. Accessed June 2, 2015.

Nader, G. (2007). *Home landscaping for fire*. UCANR Publications.

NIFC (2011). Historical year-end fire statistics by state. https://www.nifc.gov/fireInfo/fireInfo_statistics.html. Accessed, June-16-2015.

Parker, R., Steffen, R., and Torres, Z. (2013). 2 confirmed dead in black forest fire; 379 homes destroyed. http://www.denverpost.com/breakingnews/ci_23451177/black-forest-fire-evacuation-zone-expands-winds-lightning. Accessed June 2, 2015.

Porterie, B., Zekri, N., Clerc, J., and Loraud, J. (2007). Modeling forest fire spread and spotting process with small world networks. *Combust. & Flame*, 149:63–78.

Repard, P. (2014). County estimates wildfire costs at nearly $60 million. http://www.utsandiego.com/news/2014/may/24/tp-county-estimates-wildfire-costs-at-nearly-60/. Accessed June 2, 2015.

Richards, P. J., Williams, N., Laing, B., McCarty, M., and Pond, M. (2002). Numerical calculation of the three-dimensional motion of wind-borne debris. *J. Wind Eng. & Ind. Aero.*, 96:2188–2202.

Sardoy, N., Consalvi, J., Kaiss, A., Fernandez-Pello, A., and Porterie, B. (2008). Numerical study of ground-level distribution of firebrands generated by line fires. *Combustion and Flame*, 154(3):478–488.

Spatz, H.-C. and Bruechert, F. (2000). Basic biomechanics of self-supporting plants: wind loads and gravitational loads on a Norway spruce tree. *Forest Ecology and Management*, 135:33–44.

Sullivan, A. L. (2009). Wildland surface fire spread modelling, 1990–2007. 2: Empirical and quasi-empirical models. *International Journal of Wildland Fire*, 18(4):369–386.

Suzuki, S., Manzello, S. L., and Hayashi, Y. (2013). The size and mass distribution of firebrands collected from ignited building components exposed to wind. *Proceedings of the Combustion Institute*, 34(2):2479–2485.

Syphard, A. D., Brennan, T. J., and Keeley, J. E. (2014). The role of defensible space for residential structure protection during wildfires. *International Journal of Wildland Fire*, 23(8):1165–1175.

Tachikawa, M. (1988). A method for estimating the distribution range of trajectories of wind-borne missiles. *Journal of Wind Engineering and Industrial Aerodynamics*, 29(1):175–184.

Tachikawa, M. (2012). Trajectories of flat plates in uniform flow with application to wind-generated missiles. In *Wind Engineering 1983 3B: Proceedings of the Sixth international Conference on Wind Engineering, Gold Coast, Australia, March 21-25, And Auckland, New Zealand, April 6-7 1983; held under the auspices of the International Association for Wind Engineering*, volume 3, page 443. Elsevier.

Tran, H. C., Cohen, J. D., and Chase, R. A. (1992). Modeling ignition of structures in wildland/urban interface fires. pages 253–262, Arlington–VA, USA. Inter Science Communications.

Tse, S. D. and Fernandez-Pello, A. C. (1998). On the flight paths of metal particles and embers generated by power lines in high windsa potential source of wildland fires. *Fire Safety Journal*, 30(4):333–356.

Turner, J. (1969). Buoyant plumes and thermals. *Annual Review of Fluid Mechanics*, 1(1):29–44.

Vogel, S. (1996). Blowing in the Wind: Storm-Resisting Features of the Design of Trees. *Arboriculture & Urban Forestry*, 22(2):92–98.

Weiser, B. (2009). Review Report of Serious Injuries, Illnesses, Accidents and Near-Miss Incident. Technical Report CA-LPF-001479 P5EV5C, California Department of Forestry and Protection, Santa Barbara–CA, USA.

Wilson, C., Xavier, P., Schoneboom, T., Aberle, J., Rauch, H.-P., Lammeranner, W., Weissteiner, C., and Thomas, H. (2010). The hydrodynamic drag of full scale trees. In *River Flow 2010 Dittreich, Koll, Aberle & Geisenhainer (eds) ISBN 978-3-939230-00-7.*

Woycheese, J. and Pagni, P. (1999). Combustion models for wooden brands. In *Proc. 3rd Int. Conf. on Fire Research and Engineering, Society of Fire Protection Engineers, Washington, USA*, page 53.

Woycheese, J. P., Pagni, P. J., and Liepmann, D. (1998a). *Brand lofting above large-scale fires.* Building and Fire Research Laboratory, National Institute of Standards and Technology.

Woycheese, J. P., Pagni, P. J., and Liepmann, D. (1998b). Brand propagation from large-scale fires. *J. Fire Protection Eng.*, 10(2):32–44.

Zeide, B. and Pfeifer, P. (1991). A method for estimation of fractal dimension of tree crowns. *Forest Science*, 37(5):1253–1265.

Zhang, D., Samal, A., and Brandle, J. R. (2007). A Method for Estimating Fractal Dimension of Tree Crowns from Digital Images. *Journal of pattern recognition and artificial intelegence*, 21(3):561–572.

Chapter 3

Free-fall experiments

3.1 Introduction

As Climate Change leads to a rise in temperature, more severe and frequent droughts, and changes in precipitation patterns, the risk of wildfires increases dramatically. In the meantime, each year, wildfires burn almost 865 million acres of land throughout the globe in which the United States' share is approximately 7 to 9 million acres [Howard, 2014]. Wildfires expose people, property and ecosystems to a pervasive threat. Also, land development trends at the wild-land urban interface (WUI) have increased the amount of property and infrastructure at risk even further. For instance housing construction at WUIs has resulted in an increase of at-risk homes from 37 to 47 million in the U.S., according to Foster [2014]. As a result wildfires are becoming costlier than current estimates, which in the U.S. is between $20 billion and $125 billion annually [Howard, 2014].

Apart from the economic burden on the federal government, once a wildfire happens the main responsibility is to contain and protect people and property. To this end, understanding wildfire spread mechanisms is of paramount importance. Although wildfires can propagate through convective heat transfer and radiation, there is strong evidence to suggest that firebrand showers are the source of heat transfer [Coleman et al., 2013] that leads to fire spotting. While flame impingement of fuel beds (convective heat transfer), and radiation can cause fire spread in forests, firebrand spotting is a major cause of fire spread at WUIs and consequently, property and infrastructures destruction [Manzello et al., 2007; Wei et al., 2009].

Fire spotting is a complex multi-physics phenomenon that involves firebrand lofting through the envelope of buoyant plumes and thermals formed above the flame zone, various lofting to downwind transport transition scenarios [Tohidi and Kaye, 2013], flight through the atmospheric boundary layer [Albini, 1983], and fire ignition upon landing. Many factors such as size, shape, number, and mass of firebrands, moisture content of the fuel bed, terrain, meteorology and the time of exposure to radiant and convective heat fluxes [Boonmee and Quintiere, 2002] are involved in estimating the susceptibility of a region to spot fires. However, among various stages and agents that affect fire spotting, firebrand flight is a highly complex stochastic process that strongly influences the maximum downwind transport of firebrands. This is a very important measure in assessing the likelihood of a spot fire for a region. Also, the statistics of this parameter depends on the velocity field induced by the interaction of the boundary layer and the fire plume, turbulence characteristics of the velocity field, and physical & chemical properties of firebrands.

As discussed above, firebrand flight is fundamental to fire spotting and, to date, most of the transport models are based on the windborne debris flight models of Tachikawa [1983, 1988] which are written in terms of debris mass and shape. Various equations have been developed for compact [Holmes, 2004; Baker, 2007], rod-like, and plate-like debris [Richards et al., 2002]. However such models when applied to firebrand flight are not quite satisfactory as some simplifying assumptions are added to the models. For instance Anthenien et al. [2006], Kortas et al. [2009] & Koo et al. [2012] assume that the relative velocity vector is always normal to the largest area of the firebrand to get the maximum flight distance. This automatically eliminates side lift force and converts the three-dimensional (3D) trajectory of firebrands to two-dimensional (2D), despite the fact that the 3D motion is a basic characteristic of such objects [Visscher and Kopp, 2007]. Following the same trend, Kortas et al. [2009] presents the experimental validation of a numerical model for transport and combustion of cylindrical and disk-shape firebrands in which trajectories are assumed to be 2D and rotation of firebrands is neglected, since the incidence angle is prescribed beforehand.

On the same note, Bhutia et al. [2010] considers a compact (spherical) shape for firebrands to numerically investigate the differences in trajectories of embers being transported through a classical two-dimensional plume model with a coupled fire/atmosphere Large Eddy Simulator results. This is an overly simplified model given that embers are predominantly in cylindrical/disk shapes [Tohidi

et al., 2015] and the compact model is the most difficult shape of a given mass to get lofted [Koo et al., 2012]. Also, Tarifa et al. [1965, 1967]; Lee and Hellman [1969, 1970]; Fernandez-Pello [1982] and Holmes [2004] utilize the sphere model in their studies. As for of the disk-shape (low aspect ratio cylinder) firebrands, there are some studies by Himoto and Tanaka [2005]; Sardoy et al. [2007, 2008] and Koo et al. [2010] which lack thorough experimental validation.

Although there is a growing body of literature along with field observations (see this video clip, http://i.imgur.com/PveMprY.gifv, from wildfires in Fort MacMurray, Canada, on May-13 2016) and experimental evidence that thin disks and particularly long cylinders are very well representative of firebrands generated during wildfires at WUIs [Manzello et al., 2008; Koo et al., 2012], there has been little work done on the flight of this type of firebrand. The aerodynamic force coefficients of cylindrical objects are measured by Marte et al. [1976] and the results are used in a six-degree-of-freedom (6-DOF) trajectory model of Radbill and Redman [1976]. Likewise, trajectories, velocities and aerodynamic force coefficients of rectangular cylinders are measured by Tachikawa and Harra [1982]. Also, Lin [2005]; Lin et al. [2007] reports the planar trajectories of rod-like debris that are released in a wind field parallel to their symmetry plane. However, in most of these studies, the aerodynamic force coefficients and the position of the center of pressure are only functions of the angle of attack, and the center of pressure is always located on the symmetry plane. Yet, the real situation is more complex than this.

The steady aerodynamic force and moment coefficients of plate and rod-like objects were measured in wind tunnel experiments by Richards et al. [2008] which clearly shows that the coefficients are functions of both angle of attack, and tilt angle. Further, Richards et al. [2008] incorporates these coefficients into a six degrees-of-freedom (6-DOF) numerical transport model, and presents some qualitative comparison of the numerical results with the corresponding free flight experiments in a wind tunnel. It is shown, qualitatively, that the introduced developed model can fairly account for the trajectories of plates with different length and aspect ratios, and long rectangular (rod-like) objects with various side aspect ratios. Moreover, since the angular increment used in Richards et al. [2008] measurements were coarse, wind tunnel experiments with finer angular increment are conducted by Richards [2010]. Then, in a recent study, Richards [2012] recognizes that although aerodynamic force and moment coefficients might change by either rotation of the projectiles or turbulent characteristics of the velocity field, unsteady force and moment coefficients

are only important for early stages of the flight where the accelerations are high.

Given the simplifying assumptions in existing firebrand flight models, the highly stochastic behavior of firebrand (debris) flight in general, and the lack of detailed quantitative experimental validation of models, the objectives of this chapter are to characterize the aerodynamic behavior of rod-like firebrands (objects), and evaluate performance of existing transport models with experimental data.

The rest of this chapter is organized as follows. In section 3.2 governing equations of firebrand transport are discussed as well as the approach taken for characterizing their behavior. Section 3.3 presents the experimental method that is used to meet the objectives of this study. Section 3.4 presents results of the most comprehensive experimental study of firebrands (debris) flight as well as comparisons with corresponding numerical simulations. The collected experimental data would not only have applications in firebrand transport but also would be a major contribution in providing experimental evidence for debris flight through hurricanes and other storms. In section 3.5, the sensitivity of the utilized transport model is analyzed and a diffusion model for firebrand flight is proposed. Finally concluding remarks are drawn in section 3.6.

3.2 Firebrand flight numerical model

3.2.1 Adopted methodology

For rod-like and plate-like firebrands rotational effects are important [Richards et al., 2002]. This may lead to a highly convoluted task in terms of experimental and numerical modeling, and subsequent parametric studies. It is believed that there are two approaches available to tackle this issue. One is to use the *Stokes* diameter concept to parameterize the aerodynamic properties of firebrands [Huang et al., 2007]. The Stokes diameter is the diameter of the equivalent sphere that has the same mass and terminal velocity as the original particle does. Writing Newton's second law of motion for the state at which particles reach their terminal velocity, the Stokes' diameter is

written:

$$D_s = \sqrt{\frac{8mg}{\pi \rho_{air} C_D u_T^2}}. \tag{3.1}$$

Where m is the firebrand's mass, ρ_{air} is the density of air, u_T is the terminal velocity, and C_D is the drag coefficient. Huang et al. [2007] has run a series of experiments to establish the Stokes diameter for a set of disk-shaped particles. These tests are conducted by dropping each disk, measuring its terminal velocity and mass, and employing equation 3.1 to calculate D_s. However, in the case of non-spherical embers the Stokes diameter will not be a fixed value as different release angles (initial conditions) will lead to rotational states and different terminal velocities, and a stochastic equivalent geometry model would be needed. Therefore, for a given shape the Stokes diameter would be distributed about a mean value.

The second approach, is to incorporate the steady aerodynamic force and moment coefficients of the rod and plate-like debris measured in Richards [2010] study into the transport model proposed by Baker [2007], and conduct a model verification in order to evaluate whether the developed model [Richards et al., 2008] is capable of predicting the underlying physics of the stochastic behavior of firebrands' flight.

Due to the complexity of using a stochastic *Stocks* diameter to model firebrands the second methodology is adopted here. That is, we use fixed geometry and model the stochastic flight results with statistical tools.

3.2.2 Governing equations

The transport equations for an object, whose position and orientation are defined such as shown in figure 3.1, are linear and angular momentum equations given by equation 3.2 & 3.3, respectively.

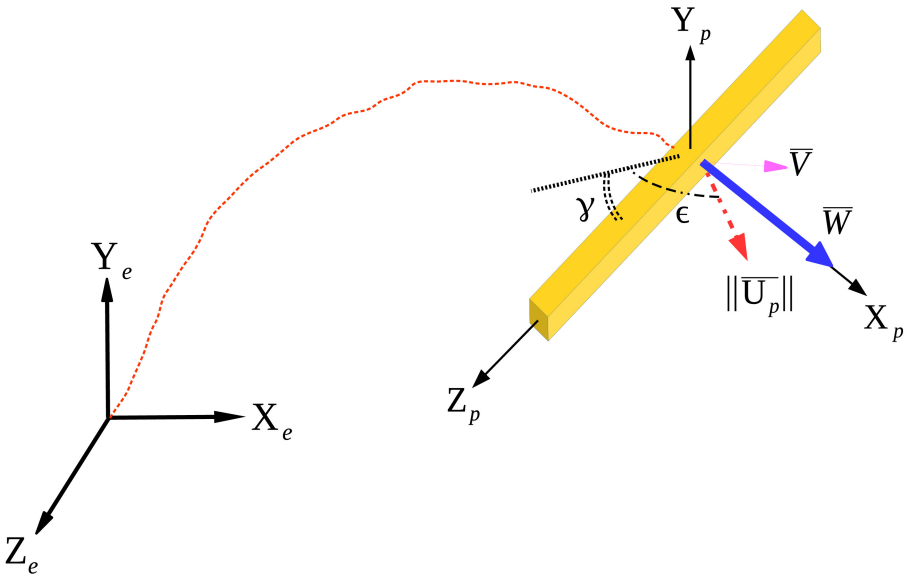

Figure 3.1: Definition of firebrand coordinates and flow angles (γ, ϵ) with respect to global translating non-rotating coordinate system (X_e, Y_e, Z_e), and principal coordinate system of the firebrands (X_p, Y_p, Z_p), respectively. $\bar{V}$ is the firebrand velocity vector, $\bar{W}$ is the ambient velocity vector, and $\bar{U}_p$ is the relative velocity vector of the firebrand in its principal coordinate system.

$$
\begin{aligned}
\ddot{\vec{x}} &= \frac{1}{m}\vec{f} - g\vec{j} \\
\vec{f} &= \mathbf{T}(\theta_x, \theta_y, \theta_z)\vec{f_p} \\
\vec{f_p} &= \vec{c_f}\frac{1}{2}\rho_a \vec{U_p}\left|\vec{U_p}\right|\vec{A} \\
\vec{c_f} &= c_f(\epsilon, \gamma, G),
\end{aligned}
\tag{3.2}
$$

$$
\begin{aligned}
\vec{L_p} &= \vec{M_p} - \vec{\omega} \times \vec{L_p} \\
\vec{M_p} &= \vec{M_E} + \vec{M_D} \\
\vec{M_E} &= \vec{c_E}\frac{1}{2}\rho_a \vec{U_p}\left|\vec{U_p}\right|\vec{V} \\
\vec{M_D} &= \vec{c_{DM}}\frac{1}{2}\rho_a\left(\left|\vec{U_p}\right| + \frac{1}{2}\left|\vec{\omega}\right|\sqrt{l^2}\right)\vec{V}\vec{\omega}\sqrt{l^2} \\
\vec{c_{DM}} &= c_{DM}(G) \\
\vec{c_E} &= c_E(\epsilon, \gamma, G).
\end{aligned}
\tag{3.3}
$$

In equation 3.2, m is the firebrand mass, $\vec{\ddot{x}}$ is the acceleration vector of the firebrand in a global translating but non-rotating coordinate system, $\vec{f}$ is the resultant force vector that is acting on the particle and g is the gravitational acceleration. In calculating the resultant force vector, forces on the principal axes of the firebrands are transformed to the global translating non-rotating coordinate system by the transformation matrix of $\mathbf{T}(\theta_x, \theta_y, \theta_z)$. θ_x, θ_y and θ_z are "roll-yaw-pitch" angles in the Tait-Bryan convention [Robinson, 1958], respectively. As it is demonstrated above the resultant force vectors along the debris principal axes are functions of the velocity along these axes, i.e. u_p and the aerodynamic force coefficients $\vec{c_f}$ which are themselves a function of angle of attack ϵ, tilt angle γ, and geometry of the firebrands. Also, in equation 3.3, $\vec{L_p}$ is the angular momentum of the firebrands, $\vec{M_p}$ is the vector of the applied moments about the object's principal axes, and $\vec{\omega}$ is the vector of angular velocity. It should be noted that for the angular momentum equation, rotational effects are not necessary to be transformed to the global coordinate system and can be directly calculated by utilizing Euler's rigid body dynamics equations. The moment vector is, also, a function of firebrand velocity along the principal axes and the aerodynamic moment coefficients $\vec{c_E}$ are themselves a function of ember geometry, angle of attack and tilt angle; see, [Richards et al., 2008]. For a more detailed derivation see Grayson and Pang [2011].

Equations 3.2 & 3.3 are nonlinear. This suggest that they may be highly sensitive to the initial conditions of the firebrands at the break-off stage prior to getting lofted through the fire plume envelope. Nonlinearity of the equations implies that a little change in initial conditions may cause a significant difference in trajectory of the firebrand's particularly upon landing. This is investigated by solving equation 3.2 & 3.3 for the free fall of a model firebrand with diameter $D = 4.77\,mm$, length $L = 86\,mm$, and aspect ratio of $\eta = L/D = 18$ from three different heights. The equations are solved by converting the 3D probabilistic debris flight model of Grayson et al. [2012], developed in the MATLAB environment, to the original deterministic model of Richards et al. [2008]. For thorough details on the MATLAB code consult with Grayson and Pang [2011]. At each release elevation all Tait-Bryan angles are put equal to zero except the one that is changed with increments of $\Delta\theta = 0.01^\circ$. In addition, a very small uniform ambient velocity, i.e. $10^{-30}\,(m/s)$, is given to the solver, as it is the required initial condition of the code to run. This change in the initial condition, even though it is very small, is reflected as a response to the change in the Roll angle. Figures 3.2-3.4, demonstrate the result of sensitivity analysis to the change in initial conditions, that is release

angles.

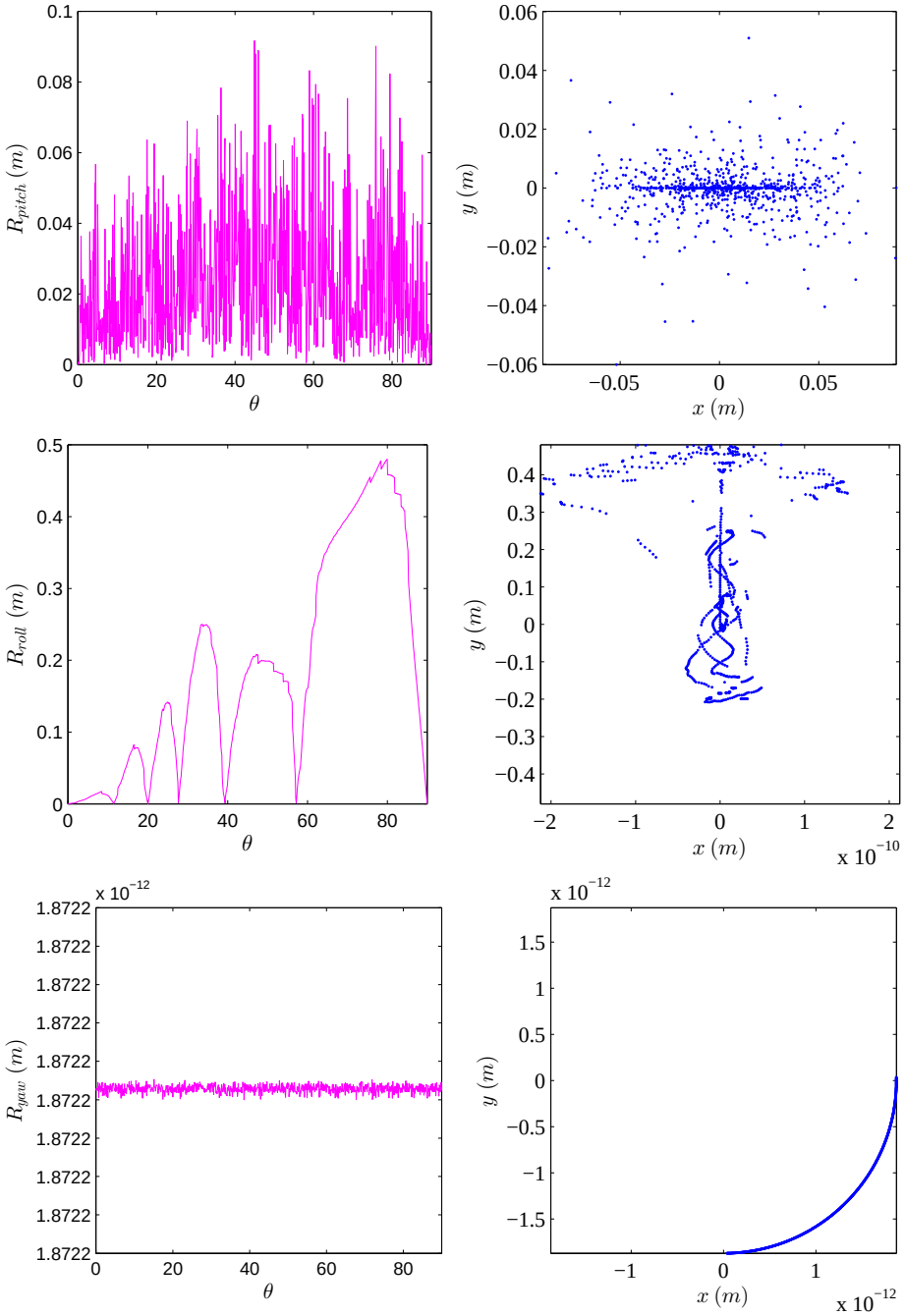

Figure 3.2: From top to bottom, analysis of sensitivity to the initial angles of pitch, roll, and yaw. (Left) Radial distances of the contact point from the projection of the release point to the ground elevation. (Right) Coordinate of the contact point to the ground. $\Delta\theta = 0.01^\circ$ and release height 5 (m).

According to figures 3.2-3.4, it is clear that, as the release hight increases, the radial distance

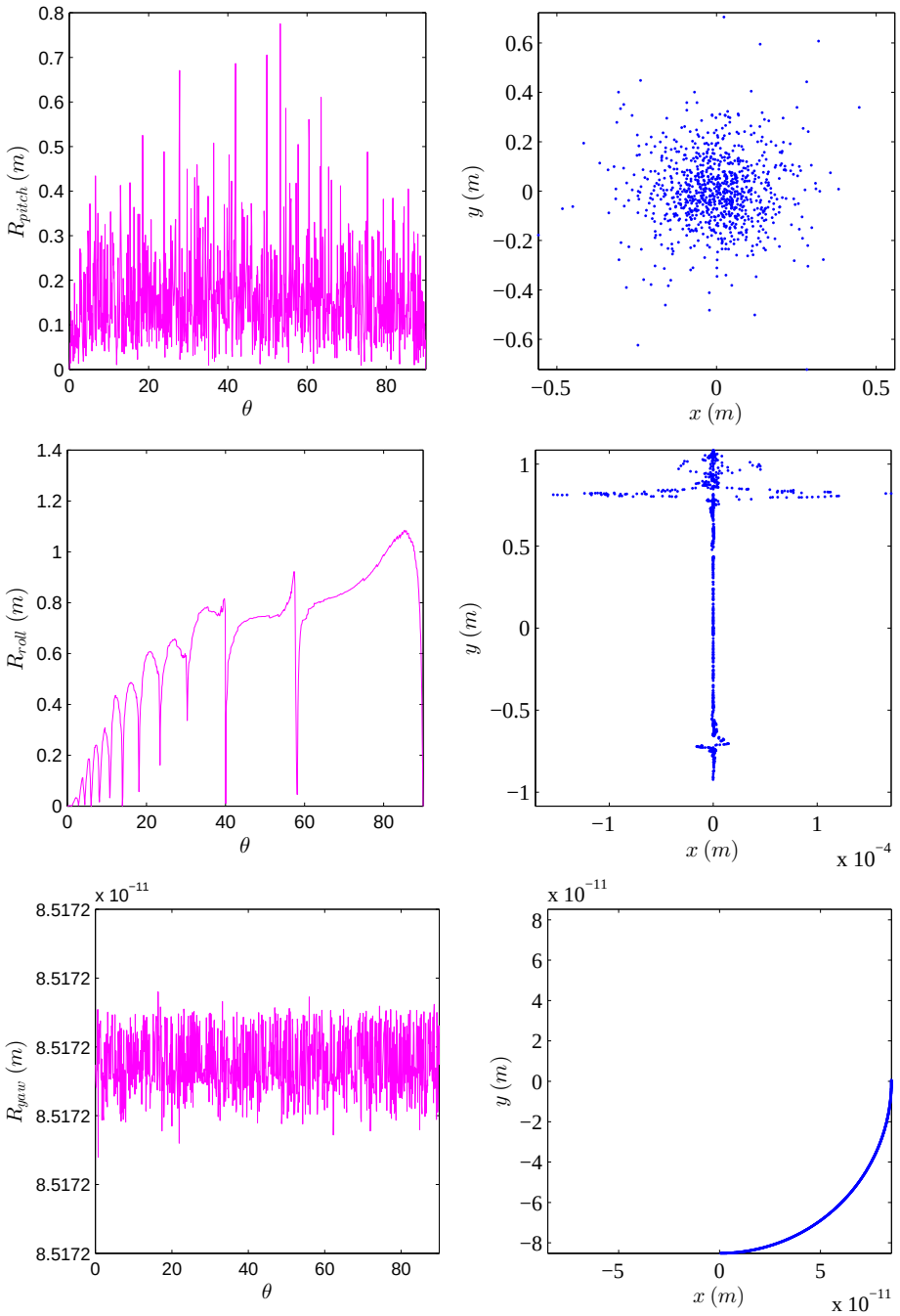

Figure 3.3: From top to bottom, analysis of sensitivity to the initial angles of pitch, roll, and yaw. (Left) Radial distances of the contact point from the projection of the release point to the ground elevation. (Right) Coordinate of the contact point to the ground. $\Delta\theta = 0.01^\circ$ and release height 10 (m).

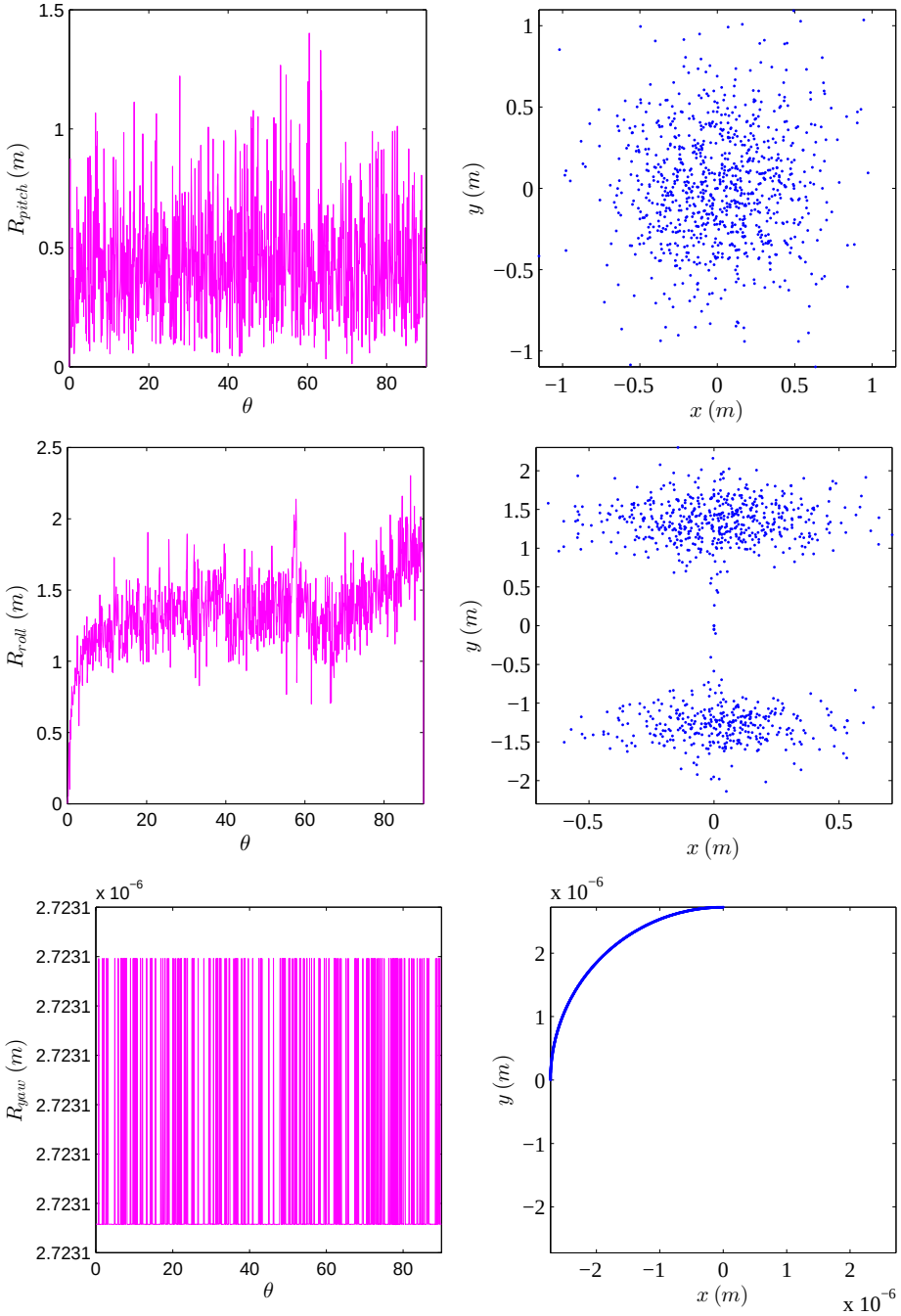

Figure 3.4: From top to bottom, analysis of sensitivity to the initial angles of pitch, roll, and yaw. (Left) Radial distances of the contact point from the projection of the release point to the ground elevation. (Right) Coordinate of the contact point to the ground. $\Delta\theta = 0.01^\circ$ and release height 20 (m).

of the contact point of a firebrand to the ground is more and more sensitive to the initial conditions of the release. This is due to the fact that nonlinear effects would have more time (domain of change) to propagate and accumulate at the final solution compared to lower release height cases. The model shows significant sensitivity to pitch and roll angles, although it is almost insensitive to the yaw angle. It should be noted that one of the key parameters in understanding the spot fire phenomenon is the ability to predict/estimate the landing location of firebrands. Hence, in contrast to Grayson et al. [2012], the initial release angles are better candidates to be subjected to the Metropolis Monte-Carlo simulations than randomly permuting angle of attack (ϵ) and tilt angle (γ) during the solution.

Sensitivity of the model to other parameters such as mass (density), aerodynamic coefficients, and irregularity in shape (mass moment of inertia) will be discussed later in section 3.5. Uncertainty quantification of the transport model to these parameters as well as assessing its ability in capturing the underlying statistics of such stochastic behavior, i.e. firebrand flight, are only possible when there is enough experimental evidence for the flight. Unfortunately, as explained in section 6.1, there hasn't been reliable and conclusive experimental data for firebrand (particle) flight. In order to fill this gap, a series of experiments is designed to capture the statistical properties of the model firebrands during free fall.

3.3 Free fall experiments

3.3.1 Experimental setup

In these experiments non-combusting model firebrands that are chosen from various tree types with different aspect ratios are released from different heights. Specifics of the experiments are shown in table 3.1. The release height from the ground, that is measured by a *FLUKE-411D* laser distance meter with $\pm 3\,mm$ accuracy, was set at $H = 1.64\,(m)$, $H = 5.6\,(m)$, and $H = 9.2\,(m)$. For each aspect ratio per release height firebrand models are released multiple times while initial conditions of firebrand models, i.e. release angles, are varied randomly for each drop. Table 3.2 shows specifics of free fall experiments in detail. The reason that drops are conducted under two populations with difference in orders of magnitude of the degrees of freedom (D.O.F.) will be discussed in section 3.4. The aim of these experiments is to record the radial distance between the contact point of the model firebrands to the ground and the projected release point to the plane of

Table 3.1: Physical properties of the model firebrands used in free experiments. Here, ρ is the mass density, D is the diameter, L is the length, and $\eta = L/D$ is the aspect ratio of the model firebrands.

Ember type	$\rho\,(kg/m^3)$	$D\,(mm)$	$L\,(mm)$	η
Cork	250	10	40	4
Birch	670	10	76	7.6
Poplar	427	4.77, 6.48, 10.55	170, 160, 130	36, 25, 12
Poplar	427	4.77	85.9, 43, 28.6, 14	18, 9, 6, 3

Table 3.2: Specifics of the free fall experiments. D.O.F. stands for degrees of freedom in each set that is number of free falls conducted.

η	$D\,(mm)$	Wood type	$H\,(m)$	D.O.F. 1^{st}	D.O.F. 2^{nd}
3	10	Poplar	1.64	101	974
			5.62	101	1036
			9.21	101	811
4	10	Cork	1.64	101	-
			5.62	98	-
			9.21	101	-
6	4.77	Poplar	1.64	100	-
			5.62	100	-
			9.21	102	-
7.6	10	Birch	1.64	56	-
			5.62	75	-
			9.21	71	-
9	4.77	Poplar	1.64	100	991
			5.62	97	1022
			9.21	110	-
12	10.55	Poplar	1.64	90	-
			5.62	98	-
			9.21	98	996
18	4.77	Poplar	1.64	100	-
			5.62	102	-
			9.21	110	-
25	6.48	Poplar	1.64	100	-
			5.62	104	-
			9.21	98	914
36	4.77	Poplar	1.64	107	-
			5.62	104	-
			9.21	86	880

contact which was determined by plumb bob. Figure 3.5 shows the experimental setup.

Using a *GC-PX100 JVC* camera, with 1920×1080 resolution at $60\,fps$, free falls are recorded from above to capture the contact point on the ground. For this purpose, it is crucial to do the

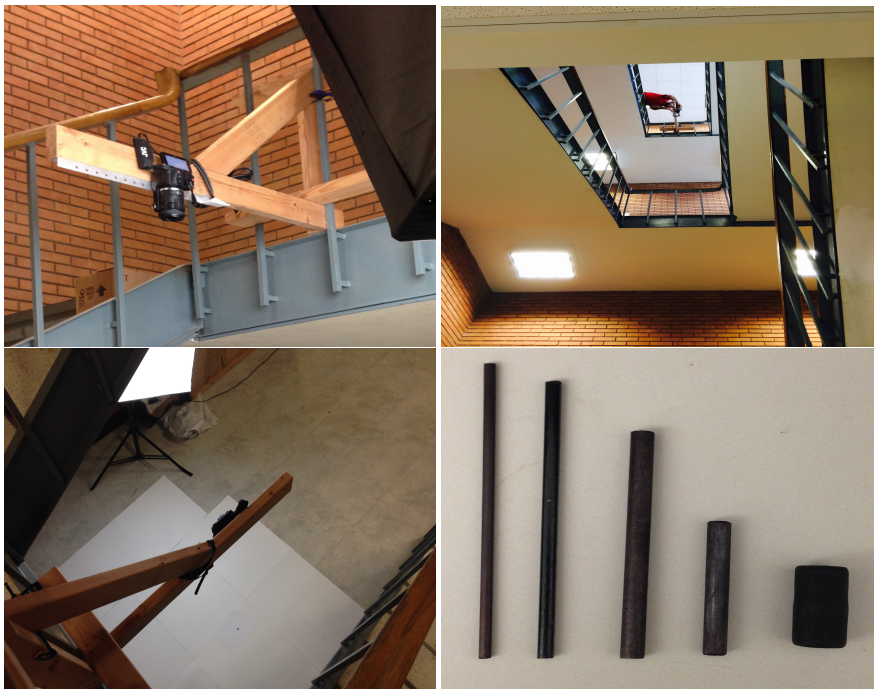

Figure 3.5: Experimental setup of non-combusting firebrand free fall experiments. (Top-left) A custom made frame with designated release location on its beam, and a place for high speed camera to be mounted on the exact location of the release. (Bottom-left) projected release point to the ground on a plane with white background. (Top-right) A sample release procedure from height $H = 9.2\,m$. (Bottom-right) Various aspect ratios of model firebrands.

image analysis on the exact image in which the firebrand model hits the ground. To find the exact frame of contact, audio signals recorded during the free fall procedure are analyzed. As is evident in figure 3.6, there is a high peak in the audio signal at the instant when microphones of the camera receive the sound waves generated from the contact. By having the exact height between the release point and the ground, and calculating the speed of sound at room temperature $22 - 25\,^oC$ for the dry air, the time delay in appearance of the peak in audio signal is found. Equation 3.4 is used for calculating the speed of sound (C_{air}).

$$C_{air} = 331.3\sqrt{T_{air}/273.15} \tag{3.4}$$

where T_{air} is the air temperature in Kelvin. For more details in this regard see Dunn et al. [2015]. The whole procedure is embedded in the image processing algorithm that is discussed below.

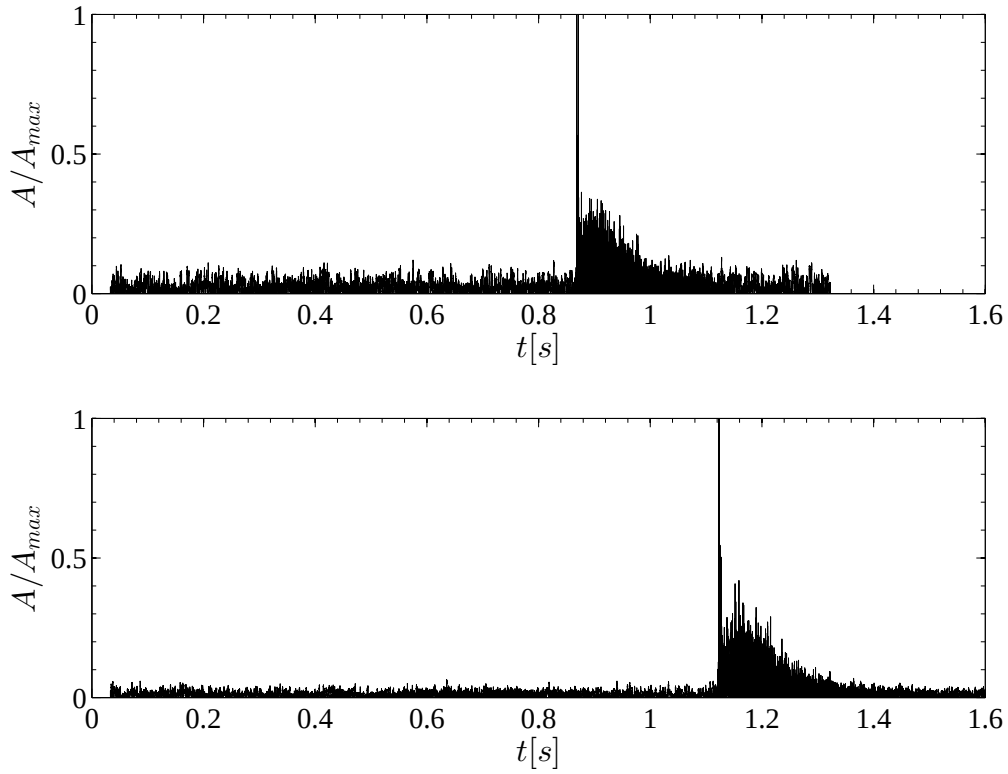

Figure 3.6: Time history of the normalized amplitude of sound waves, i.e. A/A_{max}, with maximum observed amplitude in free fall experiments of a firebrand model with aspect ratio $\eta = 3$ that is released from (Top) $H = 5.6\,m$, and (Bottom) $H = 9.2\,m$.

3.3.2 Image Processing technique

Data is collected using two image processing algorithms with slight differences. The first algorithm is designed for free falls set with D.O.F. of the order of magnitude of 100. The procedure for this method is that for each model firebrand the free fall is filmed (from above) individually, it is then removed from the camera's frame, and the next firebrand model is dropped and recorded separately from the previous one. The captured videos are analyzed by an image and audio signal processing script that is written in MATLAB to extract the images from videos and return the contact point to the ground with $\pm 1\,mm$ accuracy, as described in the previous subsection. It should be noted that uncertainty of the image processing results is less than the size of the markers used for showing the landing locations, later. One of the drawbacks of this method is that it has to be done with two individuals. One who drops the model firebrands and records each drop, and the other who is in charge of removing the landed firebrand models from the camera sight. In addition,

the image processing becomes an arduous task as the number of free falls increases and leads to more overhead preparation for the recorded videos. Hence, for the set of free falls with D.O.F. of the order of magnitude of 1000 a new procedure was designed in which the experiments conducted with only one individual, and the analysis is faster, because the model firebrands can be dropped consecutively without the need of removing landed firebrand models from the camera's sight.

In the first method, calculating coordinates of the contact point to the ground and finding the radial distance of it from the projection of the release point is trivial after extracting the exact frame when a firebrand model has landed. The rest of the procedure is as follows. Images are calibrated using the scale that was put in front of the camera before the onset of each release set. Then, the background image (a frame without any firebrand model in it) is subtracted from the frame with a firebrand at the landing instant. As it is evident in the bottom right of figure 3.7, this identifies the presence of the firebrand model in the frame. In order to reduce the noise in the image and make it ready for contrast stretching, a rotationally symmetric lowpass *Gaussian* filter with standard deviation of $\sigma_g = 5\, pixels$ and a square height matrix of $h_g = 35\, pixels$ is convoluted over the background subtracted image; See top-left of figure 3.8. Calculated intensities are stretched (mapped) to the range of $0 - 1$ and the resulting image is opened (morphed) with a linear (cylindrical shape) structuring element that is symmetric with respect to the neighboring pixels. This effectively opens a binary image that has masked the occupied pixels by the firebrand model form, as demonstrated in bottom-right of figure 3.8. Then, by finding the centroid of the identified firebrand model with respect to the predefined coordinates of the projected release point in the frame the radial distance is calculated. See Gonzalez et al. [2004] for further information about the image processing algorithms utilized. The second method creates a composite difference image from the consecutive landing frames extracted by the audio analysis. Then runs the same procedure over the composite image and calculates the radial distance. Figure 3.9 shows sample images from implementation of this stage before the rest of algorithm executes. With utilizing this method, model firebrands can be dropped consecutively without the need to remove the previous embers from the camera sight. There is no need to record video for each drop and extract the contact scene from it. Therefore, the analysis can be done on a single continuous record. The only disadvantage is that this method requires a large volume of hard drive memory because it writes all frames of the video on the hard disk. Also, in cases when the landing firebrand model hits another one in the frame the

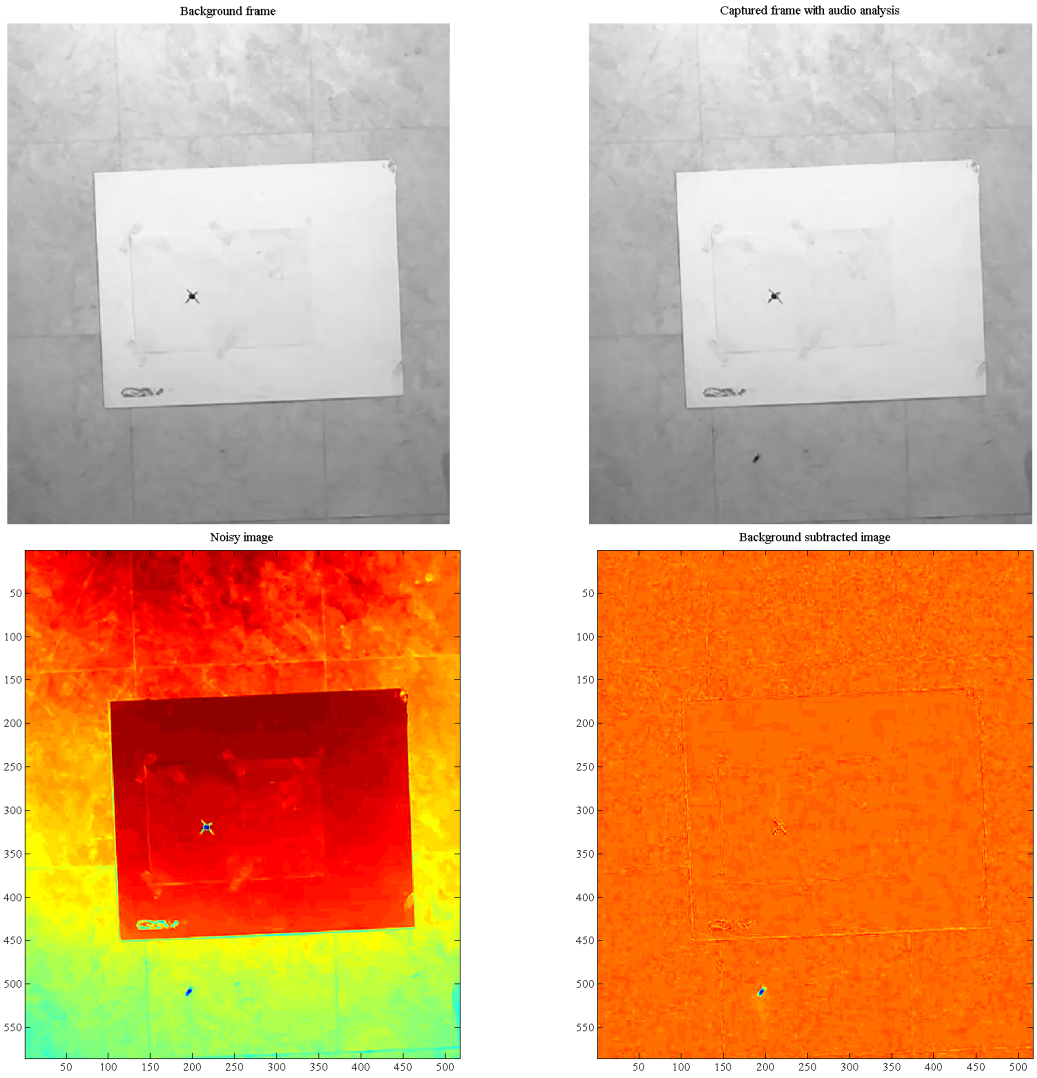

Figure 3.7: (Top-left) Background image with projected release point to the plane of contact by plumb bob; (Top-right) an image from the exact moment when firebrand model contacts to the ground, also referred to as target image. (Bottom-left) Converted traget image from RGB to double; (Bottom-right) identified firebrand model in the image from which the background image is subtracted.

recognition is not as exact as the previous method. Therefore, all runs are checked with interactive object recognition scripts in which the coordinates of the contact are confirmed and corrected with human observation.

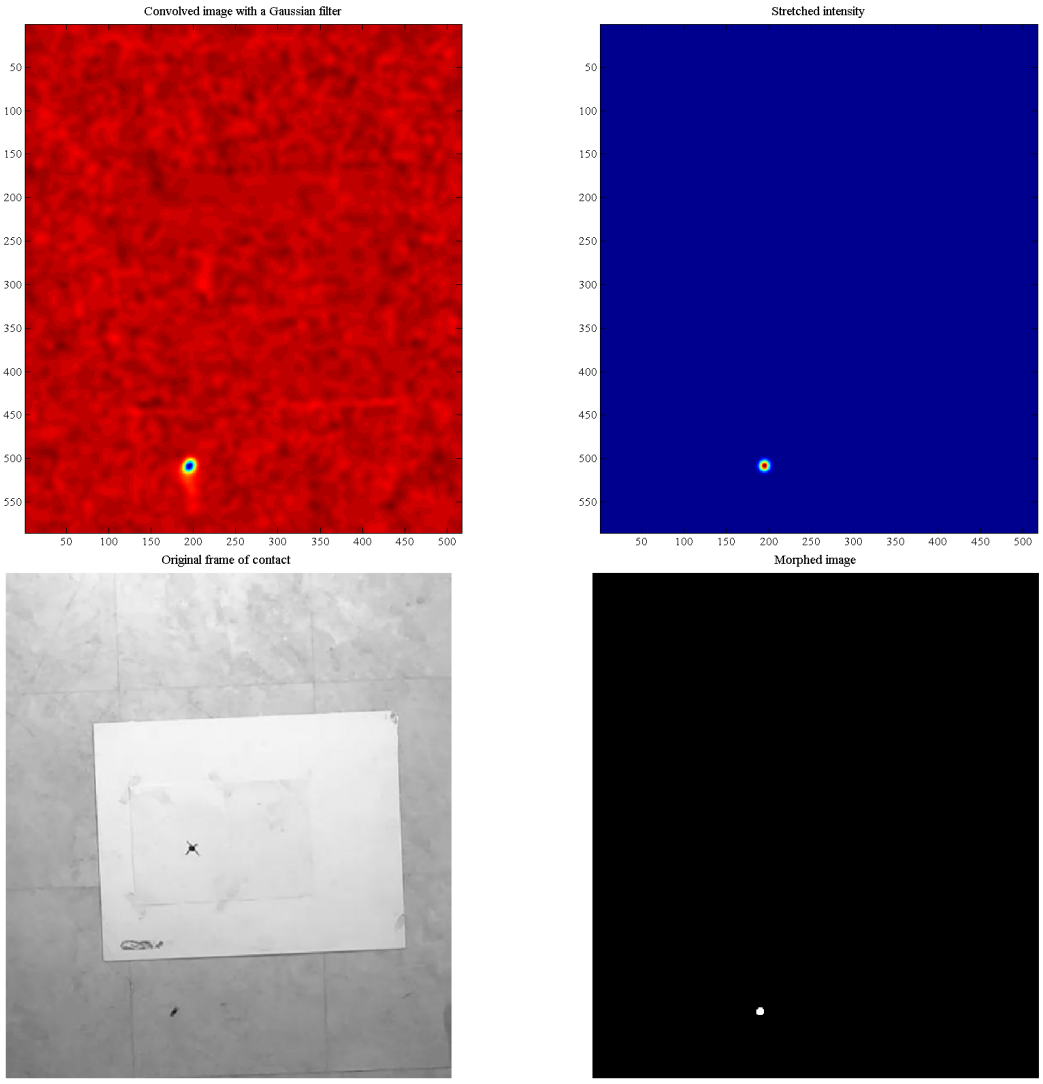

Figure 3.8: (Top-left) Shows results of convolving the explained Gaussian filter over the background subtracted image; (Top-right) demonstrates color coded image after stretching the intensities to the range of $0-1$. (Bottom-left) shows the original frame of contact in relation to the morphed image by a structuring element (bottom-right) through which centroid coordinates of the firebrand model is calculated.

3.4 Results

To address the stated objectives in section 3.2, this section deals with presenting the results of free fall experiments in relation to their corresponding numerical simulations conducted by the 3D deterministic 6-D.O.F. firebrand transport model, which uses the steady aerodynamic force and moment coefficients of Richards et al. [2008]; Richards [2010]. These results will establish a frame

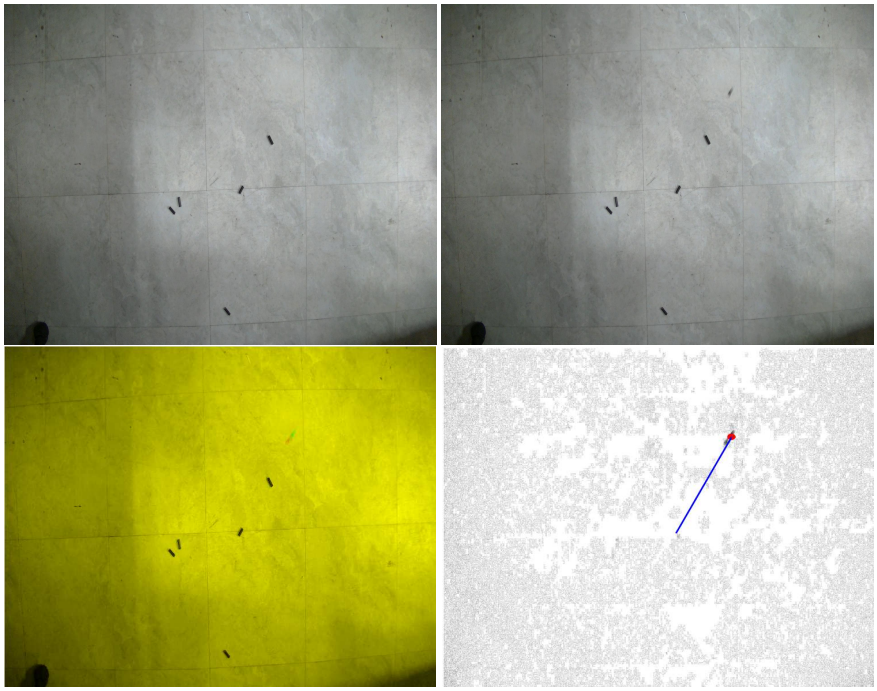

Figure 3.9: (Above) Shows before (left) and after (right) images of an independent ember model drop. (Below-left) shows the composite image of the two instances which illustrates the difference between them. The pale red and green area illustrates the difference, i.e. contact point. (Below-right) shows the coordinates of the contact point which is identified with overlay adjustment on the background subtracted image. Also, shown is a blue line between the projection of the release point to the ground and the contact point of ember to the ground which is marked with a red star.

work for quantitative evaluation of the developed firebrand transport model [Richards et al., 2008; Grayson and Pang, 2011]. Using the evaluated model, the aerodynamic behavior of firebrands' flight can be characterized.

To this end, first, experimental and numerical results of the free fall experiments with the sample size of the order of 100 drops are presented. Pursuant to this, based on the obtained insight from experimental results and their corresponding numerical simulations, the second round of free fall experiments with sample size of the order of 1000 drops are conducted and results are presented.

As discussed in section 3.2, the governing equations are highly sensitive to initial conditions of the release, that is the Tait-Bryan angles. In the numerical model, these angles are subjected to Metropolis Monte-Carlo simulation and seeded randomly from a uniform distribution with the lower and upper bounds of 0^o and 360^o, respectively. For all simulations throughout this study, the time

step is adopted to be 5 milliseconds, in order to maintain accuracy and stability of the model. Also, the number of releases per each set is chosen to be equal to the number of drops in the corresponding experiments so that they both have equal degrees of freedoms. Other parameters of the numerical model are chosen explicitly from tables 3.1 & 3.2.

Figures 3.10-3.18, show scatter plots of the contact point of firebrand models to the ground in comparison to the corresponding numerical simulations. As mentioned before, the uncertainty of the image processing analysis is ± 1 which is smaller than the size of the markers used for visualization of the scatter plots. Therefore, error bars are eliminated from these figures. Also, probability density function (PDF) and cumulative density function (CDF) of the normalized radial distances with release height are given for the purpose of quantitative comparison between the experiments and numerical simulation results.

As indicated by the PDF and CDF plots in the above figures (3.10-3.18), the numerically estimated mean of the normalized radial distance is relatively close to the experiments. However, as for of the variance, in some sporadic cases there is no agreement between the results and, for the rest of the cases the results are not very satisfying. This intermittency suggests another parameter that the numerical model is sensitive to. Since many parameters such as density, aspect ratio, aerodynamic coefficients, and etc are involved in this highly stochastic problem, it is consistent with statistical theory to first increase the number of samples (drops). A numerical experiment was done to investigate the response (sensitivity) of the model to the increase in the number of independent samples.

The sensitivity analysis to the number of independent drops was done, numerically, by releasing ten thousand firebrands with aspect ratio 18 from $9.2\,m$ of height. Figure 3.19 shows the response of calculated radial distance and its statistics to the increasing number of drops. A scatter plot of landing locations indicates that there is no correlation or tendency in the results towards a particular orientation. Also, since the drops are done passively and independent from each other, increasing the number of samples has no effect on the stochastic behavior (value) of the radial distance of other samples; See middle plot in figure 3.19. Nonetheless, increasing the number of independent samples, i.e. n, has significant influence on the statistical properties of the radial distance. As illustrated on figure 3.19-(right), the cumulative rolling mean and standard deviation of the radial

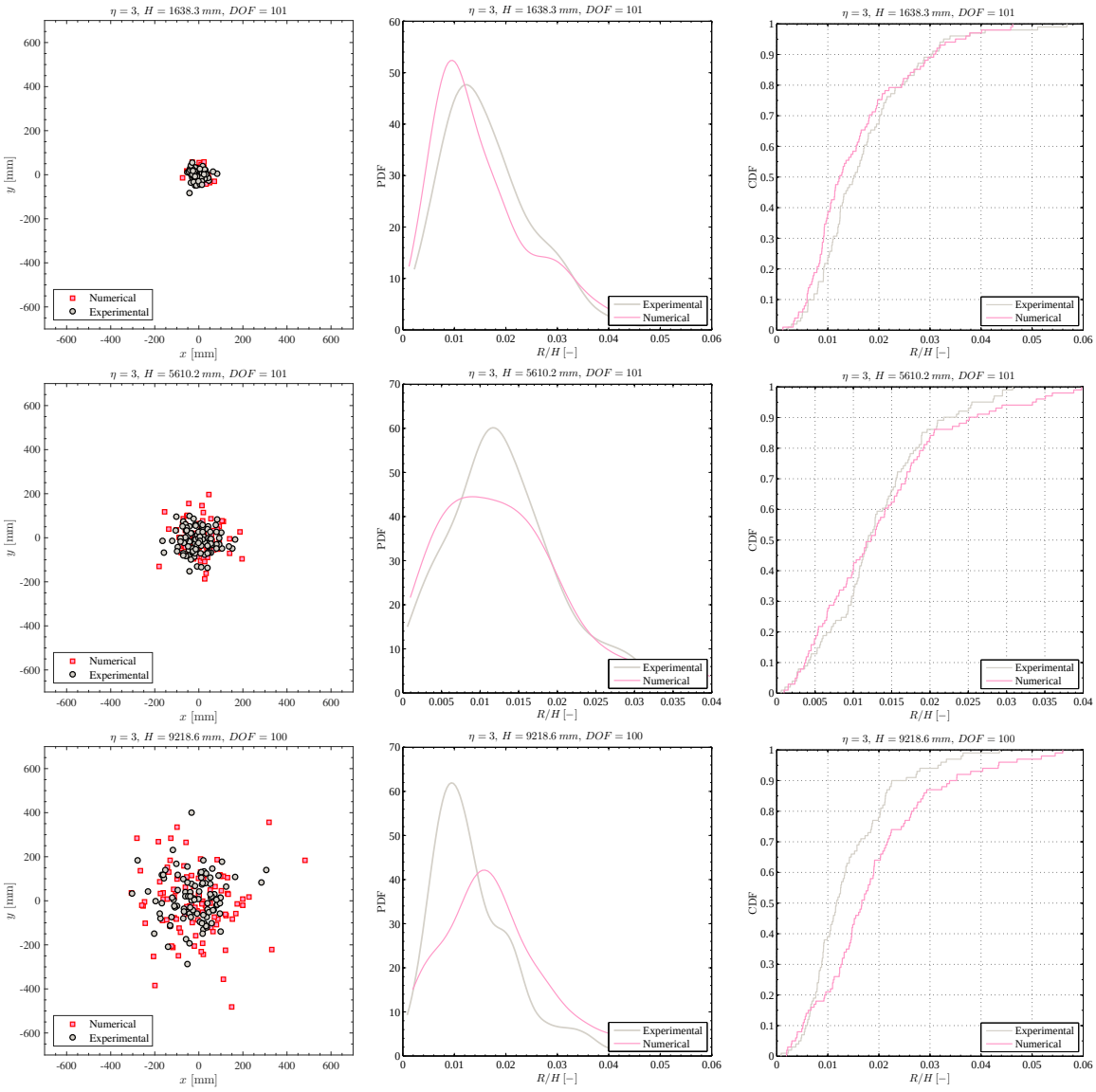

Figure 3.10: (Left) Qualitative comparison between coordinates of contact point to the ground in experiments with corresponding numerical simulations conducted for the release of firebrand models with $\eta = 3$, and D.O.F. of the orders of magnitude of 100. Also, shown are empirical PDFs (middle) and CDFs (right) of the normalized radial distances with the release height. From top to bottom the release height increases from $H = 1.64\,m$ to $5.6\,m$ and $9.23\,m$.

distance tend towards constant values after roughly one thousand drops. It can be inferred that the number of drops, that varies between $56 - 110$ in the first set of experiments is not enough for capturing the statistical characteristics of the firebrands' flight, and more reliable results may be obtained by significantly increasing the number of drops. This is also consistent with the uncertainty reduction principle that, by increasing the number of independent samples, i.e. degrees of freedoms

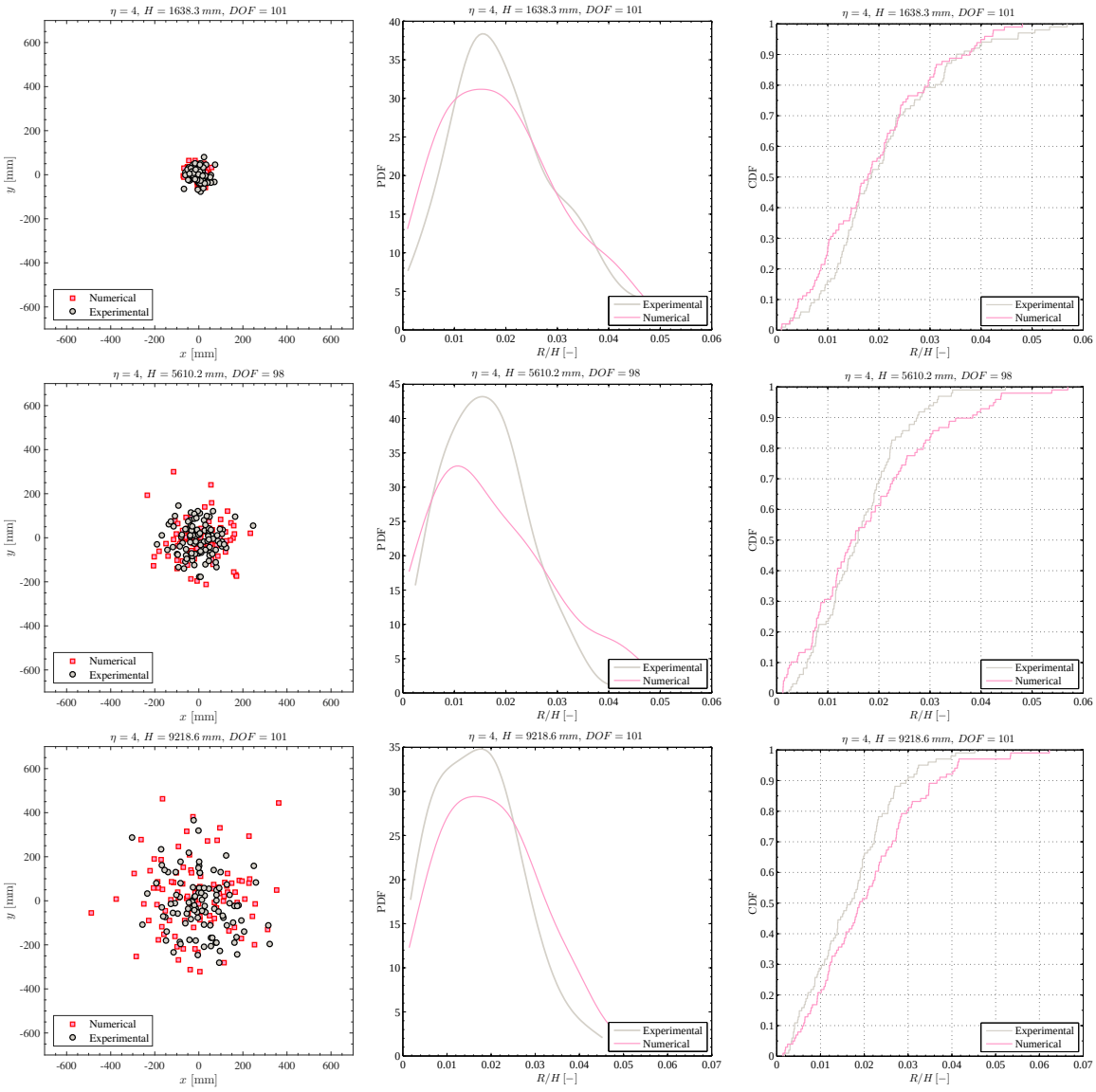

Figure 3.11: (Left) Qualitative comparison between coordinates of contact point to the ground in experiments with corresponding numerical simulations conducted for firebrand models with $\eta = 4$, and D.O.F. of the orders of magnitude of 100. Also, shown are empirical PDFs (middle) and CDFs (right) of the normalized radial distances with the release height. From top to bottom the release height increases from $H = 1.64\,m$ to $5.6\,m$ and $9.23\,m$.

n, in a stochastic event, the confidence interval would narrow down and the accuracy of the results will increase.

Results of the sensitivity analysis to the size of the sample has led to the second round of experiments where selected aspect ratios of firebrand models are released from different heights

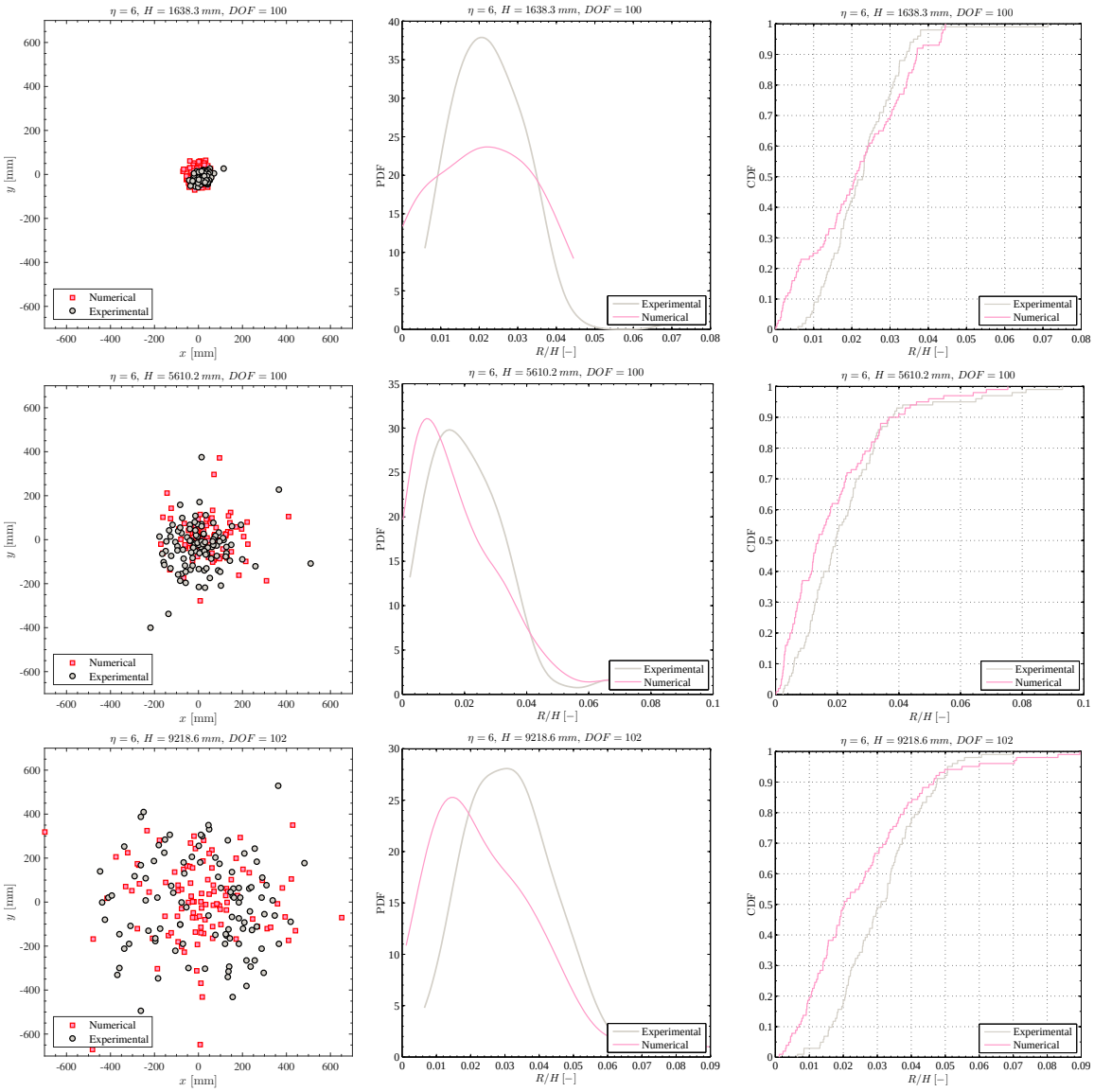

Figure 3.12: (Left) Qualitative comparison between coordinates of contact point to the ground in experiments with corresponding numerical simulations conducted for firebrand models with $\eta = 6$, and D.O.F. of the orders of magnitude of 100. Also, shown are empirical PDFs (middle) and CDFs (right) of the normalized radial distances with the release height. From top to bottom the release height increases from $H = 1.64\,m$ to $5.6\,m$ and $9.23\,m$.

as indicated in table 3.2. Parameters of these experiments are adopted such that a wide range of aspect ratios and release heights as well as large number of degrees of freedoms are covered. Based on the sensitivity analysis, it is reasonable to assume that statistics of the results will converge to a constant value in around 1000 drops. Hence, the number of drops was increased to meet this criterion. In this second set of experiments some embers landed outside the field of view of the

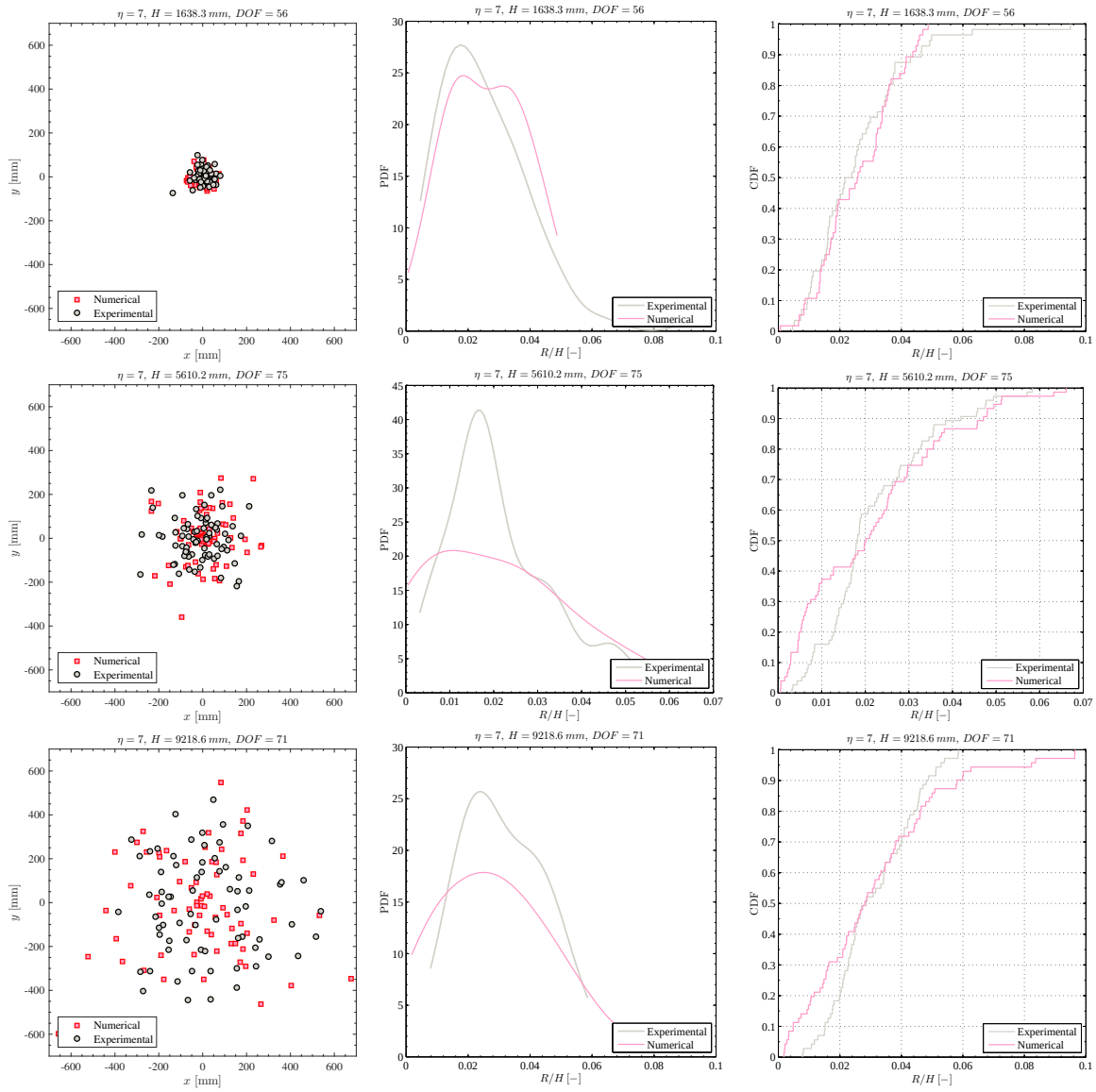

Figure 3.13: (Left) Qualitative comparison between coordinates of contact point to the ground in experiments with corresponding numerical simulations conducted for firebrand models with $\eta = 7.6$, and D.O.F. of the orders of magnitude of 100. Also, shown are empirical PDFs (middle) and CDFs (right) of the normalized radial distances with the release height. From top to bottom the release height increases from $H = 1.64\,m$ to $5.6\,m$ and $9.23\,m$.

camera and were not included in the data analysis. This will result in a slight under prediction of both the mean and standard deviation of the radial landing location. However, this effect will be small as only a couple of embers landed outside the field of view for each set of one thousand drops.

Figures 3.20-3.24 present the results obtained from the second set of experiments comparing

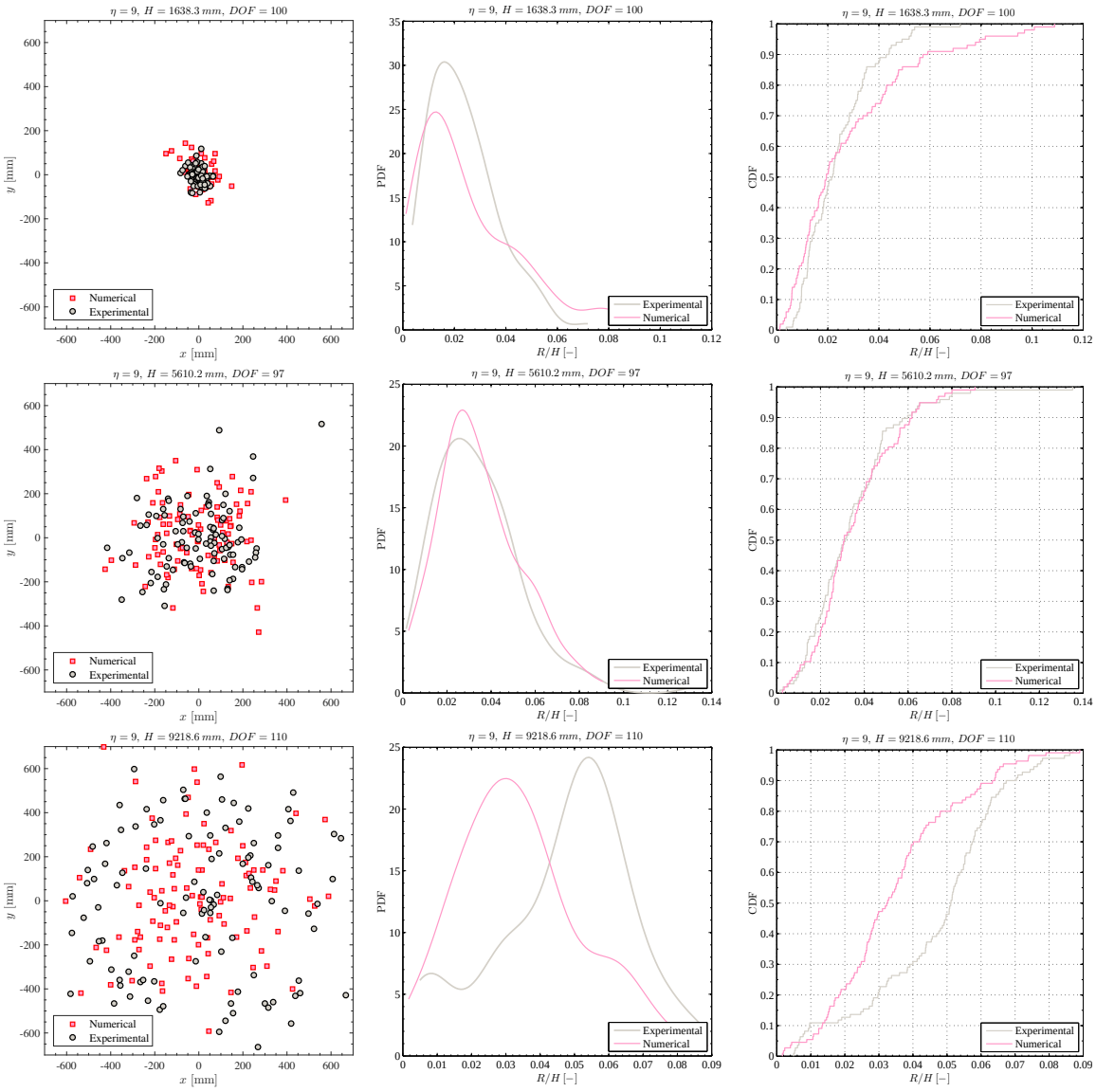

Figure 3.14: (Left) Qualitative comparison between coordinates of contact point to the ground in experiments with corresponding numerical simulations conducted for firebrand models with $\eta = 9$, and D.O.F. of the orders of magnitude of 100. Also, shown are empirical PDFs (middle) and CDFs (right) of the normalized radial distances with the release height. From top to bottom the release height increases from $H = 1.64\,m$ to $5.6\,m$ and $9.23\,m$.

to the corresponding numerical simulations. Scatter plots of landing locations along with PDFs and CDFs of the normalized radial distance with release height are presented.

There is a very good agreement between the experimental and numerical results. There is only a slight discrepancy between PDFs and CDFs which can be mostly attributed to the difference in variance of the radial distance. Further, plots of cumulative rolling average of mean and standard

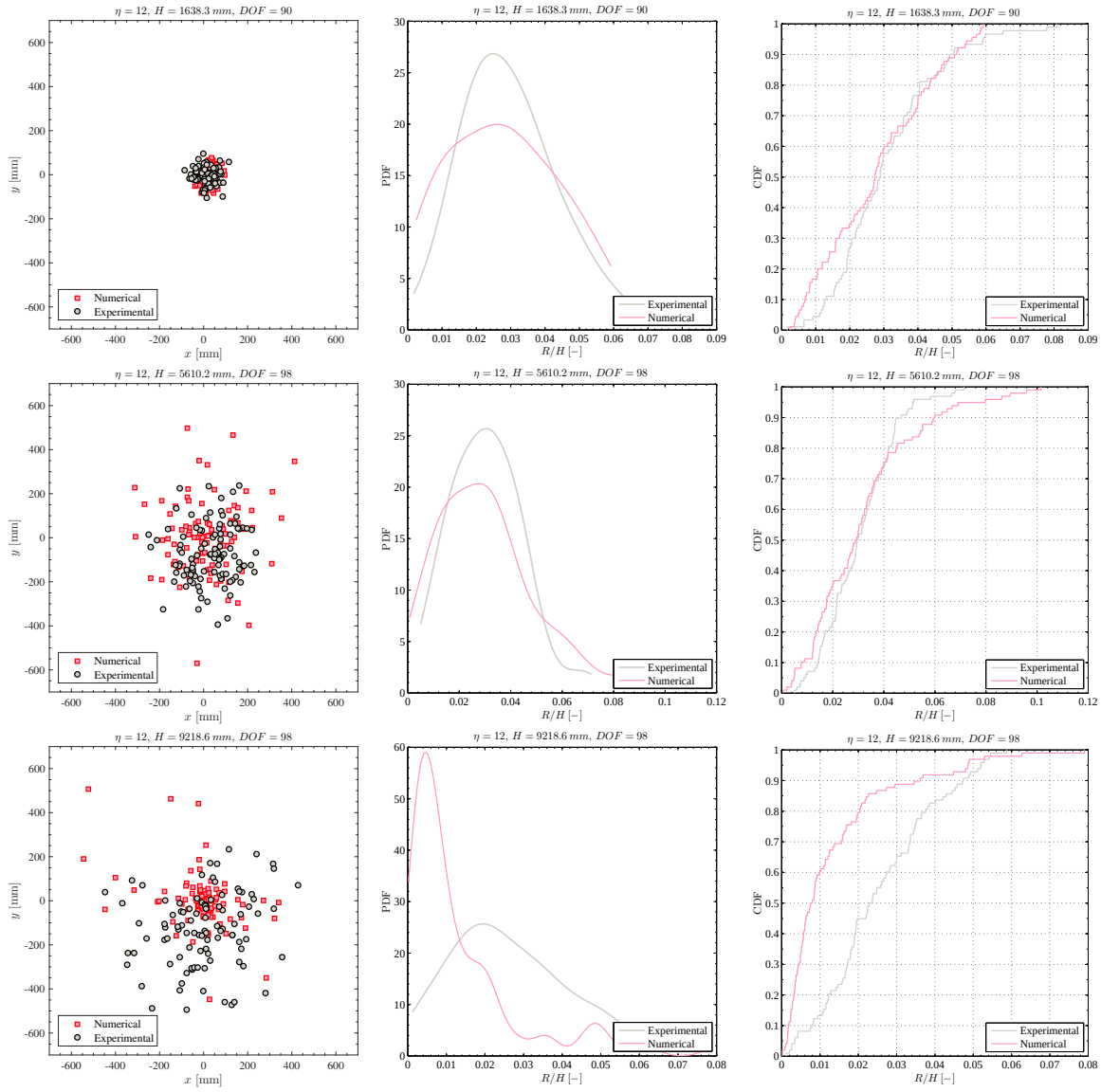

Figure 3.15: (Left) Qualitative comparison between coordinates of contact point to the ground in experiments with corresponding numerical simulations conducted for firebrand models with $\eta = 12$, and D.O.F. of the orders of magnitude of 100. Also, shown are empirical PDFs (middle) and CDFs (right) of the normalized radial distances with the release height. From top to bottom the release height increases from $H = 1.64\,m$ to $5.6\,m$ and $9.23\,m$.

deviation of the radial distance, which are shown in figures3.25-3.28, second the results of the sensitivity analysis to the sample size.

Positive agreement in both qualitative and quantitative comparisons of experimental results with numerical simulations necessitates statistical hypothesis testing in order to determine whether the results from the numerical model are statistically significantly different from the experiments.

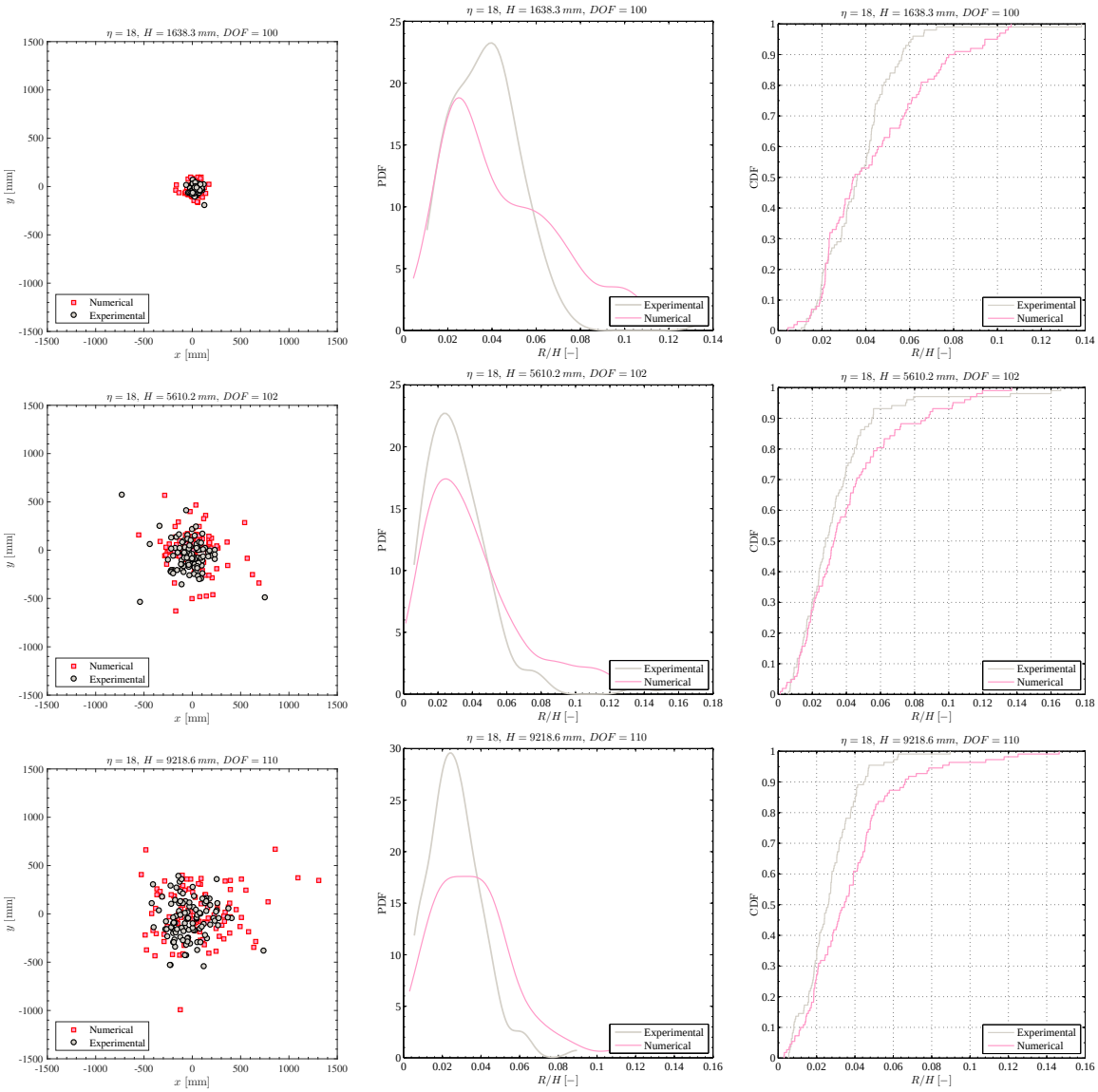

Figure 3.16: (Left) Qualitative comparison between coordinates of contact point to the ground in experiments with corresponding numerical simulations conducted for firebrand models with $\eta = 18$, and D.O.F. of the orders of magnitude of 100. Also, shown are empirical PDFs (middle) and CDFs (right) of the normalized radial distances with the release height. From top to bottom the release height increases from $H = 1.64\,m$ to $5.6\,m$ and $9.23\,m$.

Hence, in the domain of measured and simulated radial distances a null hypothesis is designed to determine if the experimental results and corresponding estimations from the numerical model are from the same continuous distributions. The test of this hypothesis is known as the two-sample Kolmogorov-Smirnov ($K - S$) test. The results are set out in table 3.3. For the majority of the cases, the K-S test rejects the null hypothesis. That is, in those with $h_0 = 1$, the measured radial

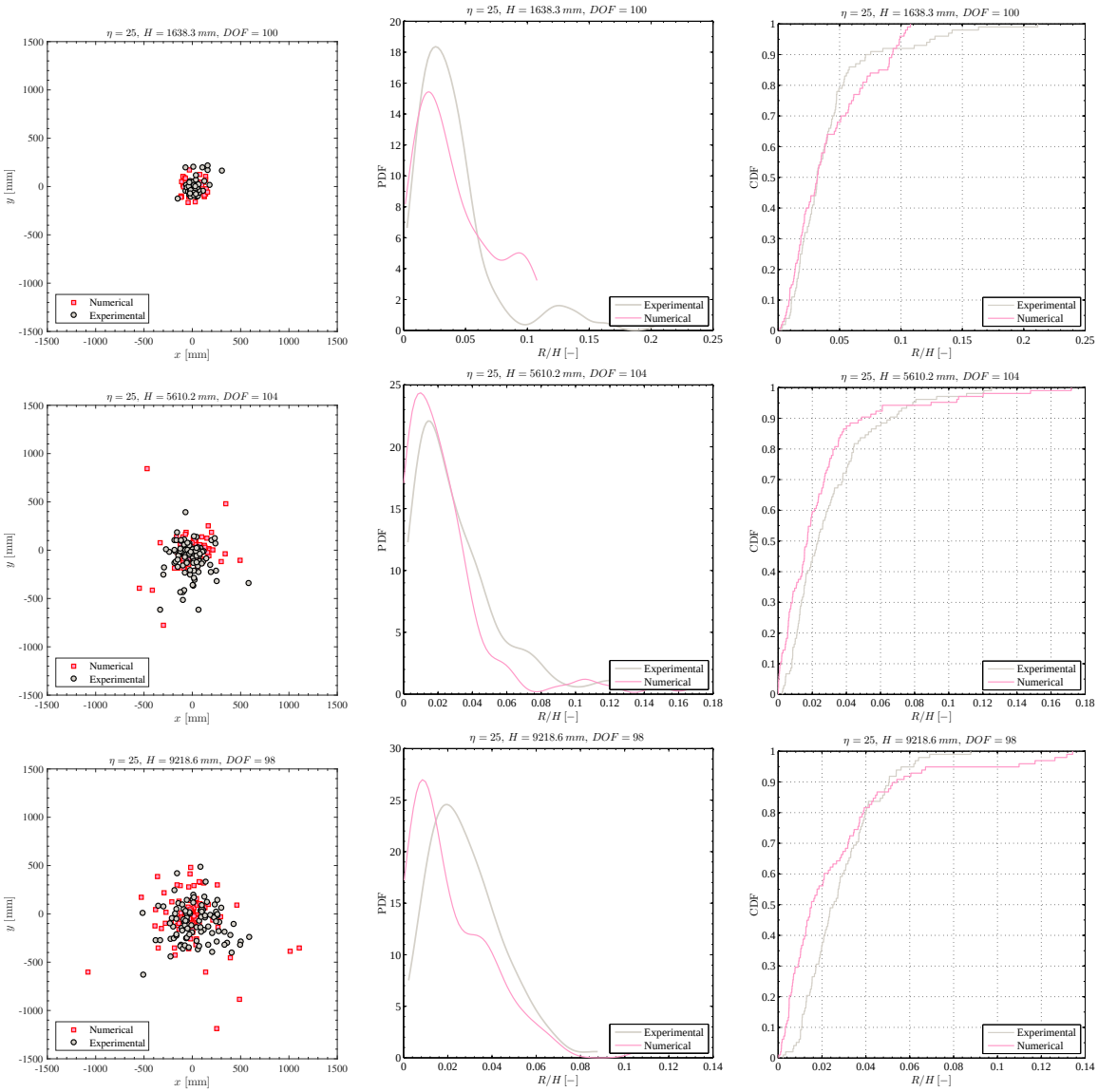

Figure 3.17: (Left) Qualitative comparison between coordinates of contact point to the ground in experiments with corresponding numerical simulations conducted for firebrand models with $\eta = 25$, and D.O.F. of the orders of magnitude of 100. Also, shown are empirical PDFs (middle) and CDFs (right) of the normalized radial distances with the release height. From top to bottom the release height increases from $H = 1.64\,m$ to $5.6\,m$ and $9.23\,m$.

distances do not share the same continuous probability distribution with the corresponding numerically simulated radial distances.

In addition to the K-S test, for the foregoing domain, a null hypothesis is designated to measure whether the mean of the numerically simulated data is equal to the experimental evidence.

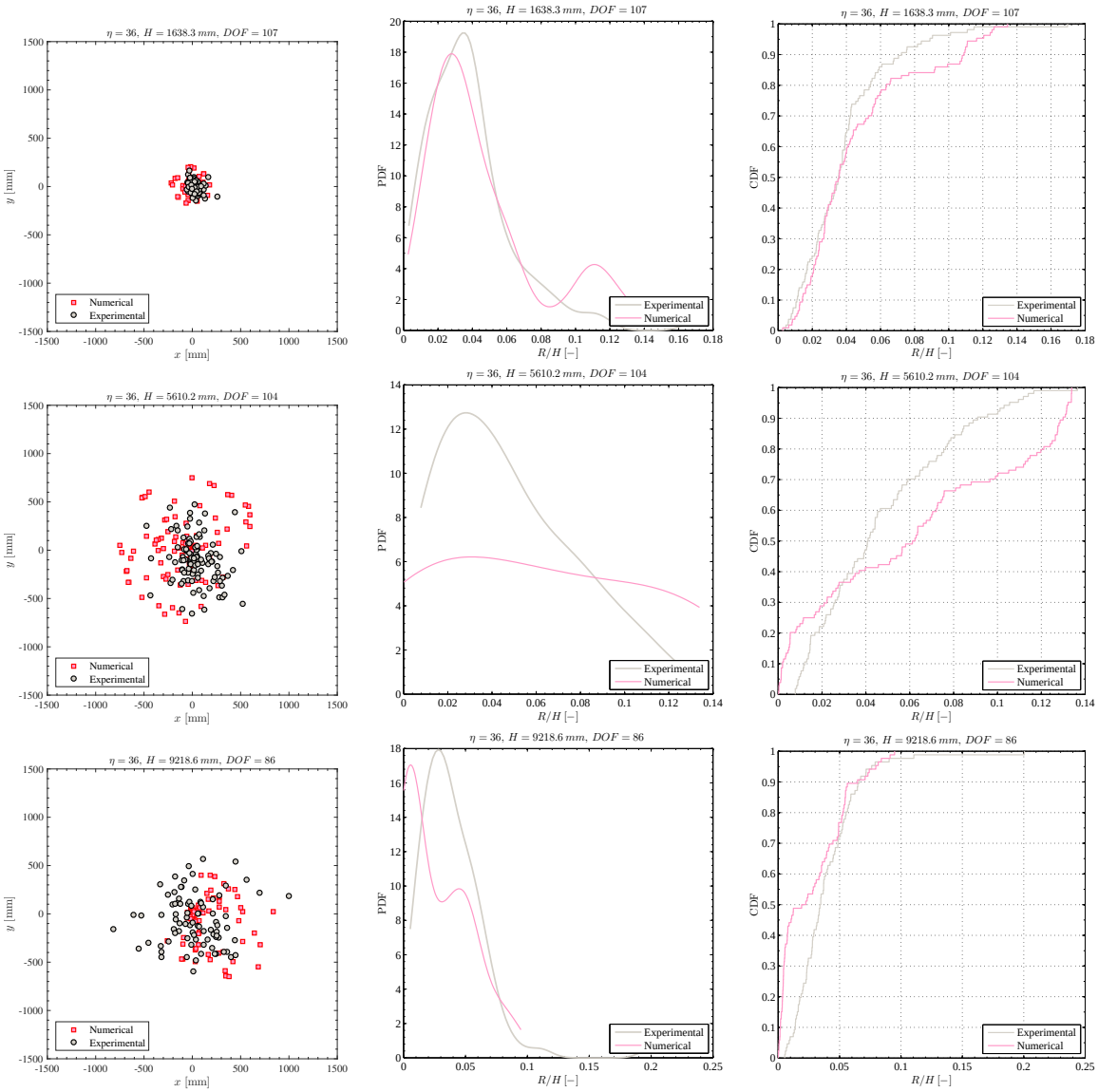

Figure 3.18: (Left) Qualitative comparison between coordinates of contact point to the ground in experiments with corresponding numerical simulations conducted for firebrand models with $\eta = 36$, and D.O.F. of the orders of magnitude of 100. Also, shown are empirical PDFs (middle) and CDFs (right) of the normalized radial distances with the release height. From top to bottom the release height increases from $H = 1.64\,m$ to $5.6\,m$ and $9.23\,m$.

A test of this hypothesis is the well known two sampled T-test. As indicated in table 3.3, for almost all cases the null hypothesis is accepted with $\alpha = 0.05$. This implies that the numerical model is capable of estimating the average statistics of the firebrand models' flight, i.e. radial distances. In those cases where T-test rejects the null hypothesis the $p - value$ is small.

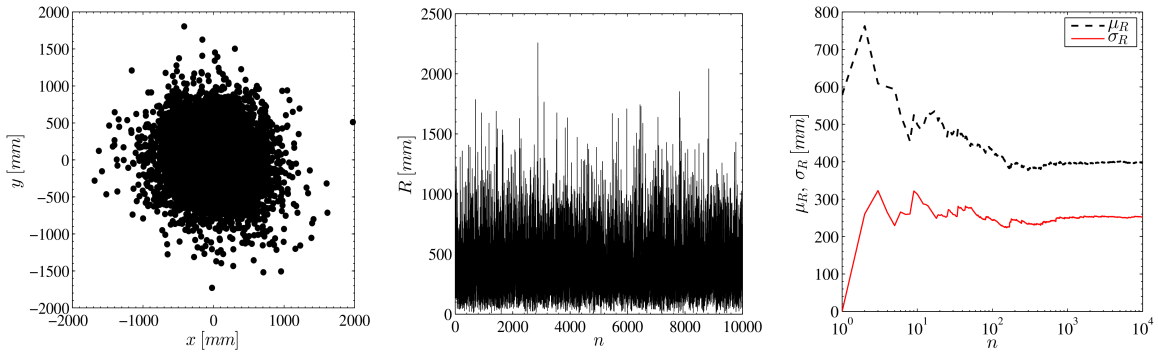

Figure 3.19: (Left) Scatter plot of simulated landing locations of firebrand models with $\eta = 18$ that are released from $H = 9.2\,(m)$. (Middle) Plot of radial distance for each independent simulated drop where n denotes the number of independent drops. (Right) Semilogarithmic plot of cumulative mean and standard deviation of the obtained radial distances, as the number of independent drops (simulations) increases up to 10000.

Given that the DOF of the tests are high, particularly in the second round of experiments, this questions the credibility of the test's results for cases with low *p-value*; meaning that the probability of observing such results with the same or even more extreme results (not having equal means) is significantly low. This is due to the fact that, the statistical tests with high DOF are more sensitive to the odd events of the sample compared to the tests on the same sample with lower size (DOF).

Further, a null hypothesis is considered to measure whether the two data sets in the aforementioned domain have equal variances. A test of this hypothesis is called the two-sample F-test of variance. Based on the results in table 3.3, for most of the test cases the null hypothesis is rejected. Although for some instances, particularly in the second round of experiments with high degrees of freedom, the $p - value$ of the test is small, this suggests that the numerical model does not estimate the variance of the firebrands' flight well. More descriptively, this is shown by figure 3.29 that summarizes all data. As figure 3.29 illustrates, the numerical model is clearly capable of predicting the mean radial distance of the free fall experiments, especially in cases where the sample size is increased to one thousand. For the same cases, the numerical model tends to overestimate the variance of the radial distance. This discrepancy seems to increase as the release height increases. Therefore, the uncertainty in predicting the landing location of the firebrand models grows with the release height.

However, if one conducts the same statistical tests on the mean and standard deviation of the radial distances that are measured experimentally and modeled numerically, the results pass the

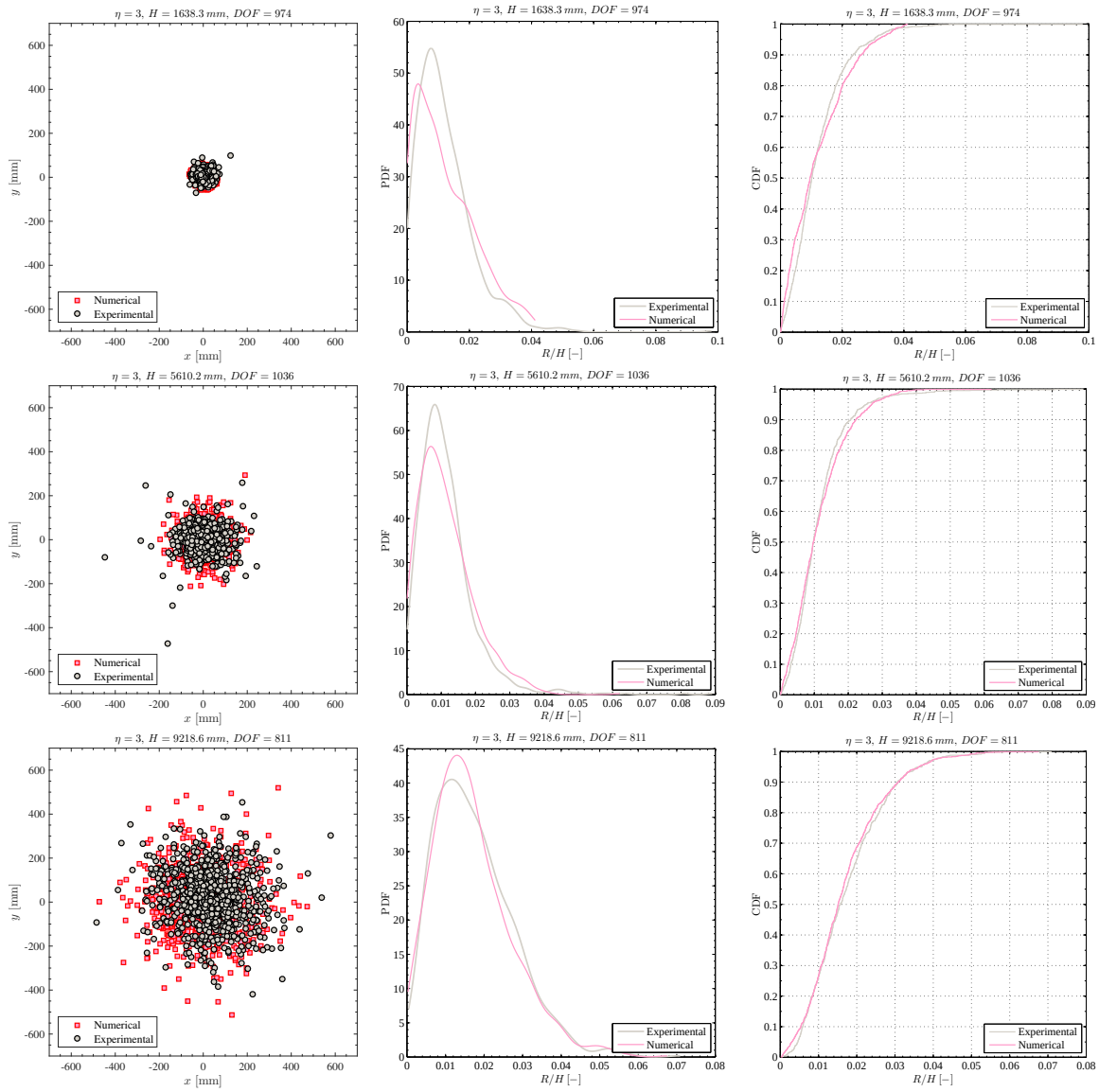

Figure 3.20: (Left) Qualitative comparison between coordinates of contact point to the ground in experiments with corresponding numerical simulations conducted for firebrand models with $\eta = 3$, and D.O.F. of the orders of magnitude of 1000. Also, shown are empirical PDFs (middle) and CDFs (right) of the normalized radial distances with the release height. From top to bottom the release height increases from $H = 1.64\,m$ to $5.6\,m$ and $9.23\,m$.

null hypothesis of each test. Details of the tests on given in table 3.4, where μ_{Exp} & μ_{Num} are, respectively, vectors of the mean radial distances that are obtained experimentally and numerically for each case in table 3.2. Also, σ_{Exp} & σ_{Num} denote vectors of the corresponding standard deviations. Results of table 3.4, implies that for a given random sample from possible (η, H) in free fall experiments, results of the numerical simulation are not statistically significantly different from the

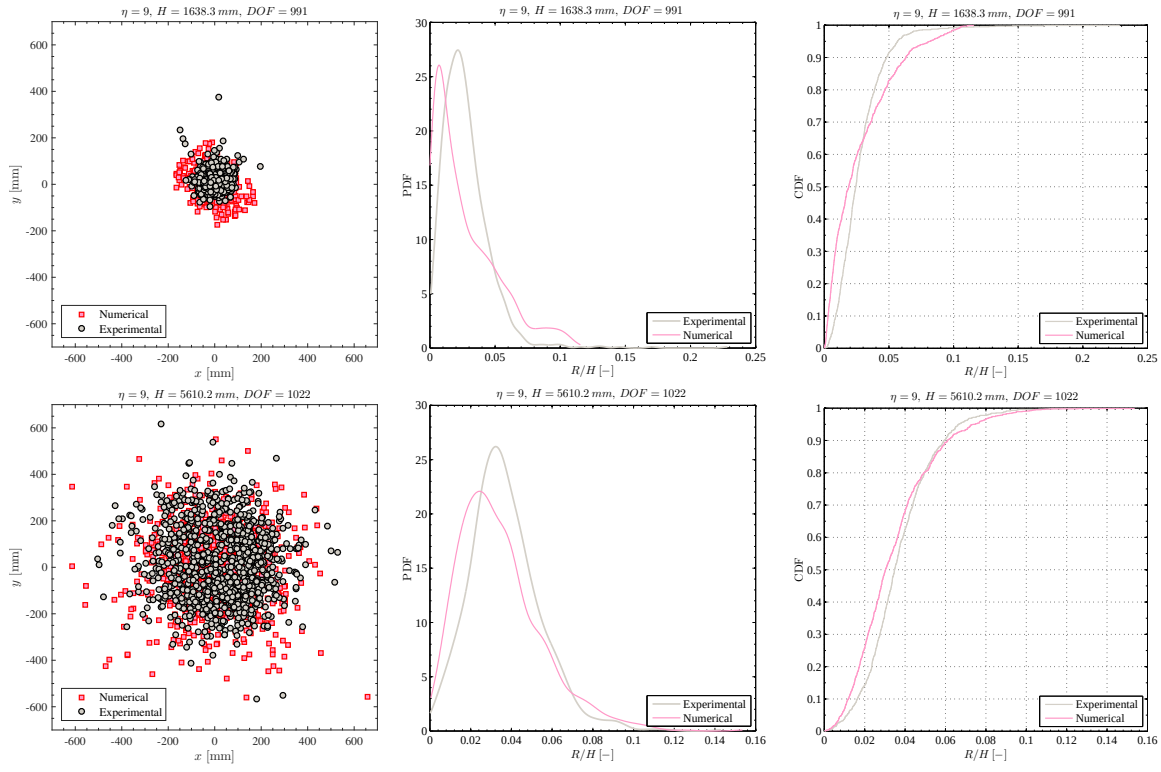

Figure 3.21: (Left) Qualitative comparison between coordinates of contact point to the ground in experiments with corresponding numerical simulations conducted for firebrand models with $\eta = 9$, and D.O.F. of the orders of magnitude of 1000. Also, shown are empirical PDFs (middle) and CDFs (right) of the normalized radial distances with the release height. From top to bottom the release height increases from $H = 1.64\,m$ to $5.6\,m$.

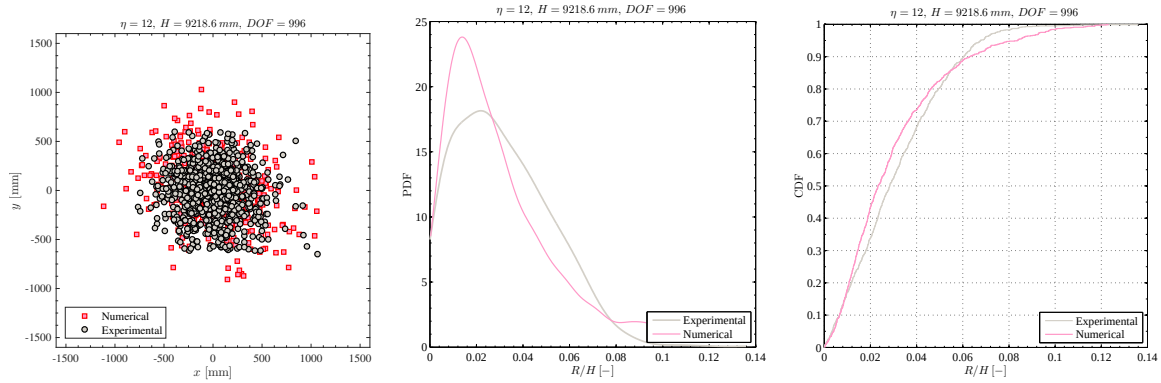

Figure 3.22: (Left) Qualitative comparison between coordinates of contact point to the ground in experiments with corresponding numerical simulations conducted for firebrand models with $\eta = 12$, and D.O.F. of the orders of magnitude of 1000. Also, shown are empirical PDFs (middle) and CDFs (right) of the normalized radial distances with the release height. The release height is $9.23\,m$.

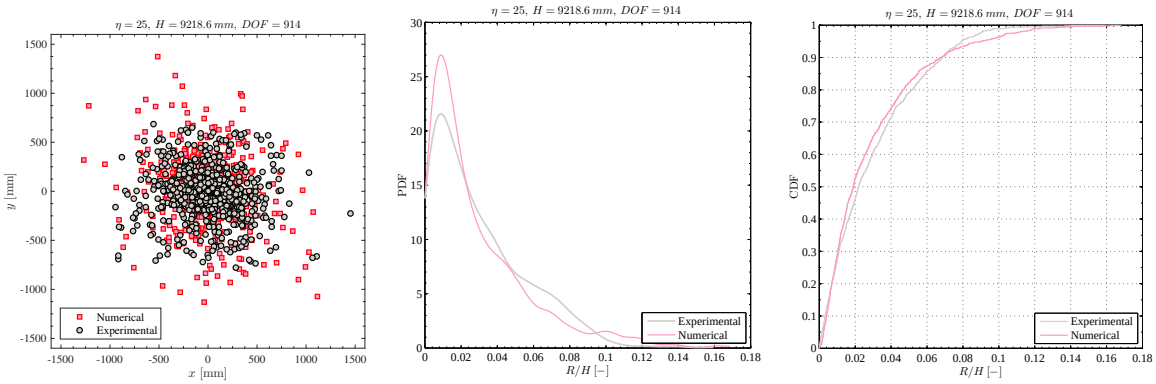

Figure 3.23: (Left) Qualitative comparison between coordinates of contact point to the ground in experiments with corresponding numerical simulations conducted for firebrand models with $\eta = 25$, and D.O.F. of the orders of magnitude of 1000. Also, shown are empirical PDFs (middle) and CDFs (right) of the normalized radial distances with the release height. The release height is $9.23\,m$.

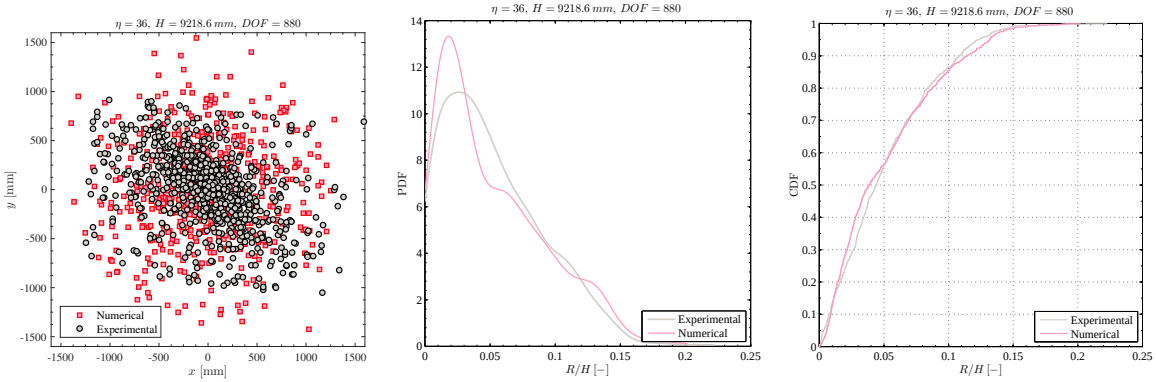

Figure 3.24: (Left) Qualitative comparison between coordinates of contact point to the ground in experiments with corresponding numerical simulations conducted for firebrand models with $\eta = 36$, and D.O.F. of the orders of magnitude of 1000. Also, shown are empirical PDFs (middle) and CDFs (right) of the normalized radial distances with the release height. The release height is $9.23\,m$.

corresponding experiments. Therefore, a thorough sensitivity analysis of the model to possible influential parameters is needed in order to find the source(s) of discrepancy in predicting the standard deviation, numerically.

3.5 Sensitivity analysis

In the free fall of rod-like firebrand models with diameter D and length L, there are two length ratios embedded in the physics of the problem. These are aspect ratio ($\eta = L/D$), and relative release height; that is D/H. Variations of these parameters changes the initial conditions

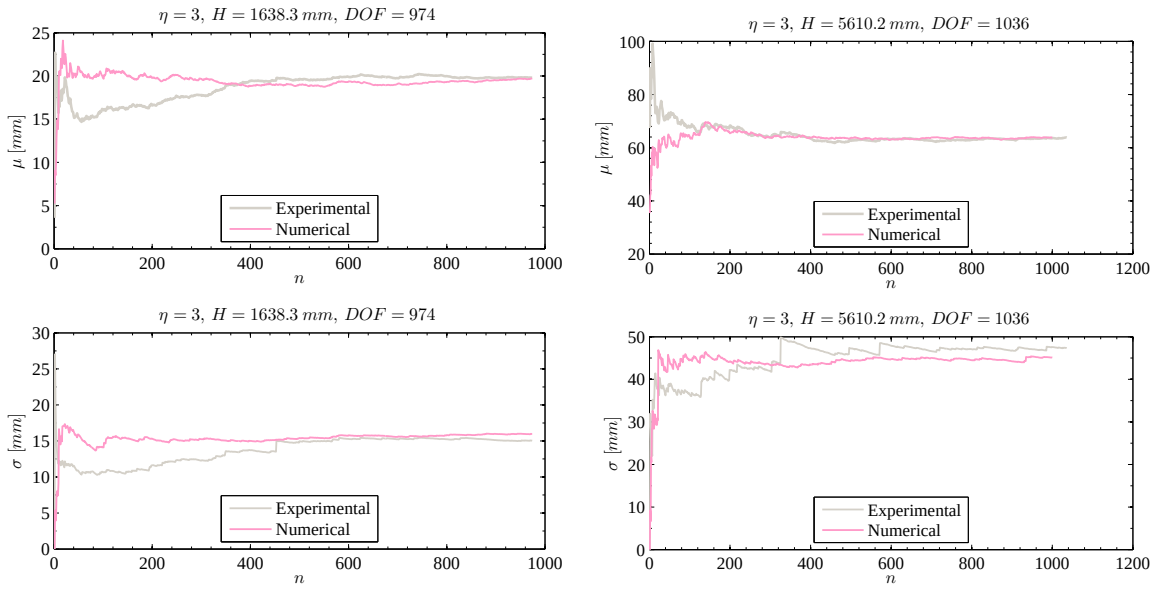

Figure 3.25: Comparison between cumulative rolling average of the mean and standard deviation of radial distances for $\eta = 3$ released from $H = 1.64\,m$ (left), and $H = 5.6\,m$ (right).

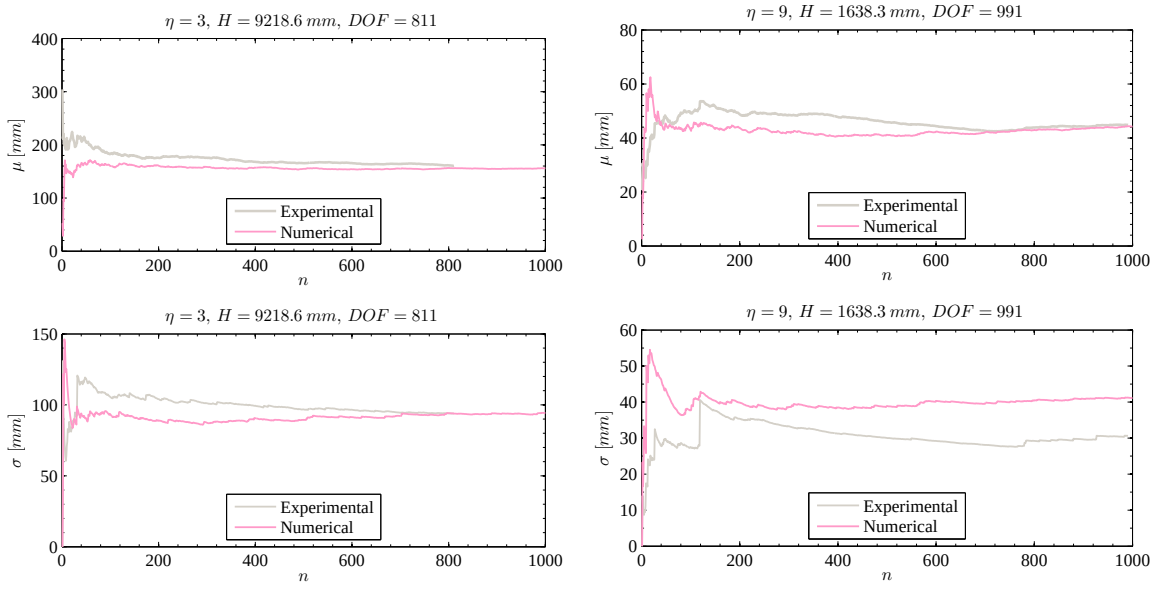

Figure 3.26: Comparison between cumulative rolling average of the mean and standard deviation of radial distances for $\eta = 3$ released from $H = 9.2\,m$ (left), and $\eta = 9$ released from $H = 1.64\,m$ (right).

(inputs) of the numerical transport model. Hence, they are subjected to the sensitivity analysis. To this end, numerical simulations were run in which the aspect ratio of the firebrand models is varied from small, $\eta = 1$, to very large $\eta = 100$. Then for a firebrand model with arbitrary diameter of

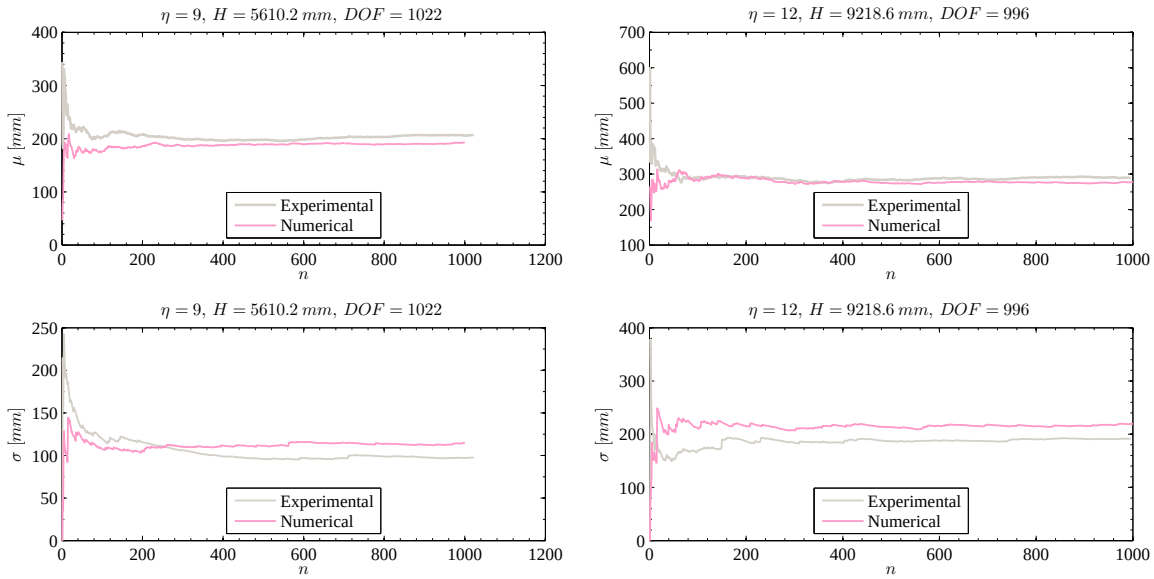

Figure 3.27: Comparison between cumulative rolling average of the mean and standard deviation of radial distances for $\eta = 9$ released from $H = 5.6\,m$ (left), and $\eta = 12$ released from $H = 9.2\,m$ (right).

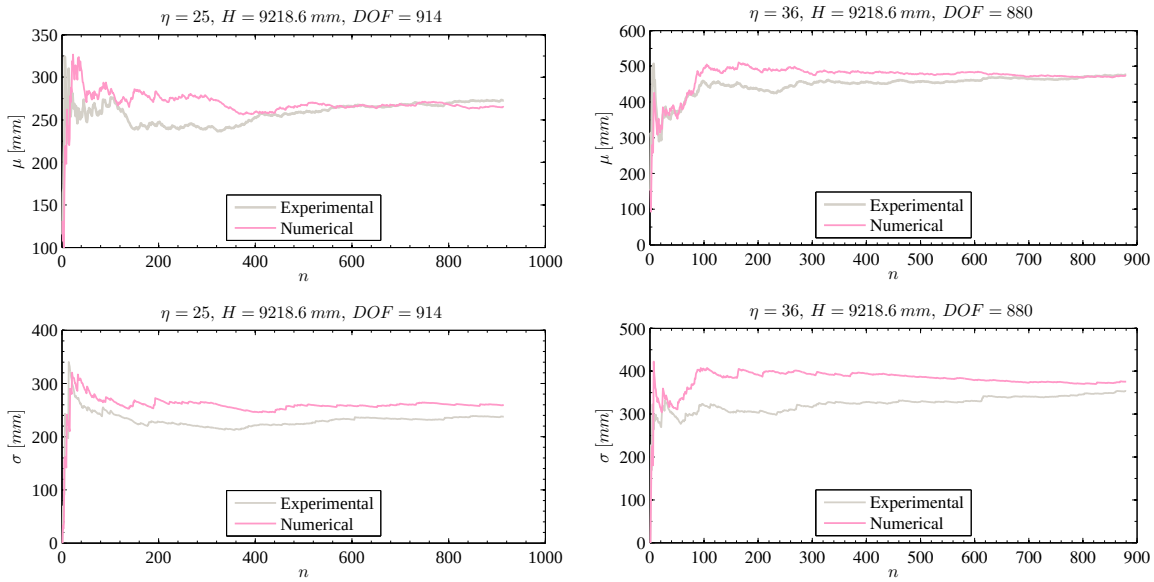

Figure 3.28: Comparison between cumulative rolling average of the mean and standard deviation of radial distances for $\eta = 25$ released from $H = 9.2\,m$ (left), and $\eta = 36$ released from $H = 9.2\,m$ (right).

$D = 10\,cm$ and density of $427\,kg/m^3$ the relative release diameter (D/H) is varied from $10^{-6} - 10^{-2}$ which resembles the free fall from very high to low elevations, respectively. The domain of variables, $(\eta, D/H)$, discretized into 41 points in a logarithmic scale. Next, for each point, that represents a

Table 3.3: Results of various statistical tests on the measured radial distances in free fall experiments against their corresponding numerical simulations. Null hypothesis status is denoted by h_0 for each test where the value of one rejects the corresponding null hypothesis of the test. DOF stands for the degrees of freedom of the test, and $p-value$ shows the probability of observing a test statistic as extreme as, or more extreme than, the observed value under the null hypothesis. For this parameter small values raises concerns about the credibility of the test. Also, significance level for all tests is set to $\alpha = 0.05$.

Population	η	$H\,(m)$	K-S test			T-test			F-test			
			h_0	$h-statistic$	$p-value$	h_0	DOF	$p-value$	h_0	DOF^1	DOF^2	$p-value$
$O(100)$	3	1.64	0	0.1683	0.1024	0	200	0.2733	0	100	100	0.9222
		5.6	0	0.1188	0.4496	0	200	0.6303	1	100	100	0.0138
		9.2	1	0.29	0.0003	1	198	0.0008	1	99	99	0.0004
	4	1.64	0	0.148	0.2077	0	197	0.2813	0	100	97	0.762
		5.6	0	0.1429	0.2498	0	194	0.2554	1	97	97	0.0001
		9.2	0	0.1782	0.0715	1	200	0.0154	1	100	100	0.0179
	6	1.64	1	0.22	0.0131	0	198	0.2973	1	99	99	0.0054
		5.6	1	0.22	0.0131	0	198	0.0553	0	99	99	0.6366
		9.2	1	0.3235	0	1	202	0.0031	1	101	101	0.0006
	7.6	1.64	0	0.1429	0.5836	0	110	0.9134	0	55	55	0.0538
		5.6	0	0.2133	0.0564	0	148	0.7678	1	74	74	0.0343
		9.2	0	0.1831	0.1654	0	140	0.9758	1	70	70	0
	9	1.64	0	0.16	0.14	0	198	0.1063	1	99	99	0
		5.6	0	0.1031	0.6576	0	192	0.7209	0	96	96	0.2943
		9.2	1	0.4091	0	1	218	0	0	109	109	0.3979
	12	1.64	0	0.1556	0.207	0	178	0.2356	0	89	89	0.6804
		5.6	0	0.1327	0.3317	0	194	0.6619	1	97	97	0
		9.2	1	0.4898	0	1	194	0	0	97	97	0.6362
	18	1.64	1	0.22	0.0131	1	198	0.0303	1	99	99	0.0002
		5.6	0	0.1471	0.2023	0	202	0.09	0	101	101	0.3889
		9.2	1	0.2727	0.0004	1	218	0.0001	1	109	109	0
	25	1.64	0	0.13	0.3439	0	198	0.9115	0	99	99	0.1242
		5.6	1	0.2115	0.016	0	206	0.1091	0	103	103	0.1319
		9.2	1	0.2755	0.0009	0	194	0.4533	1	97	97	0
	36	1.64	0	0.1215	0.3858	0	212	0.0669	1	106	106	0.0238
		5.6	1	0.2308	0.0064	1	206	0.0105	1	103	103	0
		9.2	1	0.407	0	1	170	0.0048	0	85	85	0.7605
$O(1000)$	3	1.64	1	0.1088	0	0	1946	0.8872	0	973	973	0.0616
		5.6	0	0.0518	0.1258	0	2034	0.9936	0	1035	999	0.1237
		9.2	0	0.0488	0.2312	0	1809	0.2533	0	810	999	0.9219
	9	1.64	1	0.2259	0	0	1989	0.7244	1	990	999	0
		5.6	1	0.144	0	1	2020	0.0032	1	1021	999	0
	12	9.2	1	0.1025	0	0	1994	0.1913	1	995	999	0
	25	9.2	1	0.0667	0.0325	0	1826	0.4968	1	913	913	0.0081
	36	9.2	1	0.0875	0.0022	0	1758	0.8784	0	879	879	0.0692

[1]&[2] DOF of the numerator and denominator in the F-test, respectively.

different set of initial conditions, the free fall is simulated for 1000 drops while the release angles are randomly varied. Figure 3.30 shows logarithmic contours for the average of normalized radial distances with release height over one thousand drops (left) and logarithmic contours of the standard deviation of the normalized radial distances with the release height (right). Presented results are significant, in that for a given diameter and a release height they show that increasing the aspect ratio increases the mean radial distance (spread) and the associated uncertainty (standard deviation)

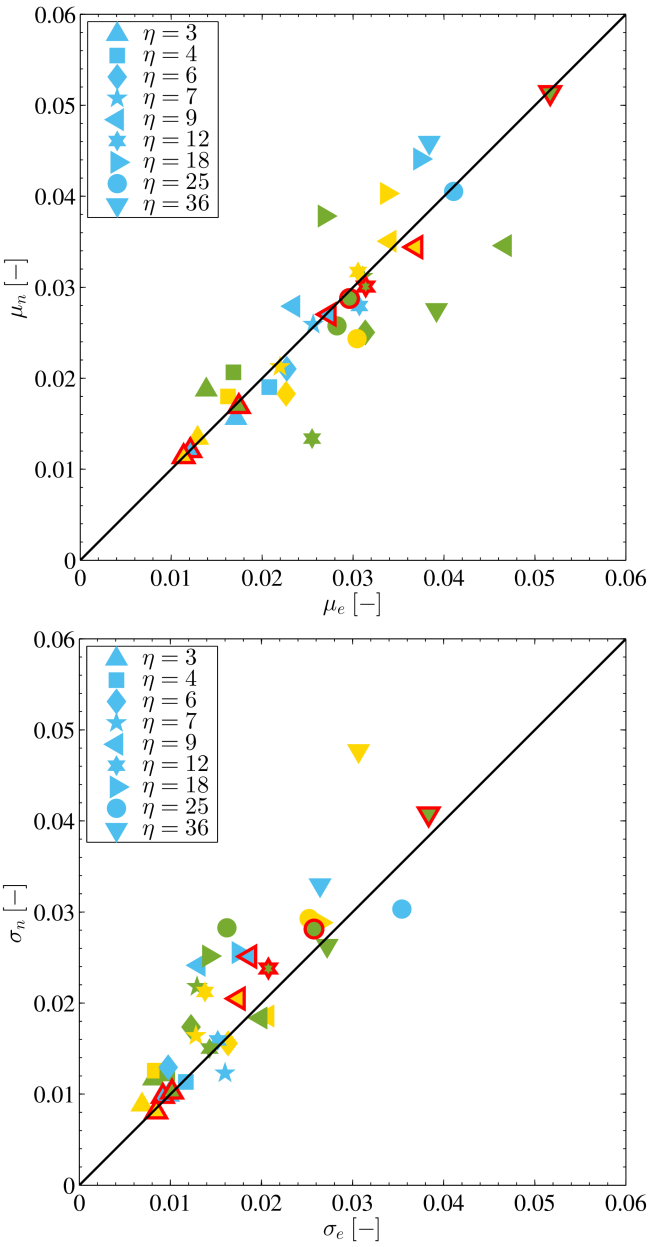

Figure 3.29: On the top, horizontal axis shows the mean normalized radial distances measured experimentally, μ_e, versus the mean corresponding numerical results; denoted by μ_n on the vertical axis. On the bottom, horizontal axis shows the standard deviation of the normalized radial distances measured experimentally, σ_e, versus the standard deviation of the corresponding numerical results; denoted by σ_n on the vertical axis. (Color version) Blue, yellow, and green markers show release of firebrand models from $H = 1.64\,m$, $5.6\,m$, and $9.2\,m$ respectively. Also, markers with bold edge line (red edge line in color paper) signify the cases where degrees of freedom is of the order of 1000.

with it, and vice versa. Also, for a given aspect ratio reducing the release height leads to decrease in the mean radial distance and the corresponding standard deviation. However this is valid for

Table 3.4: Results of the statistical tests, i.e. Kolmogorov-Simirnov, T-, and F-test, on the mean (μ) and standard deviation (σ) of the radial distances obtained from experiments (denoted by subscript $_{Exp}$) and their corresponding numerical simulations (shown by subscript $_{Num}$). The significance level α is 0.05.

Population	K-S test			T-test			F-test			
	h_0	$h-statistics$	$p-value$	h_0	DOF	$p-value$	h_0	DOF^1	DOF^2	$p-value$
(μ_{Exp}, μ_{Num})	0	0.0857	0.9991	0	68	0.8577	0	34	34	0.7419
(σ_{Exp}, σ_{Num})	0	0.1714	0.6403	0	68	0.3104	0	34	34	0.3679

[1]&[2] DOF of the numerator and denominator in the F-test, respectively.

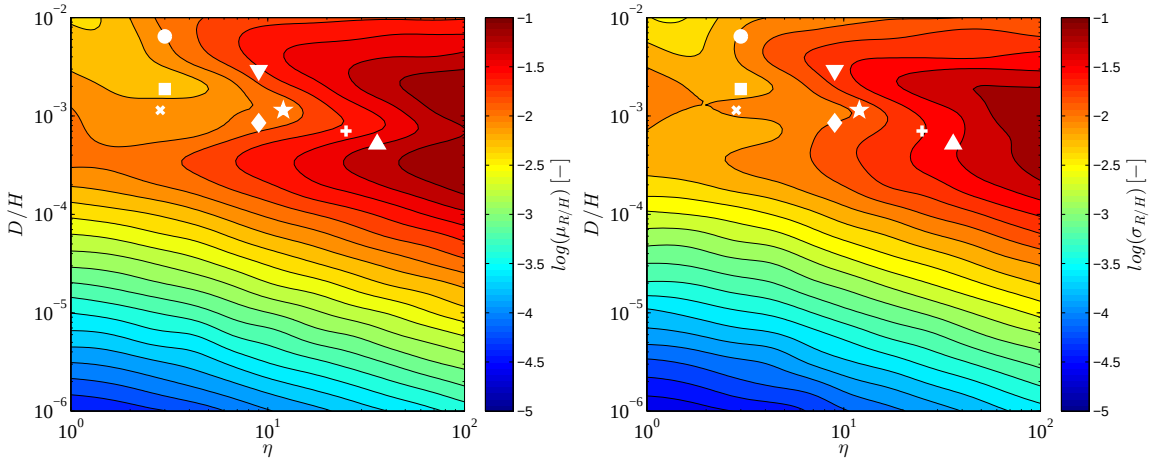

Figure 3.30: On the left, logarithmic contour plots of the average normalized radial distances with release height, over one thousand drops, due to variations in embedded length scales in firebrand free fall; On the right logarithmic contour plots of the standard deviation of the normalized radial distances with the released height, over one thousand drops. In addition, parameter space of the second round of free fall experiments is collapsed on the plots where: $\times \longrightarrow (\eta = 3,\ H = 9.2\,m)$, $\square \longrightarrow (\eta = 3,\ H = 5.6\,m)$, $\circ \longrightarrow (\eta = 3,\ H = 1.64\,m)$, $\diamond \longrightarrow (\eta = 9,\ H = 5.6\,m)$, $\triangledown \longrightarrow (\eta = 3,\ H = 1.64\,m)$, $\bigstar \longrightarrow (\eta = 12,\ H = 9.2\,m)$, $+ \longrightarrow (\eta = 25,\ H = 9.2\,m)$, $\triangle \longrightarrow (\eta = 3,\ H = 9.2\,m)$.

relatively high release elevations (small D/H) and after a certain point, that is $D/H = 10^{-4}$, a lot of variability can be observed.

To investigate the sensitivity of the model output to the choice of coefficients, numerical experiments where force and moment coefficient are changed by $\pm 20\%$ were run. Figure 3.30 indicates that μ and σ are both sensitive to η and D/H. Nonetheless, this approach is valid since table 3.4 shows that the statistics of the numerical simulations are not statistically significantly different from the experiments which are conducted within a region of the parameter space (η, D/H) that has the highest degree of variability, as can be seen on figure 3.30. While a detailed characterization of the aerodynamic coefficients is beyond the scope of this chapter, the sensitivity of the model output to

certain model parameters is examined.

The simulations were run for the free fall experiments with specifics shown in table 3.1. Also, the initial release angles (Tait-Bryan angles), are chosen randomly from a uniform distribution and remained unchanged for the rest of sensitivity analysis cases hereafter. Then, the obtained radial distances are plotted against the results from the original model in which the implemented force and moment coefficients of Richards et al. [2008], and Richards [2010] are unchanged. Figures 3.31-3.32 summarize the sensitivity analysis with respect to force and moment coefficients.

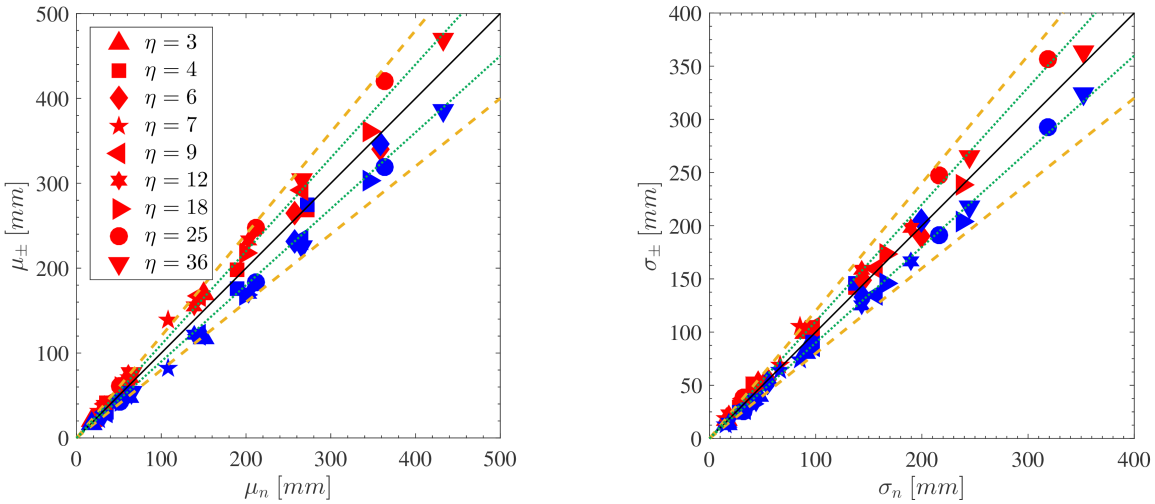

Figure 3.31: On the left, vertical axis shows the mean radial distances for the numerical simulations where the $\pm 20\%$ change in force coefficients is implemented and results, i.e. $\pm\mu$, are drawn against the corresponding estimations of the original numerical model; denoted by μ_n on the horizontal axis. On the right, vertical axis shows the standard deviation of the radial distances for the numerical simulations where the $\pm 20\%$ change in force coefficients is implemented and results, i.e. $\pm\sigma$, are drawn against the corresponding estimations of the original numerical model; denoted by σ_n on the horizontal axis. (Color version) red and blue markers show 20% increase and decrease, respectively. In addition, the (pale brown) dashed and the (green) dotted lines show 20% and 10% change from the solid line with slope $1:1$, respectively.

The obtained results are consistent with physical expectations. Reducing the aerodynamic force coefficients leads to higher accelerations that subsequently increases the velocity components of firebrands in the global coordinate system. This delivers greater angular velocities and, subsequently, higher angular momenta which gives smaller radial distances with less mean radial spread or variance. This is clearly shown in figure 3.31. It should be noted that the change in the mean

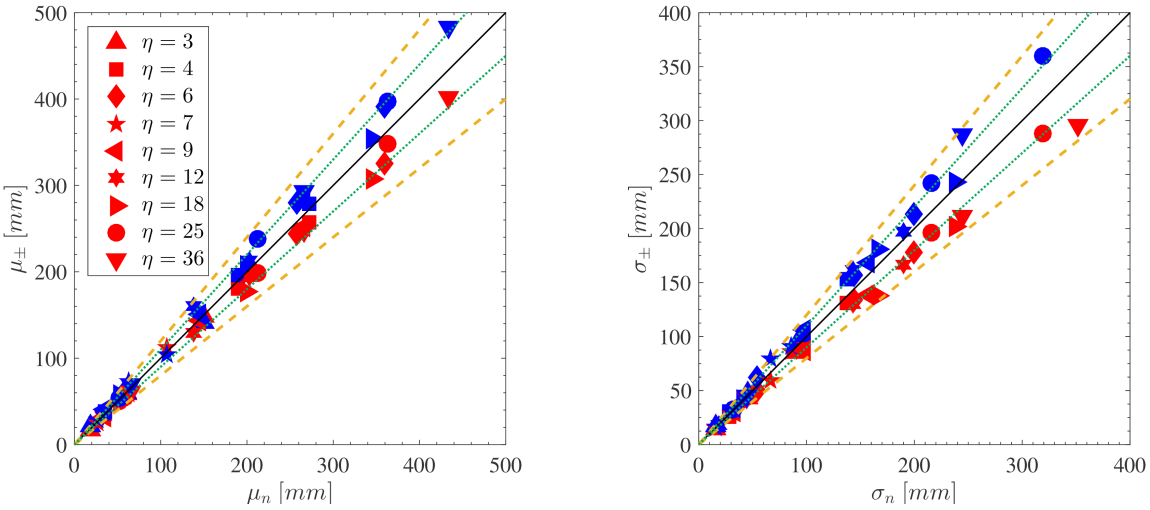

Figure 3.32: On the left, vertical axis shows the mean radial distances for the numerical simulations where the ±20% change in moment coefficients is implemented and results, i.e. $\pm\mu$, are drawn against the corresponding estimations of the original numerical model; denoted by μ_n on the horizontal axis. On the right, vertical axis shows the standard deviation of the radial distances for the numerical simulations where the ±20% change in moment coefficients is implemented and results, i.e. $\pm\sigma$, are drawn against the corresponding estimations of the original numerical model; denoted by σ_n on the horizontal axis. (Color version) red and blue markers show 20% increase and decrease, respectively. In addition, the (pale brown) dashed and the (green) dotted lines show 20% and 10% change from the solid line with slope 1 : 1, respectively.

radial distances and their corresponding variances are bounded. For the majority of cases, changes in radial distances is within the lines of 20% change, and changes in standard deviation are mostly bounded by lines of 10% change. Similarly, a 20% reduction in aerodynamic moment coefficients decreases the time rate of change of angular momentum that delivers smaller angular velocities compared to the original model. This leads to lower velocity components in the global coordinate system and subsequently smaller accelerations. The situation resembles gliding state for the firebrand model and results in more radial spread with more variance as shown in figure 3.32. Quite like the change in force coefficients, the response of governing equations to variations in aerodynamic moment coefficients are bounded within at most 20% for all cases.

With regard to the type of sensitivity, it is imperative to note that the response to variations in aerodynamic force and moment coefficients is not random in a sense that predictions corroborate with physical expectations and they are bounded. Hence, the numerical model is well-posed and bounded with respect to change in aerodynamic parameters. Further, given that a 20% change in

any given force coefficient results in, on average, less than 20% change in outcome indicates that the model is not overly sensitive to these coefficients.

On this note, we consider the possibility that overestimated radial spread (σ) by the original numerical model [Richards et al., 2008] in relation to the experimental results can be attributed to the added mass effects. As a particle moves it accelerates the adjacent fluid elements with itself as well. This can be taken into account, approximately, by adding to the mass of particle such that it accounts for the accelerated mass of the fluid around the particle. However, the current transport model does not consider the added mass effect and, in fact solves the transport equations of firebrands as passive particles released through the velocity field. Therefore, in order to examine the sensitivity of the model to the added mass effects, numerical experiments were run in which density (mass) of the model firebrands was increased by +20%. The rest of the simulation parameters are the same as the previous sensitivity analysis' studies. The response of the model to the added mass effect is shown in figure 3.33.

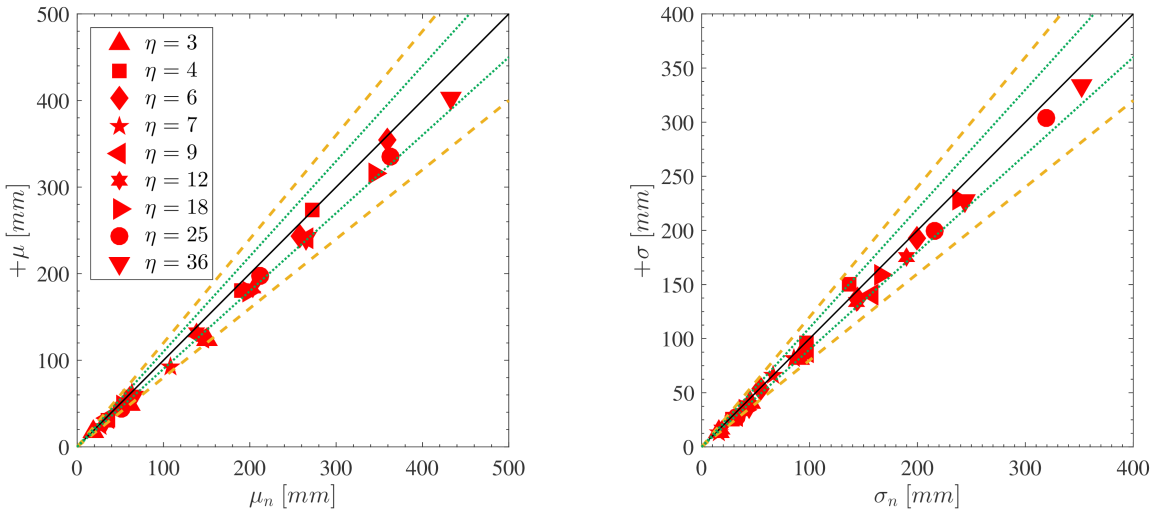

Figure 3.33: On the left, vertical axis shows the mean radial distances for the numerical simulations where the +20% change in density is implemented and results, i.e. $+\mu$, are drawn against the corresponding estimations of the original numerical model; denoted by μ_n on the horizontal axis. On the right, vertical axis shows the standard deviation of the radial distances for the numerical simulations where the +20% change in density is implemented and results, i.e. $+\sigma$, are drawn against the corresponding estimations of the original numerical model; denoted by σ_n on the horizontal axis. (Colored version) the (pale brown) dashed and the (green) dotted lines show 20% and 10% change from the solid line with slope 1 : 1, respectively.

Consistent with the previous trends in sensitivity to the aerodynamic parameters, response

of the model to the added mass is well-posed, and bounded. Increasing the linear added mass (increase in density) decreases the mean radial distance, and slightly decreases the radial spread in relation to the original model, see figure3.33-right. This can be due to the fact that the added mass is an unsteady phenomenon whereas the model uses steady aerodynamic coefficients. Thus, after a certain distance (where the particle reaches its terminal velocity) the linear added mass approaches zero as the particle's acceleration goes to zero. In the meantime, the particle maybe rotating while the linear added mass does not account for the effects of the added mass due to the rotational effects.

Looking at the governing equations, the added mass due to rotation can be modeled by increasing the mass moment of inertia about the principal axes of the model firebrands (particles). To test this hypothesis, numerical simulations of the free fall experiments were run in which the mass moment of inertia about each axis is increased by +20% in the original transport model while the rest of the parameters are kept the same as the previous simulations. The results are shown on figure 3.34.

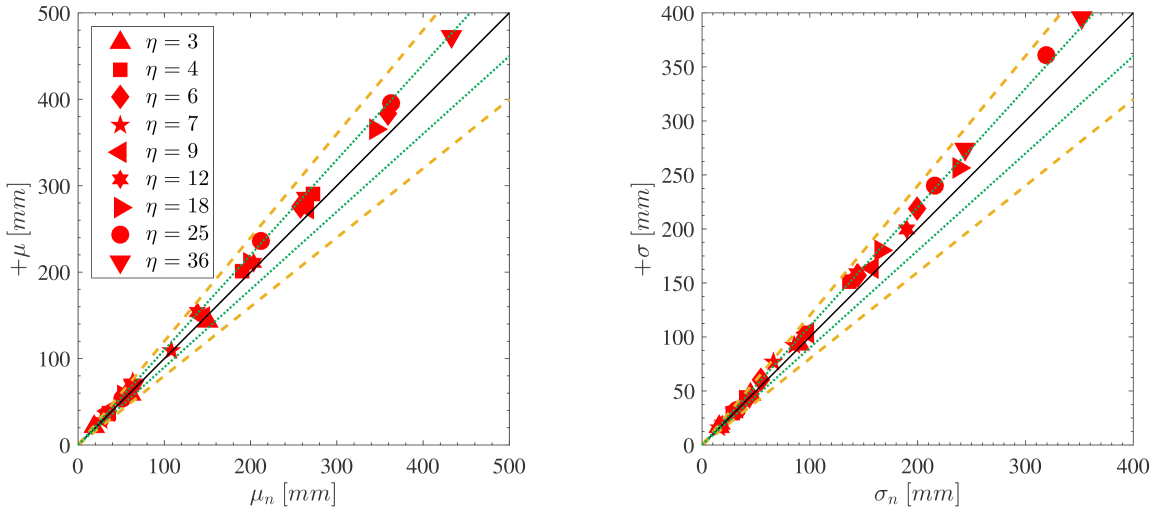

Figure 3.34: On the left, vertical axis shows the mean radial distances for the numerical simulations where the +20% change in mass moment of inertia components (I_x, I_y, I_z) is implemented and results, i.e. $+\mu$, are drawn against the corresponding estimations of the original numerical model; denoted by μ_n on the horizontal axis. On the right, vertical axis shows the standard deviation of the radial distances for the numerical simulations where the +20% change in mass moment of inertia components (I_x, I_y, I_z) is implemented and results, i.e. $+\sigma$, are drawn against the corresponding estimations of the original numerical model; denoted by σ_n on the horizontal axis. (Color version), the (pale brown) dashed and the (green) dotted lines show 20% and 10% change from the solid line with slope 1 : 1, respectively.

As demonstrated in figure 3.34-left, the mean radial distance increases by increasing the mass moment of inertia. However, the increase in the mean radial distance (μ) with respect to the original model is not as large as the increase in the radial spread (σ), see figure 3.34-right. The rotational added mass increases the mean and standard deviation of the radial distances in free fall, because by increasing the mass moment of inertia the time rate of change of angular velocity decreases for a given balance of momenta, which is obtained from the balance of forces using steady aerodynamic coefficients. The smaller angular acceleration suggests a gliding behavior for the particles that increases the radial distance and spread as opposed to the higher angular accelerations.

The results of sensitivity to the rotational added mass are important, in that they demonstrate that the added mass effects due to rotation has more influence on the radial distance spread (σ) than the linear added mass, since the larger release height leads to more spread in the radial distance; see 3.34-right. In addition, it should be emphasized that the sensitivity of governing equations to the change in mass moment of inertial is well-posed and bounded.

3.6 Concluding remarks

Given the raised concerns, reviewed in section 6.1, about the studies in firebrand (debris/-particle) transport, and the critical lack of experimental validation of the existing models, a set of firebrand free fall experiments were run. The radial distance between the landing point of the model firebrands and projection of the release point to the ground is captured using image processing techniques. The results are employed for experimental verification and evaluation of a 3D deterministic 6-DOF firebrand transport model adopted from Richards et al. [2008]; Richards [2010] and Grayson and Pang [2011]. Statistical hypothesis testing was run on the results of experiments and their corresponding numerical simulations. Outcomes of the statistical tests confirm that the transport model is capable of predicting statistics of the flight in the free fall experiments such that the results are not significantly statistically different from the experimental evidence. This holds true for any possible combination of aspect ratio and release height in the parameter space. In addition, a thorough sensitivity analysis was done in order to characterize the transport model. The results of the sensitivity analysis reveals that the model is highly sensitive to the initial conditions of the release, that is Tait-Bryan release angles. Further, results of the sensitivity analysis to the model input

parameters is done. The results corroborate with the physical expectations, and it is shown that unlike initial conditions of the flight, response of the model to these parameters are well-posed and bounded. It is shown that the effects of add mass due to the rotational effects are more important than the added mass from linear acceleration. Moreover, the experimental results are beneficial to not only firebrand transport studies but also flight of debris and other rod-like particles of various aspect ratios in severe storms.

Bibliography

Albini, F. A. (1983). Transport of Firebrands by Line Thermals. *Combustion Science and Technology*, 32(5-6):277–288.

Anthenien, R. A., Tse, S. D., and Fernandez-Pello, A. C. (2006). On the trajectories of embers initially elevated or lofted by small scale ground fire plumes in high winds. *Fire Safety Journal*, 41(5):349–363.

Baker, C. J. (2007). The debris flight equations. *Journal of Wind Engineering and Industrial Aerodynamics*, 95(5):329–353.

Bhutia, S., Jenkins, M. A., and Sun, R. (2010). Comparison of firebrand propagation prediction by a plume model and a coupledfire/atmosphere largeeddy simulator. *Journal of Advances in Modeling Earth Systems*, 2:4.

Boonmee, N. and Quintiere, J. G. (2002). Glowing and Flaming Autoignition of Wood. *Proceedings of the Combustion Institute*, 29:289–296.

Coleman, R. J., Pimlott, K., Richwine, M., and Hoover, T. (2013). *WUI Command Operations for the Company Officer*. California Department of Forestry and Fire Protection, Office of the State Fire Marshal, State Fire Training, P.O.Box. 944246, Sacramento, CA, 94244-2460.

Dunn, F., Hartmann, W., Campbell, D., Fletcher, N., and Rossing, T. (2015). *Springer handbook of acoustics*. Springer.

Fernandez-Pello, A. C. (1982). An analysis of the forced convective burning of a combustible particle. *Combustion Science and Technology*, 28(5-6):305–313.

Foster, J. M. (2014). Federal Government Loss to Fund Wildfire Fighting Without Having to Raid Wildfire Prevention.

Gonzalez, R. C., Woods, R. E., and Eddins, S. L. (2004). *Digital image processing using MATLAB*. Pearson Education India.

Grayson, J. and Pang, W. C. (2011). *Development and application of a three-dimensional probabilistic wind-borne debris trajectory model*. PhD thesis, Clemson University.

Grayson, M., Pang, W., and Schiff, S. (2012). Three-dimensional probabilistic wind-borne debris trajectory model for building envelope impact risk assessment. *Journal of Wind Engineering and Industrial Aerodynamics*, 102:22–35.

Himoto, K. and Tanaka, T. (2005). Transport of disk-shaped firebrands in a turbulent boundary layer author. In *the Eighth International Symposium on Fire Safety Science*, pages 18—-23.

Holmes, J. D. (2004). Trajectories of spheres in strong winds with application to wind-borne debris. *Journal of Wind Engineering and Industrial Aerodynamics*, 92(1):9–22.

Howard, P. (2014). Flammable Planet: Wildfires and the Social Cost of Carbon. Technical Report September, The Cost of Carbon Projec.

Huang, R. F., Wu, Y. D., Chen, H. D., Chen, C. C., Chen, C. W., Chang, C. P., and Shih, T. S. (2007). Development and Evaluation of an Air-Curtain Fume Cabinet with Considerations of its Aerodynamics. *Ann. Occup. Hyg., Vol. 51, No. 2, pp. 189206, 2007*, 51(2):189–206.

Koo, E., Linn, R. R., Pagni, P. J., and Edminster, C. B. (2012). Modelling firebrand transport in wildfires using HIGRAD/FIRETEC. *International Journal of Wildland Fire*, 21(4):396–417.

Koo, E., Pagni, P. J., Weise, D. R., and Woycheese, J. P. (2010). Firebrands and spotting ignition in large-scale fires. *International Journal of Wildland Fire*, 19(7):818.

Kortas, S., Mindykowski, P., Consalvi, J. L., Mhiri, H., and Porterie, B. (2009). Experimental validation of a numerical model for the transport of firebrands. *Fire Safety Journal*, 44(8):1095–1102.

Lee, S. L. and Hellman, J. M. (1969). Study of Firebrand Trajectories in a Turbulent Swirling Natural Convection Plume. *Combustion and Flame*, 13(6):645–&.

Lee, S.-L. and Hellman, J. M. (1970). Firebrand trajectory study using an empirical velocity-dependent burning law. *Combustion and Flame*, 15(3):265–274.

Lin, N. (2005). *Simulation of windborne debris trajectories*. PhD thesis, Texas Tech. University.

Lin, N., Holmes, J. D., and Letchford, C. W. (2007). Trajectories of Wind-Borne Debris in Horizontal Winds and Applications to Impact Testing. *J. Struct. Eng.*, 133(2):274–282.

Manzello, S. L., Shields, J. R., Hayashi, Y., and Nii, D. (2008). Investigating the vulnerabilities of structures to ignition from a firebrand attack. *Fire Safety Science*, pages 143–154.

Manzello, S. L., Shields, J. R., Yang, J. C., Hayashi, Y., and Nii, D. (2007). On the use of a firebrand generator to investigate the ignition of structures in wildland–urban interface (WUI) fires. In *Eleventh International Fire Science and Engineering Conference (INTERFLAM)*, pages 3–5.

Marte, J., Kurtz, D., and Redmann, G. (1976). Aerodynamic coefficients of missile shapes. In *Proceedings of the Symposium on Tornadoes*, pages 623–631. Texas Tech University, USA.

Radbill, J. and Redman, G. (1976). Tornado-generated missile trajectory calculations with a six degree-of- freedom model. In *Proceedings of the Symposium on Tornadoes*, pages 633–637. Texas Tech University, USA.

Richards, P. J. (2010). Steady Aerodynamics of Rod and Plate Type Debris.pdf. In *17th Australian Fluid Mechanics Conference*.

Richards, P. J. (2012). Dispersion of windborne debris. *J. Wind Eng. & Ind. Aero.*, 104-106:594–602.

Richards, P. J., Williams, N., Laing, B., McCarty, M., and Pond, M. (2002). Numerical calculation of the three-dimensional motion of wind-borne debris. *J. Wind Eng. & Ind. Aero.*, 96:2188–2202.

Richards, P. J., Williams, N., Laing, B., McCarty, M., and Pond, M. (2008). Numerical calculation of the three-dimensional motion of wind-borne debris. *Journal of Wind Engineering and Industrial Aerodynamics*, 96(10):2188–2202.

Robinson, A. C. (1958). On the use of quaternions in simulation of rigid-body motion. Technical report, DTIC Document.

Sardoy, N., Consalvi, J. L., Kaiss, a., Fernandez-Pello, a. C., Porterie, B., and a.C. Fernandez-Pello (2008). Numerical study of ground-level distribution of firebrands generated by line fires. *Combustion and Flame*, 154(3):478–488.

Sardoy, N., Consalvi, J.-L., Porterie, B., and Fernandez-Pello, A. (2007). Modeling transport and combustion of firebrands from burning trees. *Combustion and Flame*, 150(3):151–169.

Tachikawa, M. (1983). Trajectories of Flat Plates in Uniform-Flow with Application to Wind-Generated Missiles. *Journal of Wind Engineering and Industrial Aerodynamics*, 14(1-3).

Tachikawa, M. (1988). A Method for Estimating the Distribution Range of Trajectories of Wind-Borne Missiles. *Journal of Wind Engineering and Industrial Aerodynamics*, 29(1-3).

Tachikawa, M. and Harra, H. (1982). Trajectories and velocities of typhoon-generated missiles, Part 3. Aerodynamic characteristics of various missile shapes. In *Proceedings of Transactions of the Architectural Institute of Japan*, pages 23–31.

Tarifa, C. S., Del Notario, P. P., Moreno, F. G., and Villa, A. R. (1967). Transport and combustion of firebrands, final report of grants FG-SP-11 and FG-SP-146. *US Department of Agriculture Forest Service*.

Tarifa, C. S., Notario, P., and Moreno, F. G. (1965). On the flight paths and lifetimes of burning particles of wood. In *Symposium (international) on combustion*, volume 10, pages 1021–1037. Elsevier.

Tohidi, A., Kaye, N., and Bridges, W. (2015). Statistical description of firebrand size and shape distribution from coniferous trees for use in Metropolis Monte Carlo simulations of firebrand flight distance. *Fire Safety Journal*, 77:21–35.

Tohidi, A. and Kaye, N. B. (2013). The Sensitivity of Modeled Flight Distance to the Lofting to Transport Transition Criterion in Coupled Ember Flight Models. In *12th Americas Conference on Wind Engineering*, pages 433–448, Seattle, WA, USA.

Visscher, B. T. and Kopp, G. a. (2007). Trajectories of roof sheathing panels under high winds. *J. Wind Eng. & Ind. Aero.*, 95(8):697–713.

Wei, F., Ke, Z., Juan, S., and Meizhen, Y. (2009). Heat source temperature on the distribution of pollutant concentration in stack ventilation room. *Energy & Environment (Chinese)*, (3):15–19.

Chapter 4

Highly buoyant bent-over plumes in a boundary layer

Highly buoyant plumes, such as wildfire plumes, in low to moderate wind speeds have initial trajectories that are steeper than many industrial waste plumes. They will rise further into the atmosphere before bending significantly. In such cases the plume's trajectory will be influenced by the vertical variation in horizontal velocity of the atmospheric boundary layer. This paper examined the behavior of a plume in an unstratified environment with a power-law ambient velocity profile. Examination of previously published experimental measurements of plume trajectory show that inclusion of the boundary layer velocity profile in the plume model often provides better predictions of the plume trajectory compared to algebraic expressions developed for uniform flow plumes. However, there are many cases in which uniform velocity profile algebraic expressions are as good as boundary layer models. It is shown that it is only important to model the role of the atmospheric boundary layer velocity profile in cases where either the momentum length (square root of source momentum flux divided by the reference wind speed) or buoyancy length (buoyancy flux divided by the reference wind speed cubed) is significantly greater than the plume release height within the boundary layer. This criteria is rarely met with industrial waste plumes, but it is important in modeling wildfire plumes.

4.1 Introduction

The behavior of a plume in a cross flow, hereafter referred to as a bent-over plume, is ubiquitous in environmental fluid mechanics. Bent-over plumes occur in many situations such as the smoke rising from a chimney [Briggs, 1968; Marro et al., 2014], wastewater discharge into a river [Fischer et al., 2013], and pool fire dispersion [Fisher et al., 2001]. Of particular interest in this study are highly buoyant Boussinesq plumes [Morton, 1965]. Such have significant generation of vertical momentum and, therefore, have steeper trajectories, and are more influenced by vertical variation in the cross flow velocity. The underlying motivation is to investigate the spread of wildfires through the lofting of firebrands (embers) into the atmosphere by large fire plumes [Sardoy et al., 2007]. This study focuses on the role of the fire plume in ember lofting and, therefore, considers neutrally stable atmospheric conditions. The present study does not take into account the effects of convective instabilities such as boundary layer rolls on amplifying the lofting and downwind transport of firebrands [Thurston et al., 2015]. Understanding the behavior of large fire plumes blown horizontally by the atmospheric boundary layer is essential to accurate modeling of the lofting and transport of embers which can create spot fires when they land ahead of the main fire front. Bent-over fire plume dynamics are also key to modeling the dispersion of smoke from wildfires.

Simplified models of the rise of a plume into a cross-flow are very well documented in the literature. A detailed analysis of full-scale data as well as laboratory measurements was used by Briggs [1975a,b, 1984] to develop algebraic formulations for plume rise in different environmental conditions. Hoult et al. [1969] extended the local similarity assumption proposed by Morton et al. [1956] to develop a theoretical model for the plume rise in horizontal wind. The model has two empirical parameters to quantify the rate of entrainment of ambient fluid into the plume. Their model assumed that the velocity and density defect profiles are top hat and that the plume cross section is circular. Davidson [1986] discussed the importance of self-similarity profiles of the physical and chemical properties of a plume in these models and concluded that there is no significant difference between employing Gaussian profiles and top-hat profiles. However, the assumption that the plume cross section is circular is less realistic. In many cases, as the plume develops through the cross flow, a counter-rotating vortex pair in the shape of an elongated kidney evolves in the cross-wind direction [Fric and Roshko, 1994; Smith and Mungal, 1998]. This gives an elliptical form to the plume cross-section, although this vortex pair is not always evident as seen in the Buncefield oil

depot fire; See Figure 4.1. Measurements of the instantaneous plume spread were done by Bennett et al. [1992] and they found that lateral and vertical spreads are unequal, with the lateral spread greater than the vertical spread. Another assumption made in the model development of Hoult et al.

Figure 4.1: Image of the smoke plume rising from the 2005 Buncefield oil depot fire (copyright Thames Valley Police).

[1969] and Hoult and Weil [1972] is that the bent-over plume is slender, that is, the plume cross section (radius) is much smaller than the plume center-line curvature's radius. This eliminates the small-scale irregularities due to ambient turbulence [Weil, 1988]. Also, Hoult et al. [1969] assumed that the effect of atmospheric turbulence can be ignored because the turbulence intensity within the plume is significantly greater than the ambient turbulence intensity and, as a result, buoyant fluid is not being detrained from the plume envelope. See Hübner [2004] for a more detailed analysis of the conditions under which ambient turbulence will break apart a turbulent plume. A brief summary of bent-over plume models is presented in Table 4.1.

In the case of wildfire plumes, because they do not, typically, discharge substantial initial momentum, the near-source flow is dominated by buoyancy-driven acceleration and they are categorized as lazy plumes (see Hunt and Kaye [2005]). Typically a lazy plume with finite source area cannot be categorized as a slender plume. However, directly above the source the plume contracts until it reaches a minimum radius at a height approximately equal to the source radius. It then begins to expand and approach the self-similar velocity profile. Above this height, the self-similar

Table 4.1: Summery of input parameters for various bent-over plume rise models.

	Models										
Assumptions and Properties	Briggs [1965]	Briggs [1984]	Davidson [1989]	Fisher et al. [2001]	Hoult et al. [1969]	Ooms and Mahieu [1981]	Mercer and Weber [1994]	Contini et al. [2011]	Frick [1984]	Zonato et al. [1993]	Present study
Restricted to uniform boundary layer	☼	☼	☼								
No Taylor entrainment									☼		
Circular cross section	☼	☼	☼	☼	☼	☼	☼	☼			
[T]op hat or [G]aussian velocity profile	T	T	T	T	T	G	T	T	G	T	T
[P]oint, [F]inite, or [L]ine source	P	P	F	F	P	P	P/L	P	P	F	F
[F]orced or [L]azy plumes	L	L	L	L	F/L	F/L	L	F/L	F/L	L	F/L
[N]eutral or [S]tratified environment	N	N	N	N	N/S	N/S	N/S	N/S	N/S	S	N/S

bent-over plume appears to come from a point source and can be classified as a slender plume (see Baum and McCaffrey [1989]). Further, estimates of the virtual origin for a highly lazy plume can be obtained using the self-similarity entrainment model of Morton et al. [1956] provided the model is applied above the plume neck (see Kaye and Hunt [2009]). This indicates that, even if the plume is not technically slender above the neck, the modeling approach of Morton et al. [1956] provides a reasonable description of the flow.

There are a number of differences between wildfires and industrial plumes. For example, wildfires' have an unsteady source buoyancy flux that is controlled by the combustion rate of the fire. While models exist for time varying source flux conditions, see Scase et al. [2006], the time scale over which the fire buoyancy flux varies significantly is large compared to the evolution time of the bent-over plume such that steady models can provide insight into the flow dynamics. Further, wildfires may burn over areas of horizontal extent similar in order to the vertical extent of the boundary layer. Therefore, the results of te present study are mainly applicable to small wildfires and large scale industrial fires such as the Buncefield fire shown in figure 4.1. For the purpose of this study, the main relevant distinction between wildfire plumes and smaller industrial plumes is that the buoyancy flux of a wildfire is orders of magnitude greater than that of industrial plumes. Therefore, wildfire plumes generate significantly more vertical momentum over a greater vertical length scale than typical industrial waste plumes. As such, wildfire plumes will have steeper trajectories near

their source and the influence of vertical variations in time-averaged horizontal ambient velocity in the atmospheric boundary layer will have a greater impact on wildfire plume dynamics.

The goal of the present study is to examine the impact of a power-law boundary layer velocity profile on various bent-over plume parameters and establish the conditions under which the velocity profile needs to be considered in modeling. In Section 4.2 we review the model of Hoult et al. [1969], present a set of ordinary differential equations for the variation in plume fluxes along the plume centerline trajectory, and discuss alternative entrainment closures. The two entrainment models are compared to previously published experimental measurements of plume trajectory for both uniform and power-law velocity profiles in Section 4.3. The influence of the plume source conditions on the near field plume trajectory and the conditions under which the boundary layer must be modeled to get accurate trajectory predictions are discussed in Section 4.4. Full scale examples of when the boundary layer will and will not significantly influence a plume's trajectory are presented in Section 4.5 and conclusions are drawn in Section 4.6.

4.2 Evolution equations

In this section the equations of motion for a bent-over plume are presented followed by a discussion of the entrainment formulation and the appropriate choice of entrainment coefficients.

4.2.1 Bent-over plume equations

The evolution equations for the plume's specific volume flux (Q), specific momentum flux (M), specific buoyancy flux (F), and plume centerline trajectory angle (θ), along the envelope centerline (s) are as follows:

$$\frac{dQ}{ds} = Q\sqrt{\frac{2(1+\lambda^2)}{M\lambda}}\left(\alpha\left|\frac{M}{Q} - U\cos(\theta)\right| + \beta\left|U\sin(\theta)\right|\right), \tag{4.1}$$

$$\frac{dM}{ds} - U\cos(\theta)\frac{dQ}{ds} = \frac{FQ}{M}\sin(\theta), \tag{4.2}$$

$$U\sin(\theta)\frac{dQ}{ds} + M\frac{d\theta}{ds} = \frac{FQ}{M}\cos(\theta), \tag{4.3}$$

$$\frac{dF}{ds} = Q\frac{g}{\varrho_a}\frac{d\varrho}{dz}\sin(\theta) = -Q\text{N}^2\sin(\theta) \tag{4.4}$$

$$x = \int_0^s \cos(\theta)ds \tag{4.5}$$

$$z = \int_0^s \sin(\theta)ds \tag{4.6}$$

where U is the ambient velocity and λ is the ratio of the major to conjugate radii to account for the noncircular cross section of the plume. Ambient stratification is parameterized using the Brunt-Vaisala frequency (N). Equations (4.1-4.4) express, respectively, conservation of mass, momentum along s, transverse momentum, and buoyancy fluxes. A thorough derivation of the equations is presented in A. For the remainder of the paper we consider only unstratified environments such that $\text{N} = 0$, the buoyancy flux F is constant along the plume trajectory, and equation (4.4) is redundant. The coupled form of equations (4.1-4.6) can, therefore, be written in non-dimensional form as:

$$\begin{bmatrix} 1 & 0 & 0 & 0 & 0 \\ -v\,cos(\theta) & 1 & 0 & 0 & 0 \\ v\,sin(\theta) & 0 & m & 0 & 0 \\ 0 & 0 & 0 & 1 & 0 \\ 0 & 0 & 0 & 0 & 1 \end{bmatrix} \frac{d}{d\eta}\begin{Bmatrix} q \\ m \\ \theta \\ \zeta \\ \xi \end{Bmatrix} = \begin{Bmatrix} \frac{5q}{6\alpha\sqrt{m}} I_s \left(\alpha\left|\frac{q}{m} - v\cos(\theta)\right| + \beta\left|v\sin(\theta)\right|\right) \\ (2q\Gamma_0\sin(\theta))/(3m) \\ (2q\Gamma_0\cos(\theta))/(3m) \\ \cos(\theta) \\ \sin(\theta) \end{Bmatrix} \tag{4.7}$$

where $I_s = \sqrt{\frac{2(1+\lambda^2)}{\lambda}}$ is a geometric correction term to account for the plume cross-section eccentricity. The other dimensionless parameters are defined as:

$$q = \frac{Q}{Q_0}, \quad m = \frac{M}{M_0}, \quad f = \frac{F}{F_0}, \quad \xi = \frac{z}{L_{Q_0}}, \quad \eta = \frac{s}{L_{Q_0}}, \quad \zeta = \frac{x}{L_{Q_0}}, \quad v = \frac{U}{u_0}.$$

Here, $u_0 = M_0/Q_0$ is the plume source velocity, $\Gamma_0 = (5{Q_0}^2F_0)/(4\alpha{M_0}^{5/2})$, and $L_{Q_0} = (5Q_0)/(6\alpha{M_0}^{1/2})$ where the subscript '0' represents the source value. The parameter Γ_0 is a measure of relative importance of the initial fluxes of buoyancy, momentum, and volume at the source; see Hunt and Kaye

[2005] for a more detailed discussion of source length scales, Γ, and plume classification. In this study we only apply the model above the plume neck and so the source value of Γ is less important and can be thought of as a non-dimensional buoyancy flux.

Equation (4.7) can be partially decoupled using Gauss-Jordan elimination to give:

$$\frac{dq}{d\eta} = \frac{5}{6\alpha}\frac{q}{\sqrt{m}} I_s \left(\alpha \left| \frac{q}{m} - v\cos(\theta) \right| + \beta \left| v\sin(\theta) \right| \right), \tag{4.8}$$

$$\frac{dm}{d\eta} = \frac{2}{3}\Gamma_0 \frac{q}{m}\sin(\theta) + \frac{5}{6\alpha}\frac{q}{\sqrt{m}} I_s \left(\alpha \left| \frac{q}{m} - v\cos(\theta) \right| + \beta \left| v\sin(\theta) \right| \right) v\cos(\theta), \tag{4.9}$$

$$m\frac{d\theta}{d\eta} = \frac{2}{3}\Gamma_0 \frac{q}{m}\cos(\theta) - \frac{5}{6\alpha}\frac{q}{\sqrt{m}} I_s \left(\alpha \left| \frac{q}{m} - v\cos(\theta) \right| + \beta \left| v\sin(\theta) \right| \right) v\sin(\theta) \tag{4.10}$$

For a uniform wind field the far-field plume has a relatively flat trajectory (θ is small) and the plume is advected downstream at the ambient wind speed. Therefore, there is no longitudinal entrainment, only transverse entrainment. In this case analysis shows that the fluxes of momentum and volume scale on the trajectory path length raised to the $4/3^{\text{rds}}$ power. For a power-law velocity profile the plume is continuously rising into regions of larger ambient velocity. Therefore, even though the trajectory has a small slope, the plume continues to rise into regions of higher velocity and the longitudinal entrainment will remain finite and numerical solution of the equations is required.

4.2.2 Entrainment formulation

The entrainment formulation used in (4.1) was presented by Hoult and Weil [1972] and accounts for mixing due to both longitudinal and transverse shear. In this model the entrainment velocity can be written as

$$u_{e-H} = \alpha \left| \frac{M}{Q} - U\cos(\theta) \right| + \beta \left| U\sin(\theta) \right|. \tag{4.11}$$

This closure is an amalgam of the entrainment models for a vertical jet or plume, see Morton et al. [1956], and that for a horizontal cylindrical thermal. The vertical plume entrainment closure (first term on RHS of (4.11)) represents entrainment due to longitudinal shear, that is, the difference in

velocity between the ambient and the plume in a direction parallel to the local plume trajectory. The cylindrical thermal term (second term on the RHS of (4.11)) quantifies shear-driven entrainment due to ambient flow normal to the local trajectory. The entrainment mechanism is analogous to that of a long cylindrical thermal rising up into the atmosphere. Entrainment into the thermal scales on the vertical rise height of the thermal which is analogous to the component of the wind speed normal to the plume centerline.

There is an alternate closure formulation presented by Ooms and Mahieu [1981] based on a work by Abraham [1963]. The closure is quite similar to (4.11) except for a trigonometric correction to the second term that shuts off transverse entrainment when the plume is vertical. The entrainment closure then becomes

$$u_{e-O} = \alpha \left| \frac{M}{Q} - U cos(\theta) \right| + \beta \left| U sin(\theta) \right| cos(\theta). \tag{4.12}$$

This formulation approaches that of (4.11) in the far field when the trajectory angle approaches zero and $cos(\theta) \approx 1$. However, in the near field, especially for highly buoyant plumes that have a steep initial trajectory, there is a potentially significant difference. Under the Ooms and Mahieu [1981] formulation, near the source of a more vertical plume, the transverse entrainment will be significantly reduced and the plume will entrain less horizontal momentum from the ambient flow. Therefore, the Ooms formulation will predict a steeper plume trajectory than (4.11). This is discussed further in Section 4.3 where both models are compared to published experimental trajectories.

4.2.3 Entrainment coefficient values

A range of entrainment coefficient values are found in the literature based on either measurements or entrainment in quiescent ambient conditions, or based on fitting model results to plume trajectories measured in the laboratory. Typical values of the entrainment coefficients α and β cited in the literature are summarized in table 4.2. In general, the transverse entrainment coefficient (β) is similar to that for a cylindrical thermal Turner [1973]. The longitudinal entrainment coefficient (α) used is typically similar to either that for a pure jet or that for a pure plume [Lee and Chu, 2003].

The choice of whether to use the jet or plume entrainment coefficient for the no-wind case is typically based on the source conditions and the vertical extent of the flow. If the source Froude

Table 4.2: Commonly used values of longitudinal (α) and transverse (β) entrainment coefficients for top-hat formulations of the bent-over plume equations.

Closure	α	β
Hoult and Weil [1972]	0.11	0.6
Ooms and Mahieu [1981]	0.081	0.5
Vertical plume (no wind) Lee and Chu [2003]	0.12	-
Vertical jet (no wind) Lee and Chu [2003]	0.081	-
Cylindrical thermal (no cross wind) Turner [1973]	-	0.6

number (based on the source velocity, radius, and reduced gravity) is high then the flow will behave like a jet near the source. For lower values of the Froude number the flow is more like a pure plume. For any finite source of buoyancy the flow will eventually behave like a pure plume (see for example Morton and Middleton [1973] & Hunt and Kaye [2005]). Therefore, there are a number of models for how, under highly forced source conditions, the entrainment coefficient adjusts from that of a jet to the larger plume value (see for example Priestly and Ball [1955], Fischer et al. [2013] & Wang and Law [2002]). There are also a number of explanations for why the plume entrainment coefficient is larger than that of a jet. For example, Kaye [2008] used a simple scaling argument to show that the additional entrainment due to buoyancy generated baroclinic torque matches the behavior of the model of Priestly and Ball [1955] and the experimental data of Wang and Law [2002]. However, for the case of a bent-over plume, the far field flow is largely horizontal and, therefore, there will be minimal additional buoyancy driven entrainment. Therefore, the longitudinal entrainment will be dominated by longitudinal shear, the jet entrainment coefficient would be more appropriate, and the more sophisticated entrainment models in the literature for vertical plumes would not apply.

The choice of longitudinal entrainment coefficient will effect the modeled plume trajectory. Using the larger plume value of α will result in more near-source entrainment of horizontal momentum and a flatter initial trajectory compared to that predicted using the jet value of α. Again, this is of particular importance for flows with initially steep trajectories where longitudinal entrainment is significant over greater distances. In Sect. 4.3 the entrainment formulations of Hoult and Weil [1972] and Ooms and Mahieu [1981] are compared to previously published experimental results. In these plots lines are drawn for each model using both the plume and jet longitudinal entrainment coefficients.

4.3 Comparison with previous experiments

The models presented above are compared to previously published laboratory experiments in order to investigate the influence of the choice of entrainment formulations, entrainment coefficients, and the velocity profile on the trajectory of a bent-over plume. For each experimental test case the data is compared to the bent-over plume equations (4.1-4.6) using the entrainment formulation of Hoult (4.11), the entrainment formulation of Abraham (4.12), and the algebraic Briggs equation (4.14) for a plume in a uniform wind field. The test cases are taken from Contini et al. [2011] (cases 1-4), Contini and Robins [2001] (5-8), Contini et al. [2009] (9-12), and Marro et al. [2014] (13-16). The experiments for cases 1-8 were conducted by towing the plume source across a quiescent environment and, therefore, represent plumes in a uniform wind field. The experiments for cases 9-16 were conducted with a finite height plume source in a boundary layer velocity profile.

The velocity profiles in these experiments were well described by a power-law function as proposed by Hellmann [1917] and quantified by Davenport [1960]. That is,

$$U(z) = U_r \left(\frac{z}{z_r} \right)^p ; \quad 0 \leq p \leq 1 \tag{4.13}$$

where U_r is the time averaged horizontal wind speed measured at a reference height z_r. In general, p varies with wind speed, height range of the fit, upwind topography, and stability of the boundary layer. However, in this study, it is only considered to be a function of the upwind terrain surface roughness (see ASCE [1999]). Also, it is worth mentioning that the power-law expression fits best over moderate height range of $20 - 300$ meters through the boundary layer [Cook, 1997] as opposed to the logarithmic fit that does not show a good representation of the boundary layer velocity above the inertial sub-layer heights of approximately 200 meters, see Tieleman [2008] & Li et al. [2010]. The experimental conditions for each test case are summarized in Table 4.3 in terms of the source Froude number ($Fr = u_0/\sqrt{g'D}$), relative wind speed ($\mu = U_0/u_0$), the boundary layer power-law exponent (p), and the non-dimensional release height (h_s/D). Where U_0 is the effective horizontal velocity of the boundary layer at the release height of the plume, and u_0 is the plume exit velocity.

The results of the comparison for the uniform velocity profile experiments (cases 1-8) are presented in Figures 4.2 & 4.3. For each plot in Figure 4.2 & 4.3 the lengths of the vertical axis and horizontal axis are the same to allow for direct trajectory slope comparison between plots. The first four cases, in Figure 4.2, have relatively low wind speeds ($\mu \leq 0.22$) except for case 4 where

Table 4.3: Velocity ratio, source Froude number, velocity profile power-law exponent, and momentum length scale normalized on the release height for the experimental test cases. The test cases are taken from Contini et al. [2011] (cases 1-4), Contini and Robins [2001] (5-8), Contini et al. [2009] (9-12), and Marro et al. [2014] (13-16).

Experimental Data	Name	U_0/u_0	Fr	p	z_m/h_s
Contini et al. [2011]	case (1)	0.08	9.7	0	-
	case (2)	0.15	9.7	0	-
	case (3)	0.22	9.7	0	-
	case (4)	1.2	9.7	0	-
Contini and Robins [2001]	case (5)	0.3	2.9	0	-
	case (6)	0.52	2.9	0	-
	case (7)	0.76	2.9	0	-
	case (8)	1.2	2.9	0	-
Contini et al. [2009]	case (9)	0.25	84	0.23	0.042
	case (10)	0.15	126	0.23	0.063
	case (11)	0.2	70	0.23	0.059
	case (12)	0.13	104	0.23	0.089
Marro et al. [2014]	case (13)	0.76	2.9	0.21	1.287
	case (14)	0.76	4.2	0.21	0.484
	case (15)	0.79	5.6	0.21	3.182
	case (16)	0.74	9.6	0.21	1.524

$\mu = 1.2$. However, they are quite highly forced ($Fr = 9.7$) and so there is relatively little buoyancy-generated vertical momentum downstream of the plume source. Cases 5-8, in Figure 4.3, are more buoyant ($Fr = 2.9$) and have higher wind speeds, mostly $U_0/u_0 \geq 0.3$. The impact of the additional buoyancy can be seen by comparing the trajectory for case 5 with that of case 3. Case 5 has the higher relative wind speed ($\mu = 0.3$ compared to 0.22 for case 3) but also has a steeper trajectory due to the additional buoyancy-generated vertical momentum.

For all eight cases the integral model performs quite well when using the Hoult entrainment formulation (4.11). For this formulation there is little difference in the trajectories based on the choice of longitudinal entrainment coefficient (α). The Abraham formulation (4.12) performs less well, overpredicting the plume height for all cases. This is due to the reduction in entrainment of horizontal momentum resulting from the $cos(\theta)$ modification to the transverse entrainment term. These steeper trajectories also exhibit greater variation in model results with the choice of α as longitudinal entrainment of horizontal momentum plays a greater role near the source due to transverse entrainment being shut off. When the lower jet value of α is used the plume has a steeper trajectory due to lower entrianment of horizontal momentum. The Briggs generalized algebraic equation

[Briggs, 1984; Davidson, 1989] which relates the plume rise height to its downwind distance as

$$z(x) = \left[\frac{3Mx}{\beta_1^2 U_0^2} + \frac{3Fx^2}{2\beta_2^2 U_0^3}\right]^{1/3} \tag{4.14}$$

where

$$\beta_1 = 0.4 + 1.2\frac{U}{u_0} \quad , \quad \beta_2 = 0.6, \tag{4.15}$$

provides the best agreement across all the uniform-velocity profile cases, that is cases 1-8. This is primarily because the Briggs equation is an empirical curve fit based on a theoretical functional form and is, therefore, tuned to match experimental results. Whereas, the entrainment models in Hoult and Abraham were integrated using constant entrainment coefficients (given in Table 4.2) based on experiments run in quiescent environments. Therefore, the entrainment models capture more of the flow physics but will perform less well for cases similar to those from which the Briggs equation was developed.

The comparison between the models and experiments conducted using a boundary layer velocity profile are shown in Figures 4.4 (cases 9-12) and 4.5 (cases 13-16). In both figures the plume trajectory is plotted relative to the plume source height. The axis length ratios are the same as for Figure 4.2 & 4.3 so direct visual comparison of trajectory slope can be made. In all cases the plume equations are solved using the boundary layer power-law velocity profile fit specified in the original papers. Cases 9-12 are much more forced ($Fr \geq 70$) than cases 13-16 ($Fr \leq 9.6$). Cases 9-12 were also run with a much lower relative wind speed ($U_0/u_0 \leq 0.25$) than cases 13-16 ($U_0/u_0 \geq 0.74$). In all eight cases the boundary layer power law exponents are very similar, see Table 4.3.

For cases 9-12 the algebraic Briggs equation (4.14) provides the best agreement with the experimental data even though the experiments were run for a non-uniform velocity profile. However, for cases 13-16, the Hoult formulation (4.11) is clearly the most accurate. The only significant difference between the two sets of tests is the release height of the plume above the ground. The release heights scaled on the source diameter for cases 9-12 range from 43 to 60 whereas for cases 13-16 the $h_s/D = 1.5$. Therefore, the plumes from cases 13-16 will experience a greater increase in horizontal velocity variation with height than the plumes from cases 9-12 due to higher wind shear

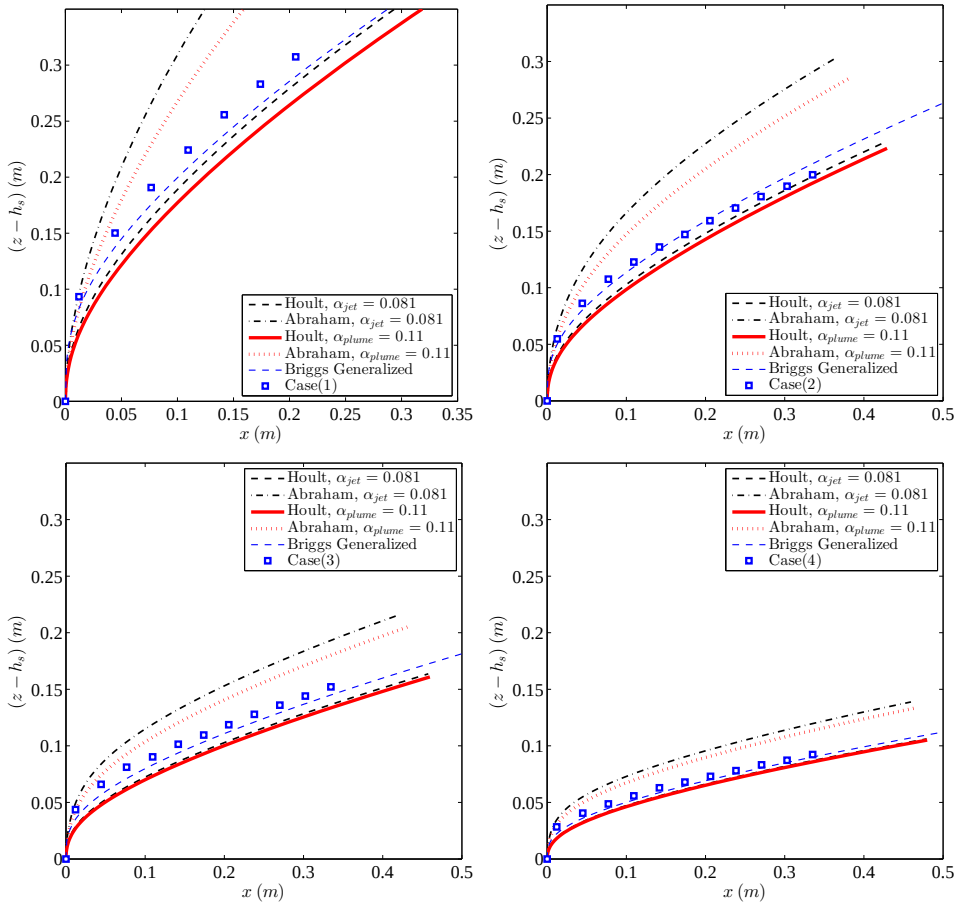

Figure 4.2: Plots of experimental trajectory (squares) for cases 1-4 (left to right and down) listed in Table 4.3 along with model results for Hoult and Weil [1972] - solid & thick dashed lines, Abraham [1963]/Ooms and Mahieu [1981] - dot-dashed & dotted lines, and the Briggs [1984] generalized algebraic equation (4.14) - thin dashed line.

near the boundary, and, therefore, the role of the boundary layer in flattening out the trajectory is greater.

The comparison of various bent-over plume models with laboratory measurements of plume trajectory in a boundary layer indicate that there are circumstances where the algebraic Briggs equation provides the best trajectory prediction (cases 9-12). However, there are also cases where the full set of plume equations must be solved, with the boundary layer velocity profile included, in order to get an accurate trajectory prediction (cases 13-16). The conditions under which the full solution of the plume equations is required is discussed next.

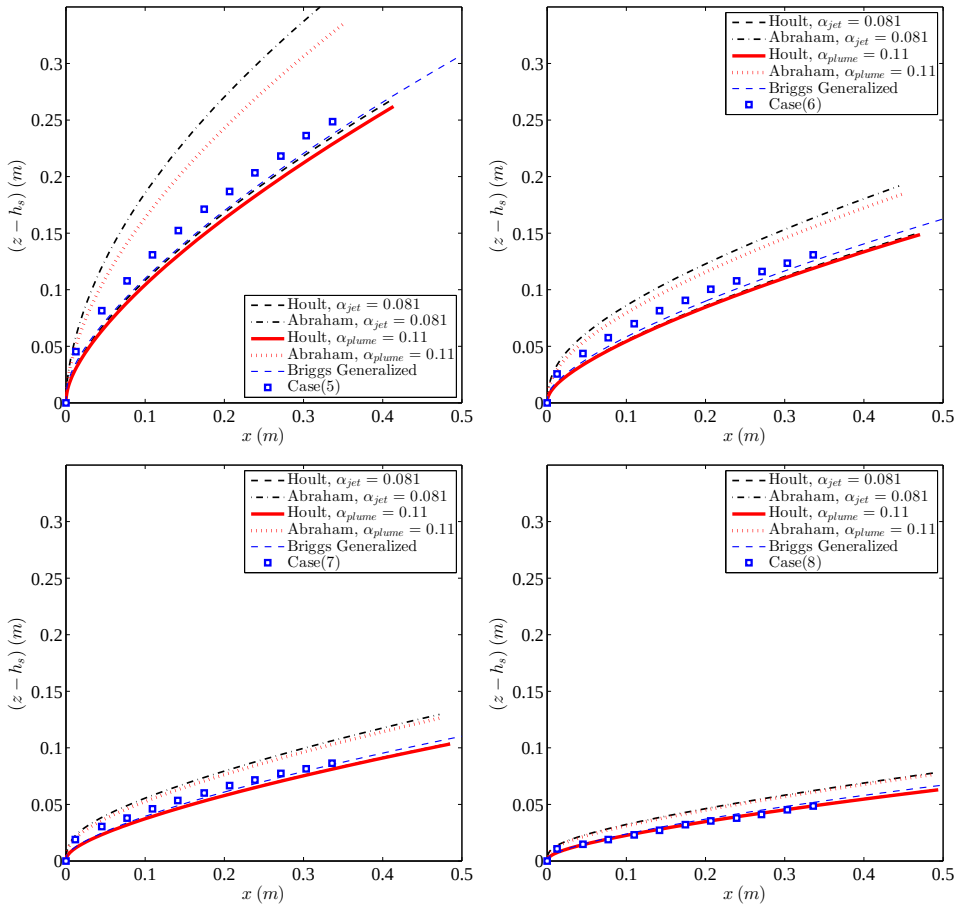

Figure 4.3: Plots of experimental trajectory (squares) for cases 5-8 (left to right and down) listed in Table 4.3 along with model results for Hoult and Weil [1972] - solid & thick dashed lines, Abraham [1963]/Ooms and Mahieu [1981] - dot-dashed & dotted lines, and the Briggs [1984] generalized algebraic equation (4.14) - thin dashed line.

4.4 Influence of source conditions

For a plume in a wind field with a power-law velocity profile the far-field plume fluxes of volume and momentum will be significantly greater than the source fluxes and the plume dynamics will only depend on the wind conditions and the plume buoyancy flux. However, this may be so far downwind as to not be of any practical significance. It is, therefore, important to understand the conditions under which the boundary layer flow significantly influences the near source flow. In this section we present a dimensional analysis of the near source flow conditions and derive a set of conditions under which the boundary layer must be modeled to correctly capture the near field flow trajectory.

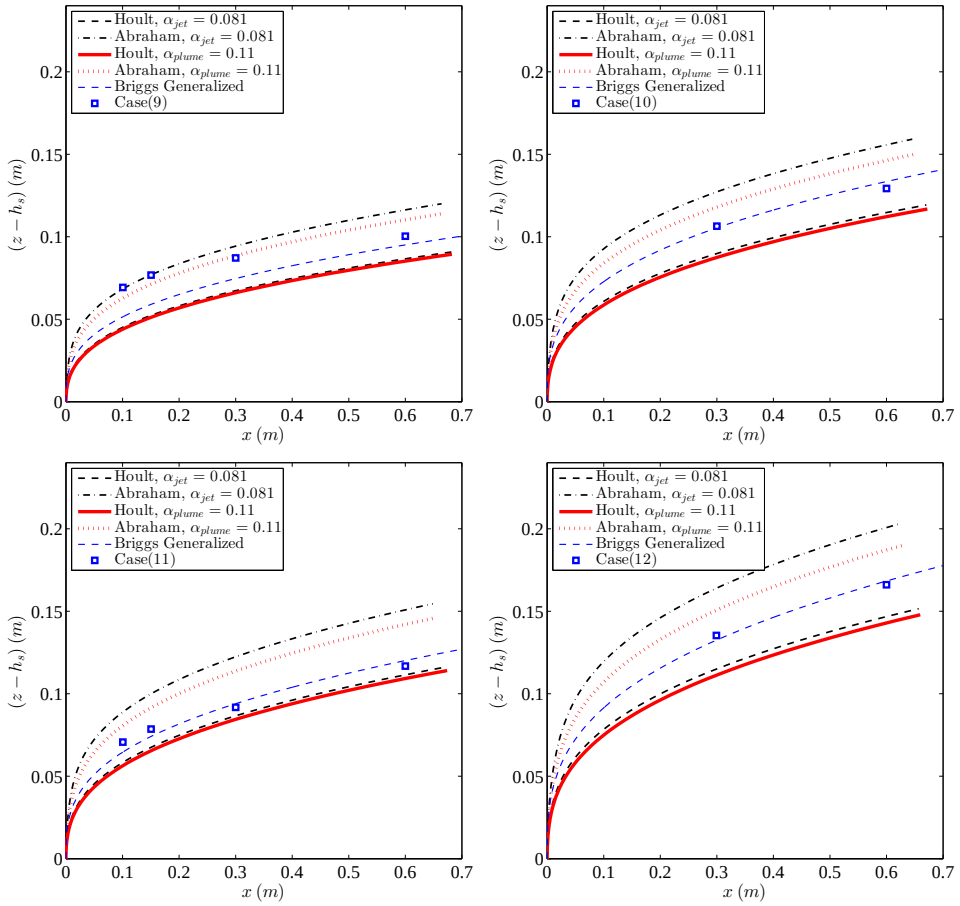

Figure 4.4: Plots of experimental trajectory (squares) for cases 9-12 (left to right and down) listed in Table 4.3 along with the model results. Lines are the same as for Figure 4.2.

4.4.1 Uniform velocity profile ($p = 0$)

For a uniform velocity profile the plume source conditions can be written in terms of the source diameter (D), source reduced gravity (g'), and the exit velocity (u_0). The wind conditions can be parameterized by the mean horizontal wind speed (U_0). This leads to two non-dimensional groups, the source Froude number and exit velocity ratio (referred to herein as the relative wind speed) given by

$$Fr = \frac{u_0}{\sqrt{g' D}} \quad \text{and} \quad \mu = \frac{U_0}{u_0} \tag{4.16}$$

respectively; See Lee and Chu [2003]. All non-dimensional downstream parameters will be functions only of these two parameters, distance from the source, the choice of entrainment closure, and the choice of entrainment coefficients. Distance from the source can be characterized in terms of the

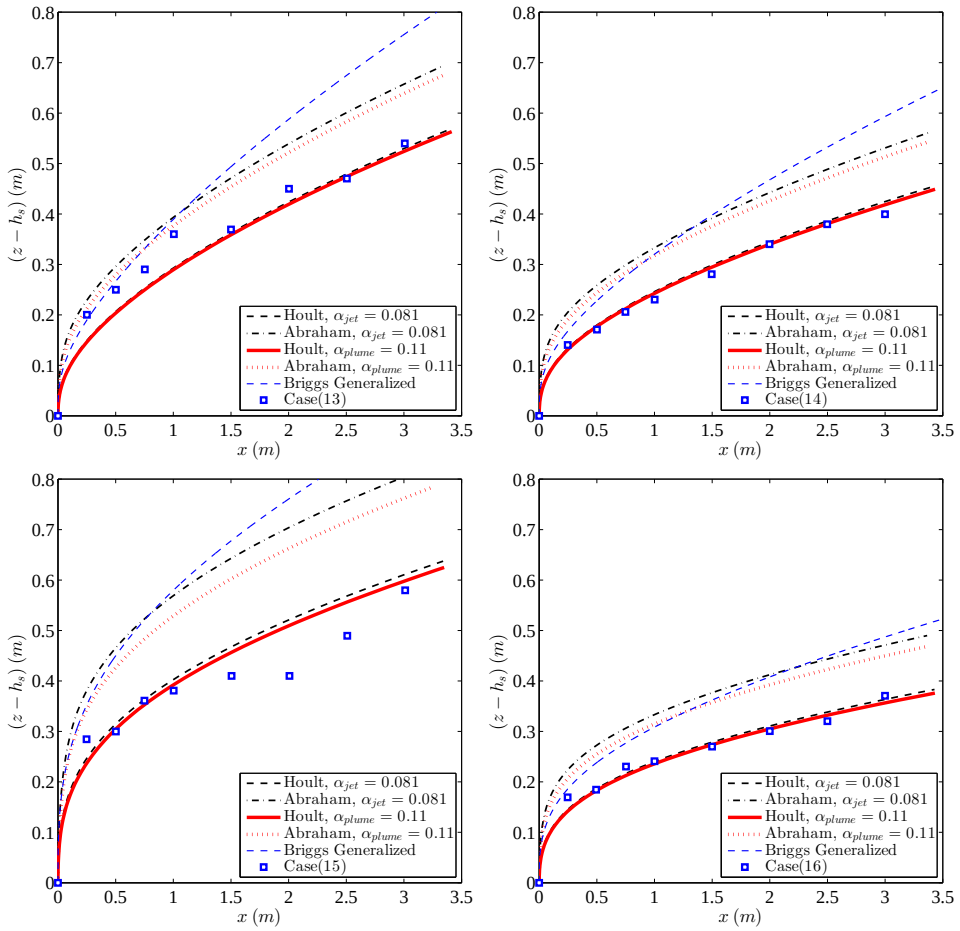

Figure 4.5: Plots of experimental trajectory (squares) for cases 13-16 (left to right and down) listed in Table 4.3 along with the model results. Lines are the same as for Figure 4.2.

distance along the plume centerline, downwind distance, or vertical distance. As we are primarily concerned with the influence of ABL flows on bent-over plumes, we focus on the vertical distance (z).

This height can be non-dimensionalized in terms of any number of length scales but the most commonly used length scales are the momentum length, buoyancy flux length, and source diameter. The first two are given by

$$z_m = \frac{M_0^{1/2}}{U_0} = \frac{u_0 D}{U_0} = \frac{D}{\mu} \quad \text{and} \quad z_f = \frac{F_0}{u_0^3} = \frac{u_0 D^2 g'}{U_0^3} = \frac{D}{\mu^3 Fr^2} = \frac{z_m}{\mu^2 Fr^2} \tag{4.17}$$

respectively. The momentum length (z_m) represents the vertical distance at which a vertical pure point source jet will have a vertical mean velocity equal to the mean wind speed. It, therefore,

represents a vertical scale over which the bent-over jet will have a relatively steep trajectory. The buoyancy length (z_f) represents the vertical distance at which a vertical pure point source plume will have a mean vertical velocity equal to that of the mean wind speed. It therefore represents a second vertical scale over which the bent-over plume will have a relatively steep trajectory. Which of these two vertical scales is most appropriate depends on the balance of momentum and buoyancy fluxes at the source (Fr) and the relative wind speed (μ). To illustrate this, the height at which the plume has a trajectory angle of 45^o (denoted by z_{45}) was calculated for a broad range of Fr and μ by integrating the plume equations (4.1-4.6) along the centerline trajectory (s) using MATLAB's built-in ODE solver (*ode15s*). Contour plots of z_{45} scaled on the two length scales z_m and z_f are shown in Figure 4.6.

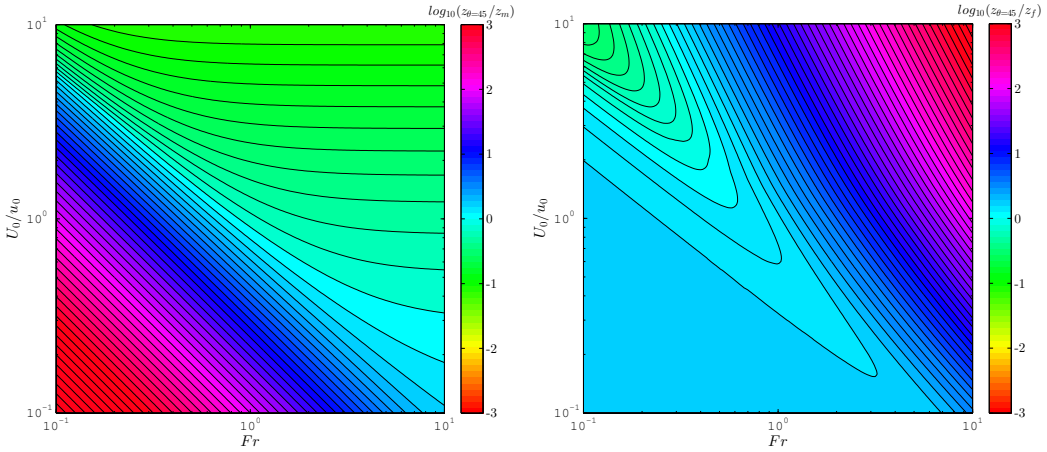

Figure 4.6: Log-log scale contour plots of z_{45} as a function of Fr and μ with z_{45} scaled on (left) z_m and (right) z_f.

Figure 4.6 (left) shows $\Pi_{45.m} = z_{45}/z_m$ in (Fr, μ) space. For much of the parameter space $\Pi_{45.m}$ is independent of the Froude number (horizontal contours) indicating that, in these regions, z_m is the appropriate vertical scale for characterizing the rate of bending of the plume. The horizontal contours are seen for large relative wind speed regardless of Froude number and large Froude numbers regardless of the relative wind speed. For large source Froude numbers the source momentum dominates and the flow behaves as a jet. As such the near field bending of the flow is controlled by the momentum length z_m. However, for small Froude numbers and large relative wind speed (μ) the bending also scales on z_m even though the plume source is buoyancy dominated. This is due to the length scales being defined in terms of pure point sources of either momentum or buoyancy. For higher wind speeds the plume will bend over more rapidly and z_{45} will get very small. In this limit

($z_{45} \to 0$) the velocity of the point source of momentum (a pure jet) ($u_{jet} \sim z^{-1}$) is larger than the velocity of the point source of buoyancy (a pure plume) ($u_{plume} \sim z^{-1/3}$). Therefore, even though the source is buoyancy-dominated, for high wind conditions the buoyancy does not have adequate vertical distance to generate enough vertical momentum to influence the height at which it becomes significantly bent over. Another way of establishing this result is to consider the relative values of the two length scales. The height at which the plume is significantly bent over will be controlled by the larger of the two source length scales. In a uniform boundary layer one can write the ratio of the length scales as

$$\frac{z_m}{z_f} = \mu^2 Fr^2 \tag{4.18}$$

indicating that the appropriate length scale will be the momentum length provided $\mu\, Fr \gg 1$.

Figure 4.6 (right) shows $\Pi_{45.f} = z_{45}/z_f$ in (Fr, μ) space. In this case $\Pi_{45.f}$ is constant for $\mu\, Fr \ll 1$. In fact, in this region the bending height is independent of both μ and Fr, whereas when z_m was the controlling length scale, the bending height was still a function of μ. This is because, for small Froude numbers, the plume velocity is controlled by the buoyancy flux and is, therefore, independent of the plume source velocity and, hence, independent of μ.

4.4.2 Power-law velocity profile ($p > 0$)

The introduction of a power-law ambient velocity profile adds two new parameters to the problem: the power law exponent p and the plume release height h_s. There are, therefore, two additional non-dimensional groups that, without loss of generality, can be written as

$$p \quad \text{and} \quad \psi = \frac{z_m}{h_s}. \tag{4.19}$$

For the boundary layer velocity profile the reference velocity is taken to be the velocity at the plume release height and the other non-dimensional groups are unchanged. For any boundary layer cross flow the plume will experience higher wind speeds than the reference wind speed at all heights above the source and will have a flatter (less steep) trajectory. For larger power-law exponents (p) the rate of increase in wind speed with height is greater and the plume will bend over more rapidly. Conversely, the higher the release height (the smaller ψ) the lower the level of local wind shear experienced by the plume and the steeper the trajectory compared to a lower release height into the

same boundary layer.

This behavior is summarized in Figures 4.7-4.10 which show contour plots of z_{45} in the power-law boundary layer, i.e. $z_{45.p}$, normalized on z_{45} in the uniform velocity profile for the same Fr and μ. This is denoted by $\chi = z_{45.p}/z_{45.u}$. The contour plots show that in all cases the height at which the plume path is at 45^o is lower for the boundary layer flow than for the equivalent uniform velocity profile case. As expected, for small p and z_m/h_s the trajectory is hardly changed (Figures 4.7 - 4.10 (a,b)). However, for lower release height (larger z_m/h_s) there is a significant flattening of the trajectory due to the boundary layer velocity profile. Further, in all cases the trajectory is flatter for low Froude number plumes in a relatively low velocity wind field. In these cases the vertical momentum is buoyancy- rather than source-generated, the wind speed is low, and the plume has a steeper initial trajectory. Therefore, it reaches higher into the boundary layer where the wind speed is greater and is bent over more rapidly compared to the same plume in a uniform wind field.

An alternative way of viewing this is to consider the definitions of the vertical length scales z_m and z_f. For a power-law velocity profile the length scale can be modified to account for the vertical variation in U. Equating the pure plume velocity scaling

$$u \sim F^{1/3}(z - h_s)^{-1/3} \tag{4.20}$$

with the power-law velocity profile (4.13) in which the vertical coordinate is measured from the plume release height leads to

$$z_f \left(\frac{z_f + h_s}{h_s} \right)^{3p} = \left(\frac{F_0^{1/3}}{U_0} \right)^3 \quad at \quad z = z_f + h_s \tag{4.21}$$

which can be solved implicitly for z_f. The equivalent definition for z_m is

$$z_m \left(\frac{z_m + h_s}{h_s} \right)^{p} = \frac{M_0^{1/2}}{U_0} \quad at \quad z = z_m + h_s. \tag{4.22}$$

When $p = 0$ both definitions reduce to the uniform velocity profile definitions given in (4.17).

In both (4.21) and (4.22) the righthand side of the equation is identical to the righthand side of the definitions for a uniform velocity profile (4.17) and the term in brackets on the lefthand side is greater than 1. Therefore, for $p > 0$ and $h_s > 0$ the values of z_f and z_m will be smaller than their uniform velocity profile definitions. The greater the difference between the uniform and

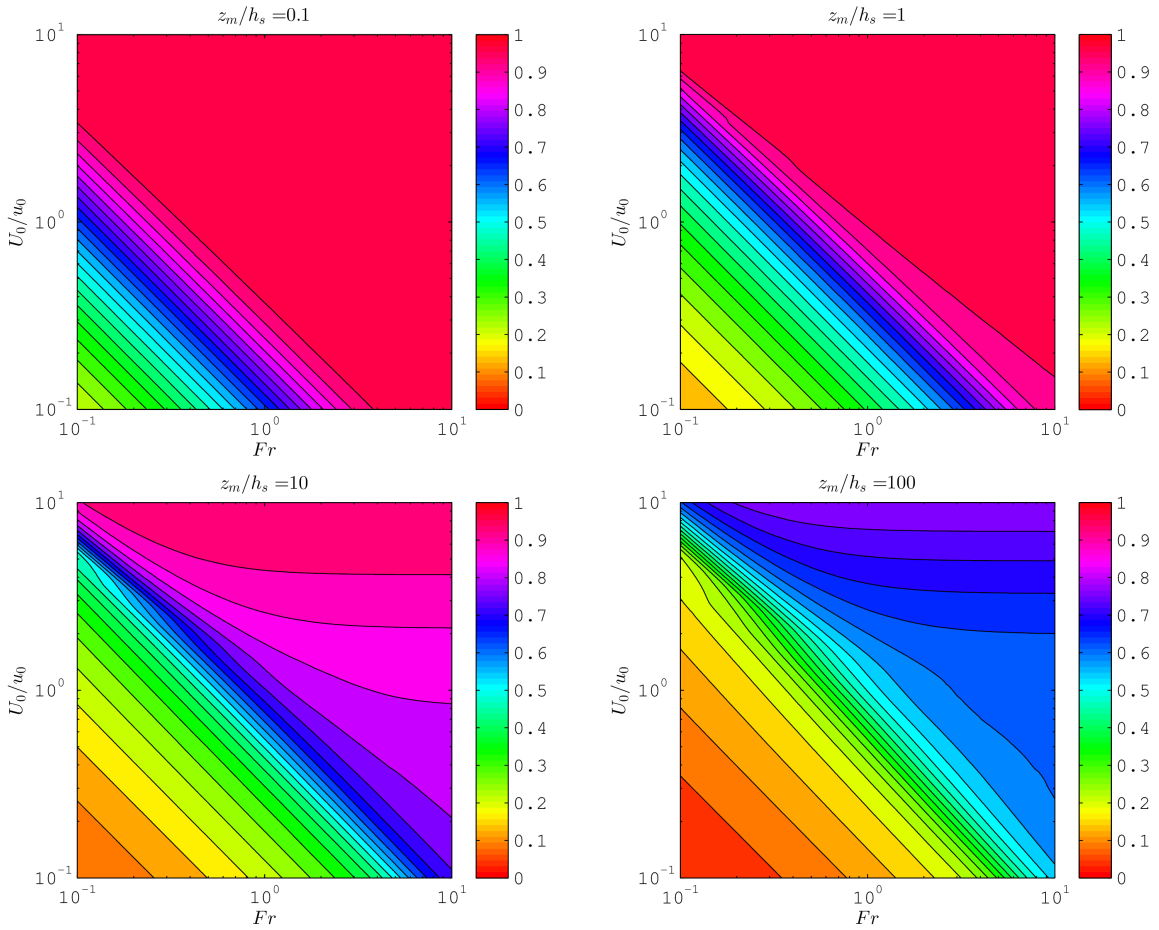

Figure 4.7: Contour plots of $\chi = z_{45.p}/z_{45.u}$ as a function of Fr and μ for $p = 0.1$ and (a) $z_m/h_s = 0.1$; (b) $z_m/h_s = 1$; (c) $z_m/h_s = 10$; (d) $z_m/h_s = 100$.

boundary layer definitions of z_m and z_f, the greater the influence of the boundary layer on the plume trajectory. This will be the case when

$$\varsigma_f = \frac{z_{f.u}}{z_{f.p}} = \left(\frac{z_f}{h_s} + 1\right)^{3p} \gg 1 \quad \text{or} \quad \varsigma_m = \frac{z_{m.u}}{z_{m.p}} = \left(\frac{z_m}{h_s} + 1\right)^{p} \gg 1 \tag{4.23}$$

where the subscripts 'u' and 'p' refer to the uniform and power-law velocity profiles respectively. This is consistent with the contour plots in Figures 4.7-4.10 which show significant flattening of the plume trajectory for larger values of z_m/h_s, p, and $z_f/h_s = (z_m/h_s)/(\mu^2 Fr^2)$. It is also consistent with the observation in the previous section that experimental cases 13-16 were more strongly influenced by the boundary layer than cases 9-12. Substituting experimental values into (4.23) gives $1.1 < \varsigma_f < 1.3$ and $2.4 < \varsigma_m < 2.8$ for cases 9-12 compared to $8.3 < \varsigma_f < 33$ and $4.4 < \varsigma_m < 5.4$ for cases 13-16.

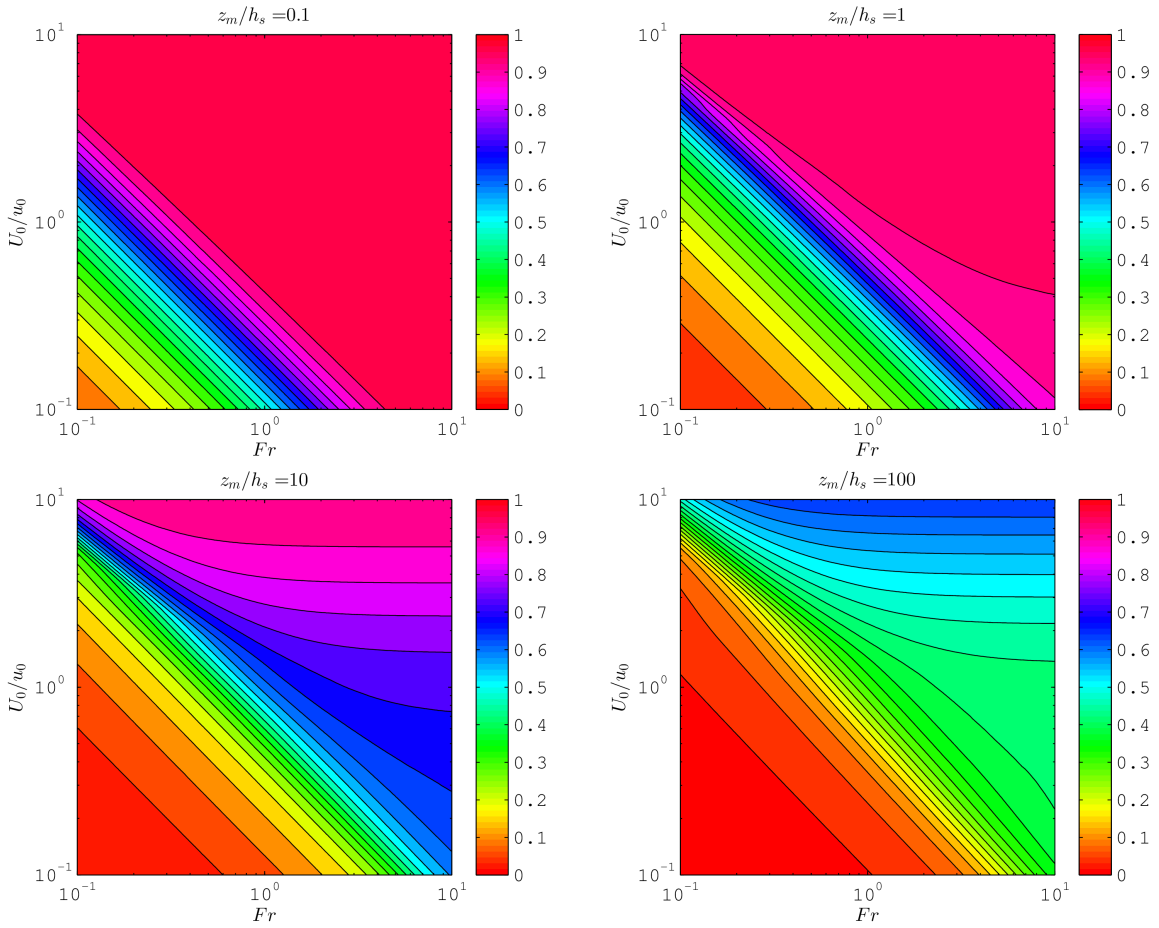

Figure 4.8: Contour plots of $\chi = z_{45.p}/z_{45.u}$ as a function of Fr and μ for $p = 0.2$ and (a) $z_m/h_s = 0.1$; (b) $z_m/h_s = 1$; (c) $z_m/h_s = 10$; (d) $z_m/h_s = 100$.

Examples of when this is significant in full-scale applications are discussed in the next section.

4.5 Model selection criteria case studies

The previous section established a criteria for when the vertical velocity variation in the atmospheric boundary layer will significantly effect a plume's trajectory (Equation 4.23) such that the algebraic Briggs equation will no longer give an accurate trajectory prediction. This section illustrates the use of this criteria by applying it to case studies of full-scale industrial and wildfire plumes. The case study parameters are presented in Table 4.4 and represent six different smoke stacks and two examples of wildfires. In general the smoke stacks produce forced plumes ($Fr > 1.2$). Wildfires are highly lazy large area plumes that accelerate and contract above the fire. However, as

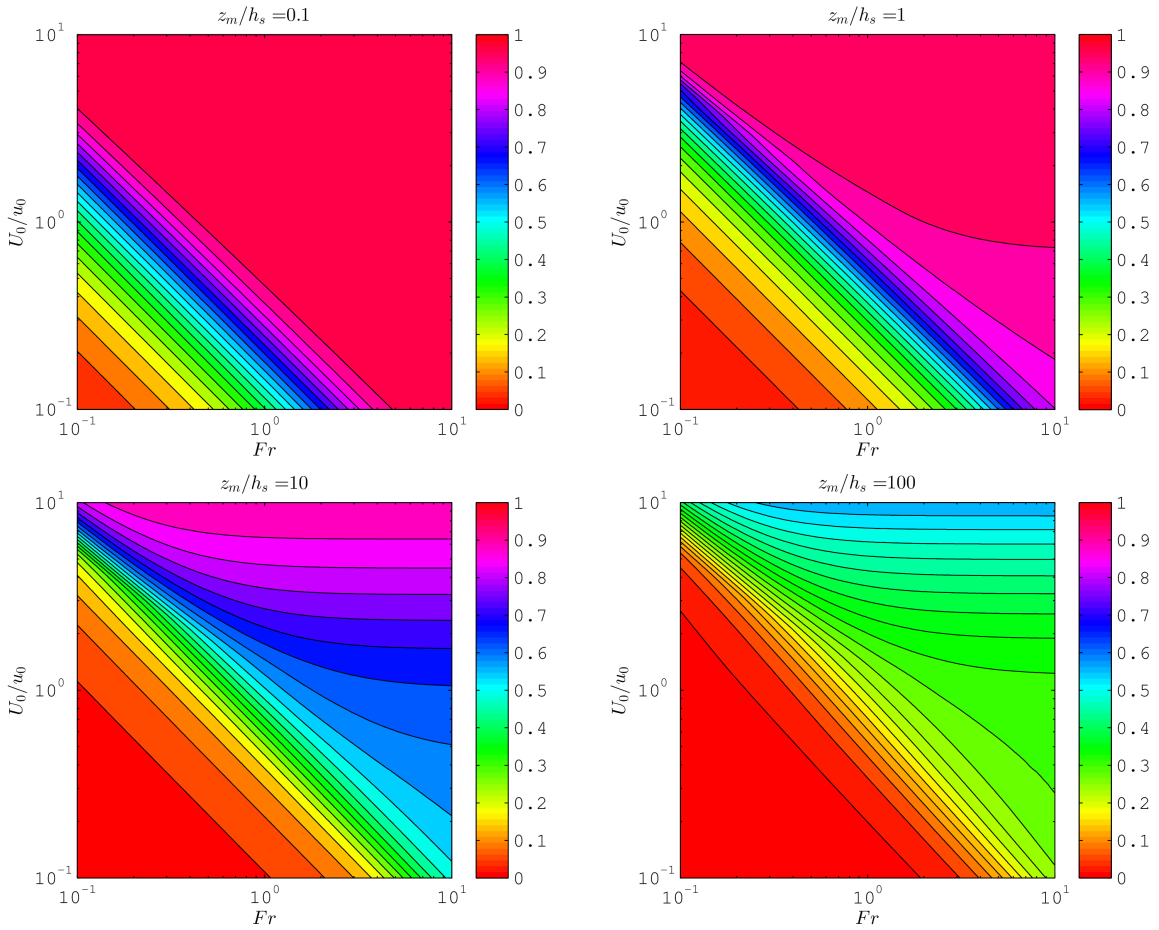

Figure 4.9: Contour plots of $\chi = z_{45.p}/z_{45.u}$ as a function of Fr and μ for $p = 0.3$ and (a) $z_m/h_s = 0.1$; (b) $z_m/h_s = 1$; (c) $z_m/h_s = 10$; (d) $z_m/h_s = 100$.

the entrainment equations have been shown to be inappropriate in the near source region below the plume neck [Linden and Kaye, 2006] the plumes are modeled as pure plumes above the neck and the flow below the neck is not modeled.

The data suggests that for almost all the industrial cases the plume trajectory will be virtually unaffected by the boundary layer velocity variation. In these cases (1-6) the values of ς_m and ς_f are very close to one. The only exception to this is for case 4 at lower wind speeds. In all cases the wildfire plumes are likely to be significantly altered by the boundary layer flow. The wildfire values for the transition criteria are $1.9 < \varsigma_m < 2.0$ and $54 < \varsigma_f < 101$. This was confirmed by locating the case study plumes in contour plots of $\chi = z_{45.p}/z_{45.u}$ as a function of U_0/u_0 and z_m/h_s for $Fr = 1.2$, 4.0, and 6.0. These contour plots are shown in Figures 4.11 to 4.13. In all cases the wildfire plumes were significantly influenced by the vertical variation in horizontal velocity

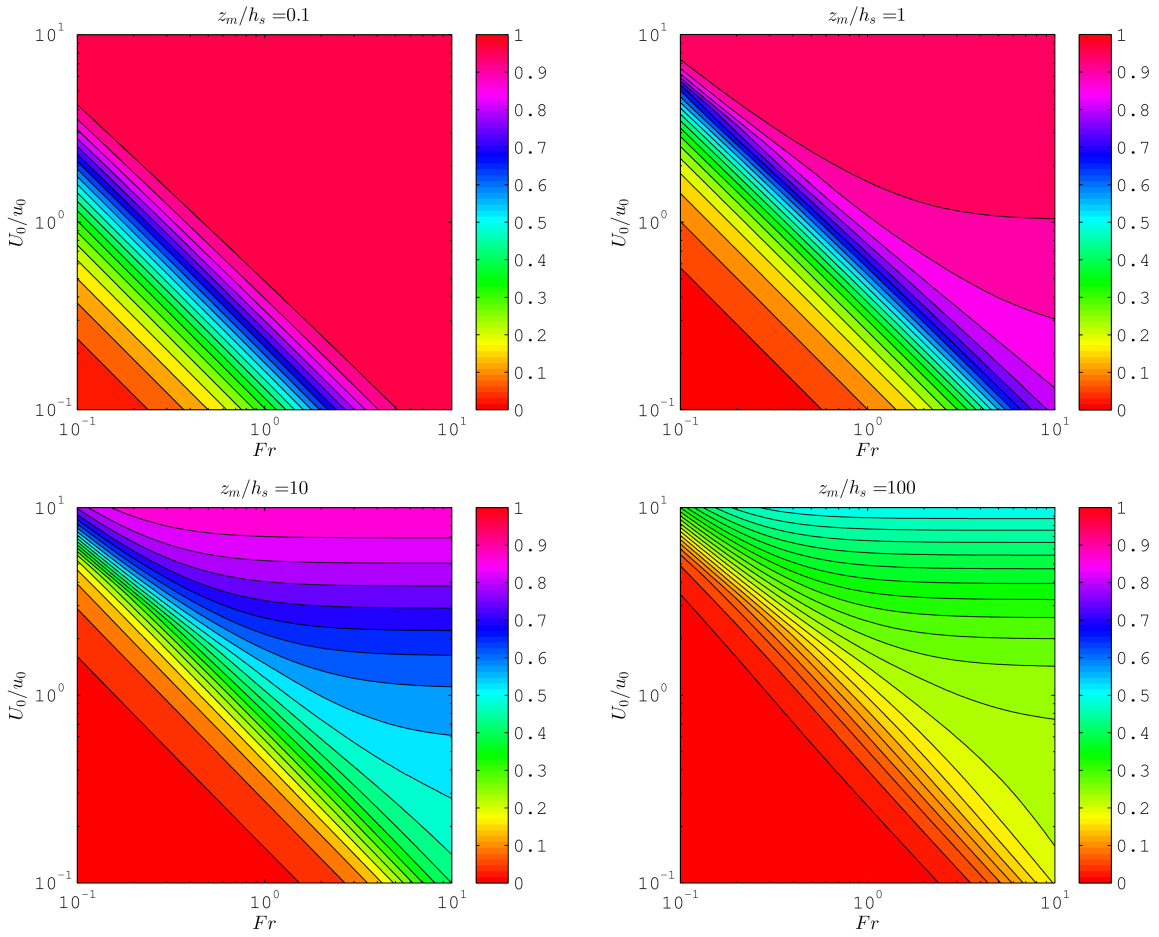

Figure 4.10: Contour plots of $\chi = z_{45.p}/z_{45.u}$ as a function of Fr and μ for $p = 0.4$ and (a) $z_m/h_s = 0.1$; (b) $z_m/h_s = 1$; (c) $z_m/h_s = 10$; (d) $z_m/h_s = 100$.

(triangles in figure 4.11) whereas the vast majority of the industrial plumes had trajectories that could be well modeled by the standard Brigg's algebraic equation.

4.6 Discussion and conclusions

The trajectory of a bent-over plume in a power-law velocity profile has many applications. This problem is particularly pertinent to large, highly buoyant fire plumes that can rise high into the atmospheric boundary layer. However, the conditions under which the ambient velocity profile needs to be considered, when modeling, have not been previously investigated. The near field plume trajectory is typically quantified in terms of length scales of either momentum (z_m) or buoyancy (z_f). These lengths represent the vertical distance that a pure point source jet (z_m) or plume (z_f) would

Table 4.4: Ranges of stack and atmospheric boundary layer parameters for the plume cases (1-6) are excerpted from Carson and Moses [1969]. Parameter values in case (7) are adopted based on Bhutia et al. [2010] for small-scale wildfires.

Case	Case Name	$U_0\ (m/s)$	$u_0\ (m/s)$	$P_o\ (MW)$	$h_s\ (m)$	$D\ (m)$	Fr	Symbol
1	Harwell	11.7-3.0	9.9	5.1	61	3.46	4.4	$\times$
2	Duisburg	10.5-1.6	12.1-3.5	10.4-4.1	125	3.5	1.0-4.2	$\square$
3	Gernsheim	9.2-1.5	5.3-2.2	4.2-1.5	75	2.3	0.7-1.5	o
4	TVA-Widow's Creek	6.6-1.5	24.5-22.9	74.9-65.7	153	6.34	5.8-6.0	$+$
5	TVA-Gallatin	8.2-1.6	16.4-14.8	74.1-62.8	153	7.63	3.4-3.6	$\diamond$
6	TVA-Paradise	11.3-2.3	19.2-15.3	102.9-71.1	183	7.93	3.4-4.0	$\star$
7	Wildfires	5-11	22.64-40.7	50-70	10-68.2	20-136.4	1.2	∇

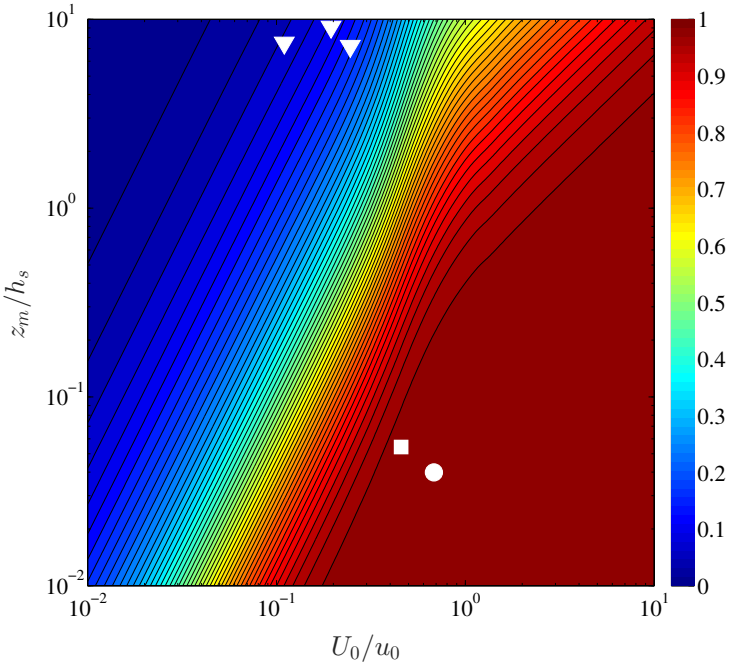

Figure 4.11: Contour plot of $\chi = z_{45.p}/z_{45.u}$ as a function of U_0/u_0 and z_m/h_s for $Fr = 1.2$. Symbols are given in Table 4.4.

have to rise for its velocity to equal the wind speed. These lengths are smaller for plumes (forced or unforced) in a power-law boundary layer because the wind speed increases with height while the plume velocity decreases. It was shown that the trajectory of a plume in a power-law boundary layer will differ significantly from that of a plume in a uniform wind field when the boundary layer length scales are significantly smaller than the equivalent uniform velocity profile length scales. An analytic expression for the ratio of the uniform and boundary layer length scales (ς_m and ς_f) was derived

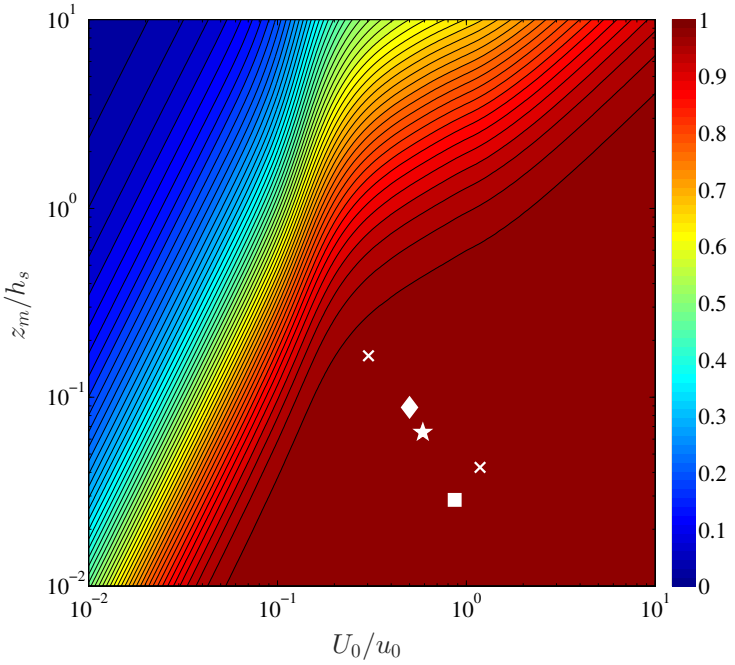

Figure 4.12: Contour plot of $\chi = z_{45.p}/z_{45.u}$ as a function of U_0/u_0 and z_m/h_s for $Fr = 4.0$. Symbols are given in Table 4.4.

(see Equation 4.23) and can be used to determine when it is important to model the boundary layer velocity profile and when the algebraic Briggs equation can be applied.

The results show that plumes that are released from relatively low heights (small h_s/z_m of h_s/z_f) within a power-law velocity profile experience greater vertical variation in wind speed as they rise through the boundary layer, due to the increased velocity gradient near the surface. The boundary layer can also be important for plumes with initially steep trajectories (large z_m or z_f). Investigation of a number of full scale industrial and wildfire plumes indicates that, in general, industrial plumes are largely unaffected by vertical variations in wind speed except for under very low wind conditions. However, wildfire plumes are significantly more buoyant than industrial plumes and have steeper trajectories that are strongly influenced by the boundary layer velocity profile.

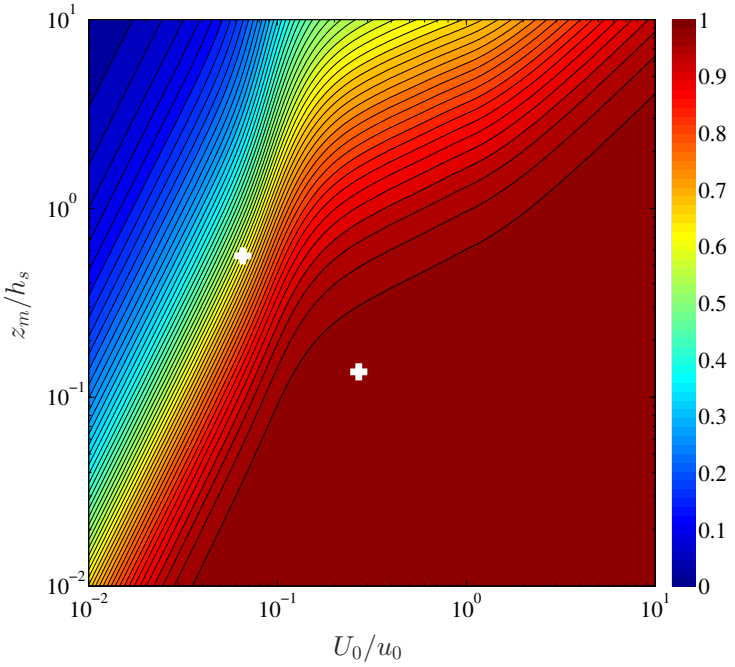

Figure 4.13: Contour plot of $\chi = z_{45.p}/z_{45.u}$ as a function of U_0/u_0 and z_m/h_s for $Fr = 6.0$. Symbols are given in Table 4.4.

Bibliography

Abraham, G. (1963). *Jet diffusion in stagnant ambient fluid.* PhD thesis, TU Delft, Delft University of Technology.

ASCE (1999). *Wind tunnel studies of buildings and structures.* American Society of Civil Engineers, Reston, VA, U.S.A.

Baum, H. and McCaffrey, B. (1989). Fire induced flow field: theory and experiment. In *Fire Safety Science: Proceedings of the Second International Symposium*, pages 129–148. Hemisphere Publishing Newport, Australia.

Bennett, M., Sutton, S., and Gardiner, D. (1992). An analysis of lidar measurements of buoyant plume rise and dispersion at five power stations. *Atmospheric Environment. Part A. General Topics*, 26(18):3249–3263.

Bhutia, S., Jenkins, M. A., and Sun, R. (2010). Comparison of firebrand propagation prediction

by a plume model and a coupled-fire/atmosphere large-eddy simulator. *Journal of Advances in Modeling Earth Systems*, 2:4. PT: J; TC: 0; UT: WOS:000208299500004.

Briggs, G. (1975a). A comparison of the trajectories of rising buoyant plumes with theoretical empirical models. *Atmospheric Environment (1967)*, 9(4):455–457.

Briggs, G. A. (1965). A plume rise model compared with observations. *Journal of the Air Pollution Control Association*, 15.

Briggs, G. A. (1968). Concawe meeting: Discussion of the comparative consequences of different plume rise formulas. *Atmospheric Environment (1967)*, 2(3):228–232.

Briggs, G. A. (1975b). Plume rise predictions, lectures on air pollution and environment impact analysis. *Am. Meteorol. Soc., Boston, USA*, 10.

Briggs, G. A. (1984). Plume rise and buoyancy effects. *Atmospheric Science and Power Production*, pages 327–366.

Carson, J. E. and Moses, H. (1969). The Validity of Several Plume Rise Formulas. *Journal of the Air Pollution Control Association*, 19(11):862–866.

Contini, D., Cesari, D., Donateo, A., and Robins, A. (2009). Effects of Reynolds number on stack plume trajectories simulated with small scale models in a wind tunnel. *Journal of Wind Engineering and Industrial Aerodynamics*.

Contini, D., Donateo, A., Cesari, D., and Robins, A. G. (2011). Comparison of plume rise models against water tank experimental data for neutral and stable crossflows. *Journal of Wind Engineering and Industrial Aerodynamics*, 99(5):539–553.

Contini, D. and Robins, A. (2001). Water tank measurements of buoyant plume rise and structure in neutral crossflows. *Atmospheric Environment*.

Cook, N. J. (1997). The deaves and harris abl model applied to heterogeneous terrain. *Journal of Wind Engineering and Industrial Aerodynamics*, 66(3):197–214.

Davenport, A. G. (1960). Rationale for determining design wind velocities. Technical report, DTIC Document.

Davidson, G. (1986). Gaussian versus top-hat profile assumptions in integral plume models. *Atmospheric Environment (1967)*, 20(3):471–478.

Davidson, G. (1989). Simultaneous trajectory and dilution predictions from a simple integral plume model. *Atmospheric Environment*, 23(2):341–349.

Fischer, H. B., List, J. E., Koh, C. R., Imberger, J., and Brooks, N. H. (2013). *Mixing in inland and coastal waters*. Elsevier.

Fisher, B. E. A., Metcalfe, E., Vince, I., and Yates, A. (2001). Modelling plume rise and dispersion from pool fires. *Atmospheric Environment*, 35(12):2101–2110.

Fric, T. and Roshko, A. (1994). Vortical structure in the wake of a transverse jet. *Journal of Fluid Mechanics*, 279:1–47.

Frick, W. E. (1984). Non-empirical closure of the plume equations. *Atmospheric Environment*, 18(4):653–662.

Hellmann, G. (1917). *Über die Bewegung der Luft in den untersten Schichten der Atmosphäre*. Königlich Preussischen Akademie der Wissenschaften.

Hoult, D. P., Fay, J. A., and Forney, L. J. (1969). A theory of plume rise compared with field observations. *Journal of the Air Pollution Control Association*, 19(8):585–590.

Hoult, D. P. and Weil, J. C. (1972). Turbulent plume in a laminar cross flow. *Atmospheric Environment (1967)*, 6(8):513–531.

Hübner, J. (2004). *Buoyant plumes in a turbulent environment*. PhD thesis, University of Cambridge.

Hunt, G. R. and Kaye, N. B. (2005). Lazy plumes. *Journal of Fluid Mechanics*, 533:329–338.

Kaye, N. B. (2008). Turbulent plumes in stratified environments: A review of recent work. *Atmosphere-Ocean*, 46(4):433–441.

Kaye, N. B. and Hunt, G. R. (2009). An experimental study of large area source turbulent plumes. *International Journal of Heat and Fluid Flow*, 30(6):1099–105.

Lee, J. H.-w. and Chu, V. (2003). *Turbulent jets and plumes: a Lagrangian approach*. Springer Science & Business Media.

Li, Q., Zhi, L., and Hu, F. (2010). Boundary layer wind structure from observations on a 325m tower. *Journal of wind engineering and industrial aerodynamics*, 98(12):818–832.

Linden, P. F. and Kaye, N. B. (2006). Interacting turbulent plumes in a naturally ventilated enclosure. *Int. J. of Vent.*, 4(4):301–310.

Marro, M., Salizzoni, P., Cierco, F., Korsakissok, I., Danzi, E., and Soulhac, L. (2014). Plume rise and spread in buoyant releases from elevated sources in the lower atmosphere. *Environmental Fluid Mechanics*, 14(1):201–219.

Mercer, G. and Weber, R. (1994). Plumes above line fires in a cross-wind. *International Journal of Wildland Fire*, 4(4):201–207.

Morton, B. and Middleton, J. (1973). Scale diagrams for forced plumes. *Journal of Fluid Mechanics*, 58(01):165–176.

Morton, B., Taylor, G., and Turner, J. (1956). Turbulent gravitational convection from maintained and instantaneous sources. 234(1196):1–23.

Morton, B. R. (1965). Modeling fire plumes. *Symposium (International) on Combustion*, 10(1):973–982.

Ooms, G. and Mahieu, A. (1981). A comparison between a plume path model and a virtual point source model for a stack plume. *Applied Scientific Research*, 36(5-6):339–356.

Priestly, C. H. B. and Ball, F. K. (1955). Continuous convection from an isolated source of heat. 81:144–157.

Sardoy, N., Consalvi, J.-L., Porterie, B., and Fernandez-Pello, A. (2007). Modeling transport and combustion of firebrands from burning trees. *Combustion and Flame*, 150(3):151–169.

Scase, M. M., Caulfield, C. P., Dalziel, S. B., and Hunt, J. C. R. (2006). Time-dependent plumes and jets with decreasing source strengths. 563:443–461.

Smith, S. H. and Mungal, M. G. (1998). Mixing, structure and scaling of the jet in crossflow. *J. Fluid Mech.*, 357:83–122.

Thurston, W., Fawcett, R. J., Tory, K. J., and Kepert, J. D. (2015). Simulating boundary-layer rolls with a numerical weather prediction model. *Quarterly Journal of the Royal Meteorological Society*.

Tieleman, H. W. (2008). Strong wind observations in the atmospheric surface layer. *Journal of Wind Engineering and Industrial Aerodynamics*, 96(1):41–77.

Turner, J. S. (1973). *Buoyancy effects in fluids*. CUP.

Wang, H. and Law, A. W.-K. (2002). Second-order integral model for a round turbulent buoyant jet. 459:397–428.

Weil, J. (1988). Plume rise. *Lectures on air pollution modeling*, pages 119–166.

Zonato, C., Vidili, A., Pastorino, R., and De Faveri, D. (1993). Plume rise of smoke coming from free burning fires. *Journal of Hazardous Materials*, 34(1):69–79.

Chapter 5

Wind tunnel experiments

5.1 Introduction

Firebrand showers are not only a perilous phenomenon in wildfires but also in urban fires or any large conflagration. As mentioned before, there is a growing body of evidence that firebrand showers are responsible for fire spread. Observations range from great fires of London (1666) [Bell, 1971] post-earthquake conflagrations of San Francisco (1906), Tokyo (1923) [Koo et al., 2010], and recently wildfires of Australia and Greece [Mell et al., 2010] to many other cases; See Koo et al. [2010]. Spot fires generated by firebrand showers are highly stochastic, and as the intensity and size of fire grows they become more severe [Albini, 1979]. This necessitates understanding of firebrand flight behavior as they pose a major threat to people, properties, and infrastructure particularly in wild-land urban interfaces (WUI).

Firebrand lofting and transport plays a significant role in the fire spotting phenomenon and many studies have been done on transport of debris and firebrands in various velocity fields. For instance, Tarifa et al. [1965, 1967] studied combustion and transport properties of firebrands along with the influence of size, shape, density, and moisture content on these processes in a small scale wind tunnel for a very simplified model of firebrands with no rotational effects. Aerodynamic behavior, and trajectories of spherical firebrand models are discussed by Lee and Hellman [1969, 1970]. Also, Tse and Fernandez-Pello [1998]; Himoto and Tanaka [2005]; Anthenien et al. [2006]; Sardoy et al. [2006, 2008], and Bhutia et al. [2010b] have modeled fate and transport of different

types of firebrands, numerically. In addition, Himoto and Tanaka [2008] developed and validated an urban fire spread model that, instead of modeling firebrand lofting and transport, uses a probabilistic approach. Further, the firebrand/debris flight models posses simplifying assumptions that raise concerns about the applicability of such models in real life events, see chapter 3. Above all, there is little [Lin et al., 2007; Richards et al., 2008; Richards, 2010] to almost no experimental work done on the rod-like firebrand transport, and the majority of the numerical models suffer from a lack of thorough experimental validation. This chapter fills this gap by presenting results of a comprehensive set of large scale wind tunnel experiments for lofting and transport of non-combusting rod-like firebrand models through the scaled-down model wildfire velocity field.

The experimental results are useful for rigorous validation of firebrand flight models. Also, the results have applications beyond firebrand flight as they provide a broad experimental analysis for transport of rod-like debris, with different aspect ratios, in a turbulent boundary layer. The remaining parts of this chapter are as follows: the experimental setup is discussed in next section 5.2. In section 5.3 the data acquisition technique is presented and in section 5.4 the results of the lofting and downwind transport of firebrand models are presented. Concluding remarks are drawn in section 5.5.

5.2 Experimental setup

5.2.1 Scaling discussion

In fluid dynamics, measurements are often performed on models, under controlled conditions, that either share the same target characteristics with the actual system or have similitudes with the phenomenon. The concept of similarity permits extension of information in experimental models to the actual phenomena or systems. The essential requirement for the complete similarity is that the geometric, kinematic, and dynamic similarity between the model and the phenomenon must hold true. However, this is not the case in modeling lofting and transport of firebrands through the velocity field of wildfires. In fact, since very little is known about firebrands generated through a real wildfire, and laboratory studies exhibit a very wide range of sizes and shapes [Manzello et al., 2006, 2007, 2008, 2009; Tohidi et al., 2015], geometric similarity would require an unfeasible amount of experiments. Dynamic similarity is also not possible in wind tunnels as pool fires need to be

created (not possible in our wooden wind tunnel) and then the wind speed scaled to match both the Froude number and plume to wind velocity ratio. For very small laboratory fires this would lead to very low wind speeds which would lead to a boundary layer that was not in the fully rough turbulent regime.

Therefore, it is not possible to run wind tunnel experiments in which geometric and dynamic similarity are satisfied. Instead, a series of wind tunnel tests, were run in which model firebrands are lofted into the wind tunnel boundary layer using a vertical air jet. The stream wise firebrand trajectory is then measured. The goal of the experiments is to develop an experimental data set that can be used to validate modeling schemes that can then be applied to full scale fires.

5.2.2 Setup

Boundary layer wind tunnel experiments of fire spotting were run using non-combusting polyurethane model firebrands with density $\varrho = 30\, kg/m^3$, side aspect ratio $\eta_s = L_x/L_y = 1$, and different longitudinal aspect rations, i.e. $\eta = L_z/L_{x,y}$, as shown in figure 5.1. Here, L_z denotes the major side and L_x & L_y show the minor sides. The dimension of all sides in the $\eta = 1$ model firebrand is $L_x = L_y = L_z = 1\, cm$ and for other aspect ratios $L_x = L_y = 0.5\, cm$.

The tests were conducted in Clemson University's wind tunnel testing facility which is classified as a low-speed boundary layer wind tunnel, as the maximum achievable velocity is less than $100\, m/s$ [Tavoularis, 2005]. Hence, the compressibility effects are negligible or very small in the experiments. The test section is comprised of a $3.05\, m$ wide by $2.03\, m$ high open boundary layer with $20\, m$ of fetch. The wind flow is generated by two $1.8\, m$ diameter fans which are controlled by adjustable frequency inverters. The flow is passed through a honeycomb grid, a set of screens and a contraction to produce low intensity uniform inflow. In order for the boundary layer to be turbulent, a combination of a spire board and surface roughness elements were used; see figure 5.2-left. The spire board consists of 6 triangles with $92.16\, cm$ height and $25.4\, cm$ base that were evenly spread across the $3.05\, m$ width of the wind tunnel immediately downwind of the contraction. The surface roughness elements are made from randomly allocated rectangular prisms of length $3.2\, cm$ and thickness of $1.6\, cm$ that are stuck to boards with glue. The surface roughness boards covered over $11\, m$ of the upstream section to generate a grass (open flat) terrain exposure [Cermak and

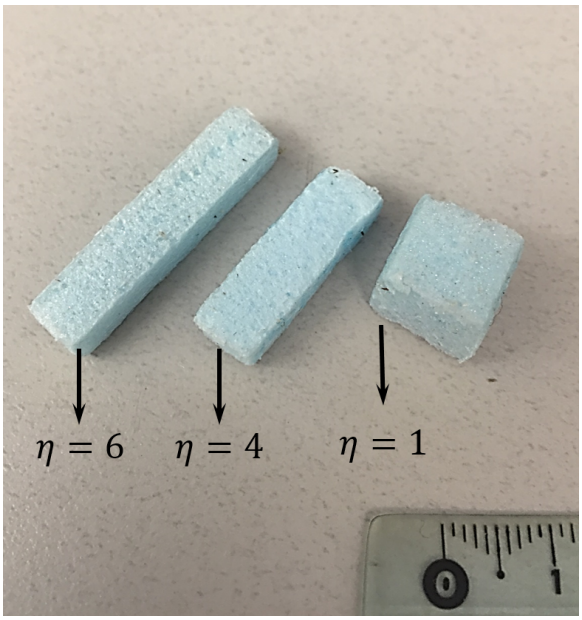

Figure 5.1: Polyurethane firebrand models; Scale shown is 1 cm in the image.

Isyumov, 1998]. For more details on the specifics of the wind tunnel see Liu et al. [2009].

The velocity field of the fire plume was modeled using an air jet installed in the floor of the wind tunnel; see figure 5.3. The 15.2 cm diameter jet was created using two 4 hp blowers that were fed into a 58.8 cm flow straightener. The jet centerline exit velocity could be adjusted between $0 - 12\, m/s$.

Experiments were run for combinations of three boundary layer reference velocities and three jet centerline velocities, in order to model the velocity field induced by the interaction of the fire plume and the boundary layer. The generated velocity fields are measured using an $Extech - 407112$ heavy duty hot-wire thermo-anemometer which has $\pm 0.1\, m/s$ resolution in the range of $0.2 - 20\, m/s$. As for of the boundary layer, the velocity measurements are conducted at the centerline of the wind tunnel test section, exactly 25 cm upstream of the jet centerline when the jet was turned off. Similarly, centerline and radial velocity profiles of the jet was measured with no wind. The cross-sectional velocities are measured at $0.138\, m$ from the jet nozzle exit where it is flushed with the wind tunnel's floor. Specific parameter combinations tested in the experiments are set out in table 5.1.

In the boundary layer the reference height is considered to be $z_0 = 0.04\, m$ to fit a the power-

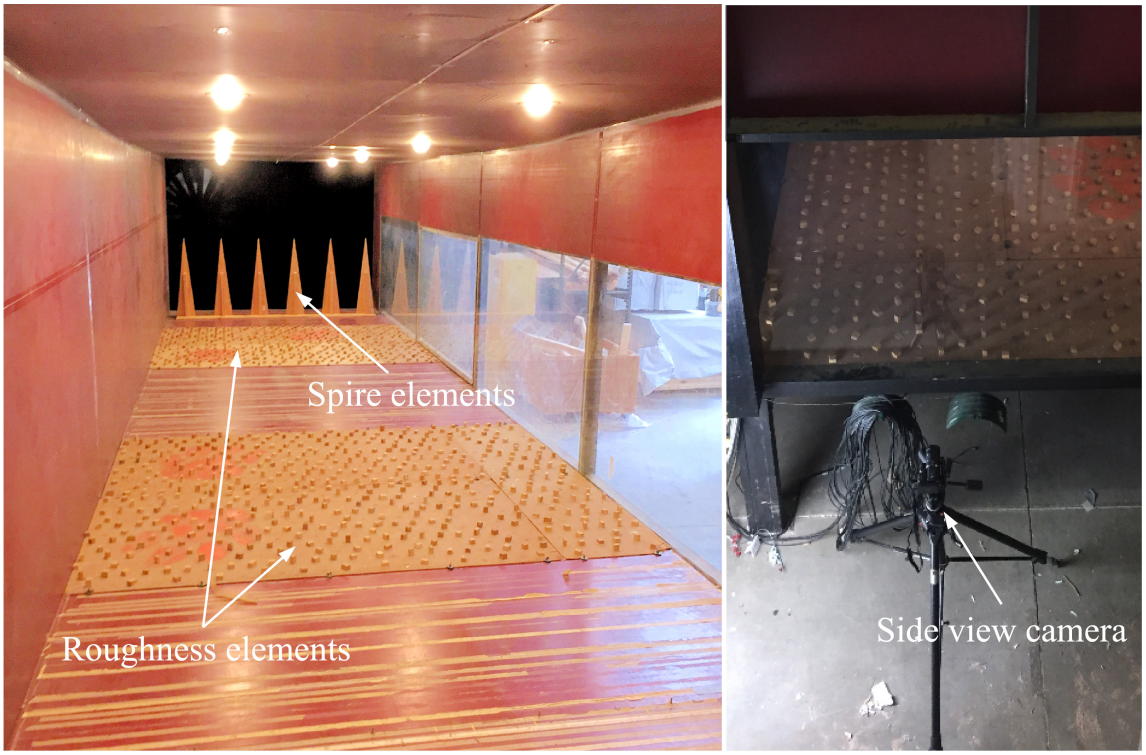

Figure 5.2: (Left) Inside the wind tunnel chamber where the surface roughness elements and spire elements are installed. Also, on the right, the camera position at the side view of the release point (jet location) is shown.

Table 5.1: Specifics of the lofting and transport experiments. Where wind setup is the wind tunnel dial that delivers U_0 at the reference height of $z_0 = 0.04\,m$, jet setup denotes dials on blowers that were connected to different regions (I, O) inside the jet nozzle and deliver the jet centerline velocity $U_{j|r=0}$, $\eta = L_z/Lx, y$ is the planks (model firebrands) aspect ratio, and D.O.F. stands for the degrees of freedom (nominal number of releases).

Wind setup	$U_0\ (m/s)$	Jet setup	$U_{j\|r=0}\ (m/s)$	η	D.O.F.
W-0.5	1.79	I10-O5	12	1, 4, 6	200
		I5-O5	8.05	1, 4, 6	200
		I5-O3	9	1, 4, 6	200
W-1.0	2.23	I10-O5	12	1, 4, 6	200
		I5-O5	8.05	1, 4, 6	200
		I5-O3	9	1, 4, 6	200
W-2.0	2.85	I10-O5	12	1, 4, 6	200
		I5-O5	8.05	1, 4, 6	200
		I5-O3	9	1, 4, 6	200

law profile. Sixty second time averages of vertical profiles of the boundary layer horizontal velocity component are shown in figure 5.4 along with their corresponding power-law fit. Also, sixty second

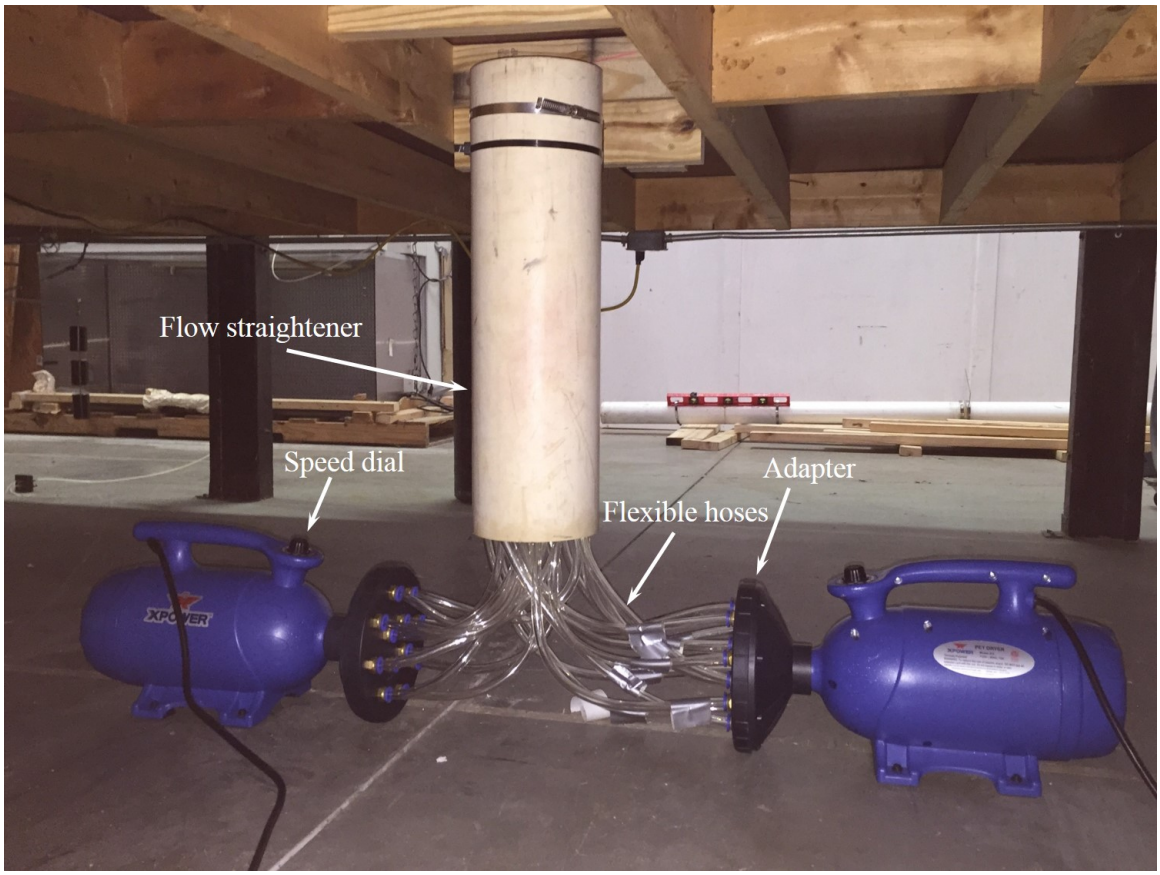

Figure 5.3: Details of the mounted air jet underneath of the wind tunnel. Also, shown are blowers, and the flow straightener.

time averages of vertical velocity profiles at the centerline of the jet nozzle along with the jet cross section velocity profiles are shown in figure 5.5 for three different outlet velocity configurations. It should be noted that associated uncertainties with the velocity measurements are not presented in graphs, as they are, at most, less than 3.33% and 1.25% for the boundary layer and jet, respectively.

As can be seen on figure 5.5-left, the normalized time-averaged vertical (stream-wise) velocity profile of the jets are similar and approximately collapse onto a single curve. The time-averaged radial variation in vertical velocity is less consistent due to the different inlet conditions and are shown in figure 5.5-right. The measurements are in good agreement with the classical data of the round jets Albertson et al. [1950]. Therefore, it is possible to use the integral model of round jets to obtain the source condition parameters. This can be done using the following equation for the

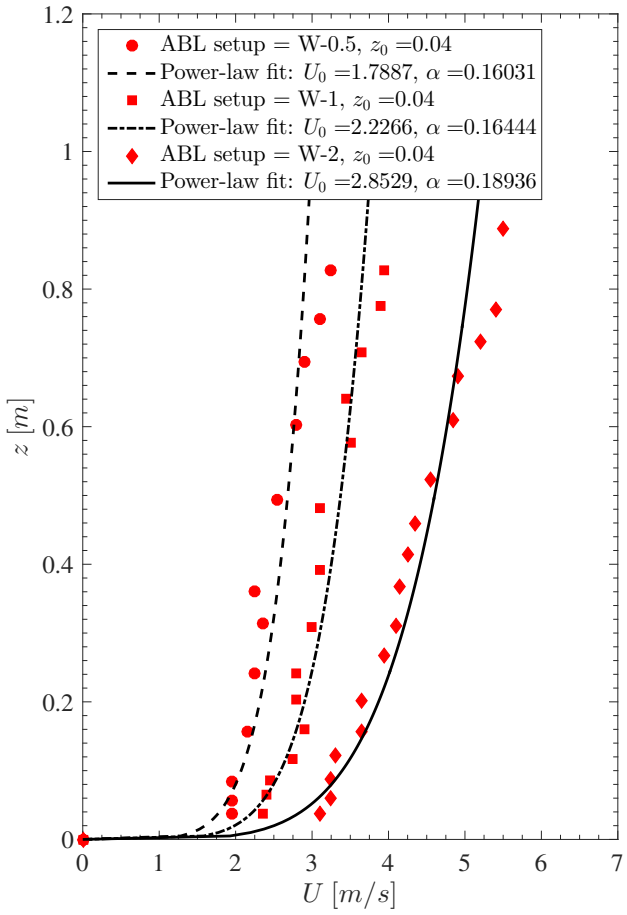

Figure 5.4: Shown are vertical profiles of the boundary layer horizontal (stream-wise) velocity component measured in the wind tunnel. Also, U_0 is the horizontal velocity of the corresponding power-law fits at reference height $z_0 = 0.04\,m$.

stream wise velocity of the jet [Lee and Chu, 2003].

$$\left\langle U_{j|r=0} \right\rangle = 7 M_0^{1/2} z^{-1}, \tag{5.1}$$

where M_0 is the initial momentum flux at the source, and z is the vertical distance from the jet virtual origin. Based on equation 5.1, the time-averaged vertical velocity is proportional to the inverse of distance from virtual origin (z). This is shown by the log-log plots of the experimental measurements and their corresponding Large Eddy Simulations (LES) in the quiescent ambient, see figure 5.6. Procedure of the simulations, that are done with `OpenFOAM`, are described in the next

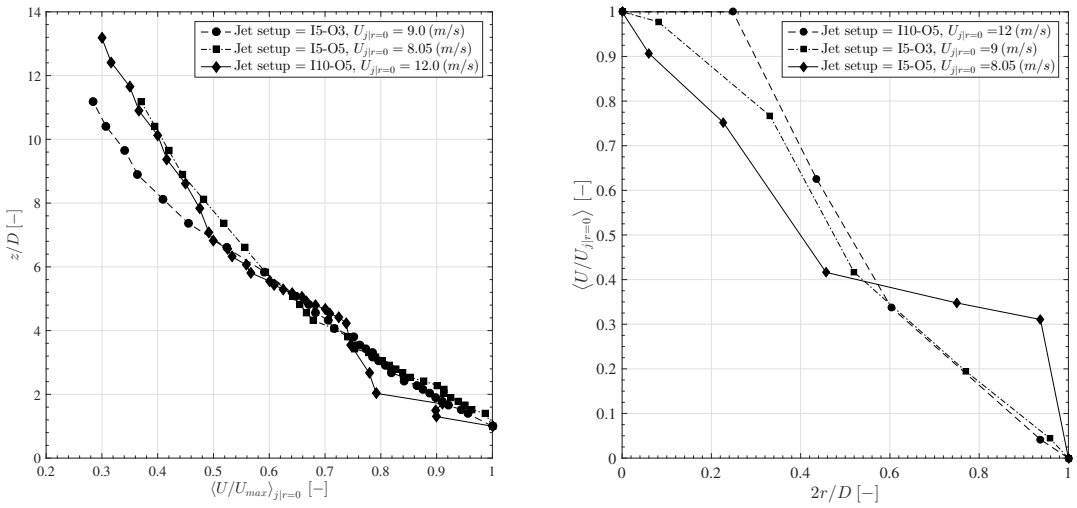

Figure 5.5: On the left are the time averaged vertical velocities of the jet at the centerline $r = 0$ where r is the radial distance from the jet center; And shown on the right are cross section vertical velocities which are measured at $z = 0.138\,m$ from the nozzle exit.

chapter.

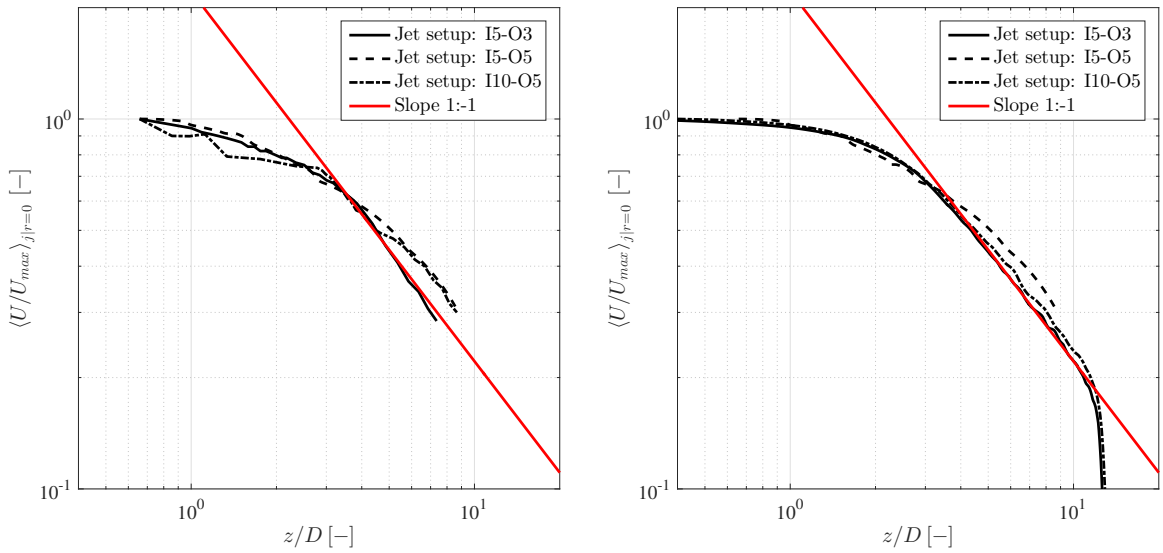

Figure 5.6: On the left are the time averaged vertical velocities of the jet at the centerline $r = 0$ where r is the radial distance from the jet center; And shown on the right are cross section vertical velocities which are measured at $z = 0.138\,m$ from the nozzle exit.

The experimental and numerical results in figure 5.6 clearly demonstrate the length of the potential core is much smaller that 6.2 times of the diameter of the jet. This is because of the

jet structure in which the generated air flow by the blowers passes through multiple flexible hoses and, then goes to a flow straightener with honeycomb mesh. Hence, the turbulence is developed in three diameters downstream which is much smaller than the $6.2D$ distance downstream that is mentioned in the literature, for instance [Fischer et al., 1979; Lee and Chu, 2003]. Also, the predicted variation of the velocity with z in equation 5.1 is well-confirmed. It should be mentioned that at very far downstream the jet impinges on the ceiling of the wind tunnel and doesn't follow the theory.

Assuming radial symmetry, linear growth for the jet width, and Gaussian velocity distribution for the jet, M_0 can be obtained from applying equation 5.1 to the experimental data. Then, given that the jet volume flux $Q_z = 0.286 M_0^{1/2}(z_v + z)$ where z_v is the virtual origin [Lee and Chu, 2003], the measured volume fluxes of the jet under different settings in table 5.1 are calculated. Table 5.2 shows the obtained values for the source condition parameters.

Table 5.2: Calculated source parameters of the jet under different settings.

Jet setup	M_0 (m^4/s^2)	z_v/D
I5-O3	0.1853	1.92
I5-O5	0.2145	1.90
I10-O5	0.3936	1.75

Different combinations of the wind tunnel boundary layer with the jet, simulate velocity fields that are analogous to the interaction of a fire plume with the atmospheric boundary layer. This is the first time the lofting and transport process of firebrands has been experimentally modeled by releasing different aspect ratios of rod-like polyurethane model firebrands within roughly the centerline of the jet exit. For each combination of the boundary layer and the jet velocity, each aspect ratio is released approximately 200 times, to provide enough samples (degrees of freedom) for statistical analysis. The entire process of lofting and downwind transport of individual model firebrands are recorded with a side view camera. Technical details of the camera are given in chapter 3.

5.3 Data acquisition method

The lofting and downwind transport of the model firebrands is recorded from the side with a camera set to be perpendicular to the centerline of the wind tunnel's test section. A similar image

processing algorithm to that described in chapter 3 is used for analyzing the recorded videos. As a result, full 2D trajectories along with the maximum rise height and downwind distance of the model firebrands are captured. The procedure for the experiments and the data acquisition technique are discussed below.

5.3.1 Procedure:

1- Calibration: In order to reach a quasi-steady state, the wind tunnel and the jet were run for $2-3$ minutes, while the camera was being installed on the side view of the test section. Then, for each set and before releasing the model firebrands into the velocity field, a calibration video was taken in which a designated scale was fixed directly over the jet exit into the wind tunnel chamber. The scale is used to calculate the picture ratio of the images and further calibrate (convert) pixels to units of length. Picture ratio is the fraction of known distances between designated black dots on the scale, here in millimeters, to the corresponding number of pixels between them [Gonzalez, 2009]. Figure 5.7 shows a sample image that is extracted from a calibration video.

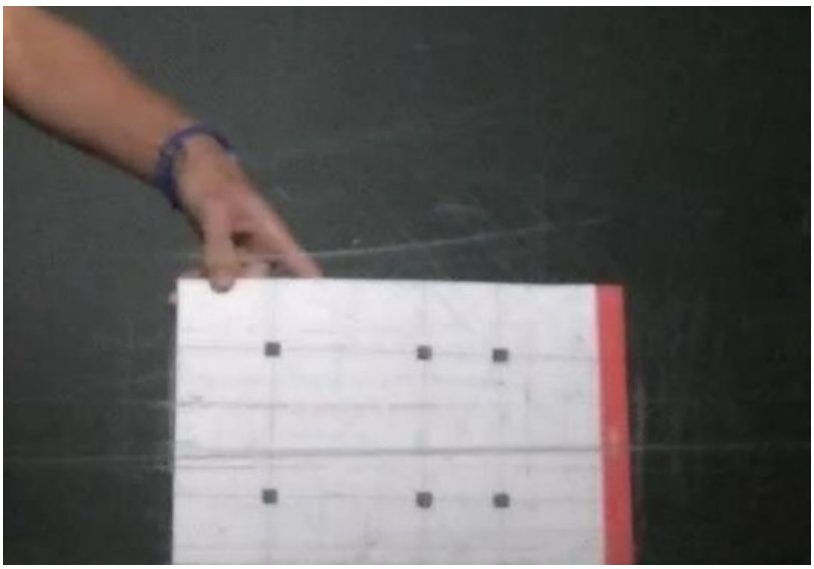

Figure 5.7: An extracted calibration image that shows the utilized scale. There are four points on the scale that build a square with sides of $100mm$, and the other two are used to check the calculated picture ratio.

2- Data collection: After the calibration operation the scene was emptied and the main

videos were recorded. Per set, model firebrands were released at least 10 s after the camera was turned on. Since the recording was being done with 60 fps, that provided more than enough frames to construct the background image. The firebrand models were, then, released from approximately the center of the jet with tweezers such that the flow field was disturbed as little as possible. During the release operation, the initial angles of each model firebrand are varied randomly. Each set of the experiments took between $8 - 11$ minutes to record the lofting and downwind transport of 200 samples.

5.3.2 Image processing

The videos collected were analyzed using a similar image processing algorithm that starts with extracting all frames in the videos and constructing a background image. The extracted frames are stored as images on an external hard disk due to the high volume of the generated data. Then, using MATLAB, images are read and converted from RGB format to double. This provides more accuracy and flexibility in image analysis. The background image is constructed by averaging over light intensities of at least 100 empty images. On figure 5.8-left a sample background image is shown versus a normal frame taken from the emptied scene of the test section.

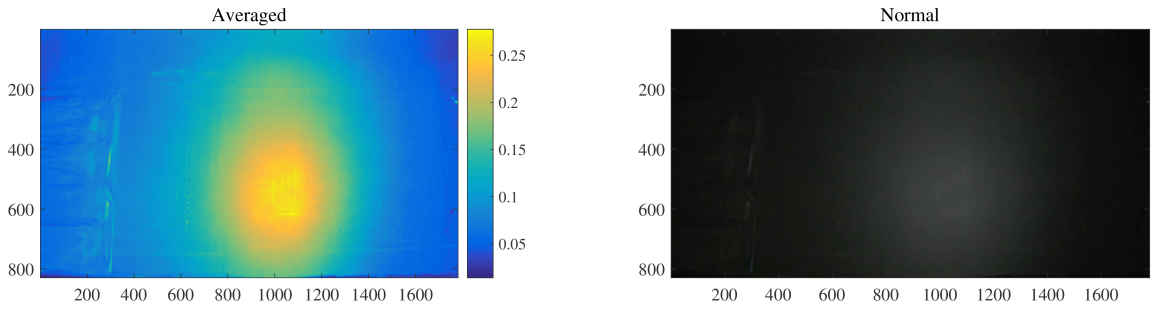

Figure 5.8: (Left) Color coded background image, with light intensities, constructed by averaging over at least 100 empty frames. (Right) an original (unprocessed) empty frame from the test section while the velocity field is running.

The background image is subtracted from all frames. This detects the presence of model firebrands in the domain. Yet, the obtained image is not practically useful for calculating its position inside the frame. This is due to the general motion of the firebrands during which they are both translating and rotating. Rotation causes firebrand models to emit various range of light intensities such that it is hard to identify all of them by just a global thresholding method at this stage; see

[Gonzalez et al., 2004]. In order to resolve this issue, background subtracted frames are convolved with a rotationally symmetric low-pass *Gaussian* filter with a square height matrix of 45 pixels and standard deviation of $\sigma_g = 5$ as shown in figure 5.9. Convolution of the *Gaussian* filter reduces the noise in image and prepares it for intensity mapping. A sample of the smoothed image is shown on figure 5.10-(top-right).

Obtained intensities are, then, mapped to the range of $0-1$ such that a global thresholding method

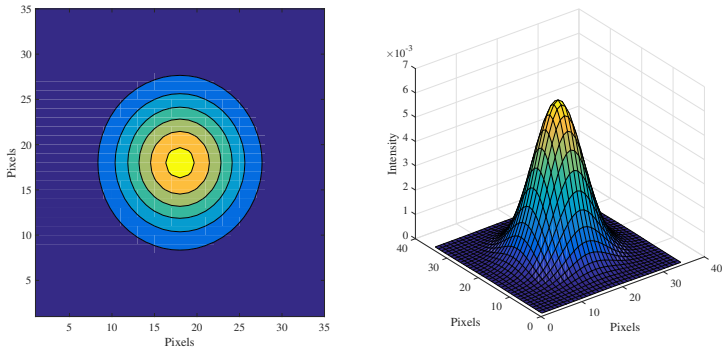

Figure 5.9: The utilized rotationally symmetric low-pass *Gaussian* filter that is used for noise reduction. The given height is color coded with the intensity range before noise reduction.

can be applied. This operation isolates the pixels that firebrand models occupy in the image; see figure 5.10-(bottom-left). Ultimately, in order to calculate the coordinates of the centroid of the firebrand model the intensity stretched image is morphed with the cylindrical (in cases with $\eta = 4$ *or* 6) and square (in cases with $\eta = 1$) structuring elements. This process is repeated over all extracted images and results in 2D trajectories of the model firebrands during lofting and downwind transport; see figure 5.10-(bottom-right). The resulting trajectories from applying this algorithm on a sample video are shown in Figure 5.11.

Two recurring problems were observed among the obtained trajectories. First, some of the trajectories do not include the exact landing location. This is primarily due to the low light intensity near the floor which makes the algorithm susceptible to miss the objects as they pass through the camera frame. This issue is resolved by the extrapolation of the trajectories to the elevation of $z = 0$. The extrapolation is conducted by converting the units from millimeter to meter such that the remaining distance to the ground, i.e. extrapolation domain, is normalized between 0-1. This reduces the extrapolation error, since the last three points on the trajectory are chosen as the

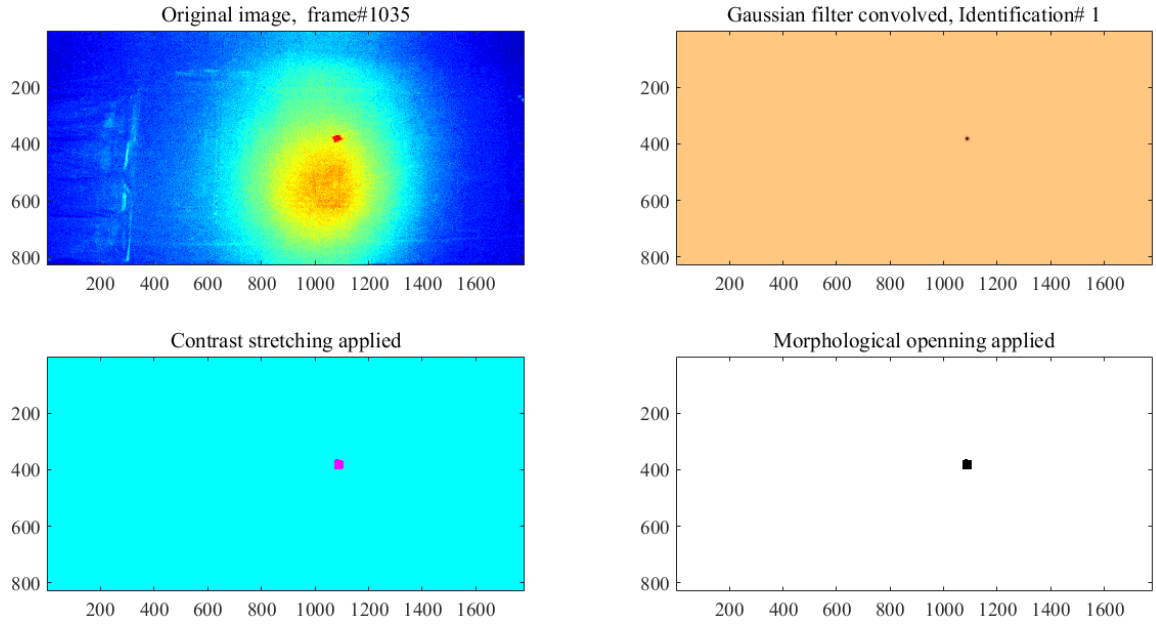

Figure 5.10: (Top-left) Untouched image from a model firebrand model during its flight through the velocity field. (Top-right) Shown is the result of background subtraction and the *Guassian* filter convolution on the original image. The image with mapped intensity along with the morphologically opened image are shown at the bottom-left and bottom right, respectively. The dot in the middle is a model firebrand with $\eta = 1$ that is identified in frame 1035 of the video, that is 17 s after the release operation has started.

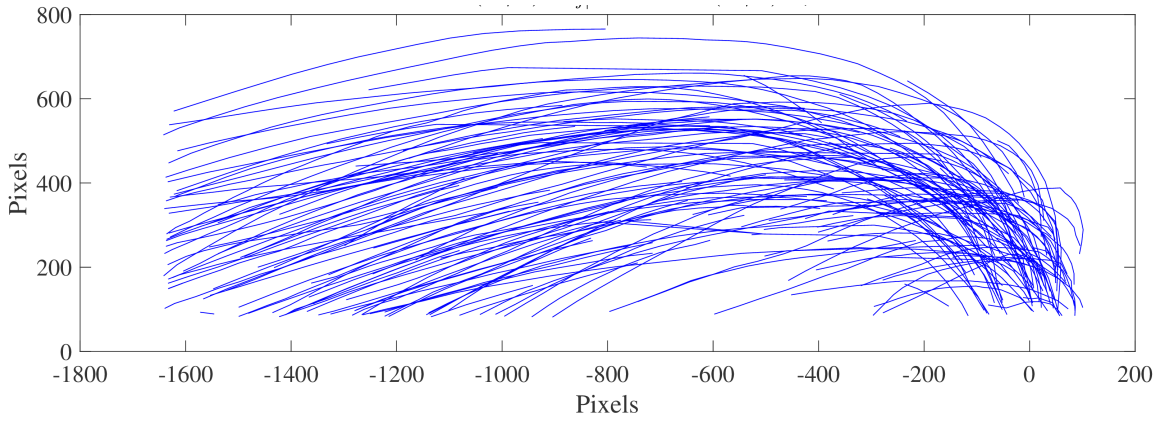

Figure 5.11: Calculated trajectories of the model firebrands with aspect ratio $\eta = 1$ in an experimental case where the boundary layer reference velocity was $U_0 = 2.23\, m/s$, and the jet centerline velocity at the exit was $8.05\, m/s$.

training set for finding the corresponding point (landing location) on the ground. The same method is applied to upstream part of the trajectory where the model firebrands lift off through the jet.

Second, these were incomplete or partially identified trajectories. This is caused by either the model firebrands leaving the frame of analysis due to high lofting velocity or low intensity of light during the flight. The later issue is resolved by the special data storage technique that is used in the algorithm. This method assigns a tag to each detected object and saves that with the coordinates of the position. In this way if a trajectory is partially recognized (say if the model firebrand is lofted out of the frame) the subsequent parts can be combined together. The former issue is solved by using characteristics of the completed trajectories. As it is evident in figure 5.12 , full trajectories have a special pattern if one calculates the adjacent difference in the rise height at each point, namely $\Delta y = y_i - y_{i-1}$. Basically, if the resulting vector (for each model firebrand trajectory) is drawn against the order by which the location coordinates is recognized (i.e. i), the pattern has three distinct parts. The first part where Δy is decreasing can be associated with the lofting part, the section with effectively zero slope can be attributed to the lofting to downwind transport transition, and finally as Δy decreases again the landing part has been started. Also, almost all of the complete trajectories have more than 10 identified location coordinates in their trajectory vectors. Incomplete and partial trajectories do not follow such patterns or simply don't have enough location points. Also, trajectories in which more than 5% of the identified points are off this pattern are assigned as incomplete; And later if there is no partial or incomplete path found for them that has the subsequent tag they are eliminated from the calculations.

Comprehensive results of the image analysis on the experiments along with statistical analysis on the maximum lofting height and downwind distance are presented in the next section.

5.4 Results

The captured trajectories by the discussed image processing technique are presented in figures 5.13-5.15. Generally, the results corroborate the physical expectations, namely, by increasing the boundary layer reference velocity (U_0) for a given jet exit velocity ($U_{j|r=0}$) and aspect ratio (η), model firebrands tend to have lower rise and land further downwind. Also, it should be mentioned that some of the model firebrands are missed during the image processing procedure. Therefore, the reported DOFs are not equal to the nominal value of 200.

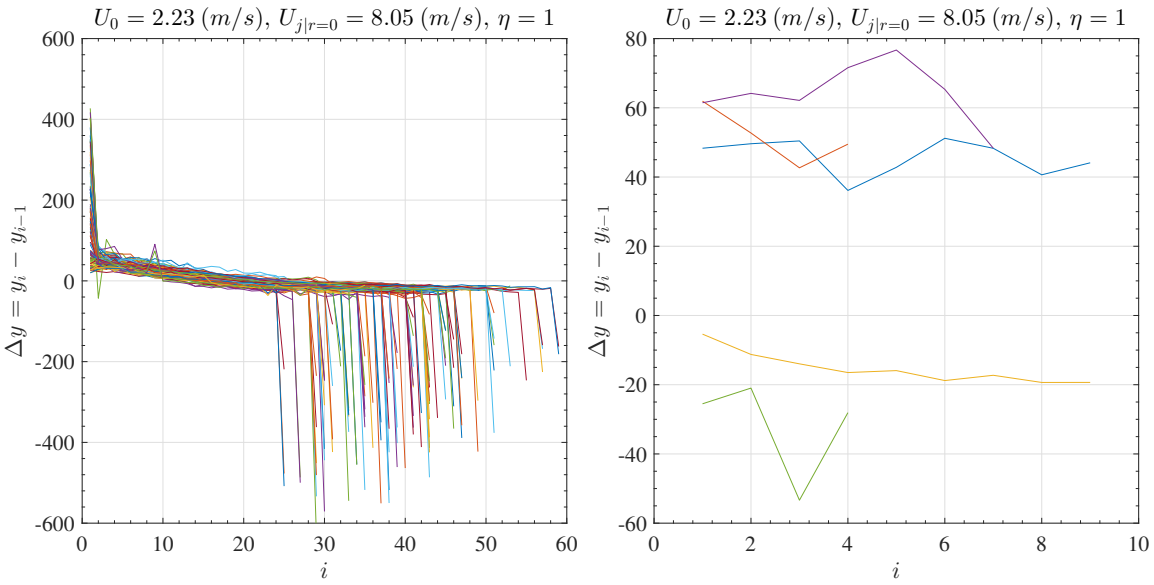

Figure 5.12: The identified pattern in complete trajectories by calculating adjacent differencing of the rise height (left). On the right shown are samples of the incomplete or partially complete trajectories that do not follow the same pattern as the completed ones.

Various data can be extracted from captured trajectories. This includes the maximum rise height (z_{max}), the maximum downwind distance (x_l), and the downwind distance normalized with the maximum rise height (x_l/z_{max}). Since the velocity field of a fire plume is modeled as a jet, the dominant length scale for the jet in a non-uniform boundary layer cross flow is the jet momentum length z_m; see chapter 4 or [Tohidi and Kaye, 2016]. The momentum length represents the vertical distance at which a pure point source jet will have a mean vertical velocity equal to the mean horizontal velocity of the boundary layer [Tohidi and Kaye, 2016]. In wind tunnel experiments, this length scale can be easily obtained by finding the height of the intersection point between the vertical (stream-wise) velocity profile of the jet at its centerline and the horizontal velocity of the boundary layer. However, in case of a real fire plume, since the buoyancy flux is dominant the buoyancy length, z_f, is the main characteristic length [Tohidi and Kaye, 2016]. The buoyancy length is the distance from source at which a pure point source plume will have a mean vertical velocity equal to the mean horizontal velocity of the cross-flow boundary layer; For details on calculating z_m and z_f; see chapter 4 or Tohidi and Kaye [2016].

Given that z_m is the dominant length scale of the jet in non-uniform boundary layer cross-flow, the maximum rise height and the maximum downwind distance are normalized with the jet

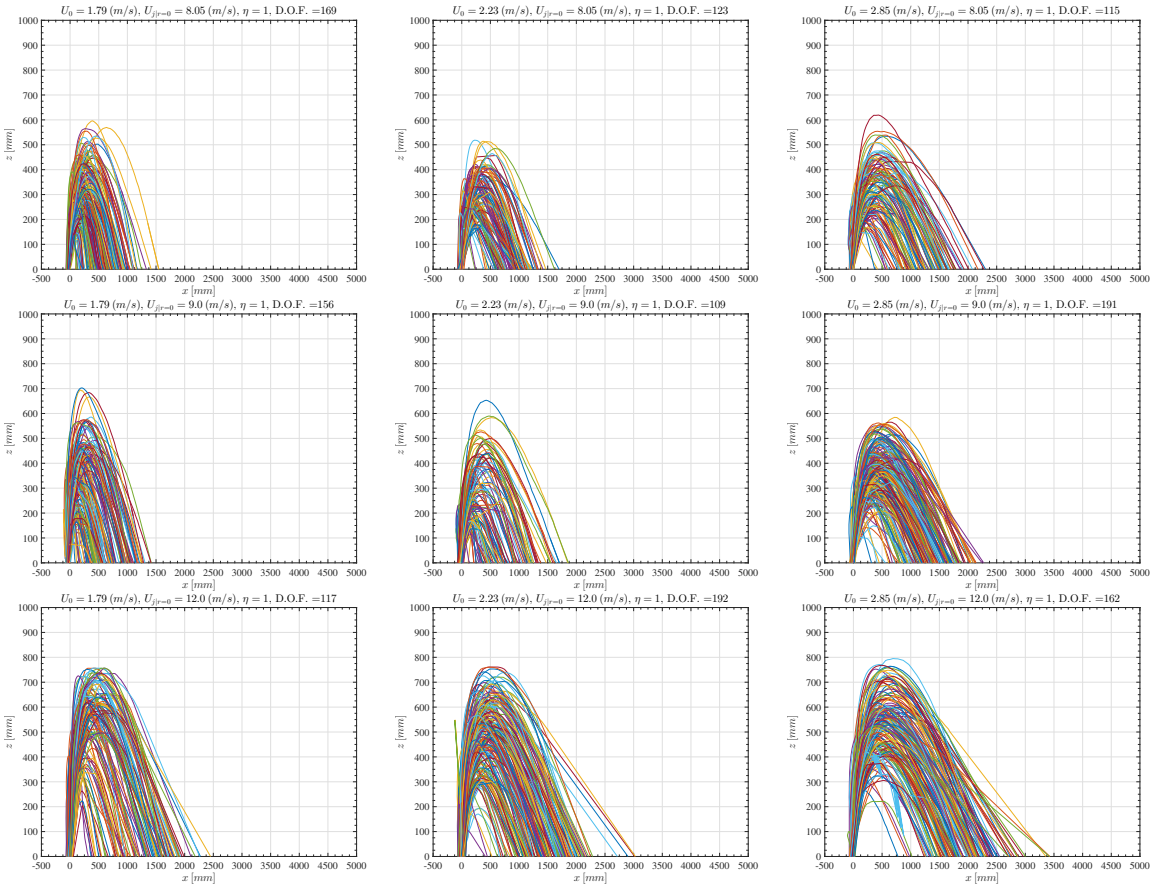

Figure 5.13: Obtained trajectories from the image processing analysis. Presented data are trajectories of the cubic firebrand models with longitudinal and side aspect ratio of one, i.e. $\eta = \eta_s = 1$. From left to right, the reference velocities of the wind tunnel boundary layer are 1.79, 2.23, and 2.85 (m/s), and from top to bottom, the jet centerline velocities are 8.05, 9.0, and 12 (m/s).

momentum length. These data are summarized in figures 5.16-5.17 where the empirical (kernel) probability density functions of each parameter are shown for the tests under the same initial conditions. Figure 5.16 illustrates variations of the normalized maximum rise height of the model firebrands with different aspect ratios subjected to different initial conditions of the wind tunnel experiments. As can be seen, for low U_0 as $U_{j|r=0}$ increases the mean increases as well as its standard deviation. The foregoing discussion is valid for the moderate boundary layer velocity too. However, for high U_0, increasing $U_{j|r=0}$ increases the mean but the standard deviation of z_{max}/z_m seems to be unchanged. Interestingly, cubic firebrand models show bimodal distribution, particularly in cases with low to moderate boundary layer reference velocities, although this may be an artifact of the DOF in the test.

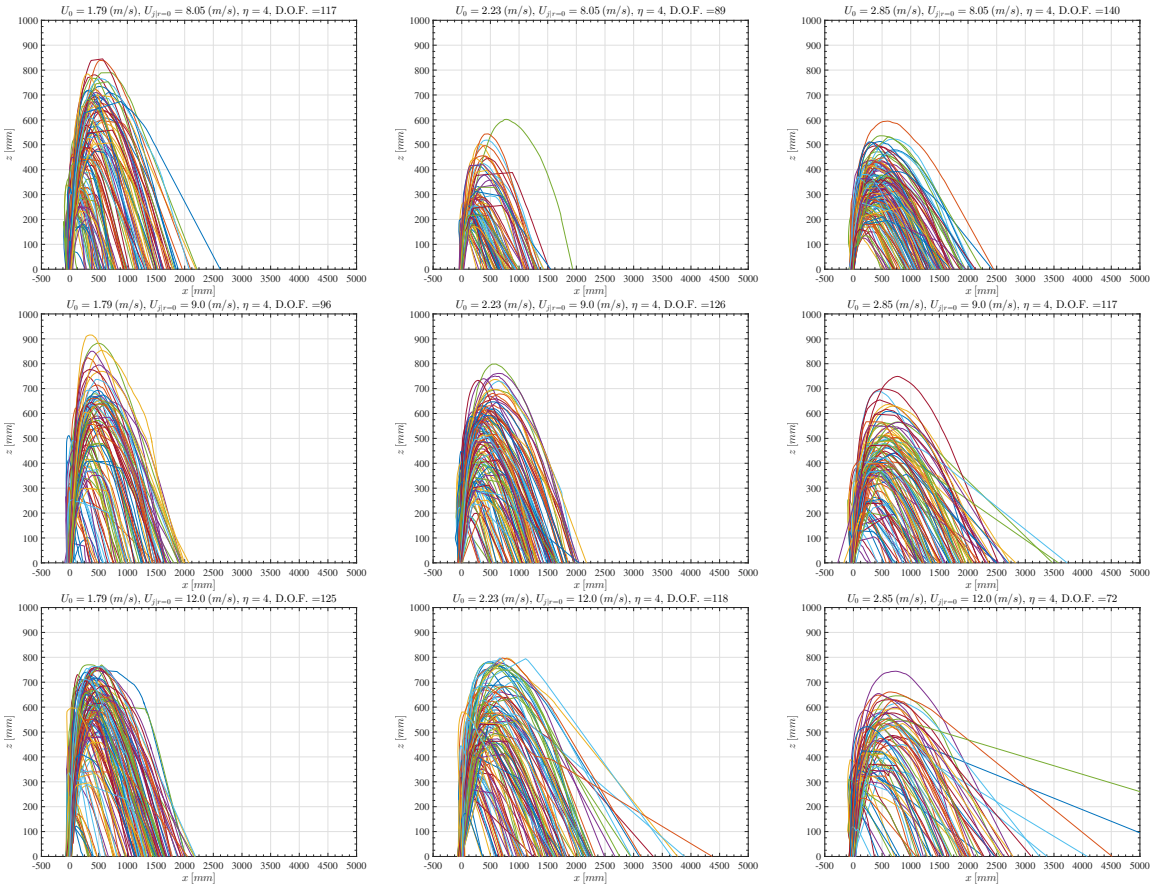

Figure 5.14: Obtained trajectories from the image processing analysis. Presented data are trajectories of the cylindrical firebrand models with longitudinal aspect ratio $\eta = 4$. From left to right, the reference velocities of the wind tunnel boundary layer are 1.79, 2.23, and 2.85 (m/s), and from top to bottom, the jet centerline velocities are 8.05, 9.0, and 12 (m/s).

As for of the normalized maximum downwind distance shown in figure 5.17, in low wind conditions, i.e. $U_0 = 1.79\,(m/s)$, increasing the jet velocity increases the mean. However for firebrands with $\eta = 1, 4$ it does not significantly increase the standard deviation. Quite the contrary, for the largest aspect ratio, increasing the jet velocity not only increases the mean and standard deviation of x_l/z_m but also leads to bimodal distribution which is not observed of any other conditions and aspect ratios. For moderate to high wind conditions of the experiment, increasing the jet velocity causes the model firebrands to loft higher and subsequently travel further downwind.

However, the most striking result emerge when the maximum downwind distance (x_l) is

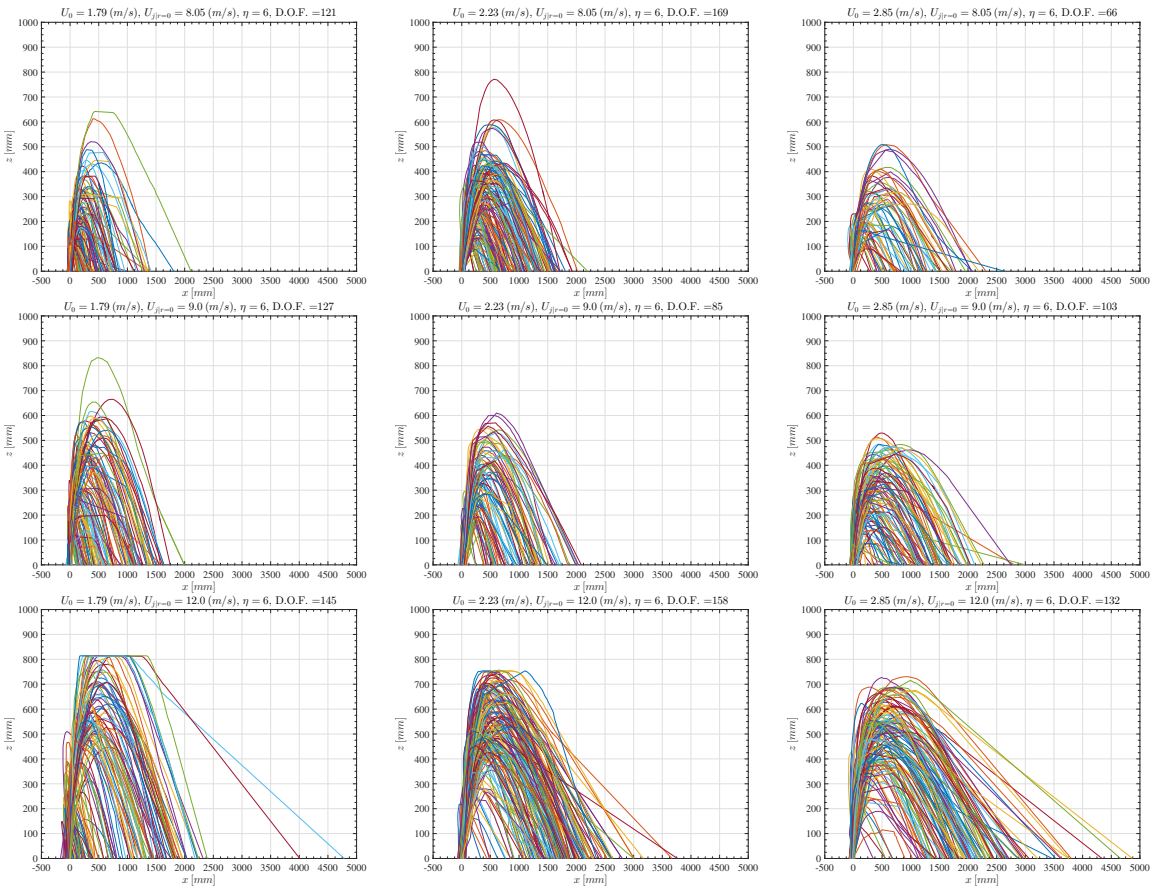

Figure 5.15: Obtained trajectories from the image processing analysis. Presented data are trajectories of the cylindrical firebrand models with longitudinal aspect ratio $\eta = 6$. From left to right, the reference velocities of the wind tunnel boundary layer are 1.79, 2.23, and 2.85 (m/s), and from top to bottom, the jet centerline velocities are 8.05, 9.0, and 12 (m/s).

normalized by the maximum lofting height (z_{max}). Despite the degrees of freedom for each aspect ratio being different, and in some cases by a lot, PDFs of x_l/z_{max} are very similar. In fact for the given velocity field PDFs of different aspect ratios collapse on each other. As can be see on figure 5.17, for a given boundary layer velocity increasing the jet speed does not result in a significant change in the mean and standard deviation. In addition, for a given jet speed, an increase in the boundary layer velocity just slightly increases the mean and standard deviation.

Similarity of PDFs in x_l/z_{max} is significant in that, it indicates there is a the relationship, even though geometric, between the maximum rise height and the maximum downwind distance that a firebrand can travel for a given velocity field. Therefore, studies [Bhutia et al., 2010a] in

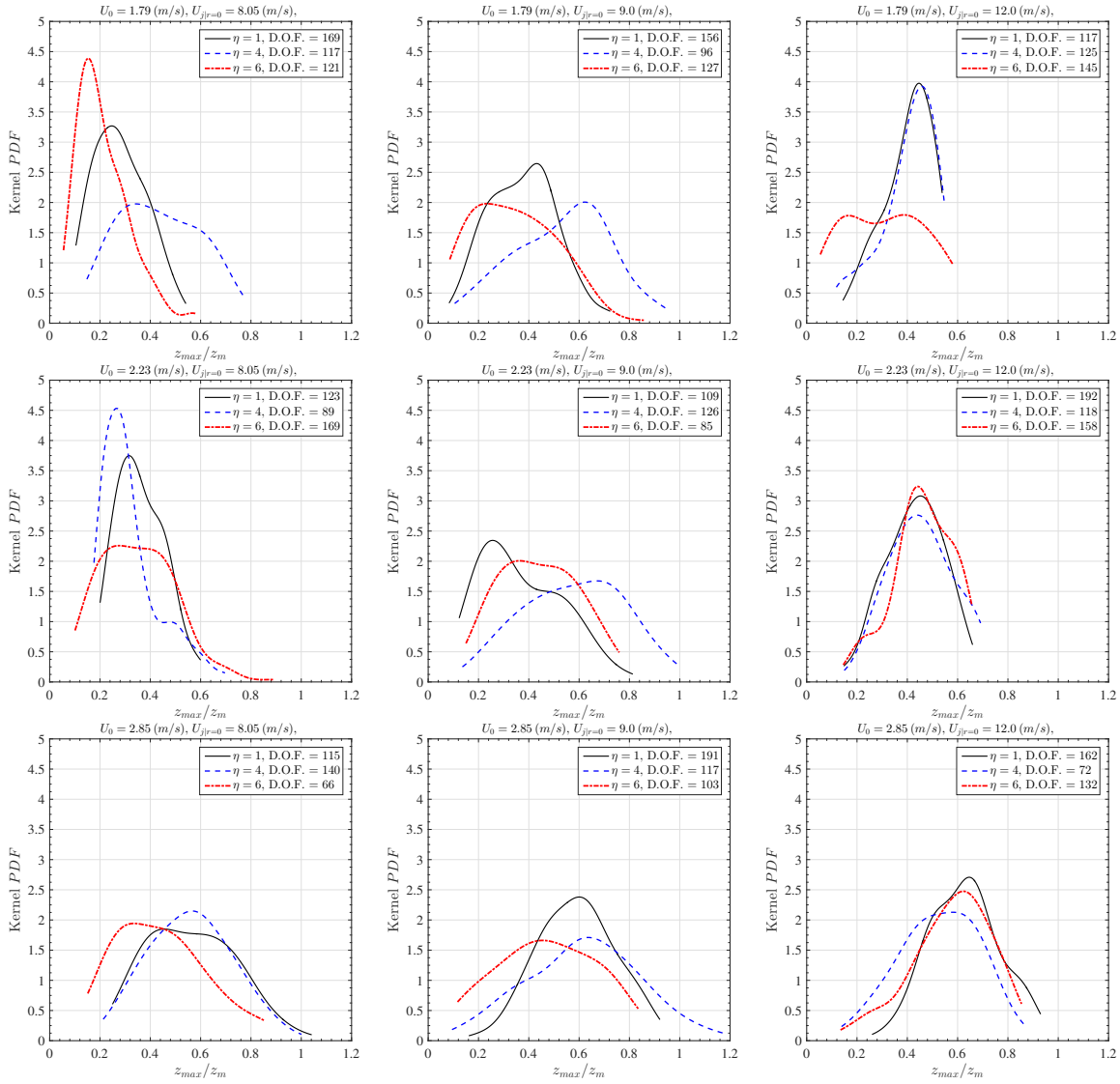

Figure 5.16: Shown are the empirical (kernel) probability density functions (PDF) of z_{max}/z_m for different aspect ratios, under various initial conditions of the wind tunnel experiments. From left to right, U_0 is constant while $U_{j|r=0}$ is increasing. From top to bottom, U_0 is increasing and $U_{j|r=0}$ is constant.

which firebrands or debris are released from fixed heights should be careful about the chosen release heights as it will have significant influence on the modeled flight distance.

Further insight may be obtained by presenting the experimental conditions in terms of

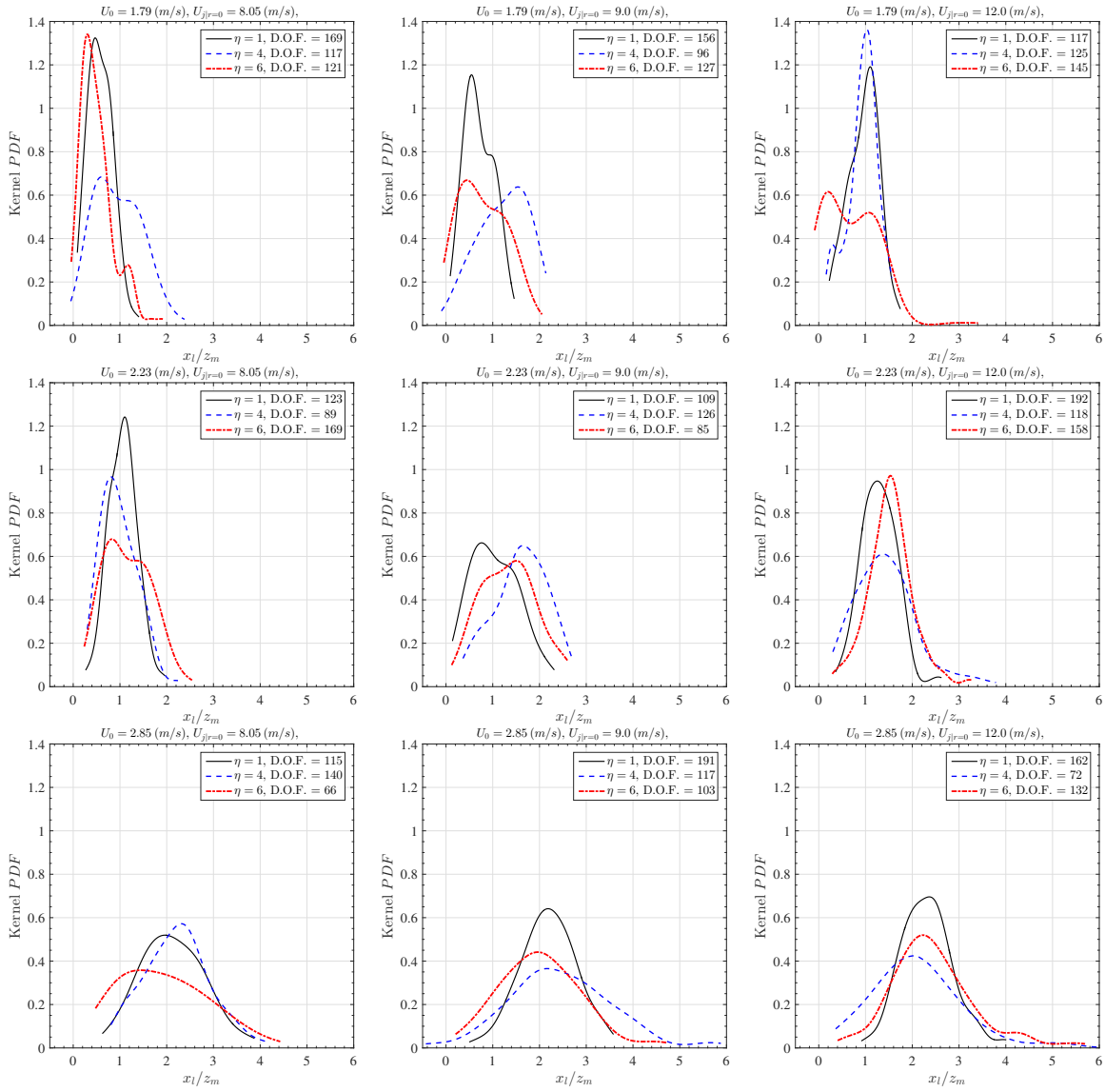

Figure 5.17: Shown are the empirical (kernel) probability density functions (PDF) of x_l/z_m for different aspect ratios, under various initial conditions of the wind tunnel experiments. From left to right, U_0 is constant while $U_{j|r=0}$ is increasing. From top to bottom, U_0 is increasing and $U_{j|r=0}$ is constant.

non-dimensional groups embedded in the physics of the problem. The non-dimensional groups are

$$\frac{U_0}{U_{j|r=0}},\ \ \eta,\ \ \Omega = \frac{\rho_a U_0^2}{\rho_s g L_z}$$

where, as mentioned before, $U_0/U_{j|r=0}$ is the ratio of the boundary layer reference velocity to the jet centerline velocity at the exit, and η is the aspect ratio of model firebrands. The new parameter

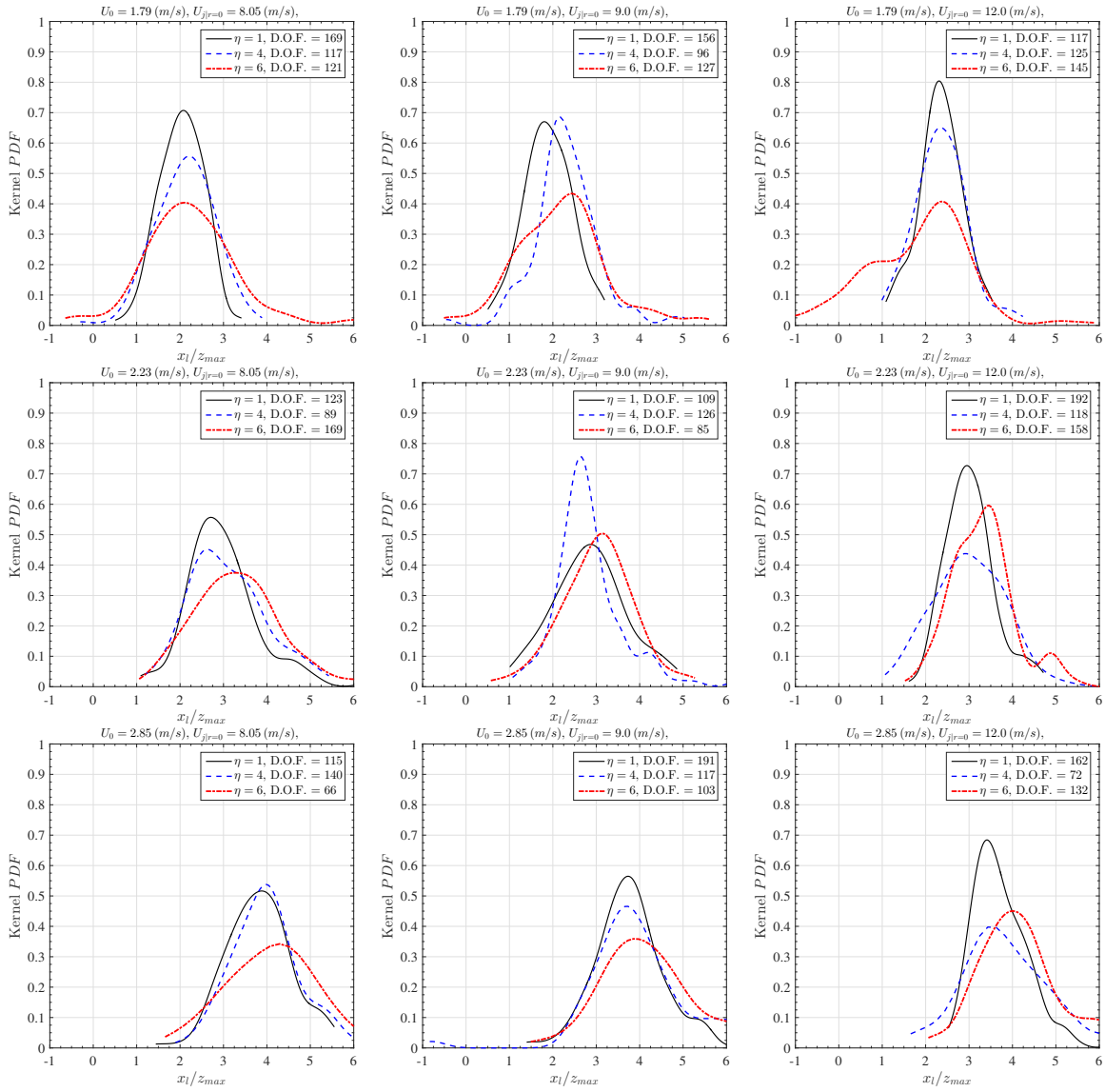

Figure 5.18: Shown are the empirical (kernel) probability density functions (PDF) of x_l/z_{max} for different aspect ratios, under various initial conditions of the wind tunnel experiments. From left to right, U_0 is constant while $U_{j|r=0}$ is increasing. From top to bottom, U_0 is increasing and $U_{j|r=0}$ is constant.

Ω is the Tachikawa number which is the ratio of the aerodynamic forces to the gravity force [Holmes et al., 2006]. Respectively, ρ_a and ρ_s are density of the ambient air and the model firebrands. Given that the important variables are x_l, z_{max}, and the jet momentum length scale can be obtained from

the measured velocity profiles, the results can be presented as

$$\left(\frac{x_l}{z_m},\ \frac{z_{max}}{z_m}\right) = \Pi\left(\frac{U_0}{U_{j|r=0}},\ \eta,\ \Omega\right) \tag{5.2}$$

Figure 5.19 shows variations of the mean (μ) and standard deviation (σ) of the normalized landing location and the normalized rise height against Ω. As can be seen, by increasing Ω, i.e. greater

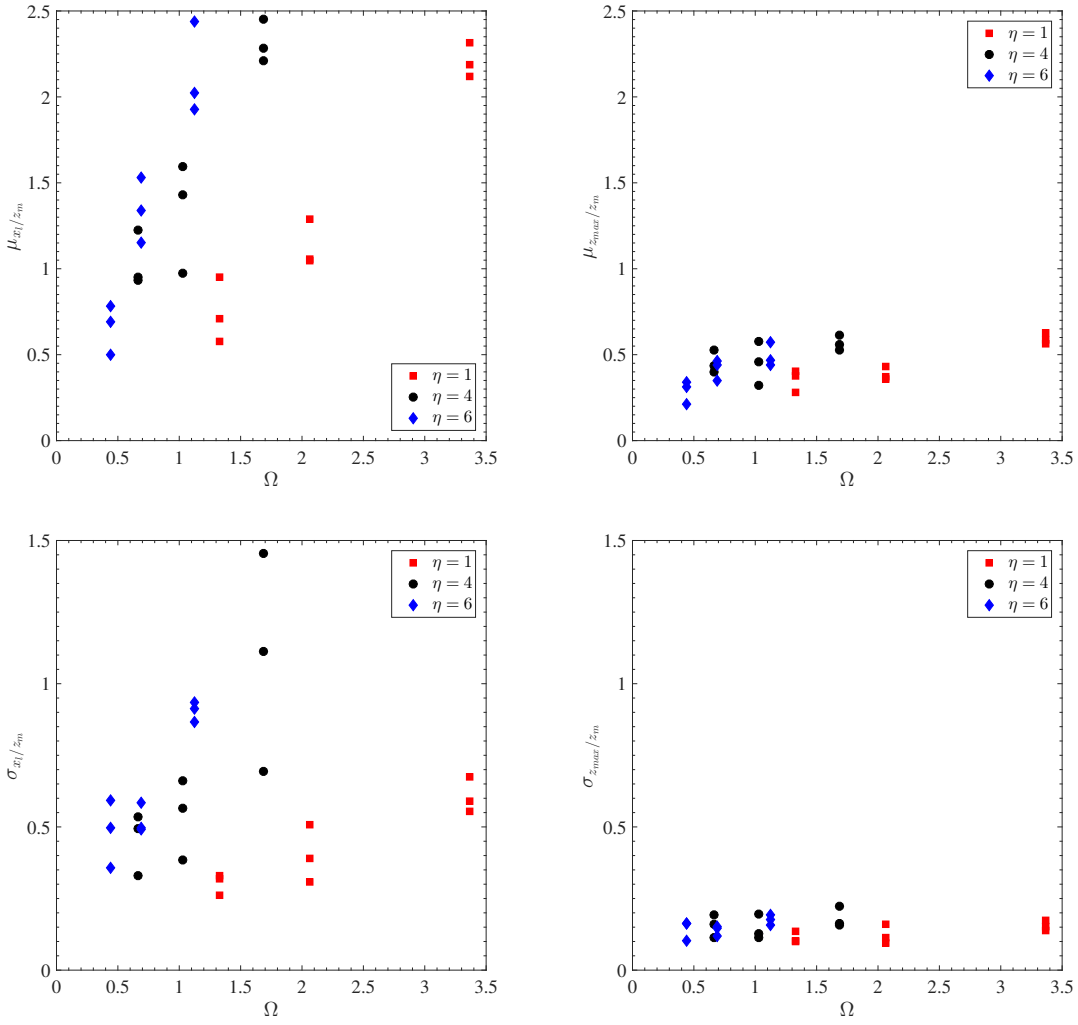

Figure 5.19: Illustrated are variations of the mean (top) and standard deviation (bottom) of the normalized landing location (left), and the normalized rise height (right) of model firebrands with respect to Ω.

boundary layer reference velocity, the mean of the normalized landing location increases. Also, The

greater the aspect ratio, the greater the rate of increase in the mean and standard deviation of x_l/z_m, see figure 5.19-left top & bottom. However, the mean and standard deviation of the normalized rise height (z_{max}/z_m) tend to increase with very mild slopes as Ω increases, see figure 5.19-right top & bottom.

Moreover, distribution of the mean and standard deviation of x_l/z_m and z_{max}/z_m within the parameter space of the experiments, given in equation 5.2, are presented by interpolated surfaces between the experimental results for each aspect ratio. These results are shown in figures 5.20-5.22.

The results of $\eta = 1$ & 6 satisfy the physical expectations, in that for a given aspect ratio and

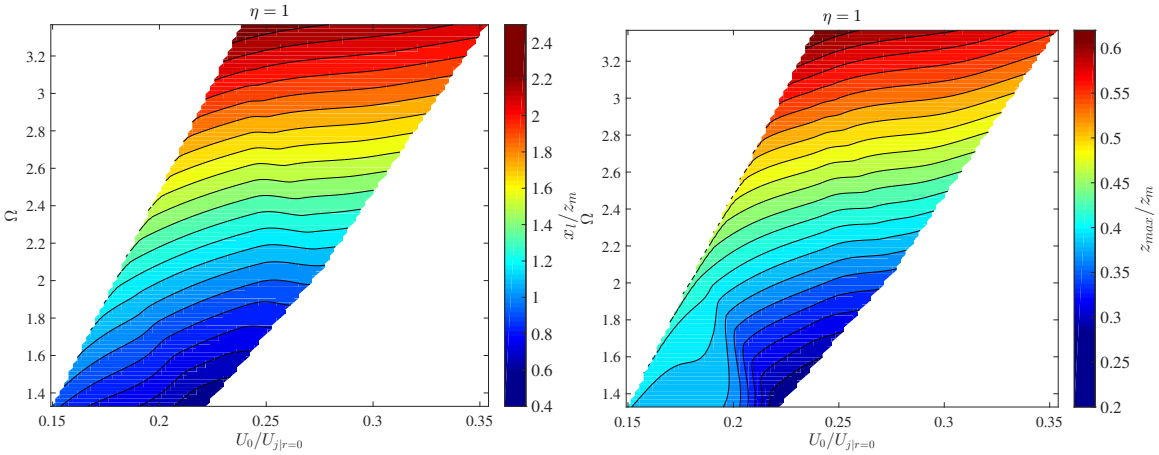

Figure 5.20: Contour plots of the mean x_l/z_m (left) and the mean z_{max}/z_m (right) for model firebrands with aspect ratio $\eta = 1$ within the parameter space of Ω-$U_0/U_{j|r=0}$

boundary layer reference velocity (Ω = const.), increasing the velocity ratio (decreasing the jet velocity) decreases the maximum rise height and subsequently the maximum downwind distance. Also, for a given wind velocity ratio ($U_{j|r=0}$ = const.) increasing Ω increases the applied aerodynamic forces on the brands and leads to greater landing locations. However, results of model firebrands with aspect ratio $\eta = 4$ do not follow this trend, and there are lot of variability in the statistics of their flight as can be seen on figure 5.21.

5.5 Conclusions

The most extensive large scale wind tunnel experiments of the lofting and downwind transport of model firebrands are conducted. The data serves as an invaluable resource for not only

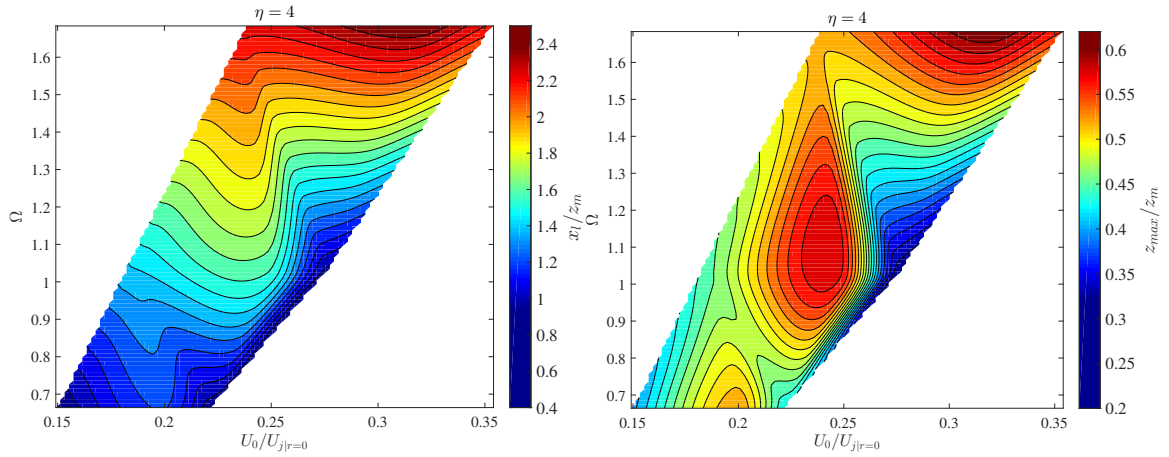

Figure 5.21: Contour plots of the mean x_l/z_m (left) and the mean z_{max}/z_m (right) for model firebrands with aspect ratio $\eta = 4$ within the parameter space of Ω-$U_0/U_{j|r=0}$

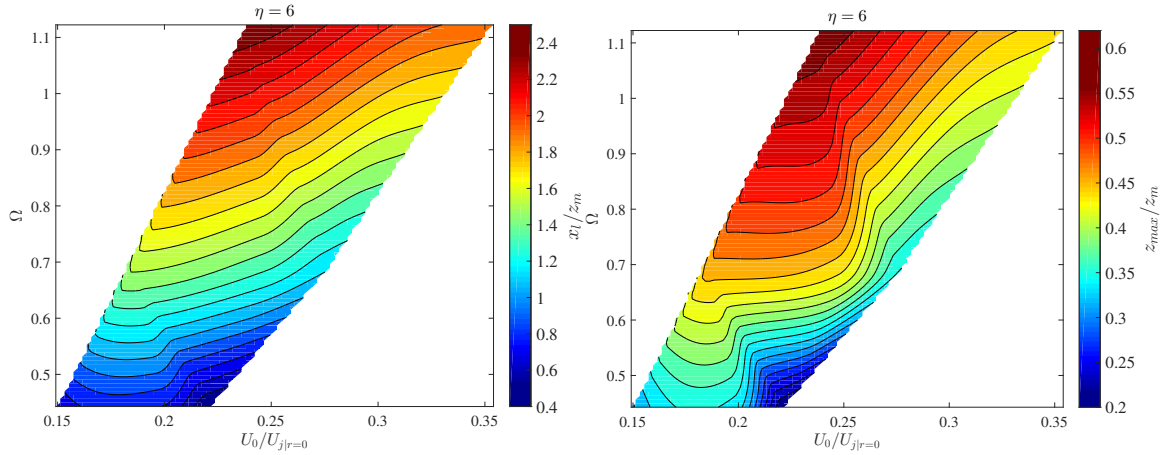

Figure 5.22: Contour plots of the mean x_l/z_m (left) and the mean z_{max}/z_m (right) for model firebrands with aspect ratio $\eta = 6$ within the parameter space of Ω-$U_0/U_{j|r=0}$

firebrand transport studies but also for the flight of rod-like debris/brands through other velocity fields in nature such as hurricanes and storms. Full trajectories of the model firebrands are captured utilizing the developed image processing algorithm. From captured trajectories, the maximum rise height and landing location of the model firebrands are obtained. It is shown that the normalized maximum landing locations with the maximum rise heights (x_l/z_{max}) have similar probability density functions (PDF) regardless of the firebrands' aspect ratio. This implies that in modeling fire spotting phenomenon unlike previous studies the lofting and downwind transport of the firebrands cannot be decoupled, as the rise height significantly affects the landing location. Also, the experiments are presented in terms of the non-dimensional parameters, i.e. velocity ratio, aspect ratio,

and Tachikawa number (Ω). It is shown that there is a strong positive correlation between the Tachikawa number and the mean and standard deviation of the normalized landing locations with the jet momentum length (z_m). However, a very weak correlation between Ω and the statistics of the normalized rise height with z_m is found. The results suggest that lofting and downwind transport of non-combusting firebrands are extremely sensitive to the initial conditions of the release as well as temporal and spatial variations of the ambient velocity field.

Bibliography

Albertson, M. L., Dai, Y., Jensen, R., and Rouse, H. (1950). Diffusion of submerged jets. *Transactions of the American Society of Civil Engineers*, 115(1):639–664.

Albini, F. A. (1979). *Spot fire distance from burning trees : a predictive model*. United States.

Anthenien, R. A., Tse, S. D., and Fernandez-Pello, A. C. (2006). On the trajectories of embers initially elevated or lofted by small scale ground fire plumes in high winds. *Fire Safety Journal*, 41(5):349–363.

Bell, W. G. (1971). *The Great Fire of London in 1666*. Greenwood Publishing Group.

Bhutia, S., Jenkins, M. A., and Sun, R. (2010a). Comparison of firebrand propagation prediction by a plume model and a coupledfire/atmosphere largeeddy simulator. *Journal of Advances in Modeling Earth Systems*, 2:4.

Bhutia, S., M.Jenkins, and Sun, R. (2010b). Comparison of Firebrand Propagation Prediction by a Plume Model and a Coupled Fire/Atmosphere Large Eddy Simulator. *J. Adv. Model. Earth Syst.*, 2:1–15.

Cermak, J. E. and Isyumov, N. (1998). Wind tunnel studies of buildings and structures. American Society of Civil Engineers.

Fischer, H. B., List, E. J., Koh, R. C. Y., Imberger, J., Brooks, N. H., and Fisher, H. B. (1979). *Mixing in inland and coastal waters*. Academic.

Gonzalez, R. C. (2009). *Digital image processing*. Pearson Education India.

Gonzalez, R. C., Woods, R. E., and Eddins, S. L. (2004). *Digital image processing using MATLAB*. Pearson Education India.

Himoto, K. and Tanaka, T. (2005). Transport of disk-shaped firebrands in a turbulent boundary layer author. In *the Eighth International Symposium on Fire Safety Science*, pages 18—-23.

Himoto, K. and Tanaka, T. (2008). Development and validation of a physics-based urban fire spread model. *Fire Safety Journal*, 43(7):477–494.

Holmes, J., Baker, C., and Tamura, Y. (2006). Tachikawa number: a proposal. *Journal of Wind Engineering and Industrial Aerodynamics*, 94(1):41–47.

Koo, E., Pagni, P. J., Weise, D. R., and Woycheese, J. P. (2010). Firebrands and spotting ignition in large-scale fires. *International Journal of Wildland Fire*, 19(7):818.

Lee, J. H. W. and Chu, V. H. (2003). *Turbulent jets and plumes: A Lagrangian approach*. Springer.

Lee, S.-L. and Hellman, J. (1969). Study of firebrand trajectories in a turbulent swirling natural convection plume. *Combustion and Flame*, 13(6):645–655.

Lee, S.-L. and Hellman, J. M. (1970). Firebrand trajectory study using an empirical velocity-dependent burning law. *Combustion and Flame*, 15(3):265–274.

Lin, N., Holmes, J. D., and Letchford, C. W. (2007). Trajectories of Wind-Borne Debris in Horizontal Winds and Applications to Impact Testing. *J. Struct. Eng.*, 133(2):274–282.

Liu, Z., Prevatt, D., Aponte-Bermudez, L., Gurley, K., Reinhold, T., and Akins, R. (2009). Field measurement and wind tunnel simulation of hurricane wind loads on a single family dwelling. *Engineering Structures*, 31(10):2265–2274.

Manzello, S. L., Cleary, T. G., Shields, J. R., Maranghides, A., Mell, W., and Yang, J. C. (2008). Experimental investigation of firebrands: Generation and ignition of fuel beds. *Fire Safety Journal*, 43(3):226–233.

Manzello, S. L., Maranghides, A., and Mell, W. E. (2007). Firebrand generation from burning vegetation. *International Journal of Wildland Fire*, 16(4).

Manzello, S. L., Maranghides, A., Mell, W. E., Cleary, T. G., and Yang, J. C. (2006). Firebrand production from burning vegetation. *Forest Ecology and Management*, 234:S119–S119.

Manzello, S. L., Maranghides, A., Shields, J. R., Mell, W. E., Hayashi, Y., and Nii, D. (2009). Mass and size distribution of firebrands generated from burning Korean pine (Pinus koraiensis) trees. *Fire and Materials*, 33(1).

Mell, W. E., Manzello, S. L., Maranghides, A., Butry, D., and Rehm, R. G. (2010). The wildland–urban interface fire problem–current approaches and research needs. *International Journal of Wildland Fire*, 19(2):238–251.

Richards, P. J. (2010). Steady Aerodynamics of Rod and Plate Type Debris.pdf. In *17th Australian Fluid Mechanics Conference*.

Richards, P. J., Williams, N., Laing, B., McCarty, M., and Pond, M. (2008). Numerical calculation of the three-dimensional motion of wind-borne debris. *Journal of Wind Engineering and Industrial Aerodynamics*, 96(10):2188–2202.

Sardoy, N., Consalvi, J. L., Kaiss, a., Fernandez-Pello, a. C., Porterie, B., and a.C. Fernandez-Pello (2008). Numerical study of ground-level distribution of firebrands generated by line fires. *Combustion and Flame*, 154(3):478–488.

Sardoy, N., Consalvi, J.-L., Porterie, B., and Kaiss, A. (2006). Transport and combustion of Ponderosa Pine firebrands from isolated burning trees. In *2006 1st International Symposium on Environment Identities and Mediterranean Area, ISEIM, July 9, 2006 - July 12*, pages 6–11, Corte-Ajaccio, France. Polytech'Marseille, Dept. of Mechanical Engineering, CNRS UMR 6595, Technopole Chateau-Gombert, 5 rue Enrico Fermi, 13453 Marseille, France, Inst. of Elec. and Elec. Eng. Computer Society.

Tarifa, C. S., Del Notario, P. P., Moreno, F. G., and Villa, A. R. (1967). Transport and combustion of firebrands, final report of grants FG-SP-11 and FG-SP-146. *US Department of Agriculture Forest Service*.

Tarifa, C. S., Notario, P., and Moreno, F. G. (1965). On the flight paths and lifetimes of burning particles of wood. In *Symposium (international) on combustion*, volume 10, pages 1021–1037. Elsevier.

Tavoularis, S. (2005). *Measurement in fluid mechanics*. Cambridge University Press.

Tohidi, A., Kaye, N., and Bridges, W. (2015). Statistical description of firebrand size and shape distribution from coniferous trees for use in Metropolis Monte Carlo simulations of firebrand flight distance. *Fire Safety Journal*, 77:21–35.

Tohidi, A. and Kaye, N. B. (2016). Highly buoyant bent-over plumes in a boundary layer. *Atmospheric Environment*, 131:97–114.

Tse, S. D. and Fernandez-Pello, A. C. (1998). On the flight paths of metal particles and embers generated by power lines in high windsa potential source of wildland fires. *Fire Safety Journal*, 30(4):333–356.

Chapter 6

Model development

6.1 Introduction

The spot fires generated by firebrand showers are the dominating propagation mechanism in major forest fires [Tarifa et al., 1965]. Firebrand flight has a key role in the determination of spot fire hazards since the interaction between firebrands and the ambient velocity field controls the maximum lofting and downwind travel distance. Due to the stochastic nature of firebrand transport, and unknown properties such as the turbulent characteristics of the velocity field, simulating exact trajectories and landing locations of firebrands is very difficult. Hence, a probabilistic approach that predicts the underlying statistics of the flight and landing locations seems to be appropriate. This may provide a more general understanding of the spotting effects on subsequent ignitions and ultimately fire spread. In this context, a substantial amount of work on the firebrand transport can be found.

Sardoy et al. [2008] modeled bimodal distribution of landing location for disk-shape firebrands with different aspect ratios that were released in a synthesized velocity field by the interaction of a boundary-layer and a plume. Kortas et al. [2009] numerically modeled combusting cylindrical and disk-shape firebrands released in a uniform wind field. Although this study, similar to Sardoy et al. [2006], is one of the few attempts to provide an experimentally validated numerical model for firebrands' transport, it neither considers a fire scenario nor a thorough aerodynamic model that accounts for the 3D characteristics of the trajectories. In addition, Tarifa et al. [1965, 1967]; Lee and

Hellman [1970]; Fernandez-Pello [1982] and Holmes [2004] use sphere (compact) forms for developing transport models of firebrands and debris, although rod and disk-like forms are the most probable shapes of firebrands from burning vegetative and woody structures [Koo et al., 2012].

In addition, many of the prior numerical studies employ simplified plume and wind field models [Tarifa et al., 1965; Albini, 1979; Woycheese and Pagni, 1999; Kortas et al., 2009] such that they separate transport into lofting and propagation stages. Indeed, practically, most of them account only for one of these stages [Tse and Fernandez-Pello, 1998; Himoto, K and Tanaka, 2005; Bhutia et al., 2010; Kortas et al., 2009]. However, similarity of the PDFs of the normalized maximum transport distance shown in the large scale wind tunnel experiments (see the previous chapter), implies that it is imperative to thoroughly examine the ramifications of making such simplifying assumptions. Therefore, a reasonable solution to these issues may be accomplished by coupling a firebrand transport model with an atmospheric dynamic model, which accounts for the detailed spatial and temporal resolutions of the velocity field induced by the interaction of the fire plume and the boundary layer. This wind field could, then, be used for conducting Monte-Carlo type simulations to reveal underlying statistics of firebrand flight within the fire spotting phenomenon.

Regarding this, the present chapter shall deal with the development procedure of a coupled stochastic parametric model of firebrand transport. The model couples fine resolution time-varying turbulent velocity field of a jet in a boundary layer cross-flow, obtained from Large Eddy Simulations (LES) of the flow field, with the fully deterministic 3D 6-D.O.F. transport model of Richards et al. [2008] in which steady aerodynamic force and moment coefficients of rod and plate-like firebrands with different aspect ratios are incorporated [Richards, 2010]. See the introduction of chapter 3 for detailed review of the existing transport models, and why Richards et al. [2008] model is adopted. Given that adding a reliable time-dependent combustion model to the transport model is relatively straightforward, the shape of firebrands does not change significantly after being charred [Barr and Ezekoye, 2013], and most of the issues with modeling fire spotting are related to the aerodynamics of the flight (as explained in chapter 3), the developed model is currently decoupled from combustion effects as well as buoyant forces in the fire plume. Further, the primary objectives of this study are, first, to develop a coupled stochastic and parametric model that does not suffer from simplifying assumptions discussed before and, second, validate the model against the most comprehensive large scale wind tunnel experiments of lofting and transport of rod-like firebrands (debris) presented in

chapter 4.

The rest of the chapter continues with a detailed description of the flows involved in the wind tunnel experiments followed by the modeling procedure with OpenFOAM computational fluid dynamics libraries. On this note, details of high performance scientific computing (HPSC) with OpenFOAM and post-processing the results on Clemson University's Palmetto cluster are described in Appendix B of the dissertation. In section 6.3, simulated flow fields are validated against the measured velocity profiles in wind tunnel experiments. Finally, in section 6.4, coupling Large Eddy Simulation results with the firebrand transport model is explained.

6.2 Model development

Since the model will be validated against the results of the large scale wind tunnel experiments of the lofting and downwind transport of non-combusting model firebrands (discussed in the previous chapter), the numerical model development deals with the simulation of these experiments. In this regard, the coupled stochastic parametric model for firebrand transport is comprised of two parts, namely the passive transport (flight) model, and the model for generating the velocity field. For the flight of firebrands the fully deterministic three dimensional 6-D.O.F. firebrand (debris) transport model of Richards et al. [2008] is adopted; See Grayson et al. [2012] for more details about the model. Also, a thorough performance evaluation and characterization of this model are discussed in chapter 3. The generation of the time-varying turbulent velocity field of the wind tunnel's test section, where the jet enters vertically from the bottom of the wind tunnel in to the boundary layer cross-flow, is done by Large Eddy Simulation, hereafter LES, of the test section using OpenFOAM.

The flow field consists of two basic wall-bounded flows. A fully developed channel flow that models the wind tunnel boundary layer and, a fully developed pipe flow which simulates the flow of the jet through the flow straightener. Interaction of these flows makes a jet in the boundary layer cross-flow which is qualitatively similar to the velocity field of a wildfire. Therefore, precursor LES of each flow type is conducted in order to provide fully developed turbulent inlet conditions for the flow inside of the wind tunnel's test section. The main domain, i.e. wind tunnel's test section, along with the domain of the precursor simulations are illustrated in figure 6.1.

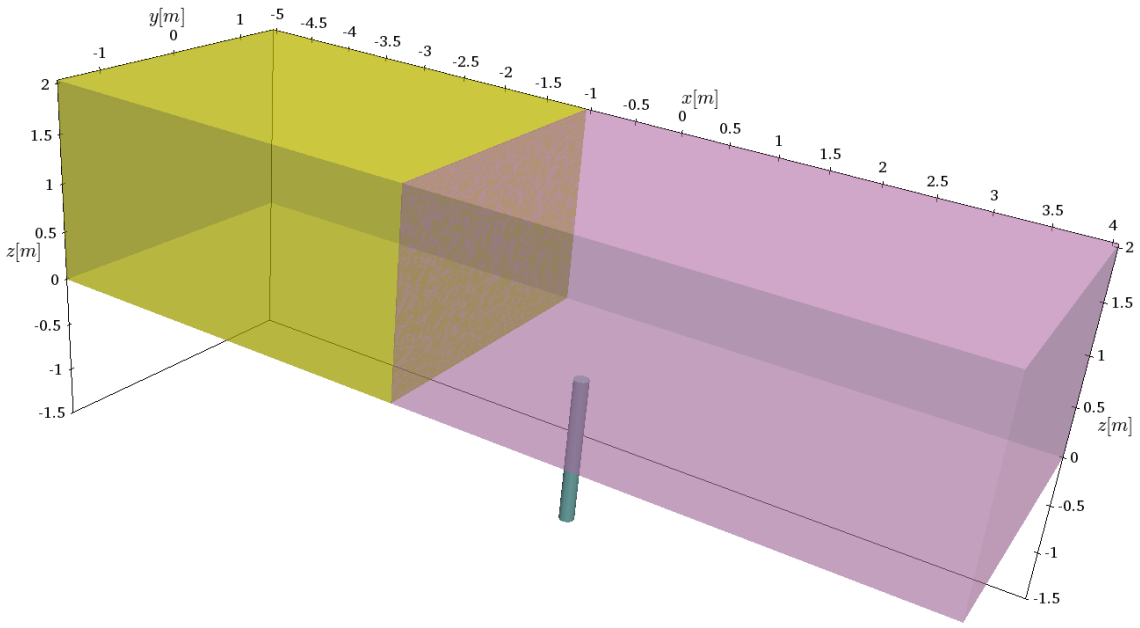

Figure 6.1: Illustrated is the computational domain of the Large Eddy Simulations. Also, shown are the dimensions of the domain. (Color version) The pink rectangular prism is the wind tunnel's test section where the model firebrands are released, the yellow (smaller) rectangular prism is the precursor channel flow domain, and the blue cylinder is the precursor pipe flow domain.

6.2.1 Flow description

Description of the flow field in each part of the computational domain is as follows.

6.2.1.1 Channel flow

The flow is considered to be through a rectangular duct with height h. Ideally, the length of the duct is long such that $L/\delta \gg 1$ and it has a large side aspect ration where $b/\delta \gg 1$. Following the notation of [Pope, 2000], δ and b denote the depth and width of the wind tunnel boundary layer, respectively. The mean flow is predominantly horizontal, i.e. in x direction (parallel to the floor and ceiling of the wind tunnel), with mean velocity varying in the vertical direction, that is z. The length of the channel in the spanwise-direction (y) is large compared to δ. Thus, the flow is assumed to be statistically independent of y. The velocities in Cartesian coordinate system are (U, V, W) with fluctuations (u, v, w). The mean velocity in y direction, i.e. $\langle V \rangle$, is zero.

In precursor simulations since the domain is considered to be periodic the flow development region vanishes after a couple of revolutions. Therefore, velocity statistics do not vary in the x direction. This ensures that in the fully developed channel the flow is statistically stationary and statistically one-dimensional where statistics of the velocities vary only in the z direction [Pope, 2000].

Initially, the depth of the boundary layer is considered to be $h/2$, according to Pope [2000]. As a result, the bulk velocity U_b can be defined as

$$U_b = \frac{1}{\delta} \int_0^{\delta} \langle U \rangle \, dz.$$

Also the Reynolds number based on the bulk velocity can be utilized for characterizing the flow, that is $Re_b = \delta U_b / \nu$; Where ν is the kinematic viscosity in m^2/s.

6.2.1.2 Pipe flow

The fully developed inlet boundary condition for the round jet that exits to the wind tunnel's test section is obtained by conducting precursor LES of the pipe flow with circular section and internal diameter of D. The length of the pipe is ten times of the jet nozzle diameter, i.e. $10D = 1.5\,(m)$ which is consistent with Ruiz et al. [2015]. Similar to the channel flow the development region will vanish in LES precursor simulations after $2-3$ revolutions. Then, the velocity statistics are solely dependent on the radial distance r from the centerline of the jet.

The jet's bulk velocity is defined as

$$U_{j,b} = \frac{4}{D^2} \int_0^{D/2} 2 \langle W \rangle \, r \, dr$$

based on which the Reynolds number can be written as $Re_{j,b} = U_{j,b} D / \nu$. The subscript "$_j$" shows the attributions to the jet, and the pipe boundary layer depth is considered to be $\delta = D/2$. For more details on the boundary layer theory, in particular pipe flows see Schlichting and Gersten [2003].

In addition to the bulk velocity, a common velocity scale for characterizing the turbulent

flow is friction velocity [Tennekes and Lumley, 1972]. The friction velocity, which is denoted by u_τ, is defined based on the wall shear stress (τ_w) and the fluid density (ρ) as $u_\tau = \sqrt{\tau_w/\rho}$. Then, the friction Reynolds number, namely $Re_\tau = u_\tau \delta/\nu$, may be used for the flow characterization. Although calculating τ_w and subsequently u_τ are straightforward [Pope, 2000], they are not known *a priori* and cannot be used as input parameters for calculating the corresponding pressure gradient in the precursor simulations. Hence, the experimentally measured velocity profiles in the wind tunnel test section are used as input parameters. Subsequently, the bulk velocity and Reynolds number are used for characterization of the flow.

6.2.2 Governing equations

The momentum and mass conservation equations for an incompressible isothermal viscous fluid are given by

$$\frac{\partial \vec{U}}{\partial t} + (\vec{U} \cdot \nabla)\vec{U} = -\frac{1}{\rho}\nabla P + \nu \nabla^2 \vec{U} \tag{6.1}$$

and

$$\nabla \cdot \vec{U} = 0, \tag{6.2}$$

respectively. Expressions 6.1 & 6.2 are the governing equations of the fluid for the described flows; Where $\vec{U}$ is the velocity vector (U, V, W), t is time, ρ is the density of the fluid (air), and P is the dynamic pressure. Also, ∇ is the vector differential operator which in the 3D Cartesian coordinate system (R^3) with coordinates (x, y, z) and basis (e_x, e_y, e_z) is written as

$$\nabla = \vec{e_x}\frac{\partial}{\partial x} + \vec{e_y}\frac{\partial}{\partial y} + \vec{e_z}\frac{\partial}{\partial z}.$$

For derivation of the governing equations and more details on the assumptions see Aris [2012].

6.2.3 Turbulence modeling

As discussed in chapter 3, temporal and spatial fluctuations in the velocity field may cause variations in the firebrand flight trajectories. Therefore, it is important to model the velocity field of the wind tunnel experiments, namely the jet in the boundary layer cross-flow, such that it accounts for the spatial and temporal scales.

In this regard, Direct numerical simulations (DNS) and Reynolds-averaged Navier-Stokes simulations (RANS) are two ends of the spectrum of possible methods for simulating/modeling turbulent flows [Fureby et al., 1997b]. In the DNS approach, all scales of the motion are simulated. However, it is computationally expensive such that it requires a number of grid points proportional to $Re^{9/4}$ in order to resolve Kolmogorov scales [Pope, 2000]. Hence, DNS is only feasible for low to moderate Reynolds' number flows. On the contrary, RANS methods are the most commonly used models in turbulence modeling, especially for industrial applications. Using RANS the ensemble-averaged mean flow is resolved, and all scales are modeled in the same way while the small and large scales of the flow are influenced by parameters of different nature.

The rationale in LES, which is a method between these two extremes, is that only the large-scales of the flow are affected by the boundaries (domain geometry), and the small-scales are similar or even self-similar in the bulk of the flow [Deardorff, 1970]. Indeed, the small-scales are assumed to be influenced only by viscosity [Schumann, 1975]. Decomposition of the scales into the large or grid-scale (GS) components and the small or sub-grid scale (SGS) components, which represent the unresolved turbulent scales, makes use of fairly coarse computational meshes along with large time-steps possible [Fureby et al., 1997a]. Therefore, in LES the GS motion or eddies that are associated with the length scales larger than the cut-off length (Δ) are explicitly simulated using relatively coarse mesh and large time-steps whilst the average effects of the SGS motion on the GS motion is accounted for by the SGS model [Pope, 2004].

In LES a general filtering operator decomposes the flow motion into grid-scale and sub-grid-scale motion [Leonard, 1974]. Following the notation of Mukha and Liefvendahl [2015], this can be shown, mathematically, as the convolution of a relevant flow field with the adopted filter kernel as

$$\bar{\phi}(\vec{x},t) = \iiint_{-\infty}^{+\infty} \phi(\vec{x},t) G(\vec{x}-\vec{\xi},\Delta)\, d\vec{\xi}. \tag{6.3}$$

Where G is the filter kernel and Δ is the cut-off length, which is a parameter that defines the size of the scales (frequencies) that are not modeled explicitly. Also, x is the position vector, and over bar symbol denotes that the variable is filtered using the G kernel in equation 6.3. Here ϕ is the

arbitrary flow field and the unresolved part of the flow (sub-grid-scale) can be obtained by

$$\phi''(\vec{x},t) = \phi(\vec{x},t) - \bar{\phi}(\vec{x},t).$$

It should be noted that the integration is over the entire domain and the kernel must satisfy the normalization condition, that is $\int G(\vec{x},\vec{\xi})d\xi = 1$ [Pope, 2000]. A large number of the filters can be found in the literature. For more discussion on various filters, see Pope [2000] and Sagaut [2006].

In this study, one of the most commonly used filters, i.e. top-hat filter, is used. The kernel of the top-hat filter can be formulated as

$$G(\vec{x}-\vec{\xi},\Delta) = \begin{cases} 1/\Delta^3, & |\vec{x}-\vec{\xi}| \leq \Delta/2 \\ 0, & |\vec{x}-\vec{\xi}| > \Delta/2 \end{cases} \tag{6.4}$$

Equation 6.4 in conjunction with equation 6.3 implies that the utilized filter averages the flow filed in a rectangular volume of Δ^3. A common choice of the Δ is the cube root of the computational cell, namely $\Delta = \sqrt[3]{\Delta x \Delta y \Delta z}$ where Δx, Δy, and Δz are the cell-sizes along the Cartesian coordinate system [Mukha and Liefvendahl, 2015]. This suggests that $\bar{\phi}$ is equal to the spatial average of the ϕ throughout the local computational cell. Hence, no explicit filtering is required during the simulation and, practically, the filter is embedded in the discretization method.

Filtering the governing equations using 6.3 & 6.4, delivers conservation equations for the filtered flow fields. The continuity equation (6.2) remains unchanged after filtering, since it is a linear equation. It can be inferred that the SGS velocity filed ($\vec{U}''$) is also solenoidal [Pope, 2000; Mukha and Liefvendahl, 2015]

$$\frac{\partial \bar{U}_i}{\partial t} + \frac{\partial}{\partial x_m}(\overline{U_i U_m}) = -\frac{\partial \bar{p}}{\partial x_i} + \nu \frac{\partial^2 \bar{U}_i}{\partial x_m \partial x_m}, \tag{6.5}$$

where $_i$ and $_m$ are subscripts in Einstein's notation, and p is the kinematic pressure, that is $p = P/\rho$. Since the advection term in 6.5 cannot be expressed in terms of $\bar{U}_i$, according to Yoshizawa and

Horiuti [1985] and Fureby et al. [1997a] the SGS stress tensor can be written as

$$B_{im} = \overline{U_i U_m} - \bar{U}_i \bar{U}_m. \tag{6.6}$$

Substituting 6.6 into the equation 6.5 gives

$$\frac{\partial \bar{U}_i}{\partial t} + \frac{\partial}{\partial x_m}(\bar{U}_i \bar{U}_m) = -\frac{\partial \bar{p}}{\partial x_i} + \nu \frac{\partial^2 \bar{U}_i}{\partial x_m \partial x_m} - \frac{\partial B_{im}}{\partial x_m}, \tag{6.7}$$

which together with the filtered conservation of mass equation are not a closed system of equations. Therefore, the SGS stress tensor needs to be modeled.

6.2.3.1 SGS closure

A large number of approaches to modeling **B** are documented in the literature and a detailed review of them is available in Pope [2000] and Sagaut [2006]. It is a common practice in SGS-modeling to use the Boussinesq approximation which suggest that the SGS-stress tensor is structurally similar to the viscous stress [Pope, 2000]. This is mathematically expressed as

$$\mathbf{B} = \frac{1}{3} Tr(\mathbf{B})\mathbf{I} + \nu_{sgs}(\nabla \bar{U} + \nabla^T \bar{U}). \tag{6.8}$$

where $Tr(\mathbf{B})$ denotes the trace of tensor **B**, **I** is the identity matrix, and ν_{sgs} is the SGS viscosity that needs to be calculated from the filtered velocity field. Assuming that only characteristic time and length scales are enough to describe the sub-grid scales [Sagaut, 2006], using dimensional analysis $\nu_{sgs} \sim l_{sgs}^2 / t_{sgs} = U_{sgs} l_{sgs}$. An intuitive choice for the l_{sgs} is the filter cut-off width Δ, yet the choice of velocity scale (U_{sgs}) is less obvious [Mukha and Liefvendahl, 2015]. In the present study, we use the one-equation eddy-viscosity model [Yoshizawa and Horiuti, 1985] in order to resolve the sub-grid kinetic turbulent energy denoted by k_{sgs}. The logic of this choice is that $U_{sgs} = \sqrt{k_{sgs}}$. This has been shown through several studies [Schumann, 1975; Yoshizawa, 1982; Yoshizawa and Horiuti, 1985; Horiuti, 1985; Kim and Menon, 1999; Stevens et al., 1999], independently.

The transport equation for the SGS turbulent kinetic energy in one-equation eddy-viscosity model is

$$\frac{\partial k_{sgs}}{\partial t} + \frac{\partial \bar{\bar{U}}_i k_{sgs}}{\partial x_i} = 2\nu_{sgs} |\bar{D}_{im}|^2 - C_e \frac{k_{sgs}^{3/2}}{\Delta} + \frac{\partial}{\partial x_i}(\nu_{sgs} \frac{\partial k_{sgs}}{\partial x_i}) + \nu \frac{\partial^2 k_{sgs}}{\partial x_i x_i}, \tag{6.9}$$

where $\bar{D}_{im}$ is the filtered strain rate tensor, $C_e = 1.048$, $\nu_{sgs} = C_k \Delta \sqrt{k_{sgs}}$, and C_k is 0.094. The right-hand-side terms of equation 6.9 are, respectively, cascade of turbulent energy from the GS (resolved) to the SGS (unresolved yet), turbulent dissipation, turbulent diffusion, and viscous turbulent dissipation. For more details on the derivation of 6.9 see [Fureby et al., 1997a], [Pope, 2000], or [Davidson, 2015].

According to [Mukha and Liefvendahl, 2015], the unresolved scales adjacent to the wall, i.e. $z \to 0$, do not show the expected behavior based on the boundary layer theory. In order to rectify this misbehavior, the Van Driest damping function [Van Driest, 2012] is used in the solver. The native function expression that is implemented in `OpenFOAM` and calculates Δ, is

$$\Delta = min(\Delta_{mesh}, \frac{\kappa}{C_\Delta})(1 - ze^{-z^+/A^+}). \tag{6.10}$$

Where $\kappa = 0.4187$ is the Von Karman constant, $C_\Delta = 0.158$, $A^+ = 26$, and z^+ is the wall coordinate normalized by ν/u_τ.

6.2.4 Discretization & Choice of the solver

The domain discretization and solution of the subsequent system of equations are done using OpenFOAM (Open Field Operation and Manipulation). OpenFOAM is primarily a set of C++ libraries, applications, and utilities for manipulation of the tensorial fields in continuum mechanics which, also, includes computational fluid dynamics (CFD) [Jasak and Weller, 1995; Jasak, 1996]. Applications of this tool are now extended to multi-physics problems and even problems in finance. The Original development of OpenFOAM started in late 1980s at Imperial College London, in order to establish a general, powerful, and flexible simulation platform for complex multi-physics problems [Jasak et al., 2007]. Being open sourced under the GPL license has empowered the libraries with the state-of-the-art algorithms and solvers that are efficiently written using the object oriented features in C++ language.

Amongst OpenFOAM features that are particularly useful in CFD applications, a few highlights are: utilization of the hierarchical object description that allows for polyhedral cells in the geometric discretization of the domain (meshing). Also, OpenFOAM solvers are highly scalable

such that some of them show linear scalability up to 1000 CPU cores with proper settings [Rivera et al., 2011; Duran et al., 2015; Lui, 2015]. This enables users to benefit from new advancements in current versions of C++ and High Performance Scientific Computing (HPSC). Further, operator overloading capability of the C++ permits human readable discretization of the partial differential equations; see the OpenFOAM user guide.

On this note, OpenFOAM uses the finite volume method for discretization of the partial differential equations. The finite volume method and its applications in solving the Navier-Stokes equations are very well documented [Ferziger and Peric, 2012; Versteeg and Malalasekera, 2007]. A detailed OpenFOAM-oriented discussion can be found in Jasak [1996]; Rusche [2003]; De Villiers [2007], and Moukalled et al. [2015]. In this study, evolution of the governing equations (6.1,6.2) along with the turbulent model equations (6.7-6.9) are numerically solved using the `pisoFoam` solver that is provided within OpenFOAM's generic package. The solver, particularly, treats the incompressible transient homogenous flows. Validation of the solver, and its applications and its potentials in modeling turbulent flows through various scales are discussed in De Villiers [2007]; Gildeh [2014], and Charmiyan et al. [2016].

6.2.5 Simulations setup

From 9 cases of the jet through the fully developed nonuniform boundary layer cross-flow in wind tunnel experiments, LES of two cases (setups), i.e. W1-I5-O3 and W2-I10-O5, are conducted. For the specifics of each setup see table 1 in chapter 4. This section presents simulation parameters, and case setup in OpenFOAM for these two cases as well as their corresponding precursor simulations.

6.2.5.1 Precursor LES of the channel flow

Physical properties of the computational domain in precursor LES of the channel flow are given in table 6.1. Given the cyclic nature of the inlet and outlet boundary conditions and the side walls (explained later) and, that $\delta = h/2$, the described conditions for channel flow are satisfied. In addition, the posterior analysis of the flow confirms that the values of l_x, l_y, and h are large enough to encompass the largest existing turbulent structures. This will be shown later in this chapter. On this note, the input parameters (initial conditions) for each precursor LES are given in table 6.2.

Table 6.1: Utilized physical properties in precursor LES of the channel flows.

Parameter	Notation	Value	Units
Channel height	h	2.032	m
Streamwise length	l_x	4	m
Spanwise length	l_y	3	m
Kinematic viscosity	ν	1.568×10^{-5}	m^2/s

Table 6.2: Initial conditions of the channel flow precursor simulations.

Channel flow setup	$U_0\,(m/s)$	$z_0\,(m)$	$U_b\,(m/s)$	Re_b
W1	2.23	0.04	3.22	2.0857×10^5
W2	2.85	0.04	4.42	2.8657×10^5

The simple geometry of the channel flow allows construction of the structured hexahedral computational meshes. On this matter, through the main firebrand transport simulations, there is no need for high resolution of the velocity scales near the walls of the wind tunnel test section, since the lofting and downwind transport occurs far from the walls. Hence, the mesh size in each direction is chosen such that the size of the smallest resolved eddy is the same as the smallest length of the model firebrands. Given the size and aspect ratios of the model firebrands in chapter 5, the maximum mesh size in the computational domain is considered to be $0.01\,m$. However, in precursor simulations, since there would be no passive release of model firebrands, nonuniform mesh grading is used in order to resolve finer flow structures in the boundary layer. Thus, the minimum mesh size argument does not hold true for precursor simulations. On this note, using mesh grading may deliver better spatial and temporal correlations within the inlet conditions of the wind tunnel's test section. Details of the nonuniform mesh grading is discussed in the OpenFOAM user guide.

Further, in order to investigate the effects of mesh on the results, case W2 is subjected to the mesh dependency (convergence) study. Where the domain of channel flow is discretized with three different mesh sizes for the precursor LES of the channel flow with W2 setup. The mesh information is summarized in table 6.3. It should be noted that the total size of the mesh in table 6.3 is twice the value that can be calculated by the number of cells along the axes. This is due to the fact that the channel flow domain is comprised of two blocks; One in the upper half and the other in the lower half. Separation of the blocks is done in order to benefit from the mesh grading capability embedded in OpenFOAM which provides smaller mesh sizes near the wall boundaries with the same number

Table 6.3: Details of the computational mesh used in precursor LES of the channel flow.

Case	Mesh	Cells	Grading	$\Delta x\ (mm)$	$\Delta y\ (mm)$	$\Delta z_{min}\ (mm)$	# Cells
W2	CM1	80×60×40	10.703	50	50	6.14	384000
	CM2	80×60×100	10.703	50	50	2.47	960000
	CM3	80×60×100	500	50	50	0.127	960000
W1	CM1	80×60×100	500	50	50	0.127	960000

of cells. Figure 6.2 shows the CM3 mesh of the precursor LES of the channel flow from different view angles.

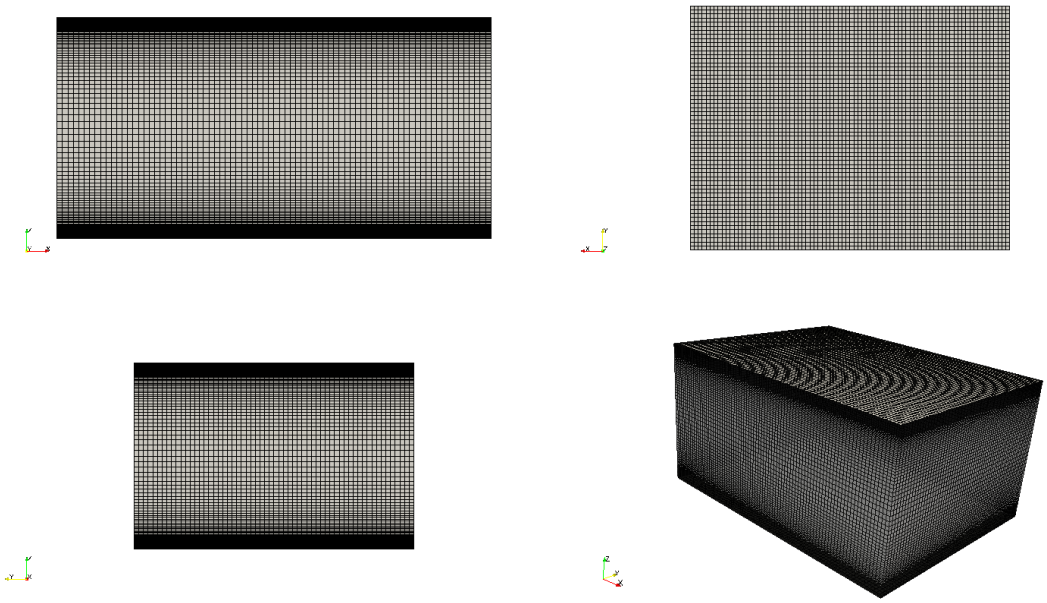

Figure 6.2: Graphical representation of the CM3 mesh from different view angles. From top left to bottom right, side view angle in $x-z$, top view angle in $x-y$ plane, side view angle in $y-z$ plane, and finally an azimuth view.

Since the computational domain has to be finite, certain type of boundary conditions are required in order to simulate a channel flow of infinite size in the streamwise and spanwise directions such that it satisfies the channel flow conditions discussed in section 6.2.1.1. To this end, periodic boundary conditions, cyclic type in OpenFOAM terminology, are introduced which physically connects the cell faces at $x = -5\,m$ with the ones at $x = l_x = -1\,m$. The second pair, connects the cell faces at $y = -1.5\,m$ with cell faces at $y = 1.5\,m$. Figure 6.3, illustrates the connectivity of

these boundary conditions in the precursor simulations of the channel and pipe flow along with their position throughout the main domain.

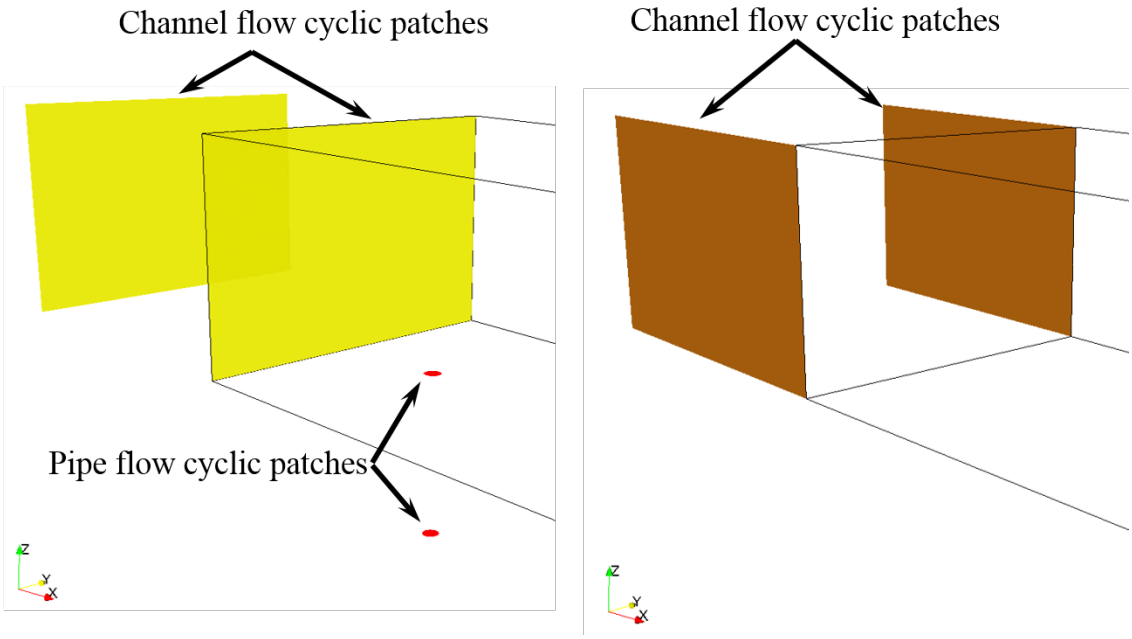

Figure 6.3: Shown are the pairs of periodic (cyclic) boundary conditions used in the precursor simulations. In OpenFOAM terminology, patch stands for boundary surface.

Other boundaries are of the wall type where the resolved GS velocity ($\bar{U}$) should be zero due to the no-slip conditions of the walls. Subsequently the no-slip condition applies to the unresolved (SGS) velocity field ($\vec{U}''$) which requires that $k_{sgs} = 0$ on the walls. As a result of Dirichlet boundary condition (no-slip) on the walls, the Von Neumann type boundary condition should be implemented on the pressure at the walls. Table 6.4 summarizes the boundary conditions on the SG parameters of the domain.

In order to meet the target initial conditions in the channel, at the start of simulations, the inlet is fed with the experimentally measured vertical profile of the streamwise velocity, and the spanwise and vertical velocities are put equal to zero. In addition, the fully developed turbulent velocity profile around the experimentally measured mean velocity is generated using the digital filtering method of Klein et al. [2003]. This not only generates accurate turbulence intensities inside the domain but also reduces the required flushing time for the flow development significantly [Ruiz

Table 6.4: Summary of the utilized boundary conditions in precursor LES of the channel flow. Here, n denotes the normal vector to the patch surface.

Patch name	Type	Pair	$\bar{U}$	$\bar{p}$	k_{sgs}	ν_{sgs}
inletABL	cyclic	outlet	—	—	—	—
outlet	cyclic	inletABL	—	—	—	—
floorWall	wall	—	0	$\partial\bar{p}/\partial n = 0$	0	$\partial\nu_{sgs}/\partial n = 0$
atmosphere	wall	—	0	$\partial\bar{p}/\partial n = 0$	0	$\partial\nu_{sgs}/\partial n = 0$
leftSideWall	cyclic	rightSideWall	—	—	—	—
rightSideWall	cyclic	leftSideWall	—	—	—	—

et al., 2015]. Nonetheless, in our simulations the flushing time is considered to be 10 flow revolutions.

As explained before, due to the special form of the velocity profile (generated in wind tunnel experiments) and *a-priori* unknown parameters, the pressure gradient is not utilized as an initial condition of the precursor simulations. Instead, the bulk velocity $\bar{U}_b$ is used. However, the pressure gradient has to be computed in order to keep the momentum of the flow constant otherwise the flow will retard after several revolutions until eventually it stops. This is resolved by adding an additional external force term into the momentum equation. The virtual force, whose magnitude is calculated at each time step based on the prescribed bulk velocity, drives the flow. The employed OpenFOAM algorithm re-calculates $\bar{U}_b$ after each time step and implements the adjustments to the virtual force in order to keep the bulk velocity constant. This is done because of the pressure outlet boundary condition at the outlet patch.

The initial time-step Δt was calculated to keep the Courant number [Ferziger and Peric, 2012] below one. For CM1-CM3 meshes in W2 case, Δt is chosen to be $0.01\,s$, $0.001\,s$, and $5\times10^{-4}\,s$, respectively. Also, for case W1 the time step was $8 \times 10^{-4}\ s$. However, the *pisoFoam* solver in OpenFOAM has an embedded ability to adjust the run time for a predefined Courant number throughout the simulation time; see OpenFOAM user guide. This leads to the efficient use of the computational resources. For all precursor LES of the channel flow the target Courant number is 0.9.

6.2.5.2 Precursor LES of the pipe flow

Similar to the channel flow, physical properties of the computational domain in the precursor LES of the pipe flow are given in table 6.5. Given the periodic boundary conditions of the pipe

Table 6.5: Physical properties of the precursor LES of the pipe flows.

Parameter	Notation	Value	Units
Pipe diameter	D	0.152	m
Pipe length	$l_p = 10D$	1.52	m
Kinematic viscosity	ν	1.568×10^{-5}	m^2/s

(see lower part of figure 6.3) and that $\delta = D/2$, the prescribed conditions of the pipe flow are met; See section 6.2.5.1. Later, posterior analysis will show that $l_p = 10D$ is large enough to contain the largest produced eddies. Table 6.6 shows the input parameters (initial conditions) of the pipe flow in precursor simulations.

Table 6.6: Input parameters of the pipe flow precursor simulations.

Pipe flow setup	$U_{j\|r=0}\,(m/s)$	$\delta\,(m)$	$U_b\,(m/s)$	Re_b
I5-O3	9.00	0.076	2.919	1.4194×10^4
I10-O5	12.00	0.076	3.998	1.9377×10^4

Unlike the channel flow, the circular geometry of the pipe cross section cannot be easily discretized by the hexahedral computational cells. In order to resolve this issue, an O-grid mesh written in the GNU-m4 macro is utilized that enables meshing curved surfaces with hexahedral cells utilizing the *blockMesh* dictionary of OpenFOAM [Beaudoin and Jasak, 2008]. Also, consult with OpenFOAMWiki on the applications of the m4 macros in parametric mesh generation.

O-grid mesh parameters, i.e. corner and arc stretch coefficients are 0.77 and 1.05, respectively. Also, in $x - y$ plane $\Delta(x, y)_{min} = 0.000438\,m$ adjacent to the pipe's wall, and $\Delta(x, y)_{max} = 0.00268\,m$ at the centerline cells. The cell size in z direction is chosen based on the equality of the smallest eddies with the smallest size of the model firebrands which returns $\Delta z = 0.01\,m$. The resulting mesh with 1.2 million cells, that will be used for the pipe flow precursor LES, is shown on figures 6.4 & 6.5.

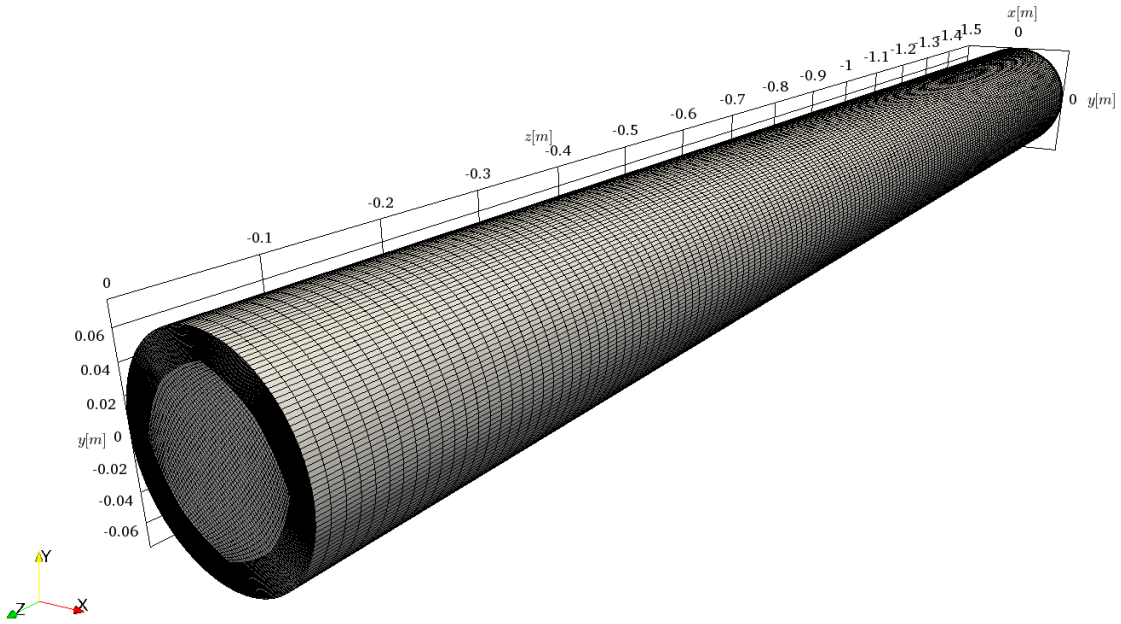

Figure 6.4: Perspective view from the pipe flow domain.

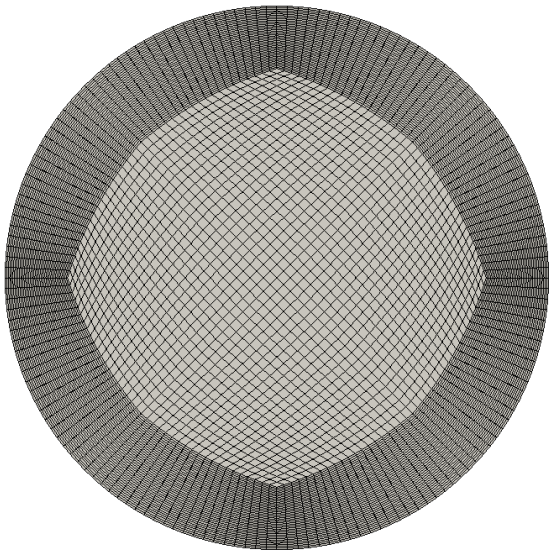

Figure 6.5: Cross-section view of the O-grid mesh used in pipe flow precursor simulations. The maximum and minimum mesh size are $0.00268\,m$ and $0.000438\,m$, respectively.

Similar to the channel flow precursor simulations, periodic boundary conditions are used for the pipe flow in order to generate a fully developed turbulent inlet velocity for the jet in the boundary layer cross-flow. The periodic boundaries, shown on figure 6.3, connect cell faces at $z = -1.5\,m$ with the cell faces at $z = 0$. Other boundary conditions are akin to what is described for channel

flow simulations. A summary of the boundary conditions for the pipe flow are given in table 6.7.

Table 6.7: Summary of the boundary conditions in precursor LES of the pipe flow where, n denotes the normal vector to the patch surface.

Patch name	Type	Pair	$\bar{U}$	$\bar{p}$	k_{sgs}	ν_{sgs}
inlet	cyclic	outlet	—	—	—	—
outlet	cyclic	inlet	—	—	—	—
pipeWall	wall	—	$\bar{U} = 0$	$\partial\bar{p}/\partial n = 0$	0	$\partial\nu_{sgs}/\partial n = 0$

The target initial conditions are satisfied using the same method discussed in section 6.2.1.1. Also, the pressure gradient is preserved by the GS bulk velocity; see the channel flow section for a detailed description of the method. The GS bulk velocity is calculated based on the time-averaged velocity fields. The time-averaging is started after the flushing time which is defined as $30\frac{D}{\overline{U}_{j|r=0}}$, according to Ruiz et al. [2015]. The flushing time values for I10-O5 and I5-O3 cases are 0.38 s and 0.51 s, respectively. However, time-averaging is started after 1 s of the flow development.

Quite like the channel flow, the initial time-steps (Δt) are obtained based on the Courant number criterion. Given that the minimum mesh size in the jet cross section is 0.000438 m, the initial time-steps for the I10-O5 and I5-O3 cases are 10×10^{-6} s, and 50×10^{-6} s, respectively. This is used along with the adaptive time-stepping capability of the `pisoFoam` solver to keep the Courant number approximately 0.9.

Calculated velocity fields at the outlet boundary of the channel and the pipe domain are issued, after their flushing time, as the inlet boundary conditions for the LES of the velocity field in the wind tunnel's test section. As mentioned before, the test section, velocity field is driven by the interaction of the jet and the wind tunnel boundary layer. This is similar to what is known as a jet-in-cross-flow (JICF) which has been studied extensively in the literature [Su and Mungal, 2004; Karagozian, 2010; Mahesh, 2013; Ruiz et al., 2015]. A detailed review of this type of flow is not within the scope of the present study but Margason [1993] provides a thorough review of the JICF. The difference between the previous studies and modeling the generated velocity field in the wind tunnel's test section is that for the majority of these studies the cross-flow is a uniform flow whereas in our case the cross-flow velocity is a fully developed turbulent nonuniform boundary layer. In the

next subsection, the model development procedure for LES of the velocity field in the main domain is explained.

6.2.5.3 Jet in nonuniform (boundary layer) cross-flow (JINCF)

Release of a round jet in cross flow has been a focus of many researchers because of its ubiquitous applications in engineering problems ranging from pollutant dispersion to designing combustion chambers. Although dimensional analysis [Baines and Keffer, 1963; Fischer et al., 1979; Tohidi and Kaye, 2016] can provide invaluable and accurate insights about the entrainment mechanisms and the time-averaged path of the jet's envelope through the boundary layer, it is of limited practical use especially in firebrand transport where unsteadiness of the flow affects the flight of firebrands. Thus, in order to account for the effects of spatial and temporal variations present in the wind tunnel experiments, the generated velocity field which is a jet in nonuniform boundary layer cross-flow (JINCF) is simulated using LES.

Physical properties of the simulated cases, which are combinations of the channel and pipe flow, are given in table 6.8. Also, the input parameters (initial conditions) of the model that

Table 6.8: Specifics of the JINCF computational domain.

Parameter	Notation	Value	Units
Streamwise length	l_x	5	m
Spanwise length	l_y	3	m
Height	h	2.032	m
Kinematic viscosity	ν	1.568×10^{-5}	m^2/s

are outputs of the precursor simulations of the channel and pipe flow are shown in table 6.9. In

Table 6.9: Input (initial) parameters in the LES of the main domain.

Case name	Boundary layer			Round jet		
	$U_0\ (m/s)$	$z_0\ (m)$	$U_{b,BL}\ (m/s)$	$U_{j\|r=0}$	$D\ (m)$	$U_{b,j}\ (m)$
W1-I5-O3	2.23	0.04	3.22	9.00	0.152	2.919
W2-I10-O5	2.85	0.04	4.42	12.00	0.152	3.998

addition, based on the dimensional analysis in Tohidi and Kaye [2016] and chapter 4, embedded non-dimensional parameters that affect the bending behavior of the jet are presented in table 6.10 along with the flow-through time scales for the jet and the boundary layer which are t_j and t_{BL},

respectively; See Ruiz et al. [2015]. Through table 6.10, μ is the velocity ratio, z_m is the jet mo-

Table 6.10: Non-dimensional parameters embedded in the physics of JINCF.

Case name	Non-dimensional parameters					
	$\mu = U_0/U_{j\|r=0}$	$z_m = D/\mu$	α	ξ_m	$t_j = h/U_{j\|r=0}$	$t_{BL} = l_x/U_0$
W1-I5-O3	0.247	0.615	0.16	1.56	0.226	2.24
W2-I10-O5	0.238	0.639	0.19	1.71	0.169	1.75

mentum length, α is the power-law fit exponent for the boundary later, and ζ_m is the ratio of z_m in a uniform boundary layer with velocity U_0 to the z_m value in a nonuniform boundary layer, that is $(z_m/z_0 + 1)^{\alpha}$; see chapter 4 or [Tohidi and Kaye, 2016]. Since reported values for ζ_m are greater than one, this confirms that it is necessary to consider vertical variations of velocity through the boundary layer in the LES of the wind tunnel experiments [Tohidi and Kaye, 2016].

As for of discretizing the computational domain, the mesh size is increased to $0.01m$ throughout the entire domain except the bounding strips of the jet, as can be seen in figure 6.2. This results in $11,696,860$ number of cells with $34,944,452$ internal faces through which flux calculations are done. The logic behind increasing the mesh size is explained in subsection 6.2.1.1. In addition, using a uniform spacing in all spatial directions does not require any *a-priori* knowledge of the jet centerline trajectory. Further, given that the mesh is parametric and written using GNU-m4 macros, this enables one to control the accuracy by just changing a single parameter. In this regard, no mesh-independence study is conducted, since the maximum cell size and subsequently the smallest resolved eddy are already smaller than the largest area of the released model firebrands through the wind tunnel experiments.

Since the main attempt is to simulate the velocity field as close as possible to the generated JINCF through lofting and downwind transport experiments in the wind tunnel test section (Chapter 5), the implemented boundary conditions are such that the side walls as well as the floor and ceiling are all considered to be of Dirichlet type, i.e. no-slip. Also, at the ending face (outlet) of the domain where the wind tunnel test section opens to the ambient and outflow condition occurs, the pressure is set to zero. This implies that the obtained pressure field is relative to the ambient. For the outflow condition the outflow velocity gradient $\partial U/\partial n+$ is set to be zero while no inlet flow is allowed

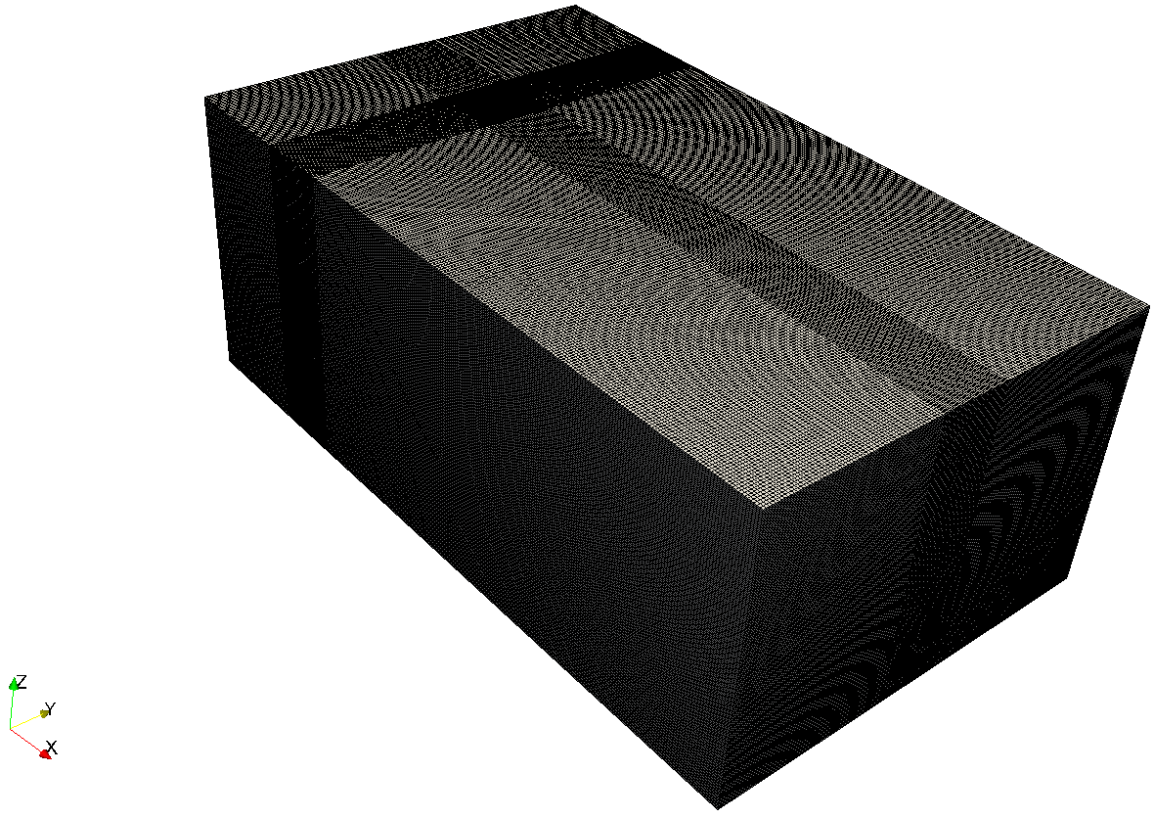

Figure 6.6: Perspective view of the computational domain discretized with hexahedral cells. Throughout the wind tunnel test section, the mesh size is kept uniform ($\Delta x = \Delta y = \Delta z = 0.01\,m$) except the jet bounding strips where the minimum and maximum mesh size are $0.00268\,m$ and $0.000438\,m$, respectively. The total number of cells is $11,696,860$ with $34,944,452$ internal faces.

through the outlet, i.e. $U_{n-} = 0$. This mixed boundary condition in OpenFOAM terminology is called `inletOutlet`. The prescribed inlet-outlet condition is also implemented on the resolved turbulent kinetic energy (k_{sgs}). The boundary conditions are summarized in table 6.11.

With the given mesh resolution, the adaptive time-stepping capability of the *pisoFoam* is used with the initial time steps of $1.5 \times 10^{-4}\,s$ and $4 \times 10^{-5}\,s$ for W1-I5-O3 and W2-I10-O5 cases, respectively. The simulations are initiated with issuing the boundary layer cross-flow and the jet into the domain simultaneously. In order to reach a quasi-steady state, the results are recorded after 20 $h/U_{j|r=0}$ seconds from the start of simulations with $0.01\,s$ intervals. This allows for both flow types to extrude over the domain, and initial turbulent intensities to flush out. The captured velocity field, for $3\,s$, is then coupled with the fully deterministic 3D 6-D.O.F. firebrand/debris transport model of Richards et al. [2008] which is developed in the MATLAB environment based on the work of Grayson and

Table 6.11: Summary of the implemented boundary conditions in LES of the wind tunnel test section.

Patch name	$\bar{U}$	$\bar{p}$	k_{sgs}	ν_{sgs}
inletABL	$U_0(\frac{z}{z_0})^{\alpha}$	P.S.C.F	P.S.C.F	P.S.C.F
inletJET	$U_{j\|r=0}e^{-4r^2/D^2}$	P.S.P.F.	P.S.P.F.	P.S.P.F.
floor	0	$\partial\bar{p}/\partial n = 0$	0	$\partial\nu_{sgs}/\partial n = 0$
sideWalls	0	$\partial\bar{p}/\partial n = 0$	0	$\partial\nu_{sgs}/\partial n = 0$
outlet	$\partial\bar{U}/\partial n+ = 0$, $U_{n-} = 0$	0	$\partial k_{sgs}/\partial n+ = 0$ $k_{sgs,n-} = 0$	$\partial\nu_{sgs}/\partial n = 0$

† **P.S.C.F.** denotes that the values are imported from precursor simulation of channel flow.

† **P.S.P.F.** denotes that the values are imported from precursor simulation of pipe flow.

† The presented velocity profiles at inlet patches are just to show the form of the velocity distribution, although the values are excerpted from correspinding precursor large eddy simulations.

Pang [2011].

6.3 Results

This section presents results of the precursor simulations as well as LES of the wind tunnel's test section.

6.3.1 Precursor LES

6.3.1.1 Channel flow

Precursor LES of channel flow is conducted to provide fully developed turbulent inlet boundary condition for the LES of the main computational domain. It is important to control the effect of mesh on the final results and evaluate the error from target velocity profiles, i.e. power-law fit through experimental measurements. However, due to the nature of this study, independence of the high order (greater than one) turbulence statistics are not investigated here. Therefore, a mesh-independence study is done for the W2 case on the mean velocity profiles. The data are sampled at the centerline of the channel domain at $x = -0.5\,m$ throughout the entire height of the channel. Figure 6.7 shows sampled velocity profiles of the precursor LES for the channel flow with W2 setup and mesh CM1-CM3; see table 6.3.

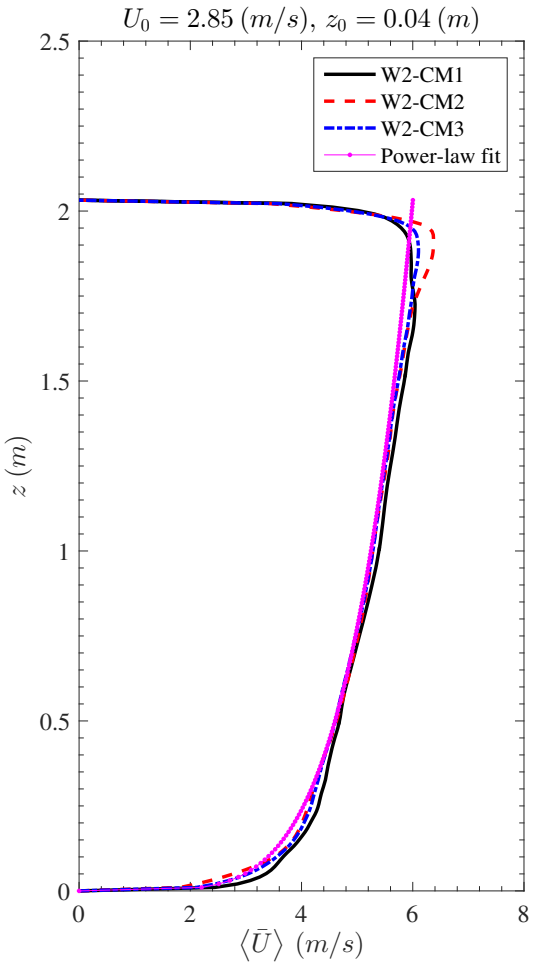

Figure 6.7: Shown are results of mesh convergence study for precursor LES of channel flow with W2 setting and three different computational mesh (CM1-CM3). See table 6.3 for details of the simulations' setup.

There is a good agreement between the time-averaged velocity profiles obtained from LES with the corresponding power-law fit to the experimental measurements. This holds true for all three meshes. Nonetheless by decreasing the mesh size in z direction from CM1 to CM3, the results show better agreement with the power-law fit velocity profile. This is shown in figure 6.8 where distribution of the relative error through height is shown. Higher percentage errors, greater than 5% margin, are observed near the walls where the velocities approach zero. Hence the first point on the obtained velocity profiles is does not match with the no-slip condition on the walls. The greater the cell size the larger this error would be as can be seen on figure 6.8 for W2-CM1. Also, high error

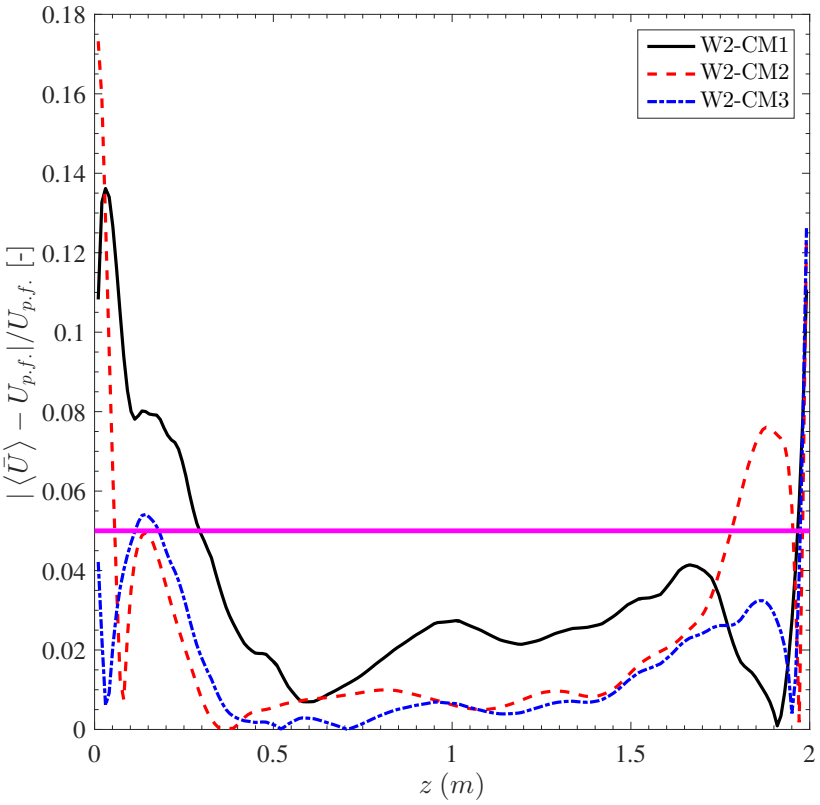

Figure 6.8: Distribution of relative error through height for mesh types CM1-CM3. See table 6.3 for details of the simulations' setup. On the vertical axes $U_{p.f.}$ stands for the power-law fit velocity profile values, and the horizontal line shows 5% error margin.

at limits of $z \to 2.032\,m$ is obtained since the power-law fit velocity profile does not account for the no-slip condition at the ceiling wall of the wind tunnel section.

For the rest of the channel height the obtained velocity profile from mesh CM3 shows the lowest percentage of error. Also, if one calculates

$$||E||_{L_2} = \sqrt{\frac{\sum_{i=1}^{N}(\langle\bar{U}(i)\rangle - U_{p.f.}(i))^2}{\sum_{i=1}^{N} U_{p.f.}(i)^2}}, \qquad i = 1, 2, ..., N$$

for each velocity profile where N is the number of points along the vertical axis, the results of L_2 relative error norm are 0.0351, 0.0185, and 0.0147 for mesh schemes CM1 to CM3, respectively. The

L_2 relative error norm values confirm that the CM3 gives the least error relative to the power-law velocity profile, and subsequently the experimental measurements. Therefore, CM3 is chosen for continuing the precursor LES for the other cases.

Utilizing the CM3 mesh through the rest of the precursor simulations of the channel flow, a comparison of the time-averaged (over 1 s), instantaneous LES resolved velocity profiles, and experimentally measured velocity profile during the wind tunnel experiments are shown in figure 6.9. Similar to mesh-convergence study, the sampling location is conducted at $x = -0.5\,m$, and $y = 0$ with z changing from $0 - h$. There is very good agreement between the time-averaged, instantaneous and experimentally measured velocity profiles as it is evident in figure 6.9.

Figure 6.9 indicates that the adopted LES approach provides adequate results in predicting the generated boundary layer velocity profile in the wind tunnel experiments. In this regard, the developed velocity field through the precursor LES of the channel flow is shown in figure 6.10. Snapshots of the flow are from LES of the wind tunnel boundary layer with W2 setting.
The developed flow structures near the walls, due to turbulence, can be observed by the vorticity structures in figure 6.11.

6.3.1.2 Pipe flow

No mesh-convergence study is done for the pipe flow precursor simulations in that the size of mesh in the pipe cross section is already very small compared to the channel flow.

Comparison of the precursor LES results in pipe flow with velocity measurements at the jet nozzle is shown below at figure 6.12. As can be seen there is an excellent agreement between the time-averaged velocity profiles ($\langle \bar{U} \rangle$), and corresponding profile of the instantaneous resolved velocity ($\bar{U}$) with the experiments.

In addition, the developed velocity field through the pipe precursor domain is illustrated by contour plots of the velocity at the centerline plane $z - y$, in figure 6.13. Further, the vorticity structures on the pipe wall is shown below on figure 6.14.

The veracity of the obtained velocity fields from precursor Large Eddy Simulations is shown by comparisons against the experimental data. Also, the flow structures signify that results account

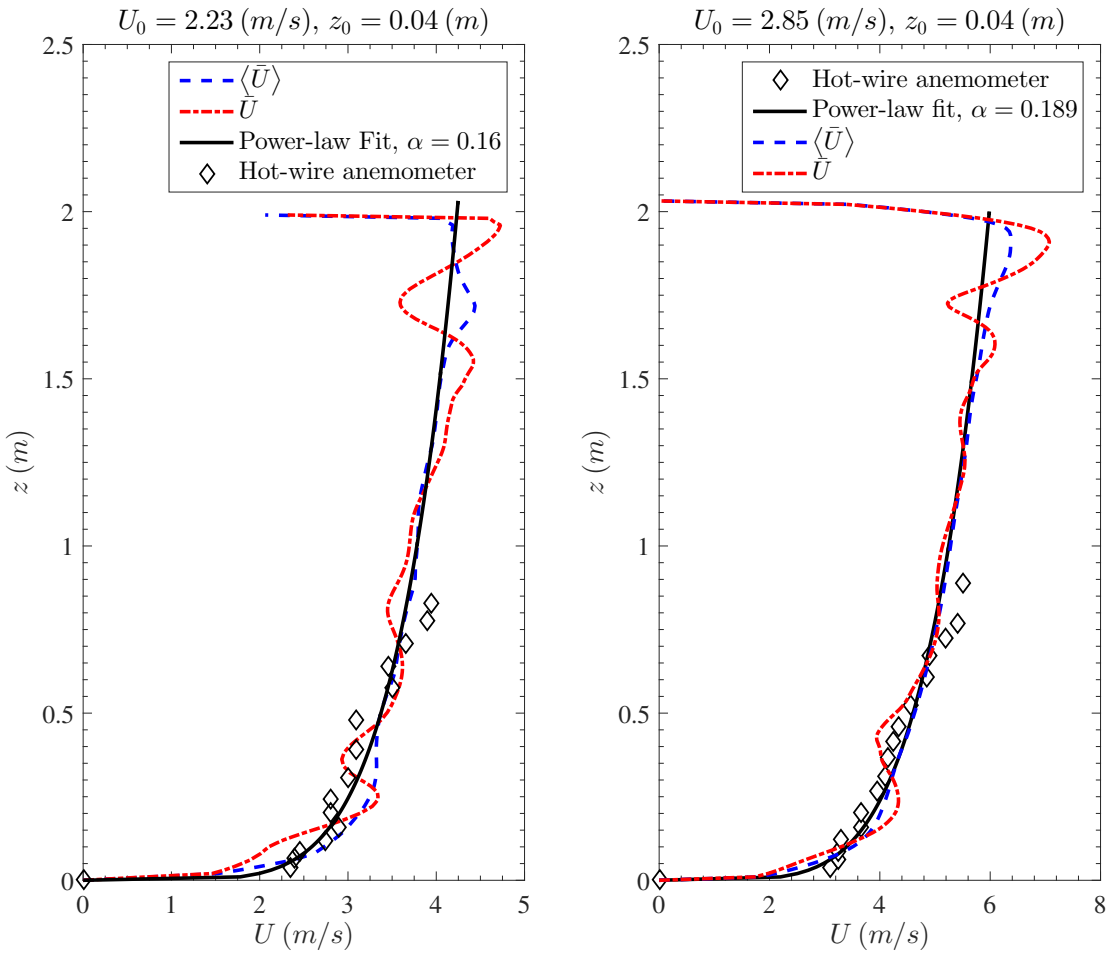

Figure 6.9: Comparison of boundary layer velocity profile throughout the height of the wind tunnel section with results from precursor LES of the channel flow for boundary layer setup W1 (left) and W2 (right). The computational mesh is CM3.

for the spatial and temporal variations of the velocity fields and, they can be issued as the inlet boundary conditions to the main computational domain.

6.3.1.3 LES of the main domain

The main objective of this section is to show that the turbulence is accurately resolved, by LES, for the JINCF in wind tunnel experiments. To this end, figure 6.15 shows the resolved SGS parameters of the case W1-I5-O3 where the boundary layer reference velocity is 2.85 (m/s) and the jet centerline is 9 (m/s). Specifics of the cases are provided in table 6.9. One can observe, from

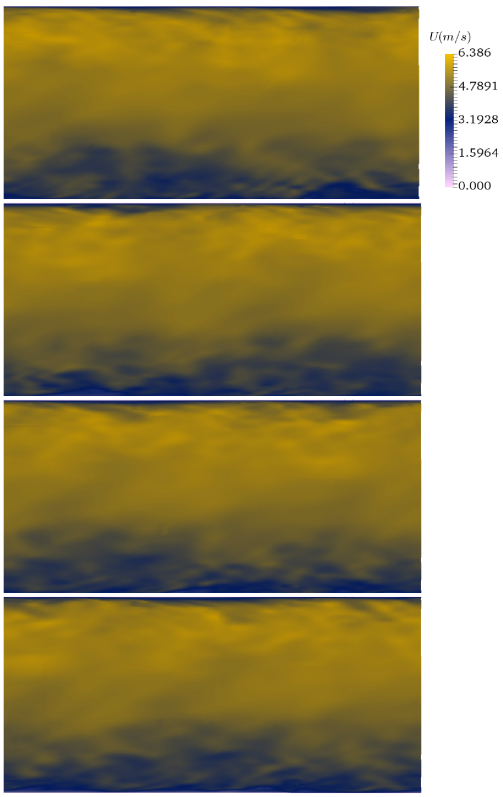

Figure 6.10: Development of the boundary layer velocity field (in $x-z$ centerline plane) where the reference velocity is 2.85 (m/s) at 0.04 m reference height. From top to bottom, shown are the contour plots of velocity at 20.06, 20.12, 20.18, and $20.24 h/U_{j|r=0}$ time unit after the start of simulations. The equivalent time interval is 0.01 s.

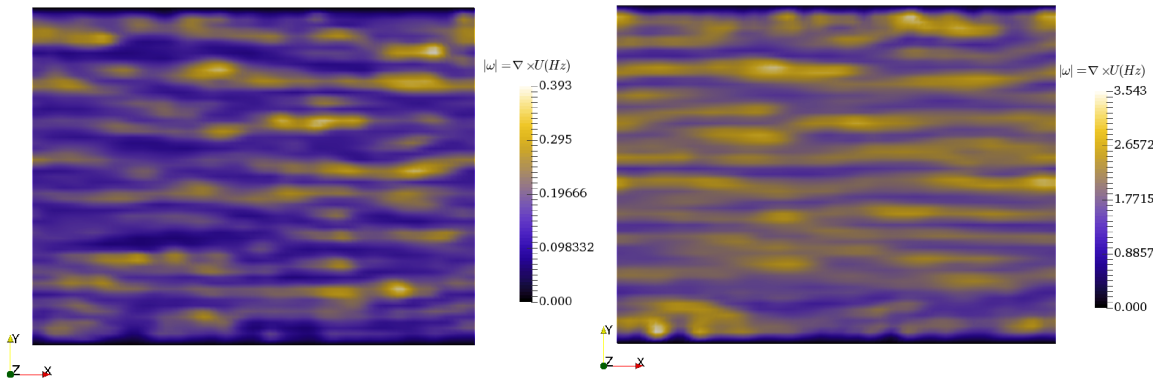

Figure 6.11: Sample vorticity structures over the floor (left) and ceiling (right) walls of the channel flow domain.

contour plots of k_{sgs} and ν_{sgs}, the disturbances in the jet shear layer at the near-field of the bent-over jet envelope. These disturbances are generated by span-wise rollers [Yuan and Street, 1998]

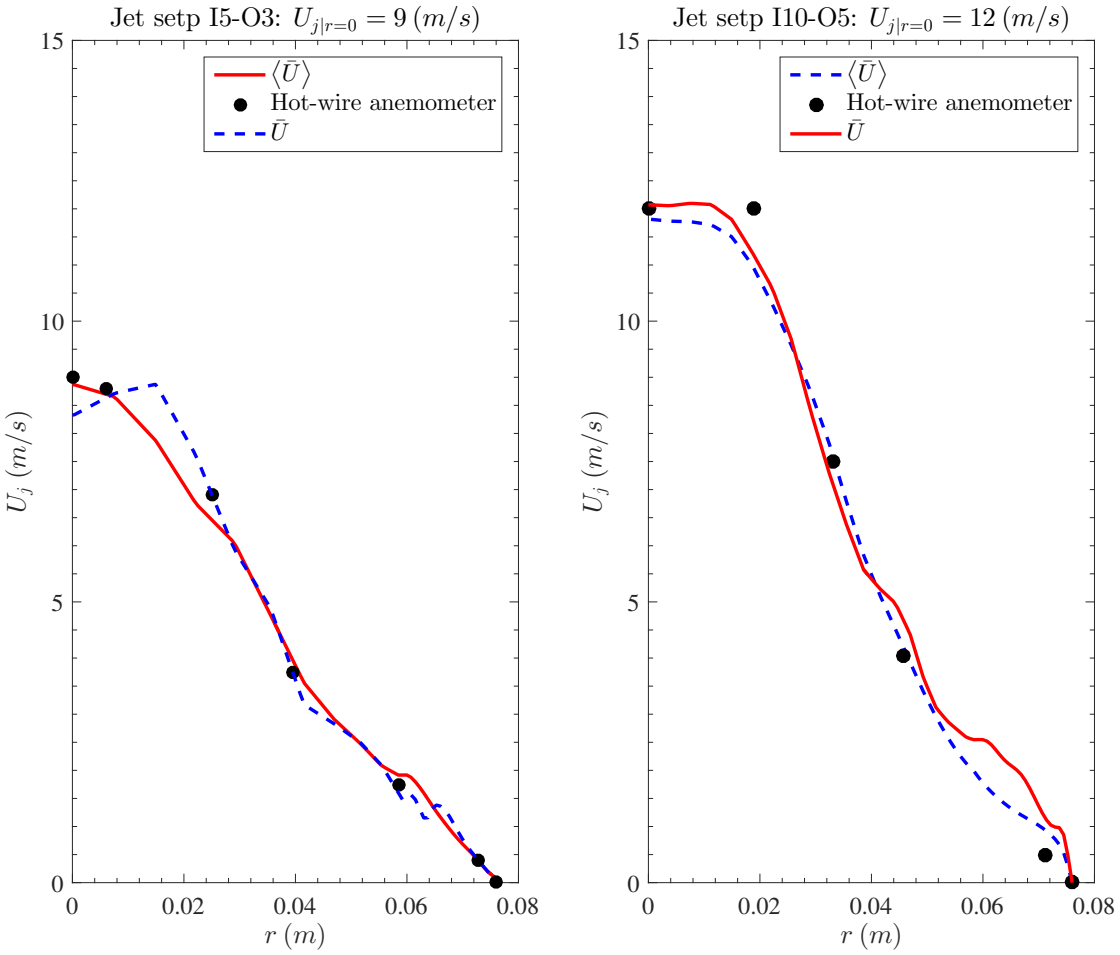

Figure 6.12: Comparison of the time-averaged and instantaneous pipe flow cross section velocity profiles with experimental measurements in the cases with centerline velocity $U_{j|r=0} = 9.0\,(m/s)$ (left) and $U_{j|r=0} = 12.0\,(m/s)$ (right).

which develop due to Kelvin-Helmholtz instability. As vorticity contours demonstrate, in immediate wake of the jet, where intermittent separation occurs. This can be attributed to the development of the counter-rotating vortex-pairs which entrain ambient fluid from the edges of the jet into the envelope. Further downstream, as the jet bends over due to the imposed pressure forces by the boundary layer, formation of wake vortices can be seen [Yuan and Street, 1998; Ruiz et al., 2015]. It should be mentioned that through the bounding box of the jet in computational domain, there is an area with small amplitude noise in the contours. This is due to the fact that, in this region the mesh size is very small such that it generates noticeable gradients.

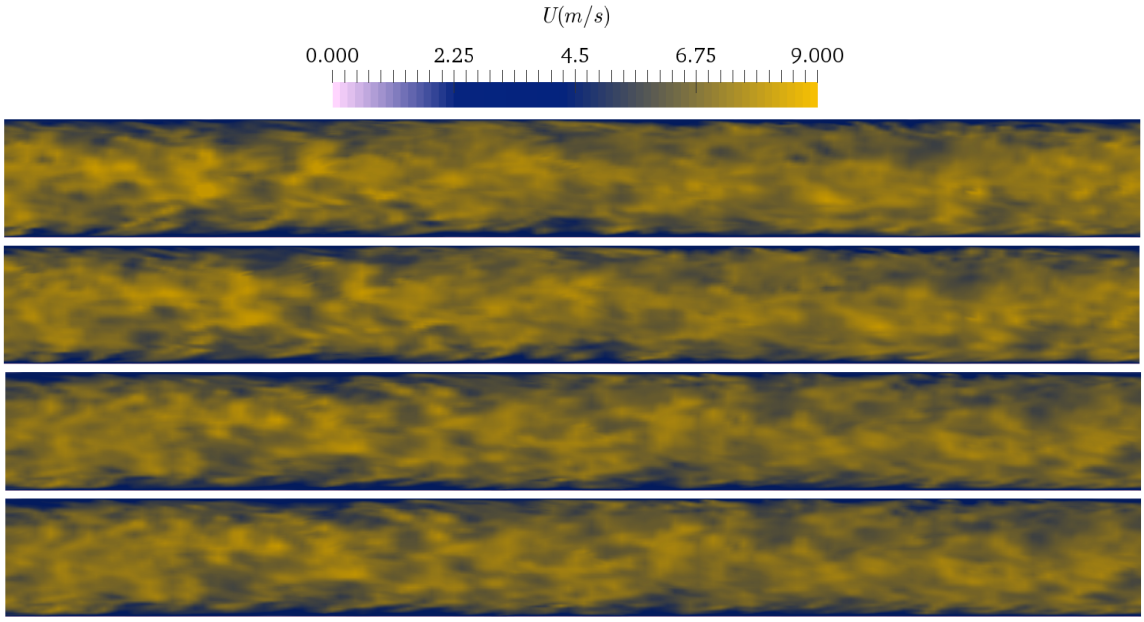

Figure 6.13: Development of the boundary layer velocity field (in $z-y$ centerline plane) for the pipe flow $U_{j|r=0} = 9\,(m/s)$. From top to bottom, shown are the contour plots of velocity at 10.06, 10.12, 10.18, and $10.24(h/U_{j|r=0})$ time unit after the start of simulations. The equivalent time interval is $0.01\ s$.

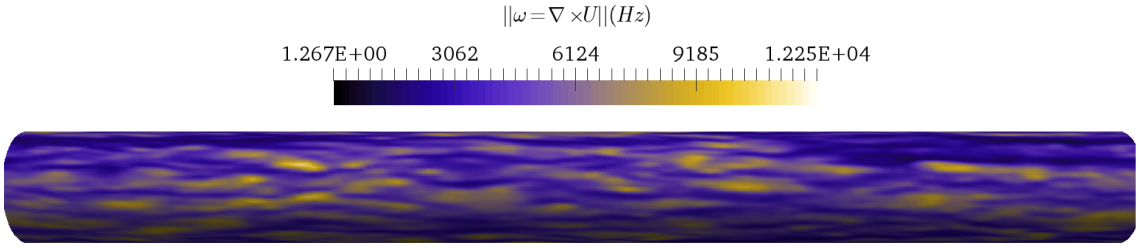

Figure 6.14: Developed vorticity structures on the pipe wall in the precursor LES of the pipe with setting I5-O3; see table 6.6 for more details.

Although it is difficult to recognize these processes from velocity contours, as complementary information, the instantaneous and time-averaged velocity contours within the symmetry plane of the domain along with the corresponding instantaneous pressure distribution are shown in figure 6.16.

Having experimentally validated the inflow condition of the computational domain, we can now examine and compare topology (coherent structures) of the resulting flow with previous experimental and numerical studies conducted on JICF [Freymuth, 1966; Becker and Massaro, 1968; Fric and Roshko, 1994]. Depending on the dominant dimensionless number (Reynolds, density ra-

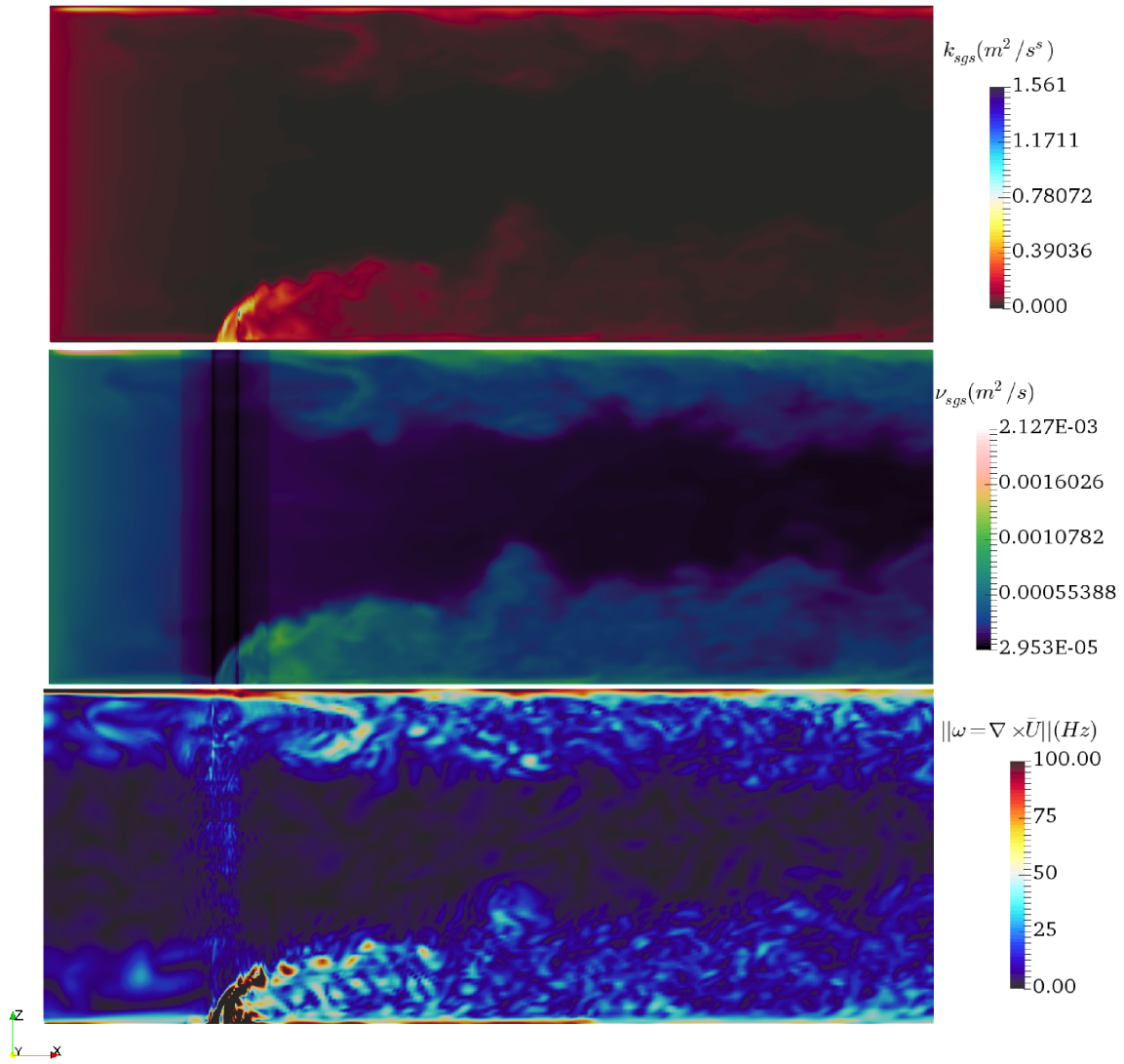

Figure 6.15: From top to bottom, shown are the contour plots of SGS turbulent kinetic velocity (k_{sgs}), and turbulent viscosity (ν_{sgs}) along with vorticity contours (ω). Results are excerpted from the symmetry plane of the computational domain, i.e. $y = 0$, at $3\,s$ after the flushing time.

tio, velocity ratio) certain class of turbulent structures are stronger [Jeong and Hussain, 1995; Ruiz et al., 2015]. Thus, in order to examine the main turbulent structures, Q-criterion is utilized [Jeong and Hussain, 1995]. The Q-criterion defines a vortex as a coherent fluid region with positive second invariant of $\nabla \bar{U}$ [Hunt et al., 1988]. This, also, requires the vortex pressure to be lower than the ambient pressure [Kolář, 2007]. Indeed, this criterion shows the local balance between shear strain rate and the vorticity magnitude, and defines vortices as flow regions where vorticity magnitude is greater than the magnitude of the rate of strain [Kolář, 2007; Holmén, 2012]. Here, Q-criterion is

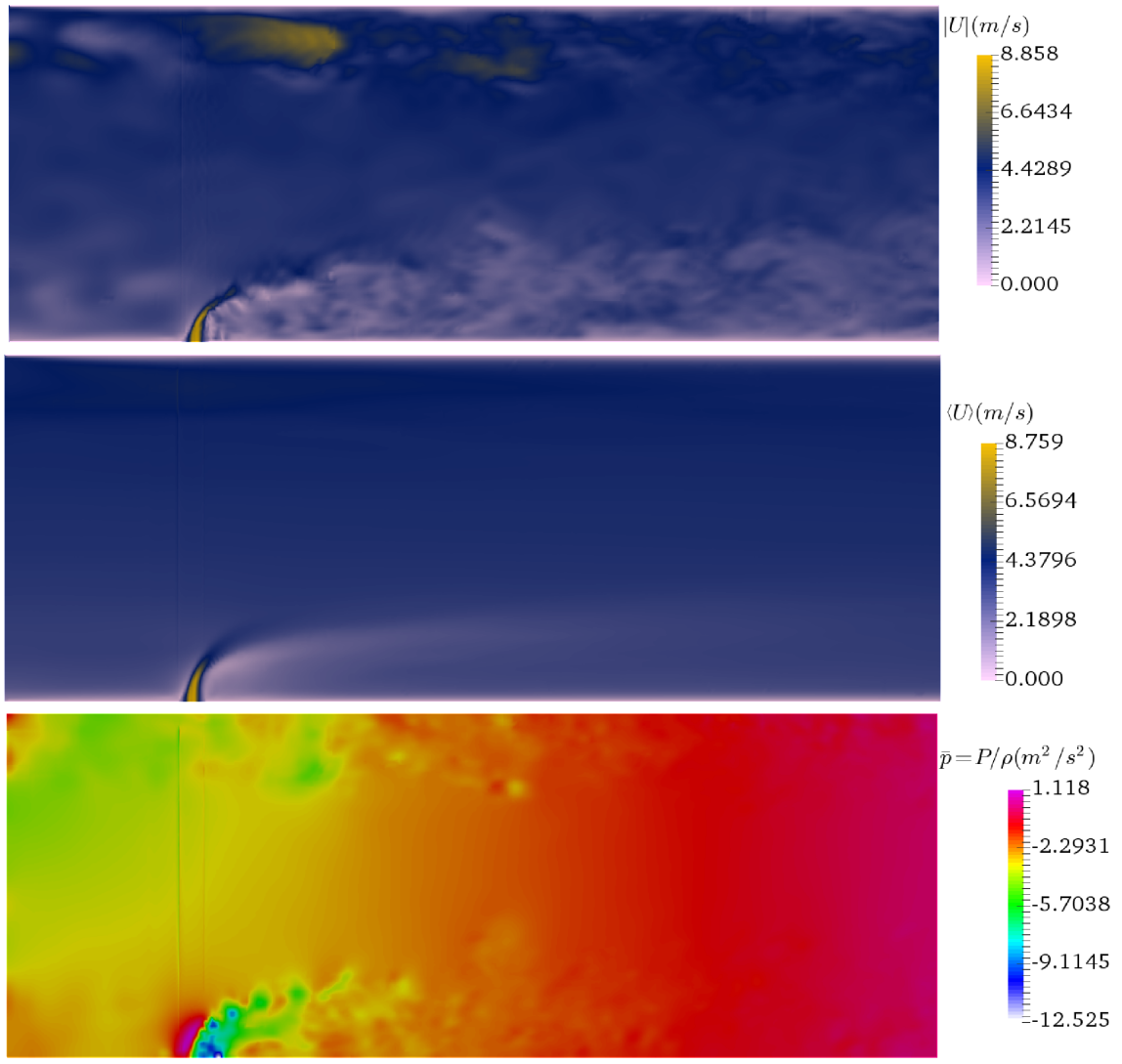

Figure 6.16: From top to bottom, shown are the contour plots of resolved instantaneous turbulent velocity field ($\bar{U}$), and time-averaged velocity field ($\langle \bar{U} \rangle$) along with the corresponding resolved instantaneous kinematic pressure ($\bar{p} = P/rho$). Results are excerpted from the symmetry plane of the computational domain, i.e. $y = 0$, at 3 s after the flushing time.

applied to the LES instantaneous velocity field of JINCF at the wind tunnel's test section.

Following the classification of Ruiz et al. [2015], four main classes of vortices observed in the current simulations are Ring-, Horse-shoe, V-shape, and Counter-rotating vortices. Figure 6.17 & 6.18 show coherent structures of the flow field by applying the Q-criterion on the instantaneous velocity fields that are resolved from LES of the W1-I5-O3 and W2-I10-O5 cases, respectively. The

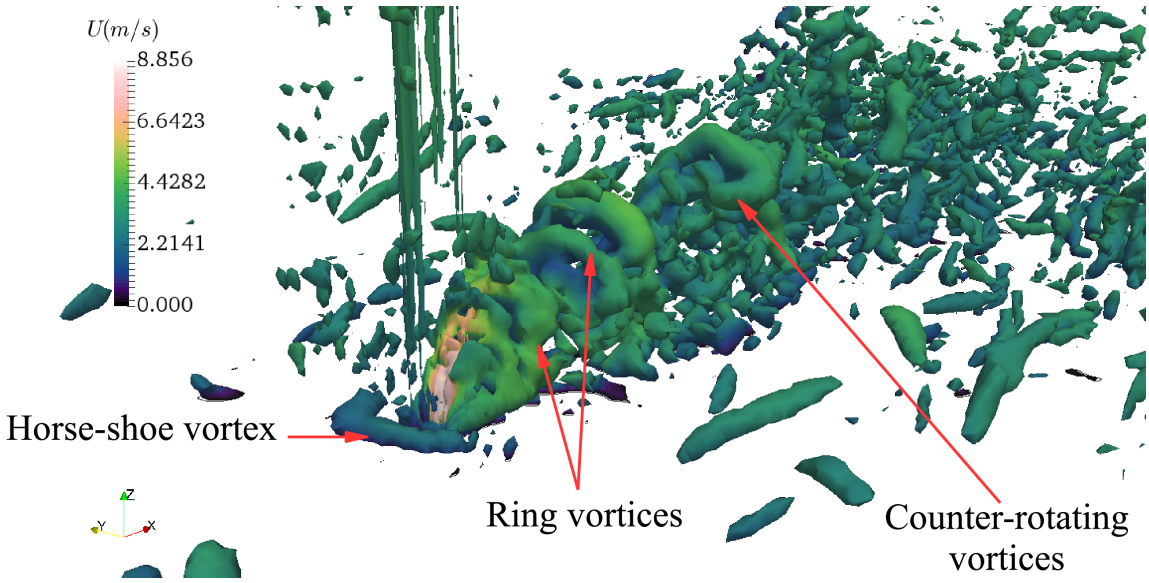

Figure 6.17: Obtained coherent structures of the JINCF in case W1-I5-O3 with iso-surfaces of the Q-criterion, where $Q = 100$ and iso-surfaces are color coded with instantaneous velocity contours.

ring-vortices, also known as shear-layer-vortices, form due to Kelvin-Helmholtz instability through shear between the edges of the jet envelope and the ambient fluid (shear layer). These types of structures can be observed in the near-field of the jet shear layer, as shown on figure 6.17, and has been studied extensively [Jones and Launder, 1972; Kolář, 2007; Holmén, 2012; Ruiz et al., 2015]. The next identified class are the large counter-rotating vortices in the wake of the JINCF. This is shown in figure 6.17. These vortices entrain ambient fluid into the centerline of the jet through the shear-layer. Quite like ring-vortices, this type is also identified through both numerical and experimental investigations [Keffer and Baines, 1963; Kamotani and Greber, 1972].

According to Ruiz et al. [2015], the v-shape vortices are instabilities that are generated by the growth of an azimuthal instability in the ring-vortices. This class is also identified in these LES simulations of JINCF; see figure 6.18. As v-shape vorticies grow through time, they produce tiny counter-rotating vortex pairs whose rotational axis is parallel to the jet envelope's centerliine [Broze and Hussain, 1996; da Silva and Métais, 2002]. Here we failed to identify these subsequent vortices because of the relatively low resolution of the computational mesh.

Lastly, the Horse-shoe vortices are identified; see figure 6.17 & 6.18. This type of vortex

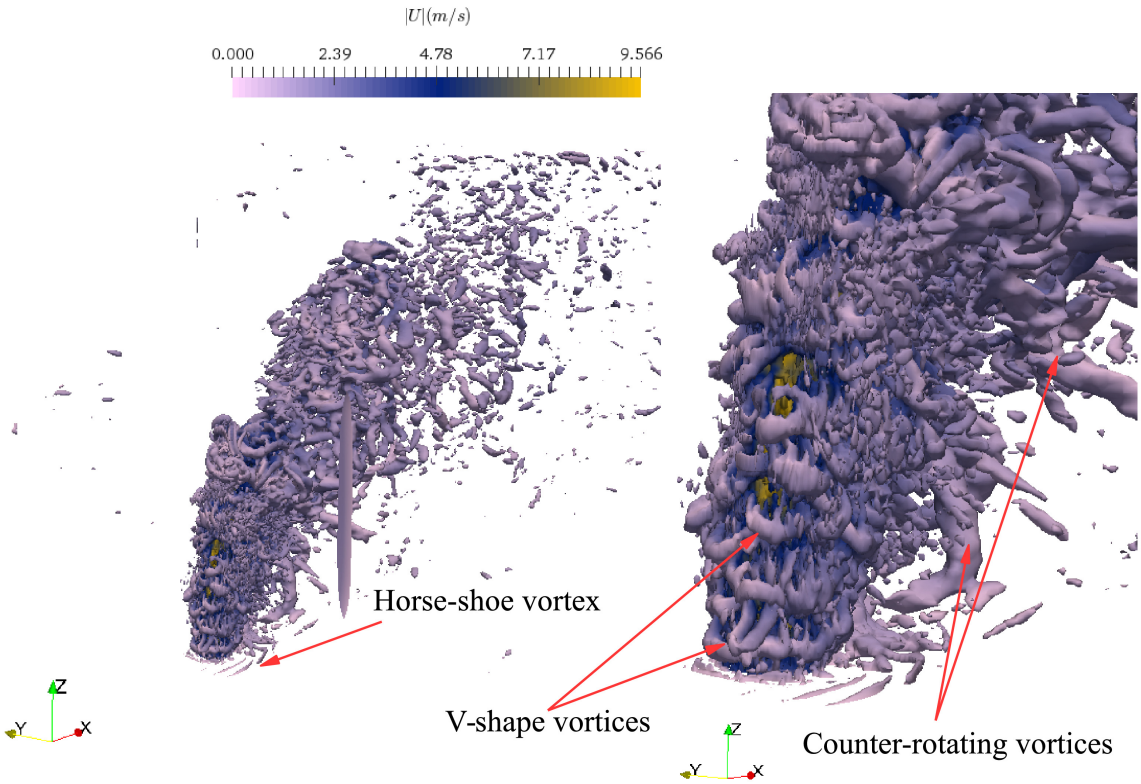

Figure 6.18: (Left) Obtained coherent structures of the JINCF in case W2-I10-O5 with iso-surfaces of the Q-criterion, where $Q = 175$ and iso-surfaces are color coded with instantaneous velocity contours. (Right) Close-up view of the iso-surfaces at near-field.

structure is very stable and forms at the upstream of the jet exit [Ruiz et al., 2015]. The horse-shoe vortices result from the varying stagnation pressure that is due to the generated adverse pressure-gradient by the non-uniform cross-flow on the jet's envelope [Yuan and Street, 1998]. However, they do not show significant influence on the velocity field far from the walls which is of interest in modeling firebrand transport.

The identified topologies from the results of LES corroborate with experimental and numerical findings in the literature. This implies that the generated velocity field accounts for the spatial and temporal variations of the velocity field of the JINCF with acceptable accuracy for modeling lofting and downwind transport of model firebrands in wind tunnel experiments.

6.4 Coupling LES with the transport model

The resolved velocity field from the LES can be coupled to the fully deterministic 3D 6-D.O.F. firebrand transport model. This delivers a 3D coupled stochastic parametric 6-D.O.F. firebrand/debris transport model that can be used to predict the statistics of the firebrand flight during wildfires and subsequently wildfire spread via fire spotting phenomenon. Eventually the model helps to map the associated risks with fire spotting phenomenon during wildfires.

The coupling procedure is done by extracting the instantaneous and time-averaged velocity field data from LES along with the computational mesh information, i.e. position of nodes, and cell-centers. This is done on Palmetto cluster, due to the high volume of data, with a python script that launches the `pvbatch` module of `Paraview`. Utilizing `pvbatch`, velocity and mesh data can be saved as CSV files.

The obtained CSV files of velocity field and mesh data are fed into a package, developed in MATLAB environment, that does the coupling with an algorithm shown in the flowchart below. Utilizing this algorithm, the relative velocity of the model firebrands is calculated by subtracting the firebrands instantaneous velocity from the interpolated ambient velocity vector. The interpolation is done, spatially, based on the position of the centroid of the model firebrands in the computational mesh. The algorithm finds the bounding cell where the centroid is located at each time step of the transport model, as shown in figure 6.20, and then takes the average of the LES resolved velocity at each node as the ambient velocity of the firebrand. This is done for all three components of the velocity vector.

As for of the temporal coupling, since the time step in the transport model is 1/10 of the time interval during which the LES data is stored (0.01 s), it is assumed that the velocity field between these intervals is steady.

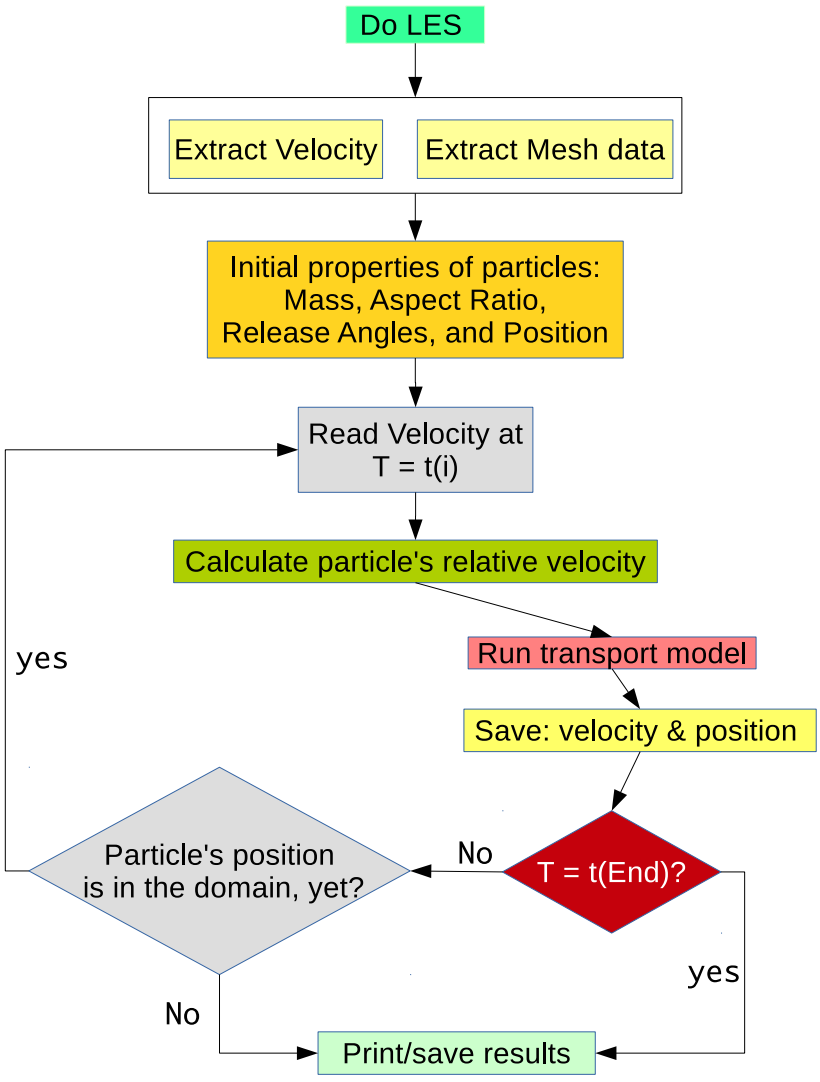

Figure 6.19: Coupling algorithm of LES data with the firebrand/debris transport model.

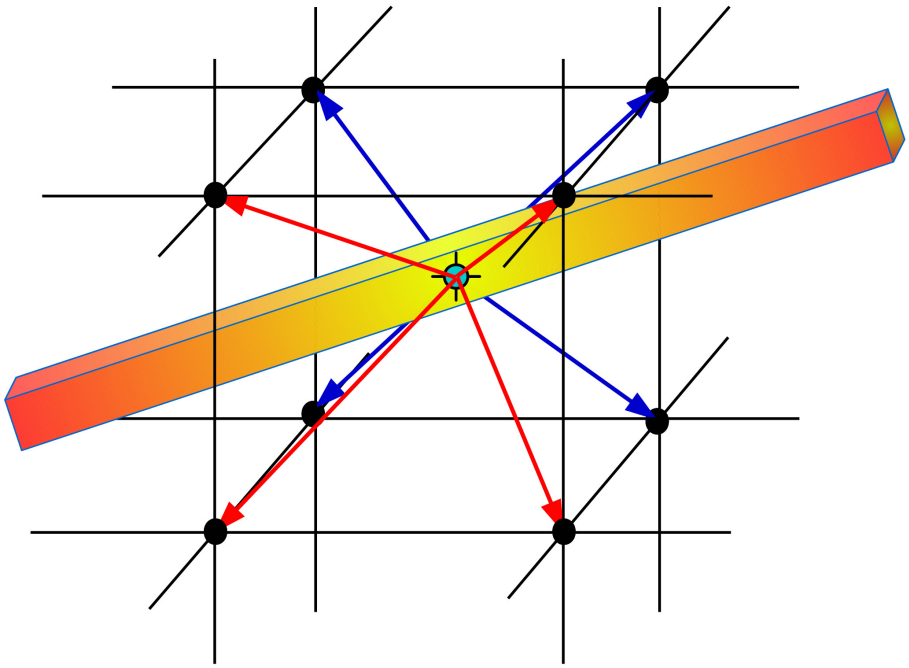

Figure 6.20: Spatial interpolation of the ambient velocity components based on the model firebrand position in the computational mesh.

Bibliography

Albini, F. A. (1979). *Spot fire distance from burning trees : a predictive model*. United States.

Aris, R. (2012). *Vectors, tensors and the basic equations of fluid mechanics*. Courier Corporation.

Baines, W. and Keffer, J. (1963). The round turbulent jet in cross wind. *J Fluid Mech*, 15:481–488.

Barr, B. W. and Ezekoye, O. (2013). Thermo-mechanical modeling of firebrand breakage on a fractal tree. *Proceedings of the Combustion Institute*, 34(2):2649–2656.

Beaudoin, M. and Jasak, H. (2008). Development of a generalized grid interface for turbomachinery simulations with openfoam. In *Open Source CFD International Conference, Berlin, Germany*, volume 468.

Becker, H. A. and Massaro, T. (1968). Vortex evolution in a round jet. *Journal of fluid mechanics*, 31(03):435–448.

Bhutia, S., Jenkins, M. A., and Sun, R. (2010). Comparison of firebrand propagation prediction by a plume model and a coupledfire/atmosphere largeeddy simulator. *Journal of Advances in Modeling Earth Systems*, 2:4.

Broze, G. and Hussain, F. (1996). Transitions to chaos in a forced jet: intermittency, tangent bifurcations and hysteresis. *Journal of Fluid Mechanics*, 311:37–71.

Charmiyan, M., Azimian, A., KeirsbulcK, L., Shirani, E., and Aloui, F. (2016). Turbulent plane impinging jet-physical insight and turbulence modeling. *Journal of Applied Fluid Mechanics*, 9.

da Silva, C. B. and Métais, O. (2002). On the influence of coherent structures upon interscale interactions in turbulent plane jets. *Journal of Fluid Mechanics*, 473:103–145.

Davidson, P. (2015). *Turbulence: an introduction for scientists and engineers*. Oxford University Press, USA.

De Villiers, E. (2007). *The potential of large eddy simulation for the modelling of wall bounded flows*. PhD thesis, Department of Mechanical Engineering, Imperial College London.

Deardorff, J. W. (1970). A numerical study of three-dimensional turbulent channel flow at large reynolds numbers. *Journal of Fluid Mechanics*, 41(02):453–480.

Duran, A., Celebi, M. S., Piskin, S., and Tuncel, M. (2015). Scalability of openfoam for bio-medical flow simulations. *The Journal of Supercomputing*, 71(3):938–951.

Fernandez-Pello, A. C. (1982). An analysis of the forced convective burning of a combustible particle. *Combustion Science and Technology*, 28(5-6):305–313.

Ferziger, J. H. and Peric, M. (2012). *Computational methods for fluid dynamics*. Springer Science & Business Media.

Fischer, H. B., List, E. J., Koh, R. C. Y., Imberger, J., Brooks, N. H., and Fisher, H. B. (1979). *Mixing in inland and coastal waters*. Academic.

Freymuth, P. (1966). On transition in a separated laminar boundary layer. *Journal of Fluid Mechanics*, 25(04):683–704.

Fric, T. and Roshko, A. (1994). Vortical structure in the wake of a transverse jet. *Journal of Fluid Mechanics*, 279:1–47.

Fureby, C., Gosman, A., Tabor, G., Weller, H., Sandham, N., and Wolfshtein, M. (1997a). Large eddy simulation of turbulent channel flows. *Turbulent shear flows*, 11:19–30.

Fureby, C., Tabor, G., Weller, H., and Gosman, A. (1997b). A comparative study of subgrid scale models in homogeneous isotropic turbulence. *Physics of Fluids (1994-present)*, 9(5):1416–1429.

Gildeh, H. K. (2014). Numerical Modeling of Turbulent Buoyant Wall Jets in Stationary Ambient Water. *Journal of Hydraulic ...*, 04014012(17).

Grayson, J. and Pang, W. C. (2011). *Development and application of a three-dimensional probabilistic wind-borne debris trajectory model*. PhD thesis, Clemson University.

Grayson, M., Pang, W., and Schiff, S. (2012). Three-dimensional probabilistic wind-borne debris trajectory model for building envelope impact risk assessment. *Journal of Wind Engineering and Industrial Aerodynamics*, 102:22–35.

Himoto, K and Tanaka, T. (2005). Transport of disk-shaped firebrands in a turbulent boundary layer author. In *the Eighth International Symposium on Fire Safety Science*, pages 18—-23.

Holmén, V. (2012). Methods for vortex identification. *Masters Theses in Mathematical Sciences*.

Holmes, J. D. (2004). Trajectories of spheres in strong winds with application to wind-borne debris. *Journal of Wind Engineering and Industrial Aerodynamics*, 92(1):9–22.

Horiuti, K. (1985). Large eddy simulation of turbulent channel flow by one-equation modeling. *Journal of the Physical Society of Japan*, 54(8):2855–2865.

Hunt, J. C., Wray, A., and Moin, P. (1988). Eddies, streams, and convergence zones in turbulent flows.

Jasak, H. (1996). *Error analysis and estimation for the finite volume method with applications to fluid flows*. PhD thesis, Imperial College London (University of London).

Jasak, H., Tukovic, Z., and Jemcov, A. (2007). OpenFOAM : A C ++ Library for Complex Physics Simulations . In *International Workshop on Coupled Methods in Numerical Dynamics*, volume m, pages 1–20, Dubrovnik, Croatia.

Jasak, H. and Weller, H. G. (1995). Interface Tracking Capabilities of the Inter-Gamma Differencing Scheme. Technical Report 2, Imperial College of Science, Technology and Medicine, London.

Jeong, J. and Hussain, F. (1995). On the identification of a vortex. *Journal of fluid mechanics*, 285:69–94.

Jones, W. P. and Launder, B. (1972). The prediction of laminarization with a two-equation model of turbulence. *International journal of heat and mass transfer*, 15(2):301–314.

Kamotani, Y. and Greber, I. (1972). Experiments on a turbulent jet in a cross flow. *AIAA journal*, 10(11):1425–1429.

Karagozian, A. R. (2010). Transverse jets and their control. *Progress in Energy and Combustion Science*, 36(5):531–553.

Keffer, J. and Baines, W. (1963). The round turbulent jet in a cross-wind. *Journal of Fluid Mechanics*, 15(04):481–496.

Kim, W.-W. and Menon, S. (1999). An unsteady incompressible navier–stokes solver for large eddy simulation of turbulent flows. *International Journal for Numerical Methods in Fluids*, 31(6):983–1017.

Klein, M., Sadiki, A., and Janicka, J. (2003). A digital filter based generation of inflow data for spatially developing direct numerical or large eddy simulations. *Journal of computational Physics*, 186(2):652–665.

Kolář, V. (2007). Vortex identification: New requirements and limitations. *International journal of heat and fluid flow*, 28(4):638–652.

Koo, E., Linn, R. R., Pagni, P. J., and Edminster, C. B. (2012). Modelling firebrand transport in wildfires using HIGRAD/FIRETEC. *International Journal of Wildland Fire*, 21(4):396–417.

Kortas, S., Mindykowski, P., Consalvi, J. L., Mhiri, H., and Porterie, B. (2009). Experimental validation of a numerical model for the transport of firebrands. *Fire Safety Journal*, 44(8):1095–1102.

Lee, S.-L. and Hellman, J. M. (1970). Firebrand trajectory study using an empirical velocity-dependent burning law. *Combustion and Flame*, 15(3):265–274.

Leonard, A. (1974). Energy cascade in large-eddy simulations of turbulent fluid flows. In *Turbulent diffusion in environmental pollution*, volume 1, pages 237–248.

Lui, P. (2015). Scalability performance analysis of openfoam on modern hpc clustering technologies.

Mahesh, K. (2013). The interaction of jets with crossflow. *Annual Review of fluid mechanics*, 45:379–407.

Margason, R. J. (1993). Fifty years of jet in cross flow research. In *In AGARD, Computational and Experimental Assessment of Jets in Cross Flow 41 p (SEE N94-28003 07-34)*, volume 1.

Moukalled, F., Mangani, L., and Darwish, M. (2015). *The finite volume method in computational fluid dynamics: An introduction with OpenFOAM and matlab*, volume 113. Fluid Mechanics and Its Applications (Springer International Publishing, 2015).

Mukha, T. and Liefvendahl, M. (2015). Large-eddy simulation of turbulent channel flow. Technical Report 2015-014.

Pope, S. B. (2000). *Turbulent Flows*. Cambridge University Press.

Pope, S. B. (2004). Ten questions concerning the large-eddy simulation of turbulent flows. *New Journal of Physics*, 6.

Richards, P. J. (2010). Steady Aerodynamics of Rod and Plate Type Debris.pdf. In *17th Australian Fluid Mechanics Conference*.

Richards, P. J., Williams, N., Laing, B., McCarty, M., and Pond, M. (2008). Numerical calculation of the three-dimensional motion of wind-borne debris. *Journal of Wind Engineering and Industrial Aerodynamics*, 96(10):2188–2202.

Rivera, O., Fürlinger, K., and Kranzlmüller, D. (2011). Investigating the scalability of openfoam for the solution of transport equations and large eddy simulations. In *Algorithms and Architectures for Parallel Processing*, pages 121–130. Springer.

Ruiz, a. M., Lacaze, G., and Oefelein, J. C. (2015). Flow topologies and turbulence scales in a jet-in-cross-flow. *Physics of Fluids*, 27(4):045101.

Rusche, H. (2003). *Computational fluid dynamics of dispersed two-phase flows at high phase fractions*. PhD thesis, Imperial College London (University of London).

Sagaut, P. (2006). *Large eddy simulation for incompressible flows: an introduction*. Springer Science & Business Media.

Sardoy, N., Consalvi, J. L., Kaiss, a., Fernandez-Pello, a. C., Porterie, B., and a.C. Fernandez-Pello (2008). Numerical study of ground-level distribution of firebrands generated by line fires. *Combustion and Flame*, 154(3):478–488.

Sardoy, N., Consalvi, J.-L., Porterie, B., and Kaiss, A. (2006). Transport and combustion of Ponderosa Pine firebrands from isolated burning trees. In *2006 1st International Symposium on Environment Identities and Mediterranean Area, ISEIM, July 9, 2006 - July 12*, pages 6–11, Corte-Ajaccio, France. Polytech'Marseille, Dept. of Mechanical Engineering, CNRS UMR 6595, Technopole Chateau-Gombert, 5 rue Enrico Fermi, 13453 Marseille, France, Inst. of Elec. and Elec. Eng. Computer Society.

Schlichting, H. and Gersten, K. (2003). *Boundary-layer theory*. Springer Science & Business Media.

Schumann, U. (1975). Subgrid scale model for finite difference simulations of turbulent flows in plane channels and annuli. *Journal of computational physics*, 18(4):376–404.

Stevens, B., Moeng, C.-H., and Sullivan, P. P. (1999). Large-eddy simulations of radiatively driven convection: Sensitivities to the representation of small scales. *Journal of the atmospheric sciences*, 56(23):3963–3984.

Su, L. and Mungal, M. (2004). Simultaneous measurements of scalar and velocity field evolution in turbulent crossflowing jets. *Journal of Fluid mechanics*, 513(1):1–45.

Tarifa, C. S., Del Notario, P. P., Moreno, F. G., and Villa, A. R. (1967). Transport and combustion of firebrands, final report of grants FG-SP-11 and FG-SP-146. *US Department of Agriculture Forest Service*.

Tarifa, C. S., Notario, P., and Moreno, F. G. (1965). On the flight paths and lifetimes of burning particles of wood. In *Symposium (international) on combustion*, volume 10, pages 1021–1037. Elsevier.

Tennekes, H. and Lumley, J. L. (1972). *A first course in turbulence*. MIT press.

Tohidi, A. and Kaye, N. B. (2016). Highly buoyant bent-over plumes in a boundary layer. *Atmospheric Environment*, 131:97–114.

Tse, S. D. and Fernandez-Pello, A. C. (1998). On the flight paths of metal particles and embers generated by power lines in high windsa potential source of wildland fires. *Fire Safety Journal*, 30(4):333–356.

Van Driest, E. R. (2012). On turbulent flow near a wall. *Journal of the Aeronautical Sciences*.

Versteeg, H. K. and Malalasekera, W. (2007). *An introduction to computational fluid dynamics: the finite volume method*. Pearson Education.

Woycheese, J. P. and Pagni, P. J. (1999). Combustion Models for Wooden Brands. In *Third International Conference on Fire Research and Engineering. Society of Fire Protection Engineers*, pages 53–71.

Yoshizawa, A. (1982). A statistically-derived subgrid model for the large-eddy simulation of turbulence. *Physics of Fluids (1958-1988)*, 25(9):1532–1538.

Yoshizawa, A. and Horiuti, K. (1985). A Statistically-derived subgrid-scale kinetic model for the Large-Eddy Simulation of turbulent flows. *Journal of physical society of japan*, 54(8):2834–2839.

Yuan, L. L. and Street, R. L. (1998). Trajectory and entrainment of a round jet in crossflow. *Physics of Fluids*, 10(9):2323–2335.

Chapter 7

Results

7.1 Introduction

This chapter presents results of the numerical simulation of the wind tunnel experiments using the developed coupled stochastic parametric model for firebrand transport. The simulations aimed at modeling two cases of the wind tunnel experiments that is W1-I5-O3 and W2-I10-O5. Specifics of the experimental cases and their corresponding numerical simulations are shown in table 7.1. In addition to modeling the aforementioned experimental cases, a set of simulations with

Table 7.1: Parameters of the simulated wind tunnel experiments where p is exponent of the power-law fit to the boundary layer velocity profile, DOF stands for the number of model firebrands released through the generated velocity fields, and R denotes the radius of the initial distribution of model firebrands within the jet nozzle area.

Case	Boundary layer			Jet	η	DOF	$R\,(cm)$	Velocity field	
	$U_0\,(m/s)$	$z_0\,(m)$	p	$U_{j\|r=0}\,(m/s)$				LES	Time-averaged LES
W1-I5-O3	2.23	0.04	0.16	9.0	1	600	5.0	✓	—
					4	600	5.0	✓	—
					6	600	5.0	✓	✓
W2-I10-O5	2.85	0.04	0.18	12.0	1	600	5.0	✓	—
					4	600	5.0	✓	—
					6	600	0, 2.5, 5, 7.6	✓	—

different release radii through the jet nozzle area are conducted in order to evaluate the sensitivity of the results to the size of the release area. Also, effects of coupling a time-averaged (steady) velocity

field with the transport model, as opposed to using the LES time resolved velocity field, on the trajectory of the model firebrands are investigated for the case shown on table 7.1. The simulations' algorithm is prescribed in chapter 6. Based on the algorithm, the detailed procedure, that is used for each case, is as follows.

According to Tohidi and Kaye [2016], since in both cases $(z_m/z_0 + 1)^p$ (where z_m is the jet momentum length scale) is greater than one, shearing effects in the boundary layer are significant in modeling the velocity field of the jet in the cross flow. Hence, the velocity fields are modeled as a jet-in-nonuniform-cross-flow (JINCF). For each case, Large Eddy Simulations (LES) of the JINCF are conducted in order to account for the spatial and temporal scales in the velocity field. Details of the LES are given in the previous chapter.

Then, the instantaneous velocity fields, which are recorded for 3 s at every 0.01 s after the flushing time, are extracted from the simulations and coupled with the transport model using the prescribed algorithm in chapter 5. Through the coupling process, physical properties of the model firebrands including dimensions of the sides, aspect ratio, and density are assigned according to the experiments; see table 7.1 or chapter 4. Next, initial conditions of the release, namely initial release angles and position of the model firebrands, are determined. The initial release angles (tait-bryan angles) are chosen randomly from a uniform distribution of $0 - 360^o$. Similarly, the initial position of the release is seeded randomly from a uniform distribution of x and y coordinates through a circular plane of the jet nozzle at $z = 5\,mm$ (effective thickness of the model firebrands) with radius R.

The simulations were run for 3 s assuming that, between each time interval (0.01 s) the velocity field is quasi-steady. Then, three dimensional locus of the centroid of the model firebrands (trajectory) during their lofting and downwind transport are recorded as the final results. Figure 7.1 shows a 3D cluster of the model firebrand trajectories that are superimposed over the iso-surface contours of the Q-criterion [Jeong and Hussain, 1995] which are color coded with the velocity magnitude at the final time step of the simulations.

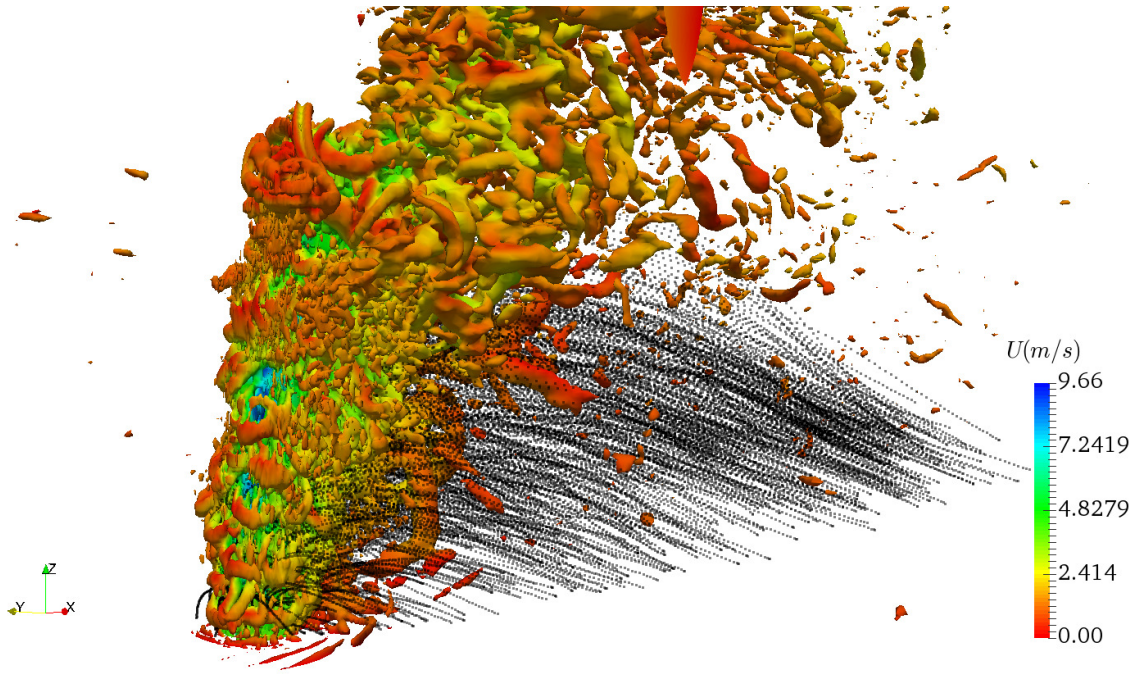

Figure 7.1: Black dotted lines are simulated trajectories which are superimposed over the Q-criterion contours of the velocity filed at 3 s. The $Q = 100$ contours are color coded with the velocity magnitude.

7.2 Comparison with experimental data

The illustrated lofting and downwind transport trend in the obtained trajectories corroborates with the physical expectations and experimental results, see figure 7.1. This is shown, also, by qualitative side view comparison of the trajectories with their corresponding experimental results. Respectively, figures 7.2 & 7.3 present results of the lofting and downwind transport for the model firebrands with $\eta = 4$ & 1 which are released through the JINCF velocity field generated for the W1-I5-O3 and the W2-I10-O5 settings.

As can be seen, the numerical results are within the domain of experimental data; Meaning that the model is capable of predicting the rise height and downwind distance with a reasonable margin. Also, the geometric form of the obtained trajectories, namely the trajectory curves, are the same as the experimental data. Nonetheless, sensitivity of the numerical model to the initial coordinates of the release, and difference in the number of released model firebrands with the experiments have led to more scatter in the landing location of the numerical results. The sensitivity of the final results to the release parameters will be discussed later in this chapter. More insight can

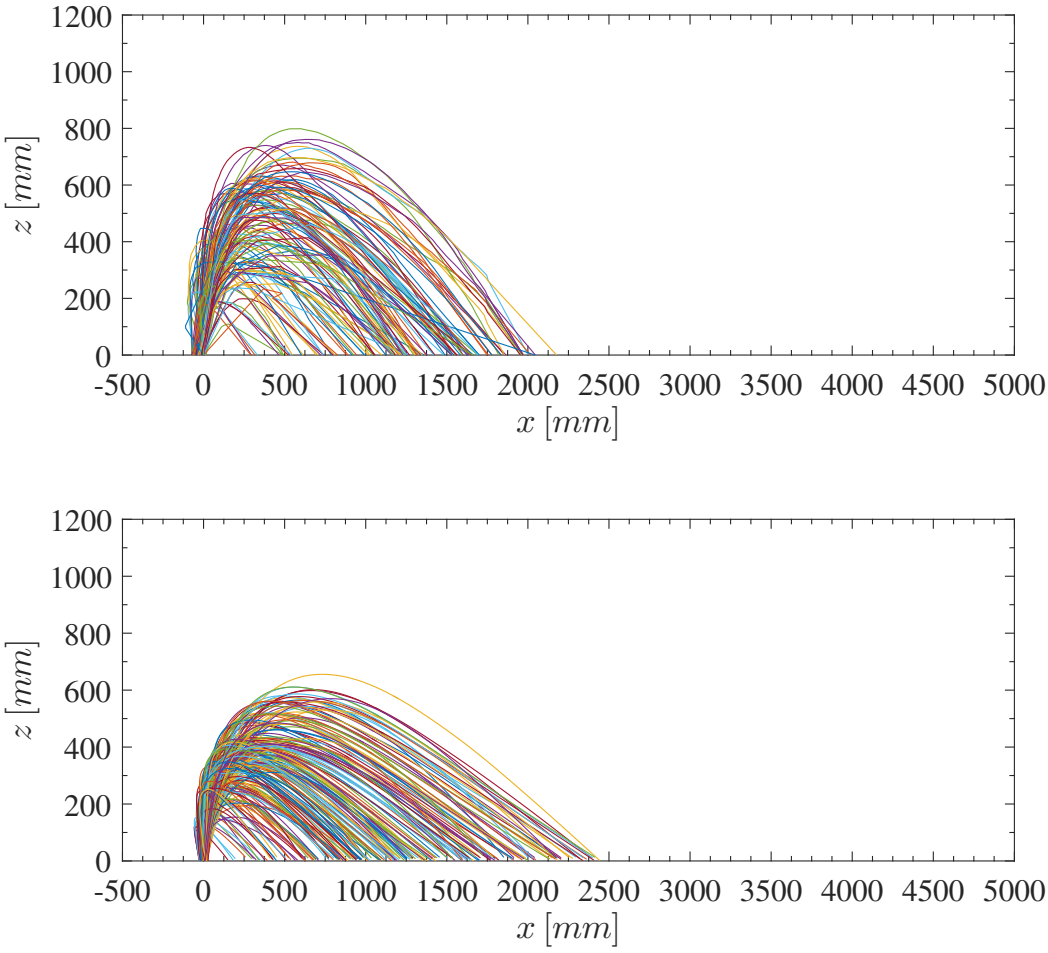

Figure 7.2: Obtained trajectory of model firebrands with aspect ratio $\eta = 4$ from wind tunnel experiments (top) in relation to trajectories from corresponding simulations (bottom) using the developed model where $U_0 = 2.23\ (m/s)$, and $U_{j|r=0} = 9.0\ (m/s)$.

be obtained by quantitative analysis of the results. In this regard, figure 7.4 shows the comparison between numerical and experimental probability density function (PDF) and cumulative density function (CDF) of the downwind distance (x_l) and rise height (z_{max}) both normalized with the jet momentum length scale (z_m) as well as the normalized downwind distance with the maximum rise height x_l/z_{max}. For a list of non-dimensional parameters in the problem see chapter 4.

There is a very good agreement between the experimental data and results of the simula-

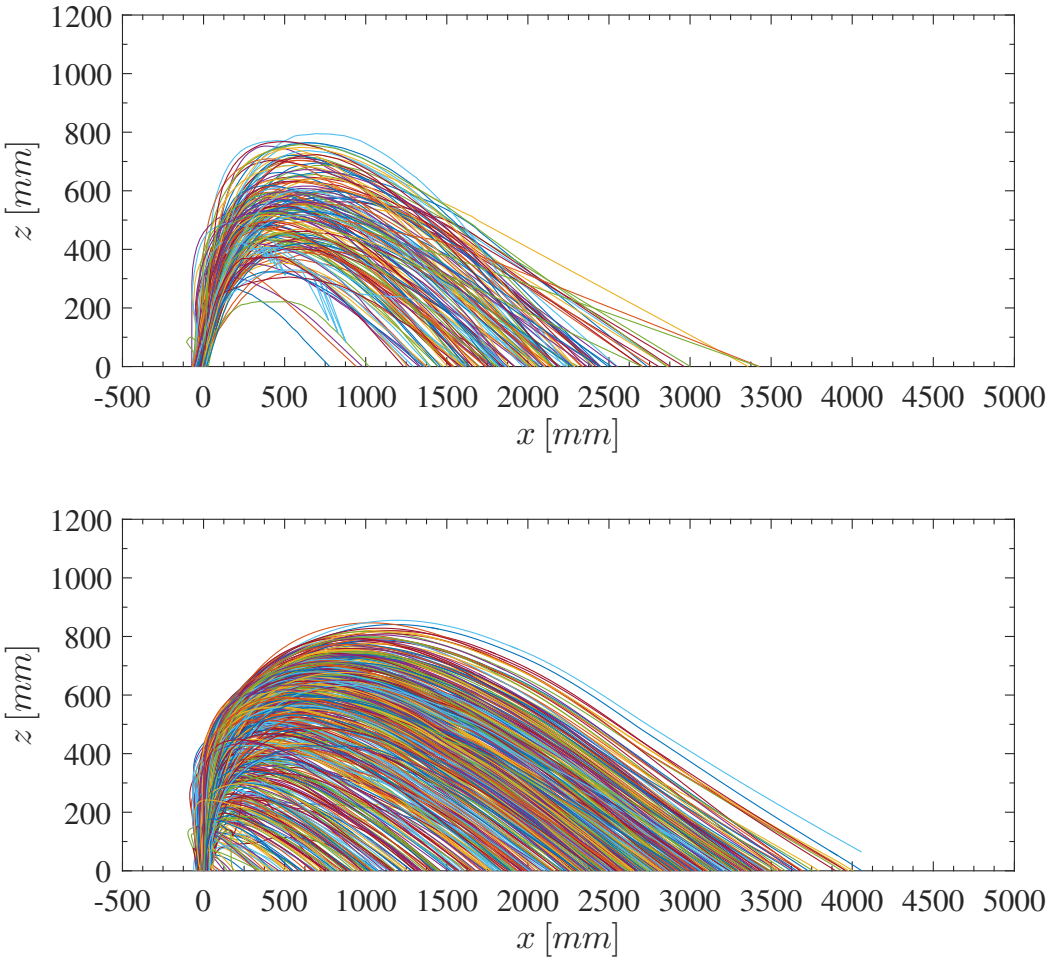

Figure 7.3: Obtained trajectory of model firebrands with aspect ratio $\eta = 1$ from wind tunnel experiments (top) in relation to trajectories from corresponding simulations (bottom) using the developed model where $U_0 = 2.85\,(m/s)$, and $U_{j|r=0} = 12.0\,(m/s)$.

tions in predicting the mean value of the normalized parameters. Also, estimation of the variance, particularly in this case, is relatively good. This seconds the adopted approach towards modeling the lofting and downwind transport of firebrands thorough the velocity field of a wildfire, despite the presence of uncertainties, and complexity of the phenomenon. The comparison between experimental data and numerical results, for all available cases in table 7.1, is summarized in figure 7.5. This is done by calculating the mean (μ) and standard deviation (σ) of x_l/z_m and z_{max}/z_m for experimental and numerical results. Then, the obtained statistics of the experiments are drawn

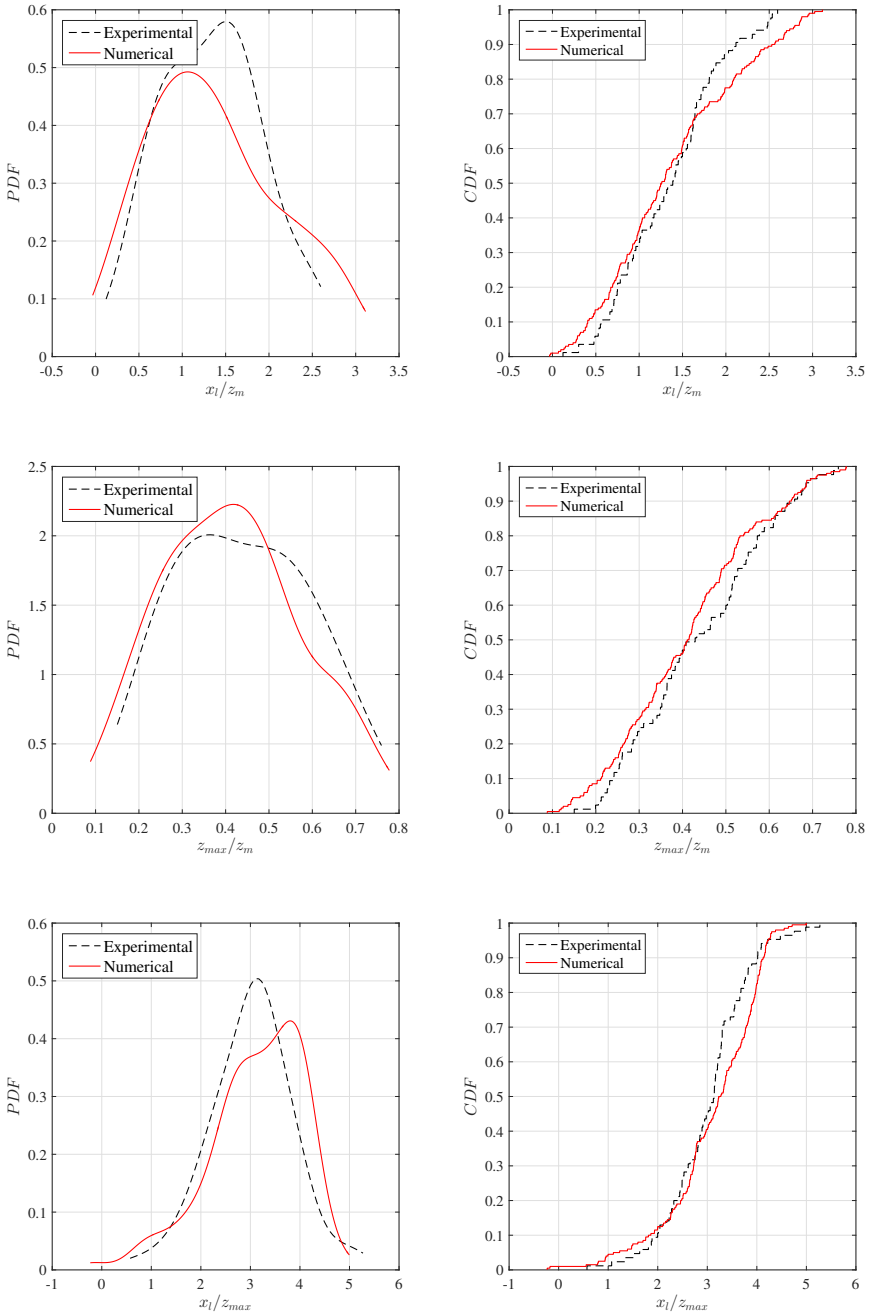

Figure 7.4: Shown are PDF (left) and CDF (right) plots of the normalized downwind distance x_l/z_m (top), normalized rise height z_{max}/z_m (middle), and normalized downwind distance with the rise height x_l/z_{max} (bottom) that are drawn for the release of $\eta = 6$ model firebrands through the JINCF velocity field generated by the W1-I5-O3 setting. The dashed lines are experimental data and the solid lines present corresponding numerical results.

against the corresponding values from the numerical results.

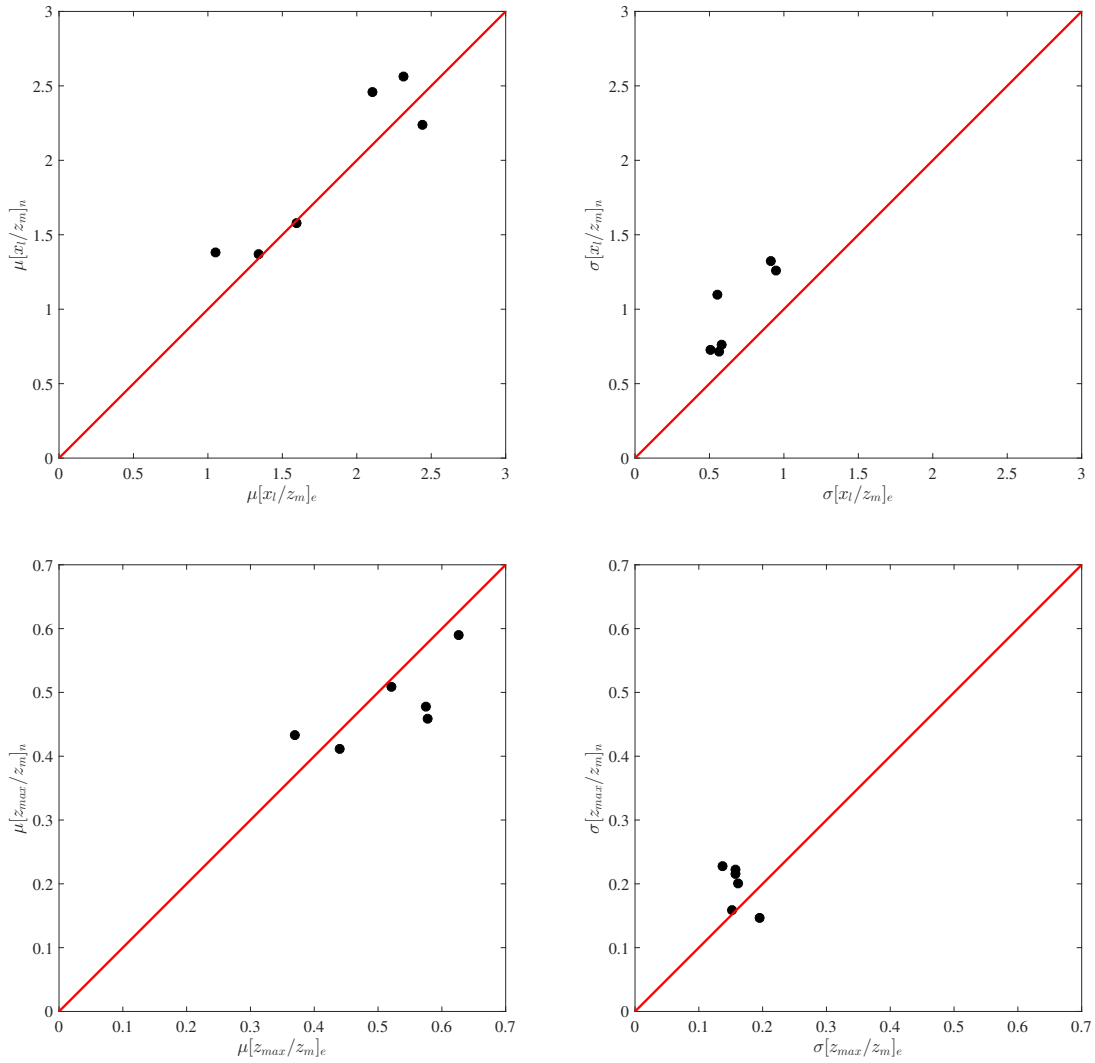

Figure 7.5: Shown are the mean μ (left) and the standard deviation σ (right) of the normalized downwind distance (top), and normalized rise height (bottom). Estimations based on the experimental data are drawn along horizontal axis and denoted with the subscript $(_e)$, whereas calculated results from the numerical simulations are presented in vertical axis with subscript $(_n)$. Also, the red solid line has $1:1$ slope.

The results, as shown in figure 7.5, indicate that there is an excellent agreement between the estimated mean value of the normalized landing location and normalized rise height obtained from the simulations with the experimental data. However, for the majority of the cases, there are discrepancies between the standard deviation of the experimental data and corresponding numerical

results. As for of x_l/z_m (figure 7.5, top-right), the numerical model overestimates the standard deviation with respect to the experimental results. This, also, holds true for the standard deviation of z_{max}/z_m except for a couple of cases. Currently, the number of available cases (DOF) are very small such that utilizing hypothesis testing may not be useful because the small DOF may raise question about the credibility of the results on the null hypothesis. Therefore, it is not possible to infer whether the numerical results are statistically significantly different from the experimental data. On this note, the observed discrepancies in prediction of the standard deviation may be due to the following reasons.

The transport model of [Richards et al., 2008; Richards, 2010], as discussed in chapter 3, utilizes the steady aerodynamic force and moment coefficients while the lofting and transport process is inherently unsteady. Also, in chapter 3, we demonstrated that the transport model shows well-posed and bounded sensitivity to the added mass effects of the rotational motion, and this delivers discrepancies (overestimation) in prediction of the standard deviation of the flight trajectories. In addition, the difference in DOF of the model and experiments may have been contributed to the error in σ. In future, this may be resolved by increasing the number of releases in experiments to the order of 1000, and conduct the numerical simulations with the same DOF. However, given the good results in prediction of the mean values, difference in DOF may not have a significant contribution into the error.

Another possible source of discrepancy in σ may be associated with the duration of resolved ambient velocity field. In each experimental case, release of 200 model firebrands took approximately 480 s while LES simulations only provided 3 s of instantaneous velocity field due to limited computational resources. Considering that the model firebrands are released within the first second of simulations, in order for them to complete the lofting and downwind transport within the resolved time (3 s), there is significant difference in the release density of the model firebrands. In fact, the release density of the simulations, on average, is 1428 times of the experiments. This suggests that the observed error in prediction of σ may be caused by the lack of content in the spatial and temporal variations of the stored velocity field through the LES [Bendat and Piersol, 2011]. Therefore, this issue may be tackled by reducing the release density that can be achieved by longer record of the velocity field data, provided that the computational resources especially enough memory is available.

As the number of released model firebrands during the numerical simulations is relatively large compared to the experiments, and the results of the model show good agreement in estimating the average statistics of the flight, it is feasible to employ the numerical results for scrutinizing the flight characteristics. In this regard, PDF and CDF plots of the normalized downwind distance (x_l/z_m) and the normalized rise height (z_{max}/z_m) are presented in figure 7.6. Based on the presented

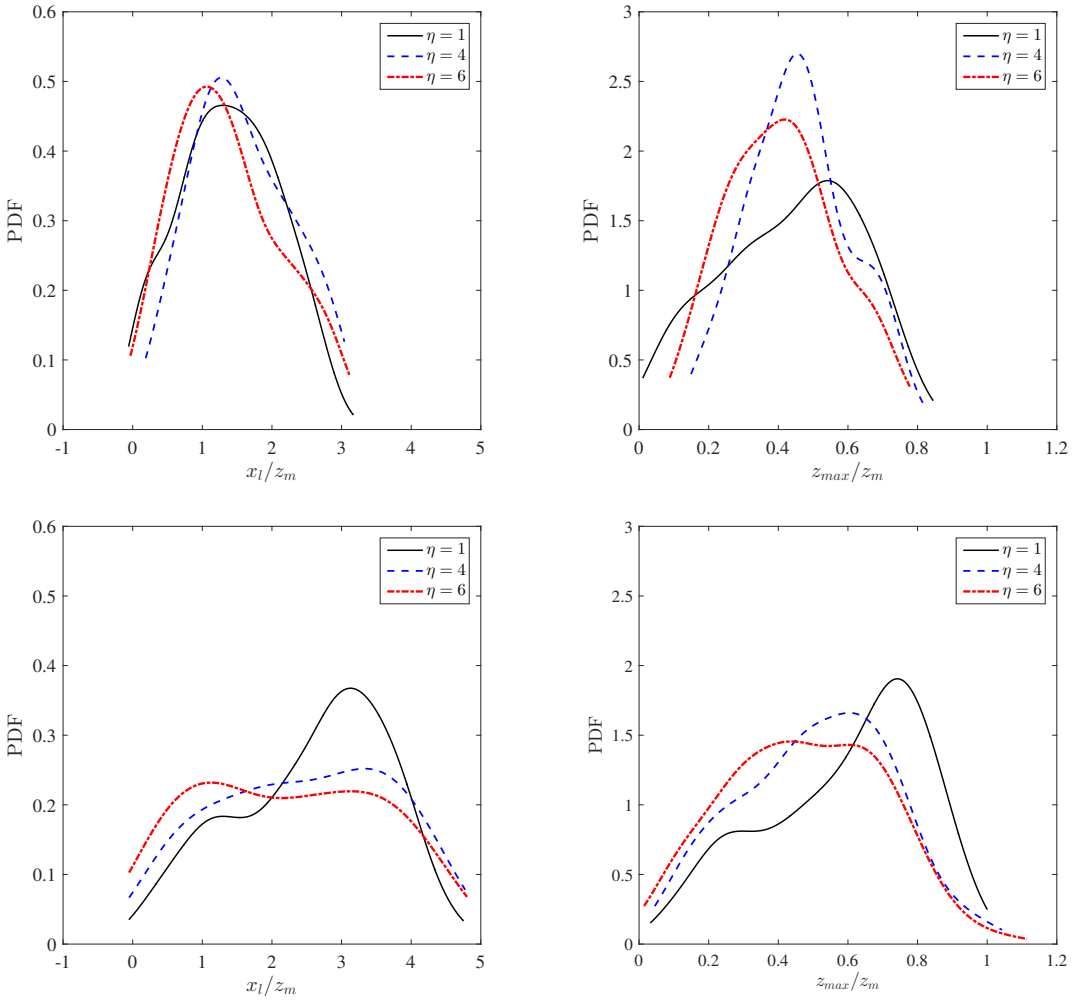

Figure 7.6: Probability density function (PDF) of the normalized downwind distance (on the left), and the normalized rise height (on the right) obtained from the simulation of model firebrands' transport through the velocity field of W1-I5-O3 (top) and W2-I10-O5 (bottom). The solid, dashed, and dotted-dashed lines show the results pertinent to the model firebrands with η = 1, 4 & 6, respectively

PDFs on figure 7.6, it is evident that although the velocity ratio ($U_0/U_{j|r=0}$) of the W1-I5-O3 and

W2-I10-O5 are very close and the jet momentum length scale in W2-I10-O5 is higher, the greater jet velocity in W2-I10-O5 (PDFs at the bottom) causes the model firebrands to rise higher into the boundary layer where the reference velocity is also greater than the W1-I5-O3 case; see details in table 7.1. This leads to greater maximum downwind distance for the particles which corroborates with the experimental results and the dimensional analysis discussed in chapter 5. In addition, a similar shape to the PDFs of x_l/z_m can be observed, except for the bimodal PDF of the $\eta = 1$ released in W2-I10-O5. This seconds our experimental findings in chapter 5 where the PDFs of the normalized downwind distance of the model firebrands have similar distributions in some cases. This suggest that the maximum lofting height may significantly influence the landing location of the firebrands. Further, unlike Tse and Fernandez-Pello [1998]; Himoto, K and Tanaka [2005]; Bhutia et al. [2010]; Kortas et al. [2009], for modeling the fire spotting phenomenon the lofting and downwind transport of firebrands cannot be separated but rather, the full unsteady velocity field must be resolved.

7.3 Sensitivity analysis

Simulations were conducted for four different radii of the release area through the jet nozzle in order to demonstrate and quantify the sensitivity of the model to the initial coordinates of the release; See table 7.1 for specific details. Also, lofting and transport of the model firebrands with aspect ratio $\eta = 6$ are simulated by coupling the $3\,s$ time-averaged velocity field of the JINCF generated through W2-I10-O5 setting. This has been done in order to measure the effects of an unsteady flow field on the final trajectories as opposed to using a steady time-averaged velocity field.

Figure 7.7 illustrates the sensitivity of the results to the release radius through PDF of the x_l/z_m and z_{max}/z_m. As can be seen on figure 7.7-left, increasing the radius of the model firebrand release through the jet nozzle area increases the variability in the landing location, i.e. downwind distance, such that in $R = 5,\ 7.6\,cm$ the distributions are bimodal and some upstream landing locations were observed. Similarly, increasing the release radius, decreases the mean of the normalized rise height and increases the variance; See figure 7.7-right. In addition, variations of the mean of the normalized landing location and the normalized rise height as well as their corresponding standard deviations against R values are shown in figure 7.8. These results imply that the model is sensitive

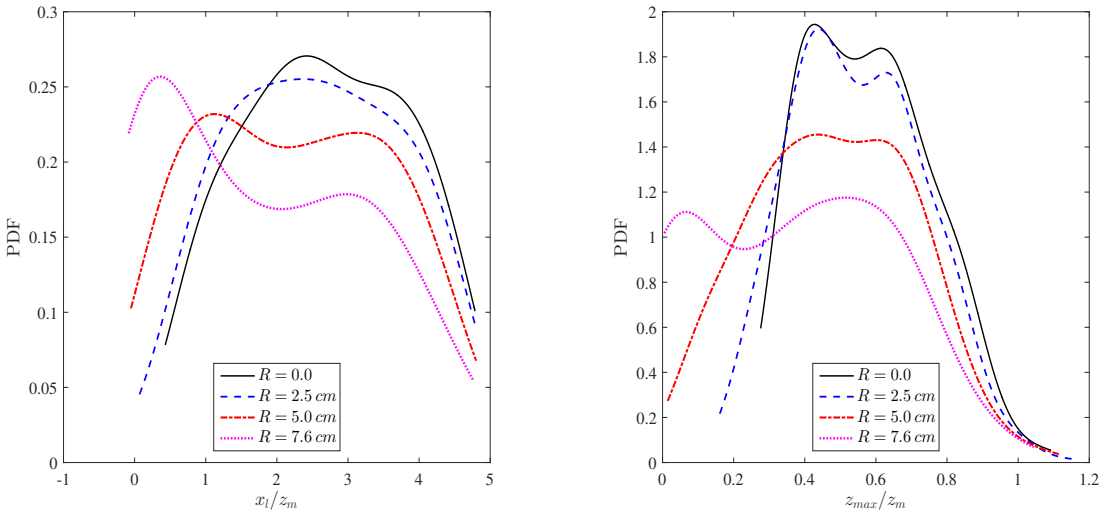

Figure 7.7: Probability density function (PDF) of the normalized downwind distance (left) and the normalized maximum rise height (right) for different release radius of the model firebrands with aspect ratio $\eta = 6$ through the velocity field of W2-I10-O5 case.

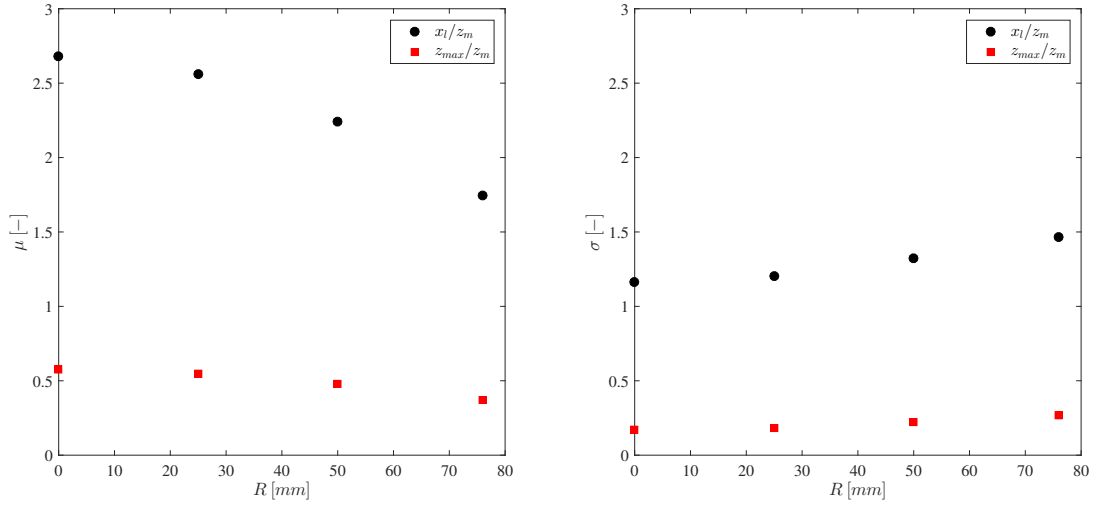

Figure 7.8: Shown are variations of the mean of the normalized landing location and rise height versus R value (left) and their corresponding standard deviation against R (right).

to the initial coordinates of the release within the velocity field. Therefore, discrepancy between the release radius in the experiments with corresponding numerical simulations may have contributed to the overestimation of the variance in the numerical results. In this regard, trajectories were spatially-averaged in the $x - z$ plane in order to visualize the effects of release radius on the landing location

and maximum rise height of the model firebrands through numerical simulations compared to the spatially averaged trajectory of the corresponding experimental case; See figure 7.9. As is evident in

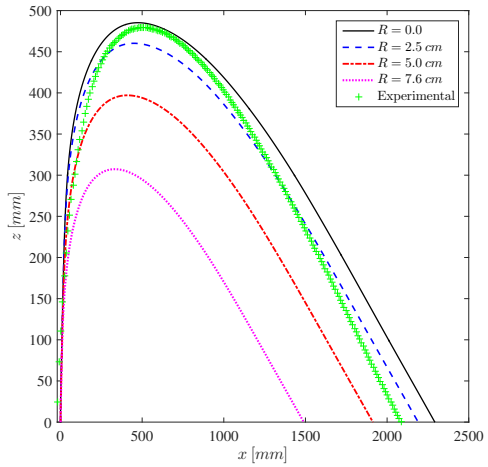

Figure 7.9: Shown are spatially-averaged trajectories of the model firebrands with aspect ratio $\eta = 6$ that are released within the circular area of the jet nozzle with different radii R. Each trajectory line is averaged over 600 sample of model firebrands' path. Also, the (green) symbolic line presents the spatially-averaged trajectory of the corresponding experimental case.

figure 7.9, that increasing R exposes more firebrands to the lower jet velocities in relation to the jet centerline velocity. Therefore, the maximum rise height decreases and subsequently the maximum downwind distance decreases. In the wind tunnel experiment model firebrands were released from approximately the centerline of the jet. However, results of the image processing in chapter 5 shows that the brands are not exactly released from the centerline of the jet. Hence for consistency with experiments, $R = 5\,cm$ was adopted for all the numerical cases, even though figure 7.9 shows that the release radius in experiments has been most likely less than $5\,cm$. Since these results are not known *apriori* for all cases, the choice of $R = 5\,cm$ is made based on the estimated operating radius of the individuals who have conducted the experiments.

Finally, the response of the model to the use of a time-averaged (steady) velocity field instead of the LES time resolved flow is investigated. To this end, the LES resolved velocity field of the W1-I5-O3 case is time-averaged over $3\,s$ and coupled with the transport model. Then, model firebrands with aspect ratio $\eta = 6$ are released through this velocity field. The spatially-averaged trajectory of model firebrands, over 600 samples, is drawn against the corresponding spatially-averaged trajectory

that is obtained from using the LES velocity field. Figure 7.10 shows the comparison between these two trajectories. A side view of the spatially averaged trajectories reveals that there is a very little

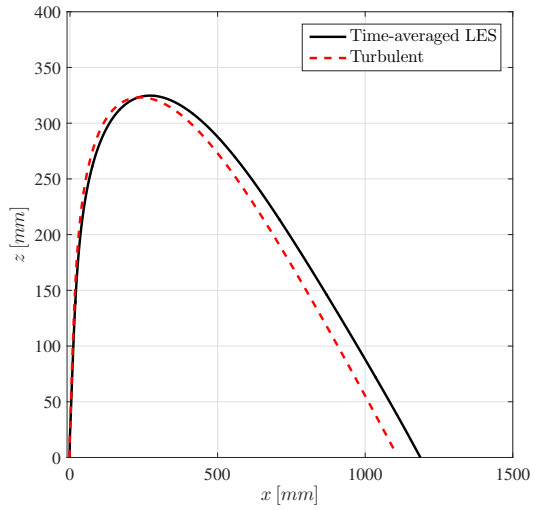

Figure 7.10: Illustrated is the side view comparison of the spatially-averaged trajectories obtained from transport simulations through the time-varying turbulent velocity field of W1-I5-O3 against simulations in the time-averaged velocity field of the same turbulent flow.

difference in estimating the maximum rise height. However, the difference gets larger in estimation of the landing location. The mean landing location in the steady and unsteady simulations are 1098.2 mm and 1188.5 mm respectively, a difference of 8%. Also, the standard deviation of landing location obtained from steady and unsteady numerical simulations are 612.32 mm and 585.28 mm respectively, a difference of 5%. Since the standard deviations are close, a possible reason for such a small difference is the short period of time over which the velocity field is time-averaged. It is likely that by increasing the length of simulations from 3 s to the order of a couple of minutes at least, the resolved turbulent flow field would have enough content of the spatial (eddies) and temporal scales that will cause larger differences in the final trajectories, given that the transport model is highly nonlinear. However, quantification of the length of the simulations as well as subsequent offset error analysis in the simulations are not within the scope of this study.

Based on the above results, the geometry and complexity of rod like debris flight is likely the major contributor to spatial variability in trajectories.

7.4 Conclusions

Numerical simulations of the large scale wind tunnel experiments of the lofting and downwind transport of model firebrands are conducted using the developed coupled stochastic parameter model that is described in the previous chapter. The model was run for two JINCF velocity fields generated by W1-I5-O3 and W2-I10-O5 settings, see table 7.1. Comparison of the numerical results with the corresponding experiments show very good agreement in estimating the average statistics of the flight of model firebrands. Nonetheless, the model overestimates the variance in landing location and rise height. The results may be improved by decreasing the release density of model firebrands through time. This can be done by increasing the total storage time of the resolved velocity field in the LES model to order of 10 minutes, although this would be very expensive due to the high volume of the required memory. Moreover, through sensitivity analysis of the model, it is shown that the results, i.e. obtained trajectories, are sensitive to the initial coordinates of the release through the jet nozzle area. In fact, one of the sources of discrepancy between the variance in numerical results with variance in experimental data, is believed to be the difference in the release radius R which was difficult to control experimentally. The results are very promising in that the developed model predicts the average statistics of the firebrand lofting and downwind transport very well.

Bibliography

Bendat, J. S. and Piersol, A. G. (2011). *Random data: analysis and measurement procedures*, volume 729. John Wiley & Sons.

Bhutia, S., Jenkins, M. A., and Sun, R. (2010). Comparison of firebrand propagation prediction by a plume model and a coupledfire/atmosphere largeeddy simulator. *Journal of Advances in Modeling Earth Systems*, 2:4.

Himoto, K and Tanaka, T. (2005). Transport of disk-shaped firebrands in a turbulent boundary layer author. In *the Eighth International Symposium on Fire Safety Science*, pages 18—-23.

Jeong, J. and Hussain, F. (1995). On the identification of a vortex. *Journal of fluid mechanics*, 285:69–94.

Kortas, S., Mindykowski, P., Consalvi, J. L., Mhiri, H., and Porterie, B. (2009). Experimental validation of a numerical model for the transport of firebrands. *Fire Safety Journal*, 44(8):1095–1102.

Richards, P. J. (2010). Steady Aerodynamics of Rod and Plate Type Debris.pdf. In *17th Australian Fluid Mechanics Conference*.

Richards, P. J., Williams, N., Laing, B., McCarty, M., and Pond, M. (2008). Numerical calculation of the three-dimensional motion of wind-borne debris. *Journal of Wind Engineering and Industrial Aerodynamics*, 96(10):2188–2202.

Tohidi, A. and Kaye, N. B. (2016). Highly buoyant bent-over plumes in a boundary layer. *Atmospheric Environment*, 131:97–114.

Tse, S. D. and Fernandez-Pello, A. C. (1998). On the flight paths of metal particles and embers generated by power lines in high windsa potential source of wildland fires. *Fire Safety Journal*, 30(4):333–356.

Chapter 8

Concluding remarks

The main goal of this dissertation was to improve understanding of the firebrands' flight. To this end, a simple mechanical break-off model is proposed for the formation of cylindrical firebrands similar to those collected from the full scale tree burn experiments of Manzello et al. [2007, 2008, 2009] and, by geometric scaling analysis, it is shown that the firebrand surface area scales on the mass raised to the $2/3^{rds}$ power [Tohidi et al., 2015]. Further, a predictive statistical model for mass and shape distributions of the firebrands is developed by applying a non-linear regression method to the available experimental data. The results of this model can be used as realistic inputs in Monte-Carlo type simulations of the firebrand transport [Tohidi et al., 2015].

Regarding firebrand transport, a set of non-combusting firebrand free fall experiments were run to experimentally verify and evaluate a fully deterministic three dimensional 6-D.O.F. firebrand flight model which is adopted from Richards et al. [2008]; Richards [2010] and Grayson and Pang [2011]. Outcomes of the statistical hypothesis testing on the experimental data and their corresponding numerical results indicate that for any possible combination of aspect ratio and free-fall release height in the parameter space of the experiments, the numerical model results are not statistically significantly different from the experiments. Also, sensitivity analysis of the model reveals that the governing equations of firebrand/debris transport are highly sensitive to the initial conditions, namely release angles (Tait-Bryan angles).

With regard to ambient velocity through which firebrand transport occurs, near field dynam-

ics of the bent-over plumes is thoroughly characterized; Where it is shown that wildfire plumes are significantly more buoyant than industrial plumes and have steeper trajectories that are strongly influenced by the boundary layer velocity profile [Tohidi and Kaye, 2016]. The conditions under which the shearing effects of the boundary layer cross-flow must be included in modeling the velocity field are quantified with an analytic expression.

This is the first study to conduct extensive large scale wind tunnel experiments of the lofting and downwind transport of model firebrands. The data serves as an invaluable resource for not only firebrand transport studies but also for the flight of rod-like debris/brands through other severe velocity fields in nature such as hurricanes and storms. It is observed that the normalized maximum landing locations of model firebrands with their maximum rise heights have similar probability density functions (PDF) regardless of the aspect ratio. This implies that in modeling fire spotting phenomenon unlike previous studies the lofting and downwind transport of the firebrands cannot be decoupled, as the rise height significantly affects the landing location. Also, a strong positive correlation between the firebrands' Tachikawa number and, the mean and standard deviation of the normalized landing locations is identified. Similar to the free-fall experiments, the results suggest that lofting and downwind transport of non-combusting firebrands are extremely sensitive to the initial conditions of the release as well as temporal and spatial variations of the ambient velocity field.

Thus, in order to account for these variations in the velocity field, and improve the transport model, a highly scalable coupled stochastic parametric model for lofting and transport of firebrands is developed. This model couples the fine resolution time-varying Large Eddy Simulation (LES) resolved velocity field of the jets/plumes in the non-uniform cross-flow boundary layers with the fully deterministic 3D 6-D.O.F. firebrand transport model. Randomly selected cases from the wind tunnel experiments are mathematically simulated with this model. Comparison of the numerical results with the corresponding experiments show very good agreement in estimating the average statistics of the flight of model firebrands. Although the results are very promising, uncertainty quantification of the model would be a fruitful area for future work.

This work is disseminated through the following material,

- **Peer-reviewed journals:**

  1) **A. Tohidi**, N. B. Kaye, "Highly buoyant bent-over plumes in a boundary layer", Atmospheric Environment, Vol: 131, Pages: 97-114, (2016)

  2) **A. Tohidi**, N. B. Kaye, W. Bridges, "Statistical description of firebrand size and shape distribution from coniferous trees for use in Metropolis Monte Carlo simulations of firebrand flight distance ", Fire Safety Journal, Vol:77, Pages: 21-35, (2015),

- **Conference papers:**

  3) **A. Tohidi**, N. B. Kaye, "Experimental and Numerical Modeling of Fire Spotting Phenomenon", 8^{th} International Colloquium on Bluff Body Aerodynamics and Applications, Northeastern University, Boston Massachusetts USA. (June-2016), DOI=to be assigned.

  4) **A.Tohidi**, N. B. Kaye, "The sensitivity of modeled flight distance to the lofting to transport transition criterion in coupled ember flight models", 12^{th} American Conference of Wind and Industrial Aerodynamics, Seattle WA, USA, (June-2013)

- **Conferences presentations:**

  5) **A. Tohidi**, N. B. Kaye, "An Experimental Study of Rod-Like Debris Flight with Particular Application to Fire Spotting", Engineering Mechanics Institute Conference (EMI), Vanderbilt University, USA, (May-2016).

  6) **A. Tohidi**, N. B. Kaye,"An Experimental Study of Stochastic Nature of Firebrands Flight", 5^{th} International Fire Behavior and Fuels Conference, Portland, Oregon, USA, (April-2016).

  7) **A. Tohidi**, N.B. Kaye, "Trajectory of a plume in a power-law velocity profile", 68^{th} Annual Meeting of the APS Division of Fluid Dynamics, Boston, MA, USA, (Nov-2015).

  8) N. B. Kaye, **A. Tohidi**, "Bent-over plume models for large-area highly-buoyant turbulent plumes", 67^{th} Annual Meeting of the APS Division of Fluid Dynamics, San Francisco, CA, USA, (Nov-2014).

  9) **A. Tohidi**, N. B. Kaye, "Comparison of experiments with stochastic modeling of cylindrical debris flight", Engineering Mechanics Institute Conference (EMI), McMaster University, Canada, (August-2014).

  10) **A. Tohidi**, N. B. Kaye, "Characterization of Firebrand Geometry and Flight Dynamics", Large Wildland Fire Conference: Social, Political and Ecological Effects, Missoula MT, USA, (May-2014)

Bibliography

Grayson, J. and Pang, W. C. (2011). *Development and application of a three-dimensional probabilistic wind-borne debris trajectory model*. PhD thesis, Clemson University.

Manzello, S. L., Maranghides, A., and Mell, W. E. (2007). Firebrand generation from burning vegetation. *International Journal of Wildland Fire*, 16(4).

Manzello, S. L., Maranghides, A., Shields, J. R., Mell, W. E., Hayashi, Y., and Nii, D. (2009). Mass and size distribution of firebrands generated from burning Korean pine (Pinus koraiensis) trees. *Fire and Materials*, 33(1).

Manzello, S. L., Shields, J. R., Hayashi, Y., and Nii, D. (2008). Investigating the vulnerabilities of structures to ignition from a firebrand attack. *Fire Safety Science*, pages 143–154.

Richards, P. J. (2010). Steady Aerodynamics of Rod and Plate Type Debris.pdf. In *17th Australian Fluid Mechanics Conference*.

Richards, P. J., Williams, N., Laing, B., McCarty, M., and Pond, M. (2008). Numerical calculation of the three-dimensional motion of wind-borne debris. *Journal of Wind Engineering and Industrial Aerodynamics*, 96(10):2188–2202.

Tohidi, A., Kaye, N., and Bridges, W. (2015). Statistical description of firebrand size and shape distribution from coniferous trees for use in Metropolis Monte Carlo simulations of firebrand flight distance. *Fire Safety Journal*, 77:21–35.

Tohidi, A. and Kaye, N. B. (2016). Highly buoyant bent-over plumes in a boundary layer. *Atmospheric Environment*, 131:97–114.

Appendices

Appendix A

Plume Fluxes Equations

A control volume analysis is presented to derive a set of ordinary differential equations for the plume properties as a function of distance along the plume centerline. As the negligible role of turbulence is discussed in Sect. 4.1, the model is thus derived for steady smooth cross-flow with arbitrary velocity profile. The concept of local similarity is extended to the bent-over plume in accordance with Baines and Keffer [1963]. As a result of the local similarity assumption and the aforementioned study conducted by Davidson [1986], the velocity and density defect profiles are considered to be top-hat. In contrast to previous studies [Briggs, 1968, 1972, 1975b,a; Hoult et al., 1969; Hoult and Weil, 1972; Davidson, 1989; Mercer and Weber, 1994] the plume cross section normal to the plume centerline trajectory is taken to be an ellipse. See Figure (A.1). The ratio of major to conjugate radii is denoted by λ.

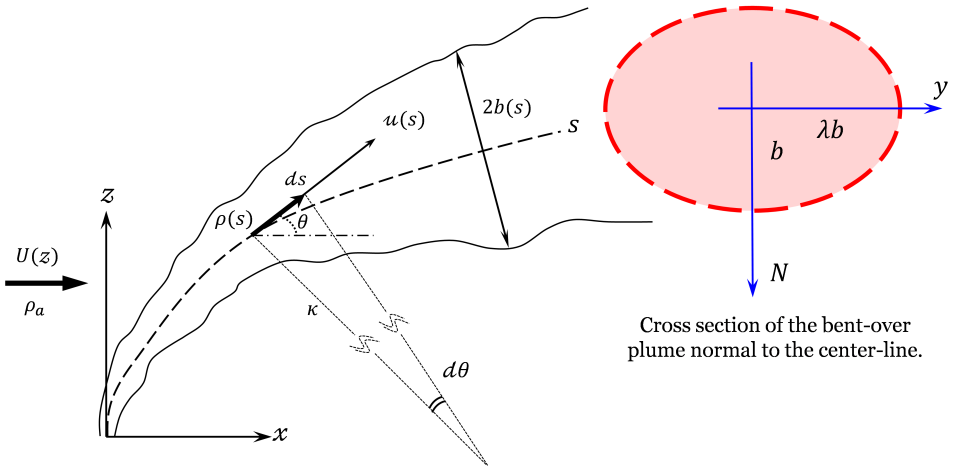

Figure A.1: (Right) Coordinate system for a bent-over buoyant plume through a cross flow; (Left) Normal cross section area of the plume perpendicular to the centerline s.

Based on laboratory observations of Jordinson [1956] it is known that the main factor in determining the trajectory of a bent-over plume is the rate at which it entrains mass from the ambient environment. According to the observations of Hoult et al. [1969], there are two entrainment mechanisms involved. One is due to the difference between the plume velocity along s, i.e. $u(s)$, and the wind velocity component parallel to the plume center-line, that is longitudinal shear driven entrainment. The other is due to the velocity component of the wind normal to the plume envelope, i.e. $U \sin\theta$; see Figure (A.2b). The two mechanisms are taken to be additive such that the entrainment velocity, u_e, can be written as:

$$u_e = \alpha \left| u - U cos(\theta) \right| + \beta \left| U sin(\theta) \right| \tag{A.1}$$

where α is entrainment coefficient for longitudinal shear driven mixing and β is the transverse entrainment coefficient that parameterizes entrainment due to transverse shear. It is assumed that both coefficients are independent of the position along the plume trajectory.

The plume trajectory's governing equations can be derived from conservation of mass, momentum, and energy. Pursuant to Figure (A.2a), for an infinitesimally thin plume cross section normal to the plume trajectory, the continuity equation reads:

$$\frac{d(\varrho \forall)}{dt} + \iint\limits_{A_e} \varrho \bar{u} \cdot \bar{n} \, dA_e = 0 \tag{A.2}$$

where $\varrho\forall$ is the control volume mass in which $\forall$ denotes volume of the plume element, A_e is the peripheral surface area of the plume element and $\bar{n}$ is the outward normal vector to A_e. Expanding the integral in the s direction leads to:

$$\begin{aligned} \pi \varrho \lambda b^2 u + \frac{d}{ds}\left(\pi \varrho \lambda b^2 u\right) ds - \pi \varrho \lambda b^2 u = 2\pi b \sqrt{\frac{1+\lambda^2}{2}} \varrho_a \beta U \sin(\theta) ds \quad + \\ 2\pi b \sqrt{\frac{1+\lambda^2}{2}} \varrho_a \alpha |u - U\cos(\theta)| ds. \end{aligned} \tag{A.3}$$

Simplifying equation (A.3) gives conservation of mass along the plume trajectory:

$$\frac{d}{ds}\left(\pi \varrho \lambda b^2 u\right) = 2\pi b \sqrt{\frac{1+\lambda^2}{2}} \varrho_a \left(\beta U \sin(\theta) + \alpha |u - U\cos(\theta)|\right). \tag{A.4}$$

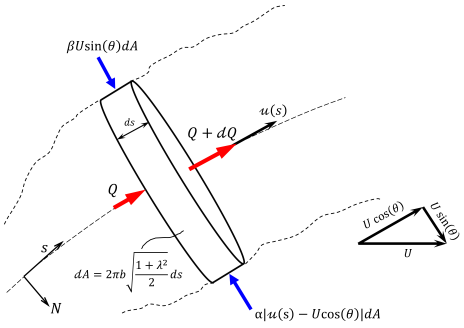

(a) Mass conservation diagram.

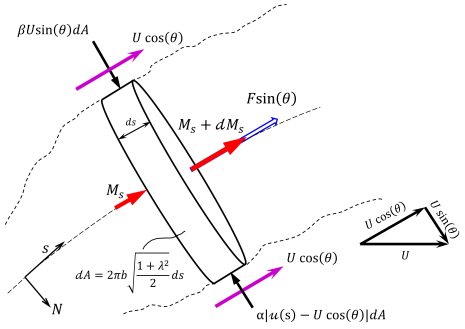

(b) Momentum diagram along s .

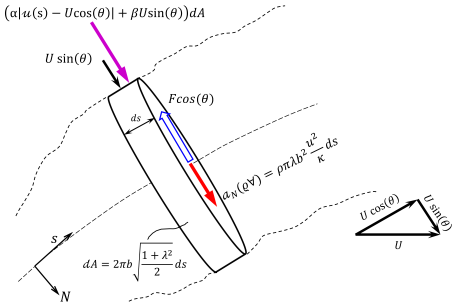

(c) Momentum diagram along N.

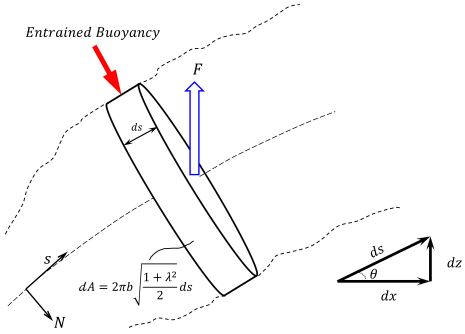

(d) Buoyancy flux diagram.

Figure A.2: Schematic of an infinitesimal bent-over plume element. Net buoyancy force, that is $(\varrho_a - \varrho)g\pi\lambda b^2 ds$, is denoted by F. Through above diagrams, sharp head arrows denote velocity vectors, bold head arrows denote flux vectors, and hollow arrows denote force vectors.

The momentum equation in the s direction is a balance of acceleration, entrianed momentum and buoyancy:

$$\tau_s = \left(\oiint_{A_e} \varrho \bar{u} \cdot \bar{n} \bar{u} \, dA_e \right)_s \tag{A.5}$$

where τ_s denotes the resultant of the external forces acting in s direction on the control volume. Considering Figure (A.2b), applying equation (A.5), and expanding its terms yields:

$$\begin{aligned}(\varrho_a - \varrho)\, g(\pi\lambda b^2 ds)\sin(\theta) = (\pi\varrho\lambda b^2 u^2) + \frac{d}{ds}\left(\pi\varrho\lambda b^2 u^2\right) ds - (\pi\varrho\lambda b^2 u^2) - \\ \left[2\pi b\sqrt{\frac{1+\lambda^2}{2}}\,\varrho_a\left(\beta U\sin(\theta) + \alpha|u - U\cos(\theta)|\right)\right] U cos(\theta) ds\end{aligned} \tag{A.6}$$

Using the continuity equation, momentum conservation in the s direction is obtained by simplifying Equation (A.6):

$$\frac{d}{ds}\left(\pi\varrho\lambda b^2 u^2\right) - U\cos(\theta)\frac{d}{ds}\left(\pi\varrho\lambda b^2 u\right) = (\varrho_a - \varrho)\, g\pi\lambda b^2 \sin(\theta) \tag{A.7}$$

Similarly, the transverse momentum equation is a balance between the centripetal acceleration, the entrained momentum, and buoyancy:

$$\tau_N = \left(\oiint_{A_e} \varrho \bar{u} \cdot \bar{n} \bar{u} \, dA_e \right)_N \tag{A.8}$$

in which, τ_n denotes the resultant force of the external forces acting in the transverse direction. Expanding each term based on Figure (A.2c) leads to:

$$-\left(\varrho_a - \varrho\right) g(\pi \lambda b^2 ds) \cos(\theta) = (\varrho \pi \lambda b^2 ds \frac{u^2}{\kappa}) - \left[2\pi b \sqrt{\frac{1+\lambda^2}{2}} \varrho_a \left(\beta U \sin(\theta) + \alpha |u - U\cos(\theta)| \right) ds \right] U sin(\theta) \tag{A.9}$$

where κ is the radius of the plume center-line's curvature. From geometrical considerations , $\kappa = -ds/d\theta$. The transverse conservation of momentum equation is derived by substituting κ into (A.9) and simplifying it using the conservation of mass equation to get

$$(\pi \varrho \lambda b^2 u^2) \frac{d\theta}{ds} + U \sin\theta \frac{d}{ds} \left(\pi \varrho \lambda b^2 u \right) = \left(\varrho_a - \varrho \right) g (\pi \lambda b^2) \cos(\theta). \tag{A.10}$$

It is assumed that all temperature differences are small, which leads to limited density defect ratios, except regions adjacent to flames (near field) (see Schatzman and Policastro Anthony J. [1984]). As a result, it is possible to use the Boussinesq approximation. Since temperature differences are small and the ambient fluid would predominantly be in gaseous phase, temperature localization is allowed and equation of excess energy can be written as buoyancy conservation

$$\iiint_{\forall} \Delta \varrho \, g \, \nabla \cdot \bar{u} \, d\forall = F_{potential}. \tag{A.11}$$

In the above expression $\Delta\varrho$ is the density defect along the plume centerline and $F_{potential}$ is the potential buoyancy that the ambient environment can provide due to the temperature differences inside the plume envelope. From Figure (A.2d) and (A.11) one can write:

$$\Delta \varrho \, g(\pi \lambda b^2 u) + \frac{d}{ds} \left(\Delta \varrho \, g \, \pi \lambda b^2 u \right) ds - \Delta \varrho \, g \, \pi \lambda b^2 u = (\varrho_a - \varrho) g \pi \lambda b^2 u \tag{A.12}$$

which can be simplified to

$$\frac{d}{ds} \left(\Delta \varrho \, g \pi \lambda b^2 u \right) = g \pi \lambda b^2 u \frac{d\varrho}{ds} \tag{A.13}$$

in which $d\varrho = (\varrho_a - \varrho)$. Substitution of $ds = dz/\sin(\theta)$ into (A.13) gives the expression for conservation of

excess energy (buoyancy) along the plume trajectory:

$$\frac{d}{ds}\left(\Delta\varrho\, g\pi\lambda b^2 u\right) = g\pi\lambda b^2 u\frac{d\varrho}{dz}\sin(\theta). \tag{A.14}$$

Finally the plume rise height (z) and downstream distance (x) of the plume are obtained by integrating along the plume trajectory centerline:

$$x = \int_0^s \cos(\theta)ds \tag{A.15}$$

$$z = \int_0^s \sin(\theta)ds \tag{A.16}$$

Thus far, (A.4), (A.7), (A.10), (A.14), (A.15) and (A.16) constitute a set of fully-coupled differential algebraic equations involving the plume velocity, buoyancy, radius, and trajectory angle. In order to simplify the set of DAEs the equations are rewritten in terms of a new set of physically meaningful dependent variables as follows:

$$Q = \lambda b^2 u \tag{A.17}$$

$$M = \lambda b^2 u^2 \tag{A.18}$$

$$F = g'\lambda b^2 u \tag{A.19}$$

$$u = M/Q \tag{A.20}$$

$$b = Q/\sqrt{\lambda M} \tag{A.21}$$

where Q is specific flow rate, M is specific momentum flux, g' is reduced gravity acceleration and specific buoyancy flux is denoted by F. The final set of dimensional equations are rewritten in terms of specific fluxes as

$$\frac{dQ}{ds} = Q\sqrt{\frac{2(1+\lambda^2)}{M\lambda}}\left(\alpha\left|\frac{M}{Q} - U\cos(\theta)\right| + \beta\left|U\sin(\theta)\right|\right), \tag{A.22}$$

$$\frac{dM}{ds} - U\cos(\theta)\frac{dQ}{ds} = \frac{FQ}{M}\sin(\theta), \tag{A.23}$$

$$U\sin(\theta)\frac{dQ}{ds} + M\frac{d\theta}{ds} = \frac{FQ}{M}\cos(\theta), \tag{A.24}$$

and

$$\frac{dF}{ds} = Q\frac{g}{\varrho_a}\frac{d\varrho}{dz}\sin(\theta) = -Q\text{N}^2\sin(\theta) \tag{A.25}$$

where N is the Brunt-Vaisala frequency.

Bibliography

Baines, W. and Keffer, J. (1963). The round turbulent jet in cross wind. *J Fluid Mech*, 15:481–488.

Briggs, G. (1975a). A comparison of the trajectories of rising buoyant plumes with theoretical empirical models. *Atmospheric Environment (1967)*, 9(4):455–457.

Briggs, G. A. (1968). Concawe meeting: Discussion of the comparative consequences of different plume rise formulas. *Atmospheric Environment (1967)*, 2(3):228–232.

Briggs, G. A. (1972). Chimney plumes in neutral and stable surroundings. *Atmospheric Environment (1967)*, 6(7):507–510.

Briggs, G. A. (1975b). Plume rise predictions, lectures on air pollution and environment impact analysis. *Am. Meteorol. Soc., Boston, USA*, 10.

Davidson, G. (1986). Gaussian versus top-hat profile assumptions in integral plume models. *Atmospheric Environment (1967)*, 20(3):471–478.

Davidson, G. (1989). Simultaneous trajectory and dilution predictions from a simple integral plume model. *Atmospheric Environment*, 23(2):341–349.

Hoult, D. P., Fay, J. A., and Forney, L. J. (1969). A theory of plume rise compared with field observations. *Journal of the Air Pollution Control Association*, 19(8):585–590.

Hoult, D. P. and Weil, J. C. (1972). Turbulent plume in a laminar cross flow. *Atmospheric Environment (1967)*, 6(8):513–531.

Jordinson, R. (1956). Flow in a jet directed normal to the wind. *R. & M*, (3074).

Mercer, G. and Weber, R. (1994). Plumes above line fires in a cross-wind. *International Journal of Wildland Fire*, 4(4):201–207.

Schatzman, M. and Policastro Anthony J. (1984). Plume rise from stacks with scrubbers: A state of the art review. *Bulletin of the American Meteorological Society*, 65(1):210–215.

Appendix B

High performance scientific computing

Large Eddy Simulations of the main domain are conducted using Clemson University's Palmetto cluster where the latest stable release of OpenFOAM, at that time i.e. `OpenFOAM-2.4.0`, was installed. For installation procedure visit official OpeFOAM website at `http://openfoam.org/` and consult with cluster administrators. This section deals with the steps that are required to be followed in high performance computing with OpenFOAM on the Palmetto cluster as well as post-processing procedures.

After compilation of all OpenFOAM libraries, they need to be loaded once the user is connected to Palmetto. To this end, the following modules/libraries should be added to the account.

```
‡ module add gcc/4.8.1
‡ module add openmpi/1.8.4
```

The double dagger sign denotes the `UNIX` prompt. If newer releases of OpenFOAM need different versions of these libraries, they need to loaded instead. Next, the OpenFOAM environment variables need to be defined for the operating system. This can be done by sourcing the `bashrc` script in the package source file and using the below command.

```
‡ source /software/OpenFOAM/OpenFOAM-2.4.0/etc/bashrc
```

Linear scalability of the OpenFOAM up to 1000 cores are discussed in previous sections. The computational domain of the LES of wind tunnel experiments are run, utilizing 800 Intel Xeon E5-2680v3 Central Processing Units (CPU). Figure B.1 illustrates distribution of the computational domain between

different processors using `scotch` parallelization method which is embedded in OpenFOAM `decomposePar` dictionary.

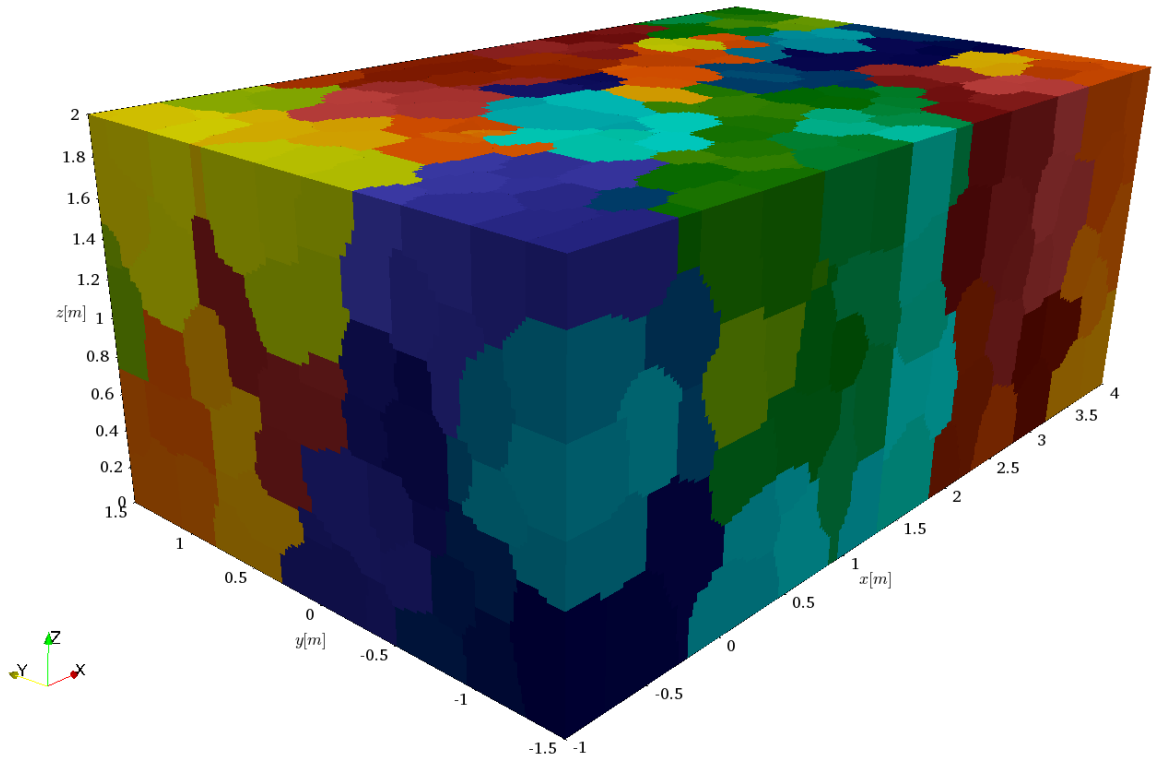

Figure B.1: Shown are the allocated zones of the computational domain to the available processors. Each zone is color coded with the processor identification number in the list of processors.

A sample PBS script for starting a parallel simulation on Palmetto cluster is given below.

```
#!/bin/bash
#PBS -N les-W1-I5-O3
#PBS -l select=40:ncpus=20:mpiprocs=20:mem=124gb
#PBS -l interconnect=fdr:node_manufacturer=intel
#PBS -l chip_type=e5-2680v3:walltime=72:00:00
#PBS -M atohidi@g.clemson.edu
#PBS -m ea
#PBS -j oe

module add gcc/4.8.1
module add openmpi/1.8.4
source /software/OpenFOAM/OpenFOAM-2.4.0/etc/bashrc
```

```
cd $PBS_O_WORKDIR

m4 ./mesh.m4 > ./constant/polyMesh/blockMeshDict

blockMesh > log.Mesh

checkMesh > log.CheckMesh

decomposePar > log.Decomp

mpirun pisoFoam -parallel > log.mpirun

reconstructPar -latestTime

sample -latestTime

touch foam.foam            # End of openfoam simulation
```

For more information on how to write a PBS script, consult with cluster admins. In case Palmetto cluster is being used, visit `http://citi.clemson.edu/palmetto/pages/userguide.html#submitting`. Three seconds of simulation (after the flushing time) for W1-I5-O3 and W2-I10-O5 cases required, respectively, $5.1876 \times 10^6\ s$ and $7.0433 \times 10^6\ s$ CPU time on the cluster.

OpenFOAM comes with its native post-processing package, namely `Paraview`. However, the original version that comes with `OpenFOAM-2.4.0` didn't have the `pvbatch` functionality by which high volume post-processing is done using a `python` script. This was needed in order to extract the velocity fields from all recorded time-steps. Therefore, binary version of the `Paraview-5.0.0` was compiled and installed on the cluster account. The author noticed that `Paraview-5.0.0` shows some display issues with `openmpi/1.8.0` libraries. Therefore, `openmpi/1.6.4` is used instead. After the simulations, there is no need to reconstruct the data from all nodes into individual times intervals. `Paraview` has this ability to read distributed data between different nodes which is very helpful in handling post-processing of the generated data from big simulations. This is done by using `Paraview` in Client-Server Mode.

It is important to have the exact same version of the Paraview as it is on the cluster installed on the local computer (PC/laptop). For launching the Paraview server an interactive job must be submitted to the cluster. However, this may be slightly different for other clusters. Steps of lunching a Paraview server on Palmetto is as follows,

```
‡ qsub -I -l select=6:ncpus=20:mpiprocs=20:ngpus=1\
:mem=120gb,walltime=05:00:00
```

This command is asking for 6 GPU cores, which do the graphic rendering, with 120 CPUS that do the post-processing calculations. Now the server can be launched with,

```
‡ module add gcc/4.8.1 openmpi/1.6.4 Qt/4.8.5
‡ mpiexec -n 120 ParaView-v5.0.0-source/build/bin/pvserver\
-display :0.0 --use-offscreen-rendering --server-port=11111
```

For detailed explanation on each part of above command and setting up a server on cluster see the official Paraview web page at http://www.paraview.org/Wiki/Setting_up_a_ParaView_Server.

Execution of above commands establishes a Paraview server called pvserver which is listening for the connection request from your local port, usually 8080 (this is arbitrary). Ports can be connected by launching another terminal on you local computer and ask for connection through SSH with,

```
‡ ssh -L 8080:node1894:11111\
USERNAME@user.palmetto.clemson.edu.
```

Where *node* < *number* > is the designated ID of the master node on the cluster upon which the sever is launched, and the USERNAME is your cluster access username. Finally, Paraview on the local computer should be launched and connected to the established port, i.e. 11111 in the above example; See the official Paraview user guide for doing so. Once the connection is established, Paraview maybe used as it is being used for data on the local computer. It should be noted that for big data files, if the results are not reconstructed back from the distributed nodes, the case type in Paraview pipeline should be selected as Decomposed.